

Precision theoretical methods for large-scale structure of the Universe

Thèse N°9315

Présentée le 4 avril 2019

à la Faculté des sciences de base

Laboratoire de physique des particules et de cosmologie

Programme doctoral en physique

pour l'obtention du grade de Docteur ès Sciences

par

Mikhail IVANOV

Acceptée sur proposition du jury

Prof. V. Savona, président du jury

Dr S. Sibiryakov, directeur de thèse

Dr P. Creminelli, rapporteur

Dr P. Valageas, rapporteur

Dr J. Blazek, rapporteur

2019

The effort to understand the universe
is one of the very few things that lifts
human life a little above the level of farce,
and gives it some of the grace of tragedy.

— S. Weinberg

Acknowledgments

First of all, I would like to thank my supervisor, Sergey Sibiryakov, for guiding me into the world of academic research. His friendly presence, and constant advice in science and life were a great source of support and inspiration during the course of my bachelor, master and PhD studies. His deep knowledge of physics along with his positive attitude toward life, combined with his wonderful sense of humor, has made for many enjoyable hours of conversation. Besides, I have always been inspired by his ability to see things from a new angle. Sergey has invested a great deal of time and care in my education and career. For me, he has always been an example to follow. Without his patience, support and encouragement, I would not be who I am today.

I am grateful to Diego Blas, Mathias Garny and Alexander Kaurov for being my co-authors in the projects that have become part of this thesis. Our conversations have given me many insights and shaped my own scientific intuition and style. I have been extremely lucky to become part of unique research environments of INR RAS (Moscow), EPFL (Lausanne), CERN (Geneva), and IAS (Princeton). I will always be amazed by these inexhaustible fertile sources of new ideas, profound conversations and the atmosphere of the proximity to discovery. The period of my life spent there was very productive. I have worked on very different topics ranging from astrophysical data analysis to theoretical aspects of quantum gravity. This resulted in ten papers [1–10], lecture notes [11], and an infinite number of ongoing projects that will hopefully be completed one day.

I would like to thank Jonathan Blazek, Paolo Creminelli and Patrick Valageas for being my referees, and Vincenzo Savona for accepting to be the jury president.

It was an incredible privilege for me to get to know, if not work with, three extremely erudite, friendly and brilliant professors, João Penedones, Riccardo Rattazzi, and Mikhail Shaposhnikov. Their incredibly coherent and balanced approach to science, each in his own style, has given me a constant source of inspiration during my studies at EPFL.

My day-to-day research work was fueled by many other people, and it is them whom I would like to thank now, even though half a page will never do justice to their friendliness. In random order, from the bottom of my heart.

This thesis in its current form would have been impossible without help and input from Andrei Shkerin, Inar Timiryasov, Anna Tokareva, Adrien Florio, David Pirtskhalva, Mario Herrero-Valea, Lorenzo Vitale, Georgios Karananas, Javier Rubio, Matias Zalzarriaga, Marko Simonović, Marcel Schmittfull, Zvonimir Vlah, Valentin Assassi, Susan Clark, Colin Hill, Benjamin Wallisch, Liang Dai, Teja Venumadhav, Fedor Popov, Dmitry Levkov, Alexander Panin, Sergey Troitsky, Grigory Rubtsov, Maxim Pshirkov, Emin Nugayev, Dmitry Gorbunov, Valery Rubakov, Mikhail Kuznetsov.

Finally, I am grateful to my friends Anatoly Kozlov, Anton Minnekhanov, Valery Vasiliev, Natasha Porayko, Bulat Nizamov, Pavel Medvedev, Alexander Kazantsev, Tim Keshelava, Pavel Yanchikov; my girlfriend Alexandra, and my family, Galina, Mikhail and Klavdia. Thank you for having supported me in darkest hours of my life and having shared with me the happiest ones.

Scientific life is full of struggle, adversity and suffering you have to go through in order to achieve even a fleeting success. But the process of dealing with these difficulties and getting over them has actually been the most fulfilling part of my life.

Abstract

We develop new analytic methods to accurately describe the formation of cosmic large-scale structure. These methods are based on the path integral formalism and allow one to efficiently address a number of long-standing problems in the field.

We describe the non-linear evolution of the baryon acoustic oscillations (BAO) in the distribution of matter. We argue for the need for resummation of large infrared (IR) enhanced contributions from bulk flows. We show how this can be done via a systematic resummation of Feynman diagrams guided by well-defined power counting rules. We formulate IR resummation both in real and redshift spaces. For the latter we develop a new method that maps cosmological correlation functions from real to redshift space and retains their IR finiteness. Our results agree well with the N-body simulation data at the BAO scales. This establishes IR resummation within our approach as a robust and complete procedure and provides a consistent theoretical model for the BAO feature in the statistics of matter and biased tracers in real and redshift spaces.

Eventually, we perform a non-perturbative calculation of the 1-point probability distribution function (PDF) for the spherically-averaged matter density field. We evaluate the PDF in the saddle-point approximation and show how it factorizes into an exponent given by a spherically symmetric saddle-point solution and a prefactor produced by fluctuations. The prefactor splits into a monopole contribution which is evaluated exactly, and a factor corresponding to aspherical fluctuations. The latter is crucial for the consistency of the calculation: neglecting it would make the PDF incompatible with translational invariance. We compute the aspherical prefactor using a combination of analytic and numerical techniques, identify the sensitivity to the short-scale physics and argue that it must be properly renormalized. Finally, we compare our result with N-body simulation data and find an excellent agreement.

Keywords: cosmology, large-scale structure, IR resummation, baryon acoustic oscillations, power spectrum, redshift space distortions, bias, probability distribution function, spherical collapse, renormalization

Résumé

Nous développons de nouvelles méthodes analytiques pour décrire fidèlement la formation des structures cosmiques à grande échelle. Notre approche est basée sur un formalisme d'intégrale de chemin et permet de résoudre efficacement de nombreuses questions de ce domaine.

Nous décrivons l'évolution non-linéaire des oscillations acoustiques des baryons dans la distribution de matière. Nous discutons de la nécessité de la sommation de grandes contributions infrarouge provenant des flux de masse. Nous montrons comment cela peut être fait via une sommation systématique des diagrammes de Feynman guidée par des règles de comptage des puissances bien définies. Nous formulons cette sommation infrarouge dans les espaces réel ainsi que redshift. Pour ce dernier, nous développons une nouvelle méthode qui relie les fonctions de corrélation cosmologique de l'espace réel à l'espace redshift et conserve le caractère fini des contributions infrarouges. Nos résultats concordent bien avec les données issus de simulations à N-corps aux échelles des oscillations acoustiques des baryons. Nous montrons comment cette nouvelle approche de la sommation infrarouge offre une procédure robuste et auto-cohérente. Cela fournit également un modèle théorique complet pour caractériser les oscillations acoustiques des baryons à partir des statistiques de la matière et des traceurs biaisés dans les espaces réel et redshift.

Enfin, nous effectuons un calcul non-perturbatif de la fonction de distribution à un point de la moyenne sphérique du champ de densité de la matière. Nous évaluons cette fonction de distribution dans l'approximation du point d'équilibre et montrons comment elle se factorise en un exposant, qui est donné par une solution de selle à symétrie sphérique et un préfacteur produit par les fluctuations. Ce préfacteur se divise en une contribution monopolaire évaluée exactement, et un facteur associé aux fluctuations asphériques. Cette dernière contribution est cruciale pour la cohérence du calcul: la négliger rendrait la fonction de distribution incompatible avec l'invariance par translation. Nous calculons ce

préfacteur asphérique en utilisant une combinaison de techniques analytiques et numériques, et identifions le rôle joué par la physique des petites échelles ainsi que l'importance de la renormaliser correctement. Enfin, nous comparons nos résultats avec des données de simulations à N-corps et trouvons un excellent accord.

Mots clés: cosmologie, structure à grande échelle, sommation infrarouge, oscillations acoustiques des baryons, spectre de puissance, distorsions de l'espace redshift, biais, fonction de distribution, effondrement sphérique, renormalisation

Contents

Acknowledgments	ii
Abstract	iv
Résumé	vi
1 Introduction	1
1.1 General remarks	1
1.2 Introduction to part I	6
1.3 Introduction to part II	10
I Non-linear evolution of baryon acoustic oscillations and IR resummation	14
2 Overview of time-sliced perturbation theory for large-scale structure	15
3 IR resummation in real space	20
3.1 TSPT and wiggly-smooth decomposition	22
3.1.1 TSPT in terms of wiggly and smooth elements	23
3.2 IR enhanced diagrams and power counting	26
3.2.1 IR enhanced vertices	26
3.2.2 Leading diagrams and power counting rules	29
3.3 Resummation of leading infrared effects	32
3.3.1 Power spectrum	32
3.3.2 Bispectrum and other n -point correlation functions	34
3.4 Taking into account hard loops	36
3.5 Resummation of infrared effects at next-to leading order	41
3.6 Practical implementation and comparison with other methods	45
3.6.1 Evaluation of IR resummed power spectrum	45
3.6.2 Comparison with other approaches	50
3.6.3 Comparison with N -body data	52
3.6.4 Shift of the BAO peak	55
3.7 Conclusions and outlook	59
4 IR resummation in redshift space	62

4.1	Review of standard redshift space mapping	62
4.2	Redshift space transformation as a 1D fluid flow	64
4.3	TSPT partition function and vertices	66
4.3.1	Density field as a composite operator	69
4.3.2	Feynman rules	71
4.4	IR resummation	71
4.4.1	Wiggly-smooth decomposition	72
4.4.2	IR-enhanced diagrams and power counting	72
4.4.3	IR resummation at leading order	75
4.4.4	Next-to-leading order corrections and hard loops	77
4.5	Bias	78
4.5.1	IR resummation for biased tracers in real and redshift space	81
4.6	Practical implementation and comparison with other methods	83
4.6.1	The power spectrum and bispectrum at leading order	83
4.6.2	The power spectrum and bispectrum at next-to-leading order	86
4.6.3	Comparison with other approaches	88
4.7	Numerical results and comparison with N-body data	89
4.7.1	2-point correlation function: quantitative study	91
4.7.2	Matter power spectrum: comparison with N-body data	93
4.8	Summary and outlook	94

II Non-perturbative probability distribution function of spherically-averaged matter density field 97

5	Path integral derivation from first principles 98
5.1	Path integral for counts-in-cells PDF 98
5.1.1	Spherical collapse saddle point 98
5.1.2	Leading exponent for top-hat window function 102
5.1.3	Prefactor from fluctuations 107
5.2	Closer look at the prefactor 110
5.2.1	Monopole 110
5.2.2	Aspherical prefactor from N-body data 113
6	Accurate calculation of aspherical prefactor 117
6.1	Perturbative calculation at small density contrast 117
6.1.1	Fluctuation determinant in standard perturbation theory 118
6.1.2	Effective field theory corrections 121
6.1.3	Aspherical prefactor at second order in background density 123
6.2	Aspherical prefactor at large density contrasts: main equations 125
6.2.1	Linearized fluctuations with $\ell > 0$ 125
6.2.2	Quadratic fluctuations in the monopole sector 127
6.2.3	Summary of the algorithm 131
6.3	Removing IR divergences in the dipole contribution 132
6.3.1	IR safety of the prefactor 132
6.3.2	Factorization of IR divergences 134
6.4	WKB approximation for high multipoles 137
6.5	Aspherical prefactor: results 144

6.5.1	Evaluation of fluctuation determinants	144
6.5.2	Renormalization of short-scale contributions	147
7	Summary of Part II	152
8	Concluding remarks	157
A	Conventions	160
B	Asymptotic behavior of the Γ_n vertices in the soft limit	163
B.1	Recursion relations for TSPT vertices	163
B.2	Γ_n vertices in the soft limit: leading order	165
B.3	Γ_n vertices in the soft limit: NLO	167
B.4	Asymptotic behavior of RSD vertices in the soft limit	171
C	NLO polynomials	174
D	Shift of the BAO in momentum space	176
E	Bias expansion at one loop	179
F	Simplification of NLO IR resummed integrands: example of bispectrum in redshift space	182
G	Dynamics of spherical collapse	185
G.1	Spherical collapse in Einstein–de Sitter universe	185
G.2	Spherical collapse in Λ CDM	188
G.3	Monopole response matrix	190
G.4	Growth factor in a spherically-symmetric separate universe	193
H	Numerical procedure for aspherical determinants	195
I	A comment on log-normal model	199
	Bibliography	201

Chapter 1

Introduction

1.1 General remarks

Cosmology is one of the most exciting and quickly advancing frontiers of modern physics. The progress in this field is driven by precise astrophysical observations, which have already initiated a revolution in our understanding of Nature. These observations have firmly established the standard cosmological model, implying the existence of new physical phenomena: dark matter, dark energy, and inflation. On the other hand, the precise nature of these phenomena is yet to be elucidated.

Dark matter is a substance analogous to ordinary matter in many ways, but not interacting with light, which makes it invisible to us. As of now, one can only be certain that dark matter interacts gravitationally. The evidence for dark matter has been found in many independent observations: galaxy cluster kinematics, gravitational lensing, galaxy rotation curves, structure formation, anisotropy patterns of the temperature of the cosmic microwave background (CMB). Despite all this evidence, the nature of dark matter remains one of the most challenging open questions in modern physics. The simplest model that fits all the observational data¹ is the so-called ‘cold dark matter’ (CDM), which consists of heavy particles that are singlets under the Standard Model gauge group and have a very weak, if any, self-interaction.

Unlike dark matter, the properties of dark energy are quite exotic. In particular, it must have negative pressure. This pressure is required to explain the

¹It should be mentioned that there are so-called short-scale CDM problems, e.g. ‘core vs. cusp’, ‘missing satellites’, ‘too-big-to-fail’ etc. However, at the moment it is not clear if they are really drawbacks of the CDM model or artifacts of numerical simulations.

accelerated expansion of the universe, which has been independently inferred from the type Ia supernovae, galaxy clusters, baryon acoustic oscillations and the CMB. The simplest model for dark energy is the so-called cosmological constant, a constant term Λ in the right hand side of the Einstein general relativity equations. However, this solution has a serious drawback as there is no mechanism that would robustly explain the smallness of the cosmological constant and its stability against quantum corrections (this issue is known as ‘the cosmological constant problem’ [12]). Despite this problem, the cosmological constant is very successful at the phenomenological level and, along with the dark matter discussed above, underlies the minimal standard cosmological model dubbed Λ CDM (Λ -Cold Dark Matter).

Another phenomenon supported by recent observations is cosmic inflation. Historically, the theory of the hot big bang did not have any natural explanation for the small spatial curvature observed in our universe. Besides, there were issues with the properties of the initial fluctuations that evolved into the observed inhomogeneities in the CMB temperature and matter distribution. Namely, the hot big bang theory could not account for the observed smallness of fluctuations and their correlation at scales that exceeded the size of causal patches in the past. Moreover, the hot big bang theory did not have a mechanism that would produce such fluctuations and could not explain their flat (frequency-independent) spectrum, suggested by observations. These issues were resolved in the theory of cosmic inflation, which suggests that the universe has undergone a period of accelerated expansion prior to the hot big bang evolution. This expansion has smoothed out the spatial curvature of the universe and stretched out initial causally-connected patches to tremendous sizes. Moreover, during inflation the fluctuations of quantum fields, whose existence is guaranteed by the uncertainty principle of quantum mechanics, have become classical and turned into inhomogeneities of classical fields sourcing primordial fluctuations. In this setup the smallness of the fluctuations is a consequence of the scale separation between the characteristic densities of the universe at inflation ($\lesssim (10^{16} \text{ GeV})^4$) and quantum gravity ($\lesssim (10^{19} \text{ GeV})^4$). In turn, the observed (approximate) flatness of the initial spectrum is a direct consequence of an exponentially fast growth of the universe during inflation. As inflation is characterized by extreme densities that could be as high as $(10^{16} \text{ GeV})^4$, the fluctuations generated at this stage provide us with a unique opportunity to probe these energy scales via cosmological observations.

Apart from exotic phenomena like dark energy or inflation, cosmology can also give us new knowledge about elementary particles that are commonly studied at

accelerators. An important example is the neutrino. In the renormalizable part of the Standard Model for particle physics the neutrinos are similar to the other leptons (electron, muon, τ -lepton), but have zero mass and couple to other particles only via the weak interactions. On the other hand, the observed oscillation of neutrino flavors implies that neutrinos must have non-vanishing masses. Due to this reason the neutrinos have become a textbook example of new physics beyond the Standard Model. Remarkably, the scale of an effective operator producing the neutrino mass in the Standard Model (the Weinberg operator) has the same order of magnitude as the typical scale of inflation, which might indicate a profound relation between the two phenomena. Neutrino masses also have a sizable effect on cosmology. Despite the fact that neutrinos interact with ordinary matter quite weakly, their gravitational interaction is non-negligible, and leaves a peculiar imprint on the CMB temperature fluctuations and cosmic matter distribution. By constraining these effects one is able to bound the neutrino mass from above an order of magnitude tighter than from the reactor and accelerator experiments [13].

The bulk of our recent progress in cosmology has been due to the CMB observations. Impressive as they are, CMB measurements are fundamentally limited in the amount of information due to the fact that this information is gathered from a two-dimensional celestial sphere. On the other hand, the distribution of matter on cosmological scales, called large-scale structure (LSS), provides us with a three-dimensional data volume (one additional dimension is given by redshift). Potentially, this helps us get access to a much bigger number of Fourier modes, which may eventually reduce measurement errors on fundamental cosmological parameters. Thus, one can expect LSS to become the leading cosmological probe in future.

Typically, the most common LSS observables are different kinds of *tracers*: galaxies, galaxy clusters, Lyman- α forest absorption lines, gravitational lensing field etc. These objects are called tracers because they trace the distribution of matter, most of which consists of dark matter. The distribution of matter and tracers is not random. Moreover, it reflects the dynamics of our universe, along with its composition and initial conditions set prior to the hot big-bang evolution. In particular, measurements of baryon acoustic oscillations (to be described in detail shortly) provide us with information on the expansion rate of the universe, its geometry, the properties of dark matter and dark energy. Another example is the effect of massive neutrinos. They suppress matter density fluctuations at scales smaller than ~ 100 Mpc, which is a detectable effect that potentially will allow one to measure the sum of neutrino masses.

At the moment, there are several LSS surveys already in operation, e.g. SDSS², DES³, and many more will be available in the future, e.g. the Euclid satellite⁴ (launch in 2020), DESI⁵ (start in 2019), LSST⁶ (start in 2023). These surveys will cover immense ranges of distances, which contain new information on the fundamental properties of the universe. However, harvesting this information will not be an easy task and will require a precise theoretical understanding of self-gravitating systems in the non-linear regime along with efficient techniques to analyze data in order to extract fundamental properties of nature from the observed signals. The most straightforward approach to this problem relies on current computer power to produce realistic N-body simulations. Despite significant progress over recent years, reaching a sub percent accuracy in these simulations still remains computationally expensive [14]. This makes desirable the development of (semi-)analytic approaches to LSS. Being perhaps less powerful than N-body simulations in the description of the standard Λ CDM cosmology, analytic approaches provide us with a large flexibility in going beyond it and a deep insight in the relevance of different physical processes, along with efficient ways of extracting the relevant cosmological information.

This thesis is devoted to the precision methods that ameliorate our theoretical understanding of large-scale structure. The main difficulty in describing LSS are non-linear effects of gravitational clustering. The density and velocity of matter rapidly grow with time as a consequence of gravitational attraction and their distribution becomes very non-Gaussian. On the other hand, the characteristic densities on largest scales (only a few times smaller than the cosmic horizon) remain small, which suggests that non-linear clustering may be captured within perturbation theory over the matter density contrast.

Standard perturbation theory (SPT) of LSS formation [15] is one of the most popular perturbative techniques. It consists of two main steps: first, one expresses the dark matter density and velocity fields at a given time as a power series of the initial conditions, assuming a perfect pressureless fluid. Next, one performs the ensemble average using the statistical distribution at the initial time when the system is well within the linear regime. The initial distribution is often taken to be Gaussian⁷, as motivated by the constraints coming from the

²<https://www.sdss.org>

³<https://www.darkenergysurvey.org>

⁴<https://www.euclid-ec.org>

⁵<https://www.desi.lbl.gov>

⁶<https://www.lsst.org>

⁷It is worth stressing that the precise form of the distribution should be provided by the theory describing the generation of primordial fluctuations. Disentangling the primordial non-Gaussianity from the secondary one induced by non-linear dynamics constitutes one of the goals of the LSS studies.

cosmic microwave background measurements. This framework leads to a loop expansion for non-linear corrections to cosmological correlation functions and has provided numerous insights into their properties.

SPT calculations are complicated by several effects, which have recently attracted significant attention. They can be attributed to the sensitivity of the SPT framework to infrared (IR) and ultraviolet (UV) modes. The coupling between different scales is a generic consequence of non-linear dynamics. It generates large contributions both from very small (IR) and very large (UV) wavenumbers in SPT loop integrals. These contributions are somewhat loosely referred to as “IR/UV divergences” even for Λ CDM, where the integrals actually converge.

Qualitatively the appearance of IR divergences in SPT stems from the use of the initial distribution to evaluate quantities at late times. This introduces non-local time dependence to large displacements of fluid particles caused by large scale bulk flows. It is well known that the IR divergences cancel out in equal-time correlators upon summing over all sub-diagrams at a fixed order in perturbation theory [16]. This cancellation has been formally proven for *leading* IR divergences to all orders of perturbation theory [17] and can be traced back to the equivalence principle [18, 19]. Recently, the cancellation has been proven also for *subleading* IR divergences showing up for the first time at 2 loops [20–24]. Still, the presence of spurious IR divergences greatly complicates numerical calculations⁸ and obscures the analysis of physical effects produced by large scale bulk flows. The latter, though finite, have a strong impact on the features in the cosmological correlation functions [26]. In particular, a resummation of physical IR contributions is essential for an accurate description of baryon acoustic oscillations (BAO) in the power spectrum [26–29].

Another problem is related to the unphysical sensitivity of SPT to short-scale (UV) modes. This sensitivity arises because the perfect fluid hydrodynamical description breaks down at short scales. This problem has been addressed within the effective field theory of large scale structure [30, 31] that captures the departures from Eulerian hydrodynamics by introducing so-called UV counterterms, which are to be fixed from data or N -body simulations, see [32, 33]. The counterterms proliferate when going to shorter scales and exhibit non-local time-dependence, which complicates the renormalization at high loop order [34] and compromises predictability of the theory.

⁸IR-safe integrands have been constructed in [20, 21] for 2 loops and in [25] for an arbitrary L -loop order.

Perturbation theory has given us many insights into non-linear clustering, however, there are questions which can be rigorously addressed only beyond perturbative calculations, e.g. one-halo corrections, the halo mass function, the distribution of the non-linear density field, etc. This thesis covers both perturbative and non-perturbative results. It is devoted to two particularly interesting questions: accurate description of baryon acoustic oscillations and counts-in-cells statistics.

Baryon acoustic oscillations are plasma waves that were propagating in the universe prior to recombination. After recombination baryons decoupled from photons and formed a single fluid with dark matter. This way BAO got imprinted in the spatial distribution of matter. The characteristic scale of the BAO is constant across redshifts, hence it provides us with a powerful ‘standard ruler’ that helps elucidate the evolution of the universe. However, the BAO pattern in the distribution of galaxies gets distorted by non-linear effects of bulk flows. These effects are studied in the first part of the thesis. The main outcome of this study is the development of a rigorous and systematic procedure for the resummation of IR-enhanced contributions that alter the BAO, so - called *IR resummation*.

The second part of the thesis is devoted to the counts-in cells statistics. The counts-in-cells method amounts to splitting the matter density field into spherical cells in position space and taking an average of this field inside each cell. The distribution of cells over the relevant variable reveals statistical properties of the underlying field. In this thesis we will compute the 1-point probability distribution function (PDF) of finding a certain average matter density in a sphere of a given fixed radius r_* . The deviation of this spherically-averaged density from the mean density of the universe need not be small, hence the desired PDF cannot be calculated within perturbation theory. The goal is to derive the PDF from first principles and figure out its dependence on cosmological parameters and initial conditions.

Below we give more detail on the questions addressed in the thesis. For convenience, each topic will be discussed in a separate section.

1.2 Introduction to part I

Part I of this thesis is dedicated to baryon acoustic oscillations.

The BAO are one of the most powerful tools of precision cosmology. The BAO pattern has been observed across various redshifts in the 2-point correlation

function of the distribution of galaxies (see [35, 36] for the first measurements and [37, 38] for recent ones), Ly α forest absorption [39, 40], quasars [6, 41], and voids [42, 43]. Recently, the BAO signal has also been detected in the 3-point correlation function [44–46]. The significance of the BAO measurements for cosmology calls for improving the analytic understanding of the BAO feature in the non-linear regime and robustly controlling the theoretical uncertainty.

Since the characteristic scale of the BAO ($r_{BAO} \sim 110 \text{ Mpc}/h$) is much larger than the non-linear scale $1/k_{NL} \sim 10 \text{ Mpc}/h$, one could a priori expect that the non-linear evolution of the BAO should be well captured by lowest-order perturbative corrections. Nevertheless, it has been observed long ago that the leading non-linear correction computed in SPT fails to reproduce the behavior seen in N-body simulations or data. The source of this disagreement is the non-linear coupling of the BAO to the bulk flows. Qualitatively, bulk flows move the pairs of tracers that used to be at separations r_{BAO} to larger or smaller distances, which degrades their spatial correlation and thus reduces the observed BAO signature. This effect is more severe in redshift space where the apparent separation of tracers along the line-of-sight is additionally altered by peculiar velocities. Besides, the BAO signal is further deformed by non-linear bias.

In Eulerian perturbation theory, the coupling between a mode with wavenumber k to bulk motions is enhanced as k/q , with $q \ll k$ being the wavelength of a large-scale fluctuation. For equal-time correlation functions, the equivalence principle implies that this infrared (IR) enhancement largely cancels out when summing all perturbative contributions at a fixed order in perturbation theory [17, 18, 20, 22–24]. However, the cancellation is incomplete if the matter power spectrum has a feature that oscillates with characteristic frequency $k_{osc} = 1/r_{BAO} \lesssim q \ll k$ [28, 29].

Several approaches have been put forward to deal with these effects. Most of the damping of the BAO is produced by Lagrangian displacements of matter. Thus, the process of erasing the BAO signal can be undone by reversing tracers' trajectories and moving them back to their initial Lagrangian positions. This method, called reconstruction [47–53], has become a standard tool in the BAO data analysis. Typically, reconstruction is used to increase the signal in measurements of the BAO scale obtained upon marginalizing over the broad-band shape and amplitude of the underlying correlation function (or power spectrum), see e.g. [54, 55]. On the other hand, full shape measurements without reconstruction reveal the rich cosmological information encoded in the entire power spectrum,

see e.g. [56–59]. In particular, the full shape measurements yield constraints on structure growth rate through redshift-space distortions [60, 61].

The interpretation of the full shape BAO measurements relies on theoretical modeling based on perturbation theory. Following early works on the subject [26, 27, 62, 63], it has been realized how the physical effects of bulk flows can be resummed to all orders in perturbation theory [28, 64–66], and how this procedure, called IR-resummation, is related to the equivalence principle [29, 67]. The analysis was also extended to the power spectrum of biased tracers in redshift space [68–70].

In the references mentioned above IR resummation was performed for the power spectrum at leading order in the soft corrections. Generalization of these results to arbitrary n -point correlation functions and subleading soft corrections along with a robust estimation of the theoretical error remain open problems. To confidently solve these problems one has to develop a systematic framework for IR resummation that would allow one to go to an arbitrary order of precision in a controllable way. Besides, it is desirable that this method has a diagrammatic representation similar to that of the procedure to eliminate IR divergences in gauge theory and gravity amplitudes.

In the first part of the thesis, we introduce a systematic approach to describe non-linear effects on the BAO feature in equal-time correlation functions based on time-sliced perturbation theory (TSPT) [1]. TSPT is a proposal to describe the statistical properties of the large-scale structure based on the evolution of the distribution function, as opposed to SPT where the individual field variables are evolved. A major advantage of this description is that it eliminates spurious IR contributions from the beginning, and therefore allows for a transparent description of the physical effects of bulk motion on the BAO feature.

We will also show that TSPT provides one with a convenient framework to study redshift space distortions. The key observation is that the coordinate transformation relating real and redshift spaces can be seen as a free 1-dimensional fluid flow. We introduce a fictitious time, over which this flow evolves, and study the evolution of statistical properties of the flow along the lines of TSPT. This auxiliary time will be loosely referred to as ‘redshift time’. In this picture the initial redshift time slice corresponds to real space, the final one to redshift space. Using this scheme, the redshift space statistical cumulants can be easily obtained from their real space counterparts.

We also discuss how to incorporate bias into our framework. In the case of deterministic bias the tracers' density is a function of the matter density field and thus it is not a statistically independent variable. Such variables are naturally described in TSPT as composite operators. We will show how the correlation functions of biased tracers can be obtained within TSPT and discuss the effect of IR resummation on them.

Our method gives an alternative way to compute equal-time correlation functions of cosmological fields in redshift space that explicitly retains their IR safety. This property helps us identify the physical IR-enhanced contributions and resum them in a systematic and controllable way, which provides us with a powerful tool to explore the non-linear BAO physics both in real and redshift spaces. Our main result is a systematic technique to identify and resum enhanced infrared contributions affecting the BAO feature. It admits a simple diagrammatic representation within TSPT and allows one to compute higher-order corrections and IR resum arbitrary n -point functions in a systematic way.

Part I is organized as follows. In Chapter 2 we outline the basic formalism. Chapter 3 is devoted to IR resummation in real space. In Sec. 3.2 we describe how to identify the enhanced IR-effects and establish the power counting rules. The resummation of LO contributions is performed in Sec. 3.3 for the power spectrum and bispectrum. In Sec. 3.4 we extend the resummation to diagrams with loops of short modes. Next-to-leading IR contributions are resummed in Sec. 3.5 and a concise formula for the resummed correlation functions is derived. In Sec. 3.6 we discuss the practical implementation of our procedure, compare our result to N -body data and discuss the BAO shift. Section 3.7 is devoted to conclusions and discussion of future directions. Appendices B.1–D contain details of the calculations.

Chapter 4 is dedicated to IR resummation in redshift space. In Section 4.1 we review the standard approach to redshift space distortions. In Section 4.2 we introduce a new redshift space mapping by means of the 1D flow analogy. In Section 4.3 we construct the redshift-space probability distribution function and the corresponding TSPT generating functional. In Section 4.4 we discuss the IR resummation of matter correlation functions in redshift space. In Section 4.5 we include bias in our IR resummation procedure. In Section 4.6 we describe how to practically evaluate IR resummed power spectra and bispectra at leading and next-to-leading order. Section 4.7 is devoted to a quantitative analysis of our results and their comparison to N -body data. Section 4.8 draws conclusions and points future directions. Appendix E is devoted to some useful expressions

for the bias and RSD kernels. In Appendix F we discuss possible simplifications of the redshift-space IR-resummed integrands that make them convenient for numerical evaluation.

1.3 Introduction to part II

In the second part of the thesis we will present a non-perturbative calculation for the probability distribution function of the spherically-averaged matter density field.

The counts-in-cells statistics are one of the classic observables in LSS. The distribution of galaxies in 2-dimensional angular cells on the sky was first measured by E. Hubble [71], who noticed that it is close to log-normal. For the total matter density this has been recently tested in [72, 73]. The log-normal distribution was also suggested as a model for the 1-point PDF in the case of three-dimensional cells [74] and has been quite successful in describing both N-body simulations [75, 76] and observational data [77, 78]. However, as pointed out in [79, 80], this success appears to be accidental and is due to the specific shape of the power spectrum at mildly non-linear scales. Recent high-accuracy N-body simulations performed in [81] revealed significant deviations of the measured PDF from the log-normal fit.

Pioneering calculations of the counts-in-cells PDF from first principles were performed in Refs. [79, 82] using insights from perturbation theory. This study was extended beyond perturbation theory in Refs. [83–85], where it was argued that the most probable dynamics producing a given overdensity in a spherical cell respects the symmetry of the problem, i.e. it is given by spherical collapse. Recently, these calculations were revisited in the context of the Large Deviation Principle (LDP) [86]. In particular, Ref. [87] introduced the logarithmic density transformation to avoid certain problems associated with the application of LDP directly to the density PDF [88]. This formalism has been applied to joint PDF of densities in two cells [89–91] and to biased tracers [92]. An alternative approach to the counts-in-cells statistics developed in [93–95] is based on the Lagrangian-space description of LSS. Ref. [96] recently derived 1-point PDF in a toy model of $(1 + 1)$ dimensional universe. Counts-in-cells statistics were suggested as promising probes of primordial non-Gaussianity [97, 98] and as a suitable tool to analyze the future 21 cm intensity mapping data [99].

We will use the path-integral approach to counts-in-cells pioneered in [85, 97]. In this approach the calculation of the 1-point PDF closely resembles a calculation of instanton effects in quantum field theory (QFT). Following Part I of this thesis, we introduce a formal parameter characterizing the overall amplitude of the matter power spectrum and argue that it plays a role of the coupling constant in the theory. When the coupling is small, the path integral defining the 1-point PDF can be evaluated in the saddle-point (‘semiclassical’) approximation. Thereby the PDF factorizes into the exponential part given by the leading saddle-point configuration and a prefactor coming from integration over small fluctuations around the saddle-point solution. We confirm the assertion [85] that the saddle-point configuration corresponds to the spherically symmetric dynamics. In this way we recover the well-known result [85–87, 94, 95] for the leading exponential part of the PDF. Our key result is computation of the prefactor due to aspherical perturbations around the spherical collapse which has not been done in the previous works. We will demonstrate that this ‘aspherical prefactor’ is crucial for the consistency of the saddle-point calculation. In particular, it is required to ensure that the mean value of the density contrast vanishes.

In the QFT analogy, evaluation of the aspherical prefactor amounts to a 1-loop computation in a non-trivial background. As such, it is instructive in several respects. First, it shows how the vanishing of the mean density contrast is related to the translational invariance of the theory, spontaneously broken by the position of the cell. Second, the sector of dipole perturbations exhibits ‘IR divergences’ at intermediate steps of the calculation associated to large bulk flows. We show that the equivalence principle ensures cancellation of these divergences. We devise a procedure to isolate the IR-enhanced contributions and cancel them analytically, prior to any numerical evaluation. Finally, the contributions of high multipoles are sensitive to short-distance dynamics and must be renormalized. Unfortunately, it is impossible to unambiguously fix the renormalization procedure from first principles. We isolate the ‘UV-divergent’ part of the prefactor and consider two models for its renormalization, differing by the dependence of the corresponding counterterm on the density contrast. Both models use as input the value of the counterterm for the 1-loop power spectrum, and thus do not introduce any new fitting parameters. We suggest to use the difference between the two models as an estimate of the theoretical uncertainty introduced by renormalization. This uncertainty is less than percent in the range of moderate cell densities, $\rho_{\text{cell}}/\rho_{\text{univ}} \in [0.5, 2]$, where ρ_{univ} is the average density of the universe, and degrades to 30% for extreme values $\rho_{\text{cell}}/\rho_{\text{univ}} = 0.1$ or $\rho_{\text{cell}}/\rho_{\text{univ}} = 10$ at $z = 0$.

To verify our approach we ran a suite of N-body simulations⁹ using the **FastPM** code [100]. The numerical studies are performed for the following cosmology: a flat Λ CDM with $\Omega_m = 0.26$, $\Omega_b = 0.044$, $h = 0.72$, $n_s = 0.96$, Gaussian initial conditions, $\sigma_8 = 0.794$. This is the same choice as in Ref. [91] which used the counts-in-cells distribution extracted from the Horizon run 4 simulation [101]; it facilitates a direct comparison between our results and those of [91].

The predictions of our method are found to be in complete agreement with the results of N-body simulations. First, the 1-point PDF clearly exhibits the semiclassical scaling. The aspherical prefactor extracted from the N-body data shows a very weak dependence on redshift or the radius of the cell, as predicted by theory. Second, the data fall inside the range spanned by our theoretical uncertainty. Remarkably, one of the counterterm models matches the data within the accuracy of the simulations throughout the whole range of available densities, $\rho_{\text{cell}}/\rho_{\text{univ}} \in [0.1, 10]$, at all redshifts and for different cell radii.

Part II of the thesis is organized as follows. In Sec. 5.1 we introduce the path integral representation of the 1-point PDF, identify its saddle point and demonstrate the factorization of the PDF into the leading exponent and prefactor. We evaluate the leading exponential part. In Sec. 5.2 we evaluate explicitly the prefactor due to spherically symmetric perturbations and discuss the general properties of the aspherical prefactor. We compare the theoretical expectations with the prefactor extracted from the N-body data and provide simple fitting formulas for it. The rest of part II is devoted to the calculation of the aspherical prefactor from first principles. In Sec. 6.1 we compute the aspherical prefactor at small values of the density contrast using perturbation theory. In Sec. 6.2 we derive the set of equations describing the prefactor in the non-perturbative regime of large density contrasts and present an algorithm for its numerical evaluation. In Sec. 6.3 we modify the algorithm for the sector of dipole perturbations in order to explicitly factor out and cancel the IR-enhanced contributions. In Sec. 6.4 we compute the contributions of high multipoles using the Wentzel–Kramers–Brillouin (WKB) approximation. In Sec. 6.5 we present our numerical results for the aspherical prefactor, discuss the contribution of short-distance physics and its renormalization. Section 7 contains a summary of our results and discussion.

Several appendices contain supplementary material. Appendix A summarizes our conventions. In Appendix G we review the dynamics of spherical collapse in Einstein–de Sitter (EdS) and Λ CDM universes. Appendix H contains details of our numerical procedure. In Appendix I we comment on the log-normal model

⁹The details of the simulations are described in Appendix B of the original paper [9].

for the counts-in-cells statistics. Some other additional material relevant for the calculation of the aspherical prefactor can be found in the appendices of the original paper Ref. [9].

Finally, Chapter 8 discusses main results of the thesis and draws conclusions.

Part I

Non-linear evolution of baryon acoustic oscillations and IR resummation

Chapter 2

Overview of time-sliced perturbation theory for large-scale structure

In this section we give a brief review of TSPT for matter in real space [1]. We are interested in the correlation functions of the overdensity field $\delta = (\rho - \bar{\rho})/\bar{\rho}$ and the velocity divergence field $\Theta \propto \nabla \cdot \mathbf{v}$, whose time-evolution is governed by the continuity and Euler equations for the peculiar flow velocity \mathbf{v} ,

$$\frac{\partial \delta}{\partial \tau} + \nabla \cdot [(1 + \delta)\mathbf{v}] = 0, \quad (2.1a)$$

$$\frac{\partial \mathbf{v}}{\partial \tau} + \mathcal{H}\mathbf{v} + (\mathbf{v} \cdot \nabla)\mathbf{v} = -\nabla\phi, \quad (2.1b)$$

where $\nabla^2\phi = \frac{3}{2}\mathcal{H}^2\Omega_m\delta$ and $\mathcal{H} = aH$. Here τ is conformal time and Ω_m is the matter density fraction. It is well-known [15] that in the case of an Einstein–de Sitter universe these equations can be cast in a form free from any explicit time dependence by introducing the time parameter $\eta = \ln D$, where D is the linear growth factor, and appropriately rescaling the velocity divergence

$$\Theta = -\frac{\nabla \cdot \mathbf{v}}{\mathcal{H}f} \quad (2.2)$$

with $f = d \ln D / d \ln a$. For the realistic Λ CDM cosmology, the substitution (2.2) into (2.1) leaves a mild residual time dependence which, however, has little effect on the dynamics. Following conventional practice we will neglect this explicit time dependence in the equations of motion, but keep the factor f when it appears in redshift space quantities.

The linear growth factor D plays the role of the expansion parameter in TSPT. In order to emphasize this, and in analogy to notation used in quantum field theory, we denote it by

$$g(\eta) \equiv e^\eta = D(z). \quad (2.3)$$

In Fourier space Eqs. (2.1) can be rewritten as¹

$$\begin{aligned} \partial_\eta \delta_{\mathbf{k}} - \Theta_{\mathbf{k}} &= \int_{\mathbf{q}_1} \int_{\mathbf{q}_2} (2\pi)^3 \delta_{\mathbf{D}}^{(3)}(\mathbf{k} - \mathbf{q}_{12}) \alpha(\mathbf{q}_1, \mathbf{q}_2) \Theta_{\mathbf{q}_1} \delta_{\mathbf{q}_2}, \\ \partial_\eta \Theta_{\mathbf{k}} + \frac{1}{2} \Theta_{\mathbf{k}} - \frac{3}{2} \delta_{\mathbf{k}} &= \int_{\mathbf{q}_1} \int_{\mathbf{q}_2} (2\pi)^3 \delta_{\mathbf{D}}^{(3)}(\mathbf{k} - \mathbf{q}_{12}) \beta(\mathbf{q}_1, \mathbf{q}_2) \Theta_{\mathbf{q}_1} \Theta_{\mathbf{q}_2}, \end{aligned} \quad (2.4)$$

with non-linear kernels

$$\alpha(\mathbf{k}_1, \mathbf{k}_2) \equiv \frac{(\mathbf{k}_1 + \mathbf{k}_2) \cdot \mathbf{k}_1}{k_1^2}, \quad \beta(\mathbf{k}_1, \mathbf{k}_2) \equiv \frac{(\mathbf{k}_1 + \mathbf{k}_2)^2 (\mathbf{k}_1 \cdot \mathbf{k}_2)}{2k_1^2 k_2^2}. \quad (2.5)$$

In this thesis we will use the notation

$$\mathbf{q}_{1\dots n} = \mathbf{q}_1 + \mathbf{q}_2 + \dots + \mathbf{q}_n. \quad (2.6)$$

The initial distribution of the density and velocity fields is Gaussian, i.e. it is fully characterized by a two-point cumulant, called the power spectrum,

$$\langle \delta_{\mathbf{k}} \delta_{\mathbf{k}'} \rangle = \langle \Theta_{\mathbf{k}} \Theta_{\mathbf{k}'} \rangle = (2\pi)^3 \delta_{\mathbf{D}}^{(3)}(\mathbf{k} + \mathbf{k}') P(k) \quad \text{at} \quad \eta \rightarrow -\infty. \quad (2.7)$$

The main idea of the TSPT approach is to substitute the time evolution of δ and Θ by that of their time dependent probability distribution functional. This idea is particularly useful when one is only interested in equal time correlation functions. For adiabatic initial conditions only one of the two fields is statistically independent. We choose it to be the velocity divergence field Θ and denote its probability distribution functional by $\mathcal{P}[\Theta; \eta]$. At any moment in time, the field δ can be expressed in terms of Θ as

$$\delta_{\mathbf{k}} = \delta[\Theta; \eta, \mathbf{k}] \equiv \sum_{n=1}^{\infty} \frac{1}{n!} \int_{\mathbf{q}_1} \dots \int_{\mathbf{q}_n} K_n^{(r)}(\mathbf{q}_1, \dots, \mathbf{q}_n) (2\pi)^3 \delta_{\mathbf{D}}^{(3)}(\mathbf{k} - \mathbf{q}_{1\dots n}) \prod_{j=1}^n \Theta(\eta, \mathbf{q}_j), \quad (2.8)$$

with $K_1^{(r)} = 1$. In what follows we will use the superscript (r) to denote quantities defined in usual position space, which is also called ‘real space’ as opposed to redshift space, for which we will use the superscript (s) .

¹Our conventions are discussed in Appendix A.

Equation (2.8) can be used to eliminate the density field from Eq. (2.1) and obtain a closed equation for the velocity divergence,

$$\partial_\eta \Theta(\eta, \mathbf{k}) = \mathcal{I}[\Theta] \equiv \sum_{n=1}^{\infty} \frac{1}{n!} \int_{\mathbf{q}_1 \dots \mathbf{q}_n} I_n^{(r)}(\mathbf{q}_1, \dots, \mathbf{q}_n) (2\pi)^3 \delta_D^{(3)}(\mathbf{k} - \mathbf{q}_{1\dots n}) \prod_{j=1}^n \Theta(\eta, \mathbf{q}_j), \quad (2.9)$$

with $I_1^{(r)} \equiv 1$ corresponding to the growing mode in the perfect fluid approximation. The kernels $K_n^{(r)}$ and $I_n^{(r)}$ are found recursively using the relations,

$$K_2^{(r)}(\mathbf{k}_1, \mathbf{k}_2) = \frac{4}{7} \left(1 - \frac{(\mathbf{k}_1 \cdot \mathbf{k}_2)^2}{k_1^2 k_2^2} \right), \quad (2.10a)$$

$$I_2^{(r)}(\mathbf{k}_1, \mathbf{k}_2) = 2\beta(\mathbf{k}_1, \mathbf{k}_2) + \frac{3}{2} K_2^{(r)}(\mathbf{k}_1, \mathbf{k}_2), \quad (2.10b)$$

$$\begin{aligned} K_n^{(r)}(\mathbf{k}_1, \dots, \mathbf{k}_n) = & \frac{2}{2n+3} \left[\sum_{i=1}^n \alpha(\mathbf{k}_i, \sum_{1 \leq j \leq n, j \neq i} \mathbf{k}_j) K_{n-1}^{(r)}(\mathbf{k}_1, \dots, \check{\mathbf{k}}_i, \dots, \mathbf{k}_n) \right. \\ & - \sum_{1 \leq i < j \leq n} I_2^{(r)}(\mathbf{k}_i, \mathbf{k}_j) K_{n-1}^{(r)}(\mathbf{k}_i + \mathbf{k}_j, \mathbf{k}_1, \dots, \check{\mathbf{k}}_i, \dots, \check{\mathbf{k}}_j, \dots, \mathbf{k}_n) \\ & \left. - \frac{3}{2} \sum_{p=3}^{n-1} \frac{1}{p!(n-p)!} \sum_{\sigma} K_p^{(r)}(\mathbf{k}_{\sigma(1)}, \dots, \mathbf{k}_{\sigma(p)}) K_{n-p+1}^{(r)}\left(\sum_{l=1}^p \mathbf{k}_{\sigma(l)}, \mathbf{k}_{\sigma(p+1)}, \dots, \mathbf{k}_{\sigma(n)}\right) \right], \quad (2.10c) \end{aligned}$$

$$I_n^{(r)}(\mathbf{k}_1, \dots, \mathbf{k}_n) = \frac{3}{2} K_n^{(r)}(\mathbf{k}_1, \dots, \mathbf{k}_n), \quad n \geq 3. \quad (2.10d)$$

Equal-time correlation functions for Θ and δ can be obtained by taking functional derivatives with respect to the external sources J and J_δ , respectively, of the following partition function,

$$Z[J, J_\delta; \eta] = \int [\mathcal{D}\Theta] \mathcal{P}[\Theta; \eta] \exp \left\{ \int_{\mathbf{k}} \Theta_{\mathbf{k}} J(-\mathbf{k}) + \int_{\mathbf{k}} \delta[\Theta; \eta, \mathbf{k}] J_\delta(-\mathbf{k}) \right\}. \quad (2.11)$$

The probability density functional satisfies the Liouville equation which reflects the conservation of probability,

$$\frac{\partial}{\partial \eta} \mathcal{P}[\Theta; \eta] + \int_{\mathbf{k}} \frac{\delta}{\delta \Theta(\mathbf{k})} (\mathcal{I}[\Theta; \eta] \mathcal{P}[\Theta; \eta]) = 0. \quad (2.12)$$

In perturbation theory one can represent (logarithm of) $\mathcal{P}[\Theta; \eta]$ as a power series in Θ ,

$$\mathcal{P}[\Theta; \eta] = \mathcal{N}^{-1} \exp \left\{ - \sum_{n=1}^{\infty} \frac{1}{n!} \int_{\mathbf{k}_1 \dots \mathbf{k}_n} \Gamma_n^{(r) \text{tot}}(\eta; \mathbf{k}_1, \dots, \mathbf{k}_n) \prod_{j=1}^n \Theta_{\mathbf{k}_j} \right\}, \quad (2.13)$$

where \mathcal{N} is a normalization factor. Substituting this representation into (2.12) and using Eq. (2.9) we obtain the following chain of equations on the vertices,

$$\begin{aligned} & \partial_\eta \Gamma_n^{(r) tot}(\eta; \mathbf{k}_1, \dots, \mathbf{k}_n) + \sum_{m=1}^n \frac{1}{m!(n-m)!} \sum_{\sigma} I_m^{(r)}(\eta; \mathbf{k}_1, \dots, \mathbf{k}_m) \\ & \times \Gamma_{n-m+1}^{(r) tot}(\eta; \sum_{l=1}^m \mathbf{k}_{\sigma(l)}, \mathbf{k}_{\sigma(m+1)}, \dots, \mathbf{k}_{\sigma(n)}) = (2\pi)^3 \delta_D^{(3)}(\mathbf{k}_{1\dots n}) \int_{\mathbf{p}} I_{n+1}^{(r)}(\eta; \mathbf{p}, \mathbf{k}_1, \dots, \mathbf{k}_n). \end{aligned} \quad (2.14)$$

It is convenient to decompose the solution of these equations into two pieces:

$$\Gamma_n^{(r) tot} = \Gamma_n^{(r)} + C_n^{(r)}, \quad (2.15)$$

where $\Gamma_n^{(r)}$ is the solution of the homogeneous equations (2.14) with the initial conditions reflecting the initial statistical distribution, and $C_n^{(r)}$ is the solution of the inhomogeneous equations with vanishing initial conditions. The $\Gamma_n^{(r)}$ vertices have the physical meaning of 1-particle irreducible tree-level correlators with amputated external propagators, and $C_n^{(r)}$ are *counterterms*, whose role is to cancel divergences in the loop corrections [1].

For the Gaussian initial conditions the time-dependence of the vertices $\Gamma_n^{(r)}$ factorizes,

$$\Gamma_n^{(r)} = (2\pi)^3 \delta_D^{(3)}(\mathbf{k}_{1\dots n}) \frac{\bar{\Gamma}_n^{(r)}}{g^2(\eta)}, \quad (2.16)$$

where the time-independent kernels $\bar{\Gamma}_n^{(r)}$ are given by

$$\bar{\Gamma}_2^{(r)}(\mathbf{k}_1, \mathbf{k}_2) = \frac{1}{\bar{P}(k_1)}, \quad (2.17a)$$

$$\begin{aligned} \bar{\Gamma}_n^{(r)}(\mathbf{k}_1, \dots, \mathbf{k}_n) = & -\frac{1}{n-2} \sum_{1 \leq i < j \leq n} I_2^{(r)}(\mathbf{k}_i, \mathbf{k}_j) \bar{\Gamma}_{n-1}^{(r)}(\mathbf{k}_i + \mathbf{k}_j, \mathbf{k}_1, \dots, \check{\mathbf{k}}_i, \dots, \check{\mathbf{k}}_j, \dots, \mathbf{k}_n) \\ & - \frac{3}{2(n-2)} \sum_{p=3}^{n-1} \frac{1}{p!(n-p)!} \sum_{\sigma} K_p^{(r)}(\mathbf{k}_{\sigma(1)}, \dots, \mathbf{k}_{\sigma(p)}) \\ & \times \bar{\Gamma}_{n-p+1}^{(r)}\left(\sum_{l=1}^p \mathbf{k}_{\sigma(l)}, \mathbf{k}_{\sigma(p+1)}, \dots, \mathbf{k}_{\sigma(n)}\right), \quad n \geq 3. \end{aligned} \quad (2.17b)$$

Note that the Gaussian part of the integral (2.11), given by (2.17), is the seed in the recursion relations (2.17b) so the $\bar{\Gamma}_n$ vertices can be seen as functionals of the initial power spectrum $\bar{P}(k)$. The counterterms $C_n^{(r)}$ do not depend on time

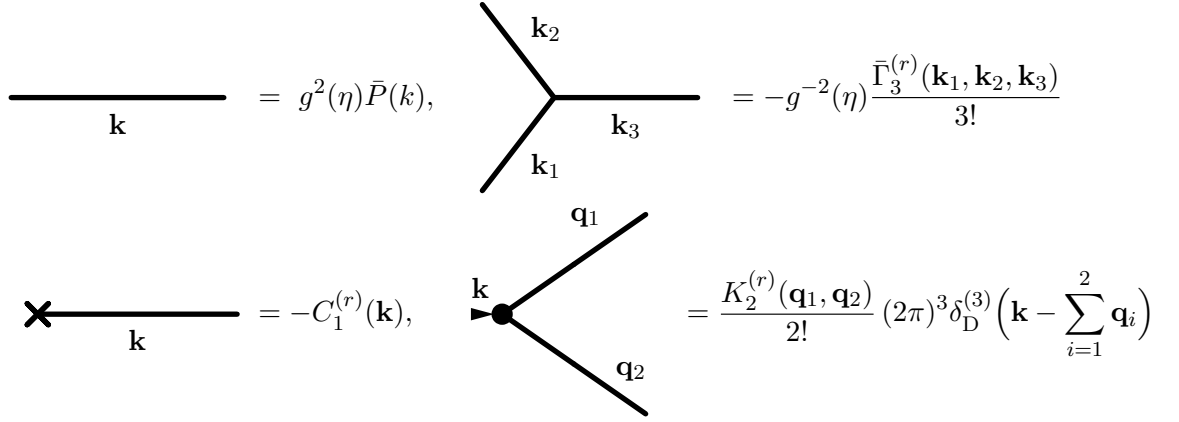


FIGURE 2.1: Example of TSPT Feynman rules.

and are given by:

$$\begin{aligned}
 C_n^{(r)}(\mathbf{k}_1, \dots, \mathbf{k}_n) &= \frac{1}{n} \left[(2\pi)^3 \delta_{\text{D}}^{(3)}(\mathbf{k}_{1\dots n}) \int_{\mathbf{p}} I_{n+1}^{(r)}(\mathbf{p}, \mathbf{k}_1, \dots, \mathbf{k}_n) \right. \\
 &\quad \left. - \sum_{p=2}^n \frac{1}{p!(n-p)!} \sum_{\sigma} I_p^{(r)}(\mathbf{k}_{\sigma(1)}, \dots, \mathbf{k}_{\sigma(p)}) C_{n-p+1}^{(r)} \left(\sum_{l=1}^p \mathbf{k}_{\sigma(l)}, \mathbf{k}_{\sigma(p+1)}, \dots, \mathbf{k}_{\sigma(n)} \right) \right].
 \end{aligned} \tag{2.18a}$$

The TSPT perturbative expansion is organized by expanding the generating functional (2.11) over the Gaussian part of \mathcal{P} , which is equivalent to an expansion in the coupling constant $g(\eta)$. This calculation can be represented as a sum of Feynman diagrams, whose first elements are summarized in Fig. 2.1: Γ_2 is represented by a line (propagator), the different elements Γ_n (with $n > 2$) and C_n correspond to vertices, and K_n are depicted as vertices with an extra arrow. To compute an n -point correlation function of the velocity divergence Θ one needs to draw all diagrams with n external legs. For the correlators of the density field δ one has to add diagrams with external arrows.

Chapter 3

IR resummation in real space

In this chapter we will discuss IR resummation only in real space and for compactness omit superscripts (r) in all the quantities.

The main idea of TSPT is to disentangle time-evolution from statistical ensemble averaging. In a first step, the probability distribution \mathcal{P} for the perturbations is evolved from the initial time to a finite redshift and expressed in terms of an expansion in powers of the density- and velocity divergence field at this redshift. In a second step, the statistical averages are computed perturbatively. The latter step can be conveniently represented by a diagrammatic series, where the quadratic cumulant represents a propagator, and the higher cumulants — n -point vertices Γ_n . In [1] it has been shown that these vertices are IR safe, *i.e.* free from spurious enhancements $\propto k/q$ when any of the wavenumbers become small.

In order to identify enhanced contributions related to the BAO, we split the initial power spectrum into a smooth (‘non-wiggly’) component P_{nw} and an oscillatory (‘wiggly’) contribution P_w . Then the TSPT three-point vertex expanded for $q \ll k$ and to first order in P_w is given by

$$\Gamma_3(\mathbf{k}, \mathbf{q}, \mathbf{q}') \rightarrow \delta_D^{(3)}(\mathbf{k} + \mathbf{q} + \mathbf{q}') \frac{\mathbf{k} \cdot \mathbf{q}}{q^2} \left(\frac{P_w(|\mathbf{k} + \mathbf{q}|) - P_w(k)}{P_{nw}(k)^2} \right). \quad (3.1)$$

In the limit $q \rightarrow 0$ the difference of the two power spectra in the numerator goes to zero and cancels the $1/q$ enhancement from the vertex, as required by the equivalence principle. However, as emphasized in [29], the Taylor expansion of $P_w(|\mathbf{k} + \mathbf{q}|)$ becomes unreliable for $k_{osc} \lesssim q \ll k$. This means that non-linear corrections to the correlation functions at scale k receive large corrections from IR modes q within this range. Note that Eq. (3.1) has a counterpart in standard

perturbation theory. Indeed, taking the IR limit of the one-loop integrals, $q \ll k$, where q is a loop momentum, one finds

$$\begin{aligned}
 P_{1\text{-loop}}(k) = & P_{\text{lin}}(k) \\
 & + \underbrace{\int_{|\mathbf{q}| \ll k} \frac{(\mathbf{k} \cdot \mathbf{q})^2}{q^4} P_{\text{lin}}(|\mathbf{k} + \mathbf{q}|) P_{\text{lin}}(q)}_{P_{22}} - \underbrace{\int_{|\mathbf{q}| \ll k} \frac{(\mathbf{k} \cdot \mathbf{q})^2}{q^4} P_{\text{lin}}(k) P_{\text{lin}}(q)}_{P_{13}}.
 \end{aligned} \tag{3.2}$$

First, one sees that if the linear power spectrum were a simple power-law, the two contributions above would cancel from $O(q^{-2})$ down to $O(q^0)$ correction in the integrand. This is the famous IR-cancellation between the individual SPT diagrams related to the equivalence principle. However, since the linear power spectrum does oscillate with frequency k_{osc} , a naive Taylor expansion of $P_{\text{lin}}(|\mathbf{k} + \mathbf{q}|)$ would yield a somewhat useless power series of $q/k_{\text{osc}} \geq 1$. Hence, because of the BAO, we cannot fully eliminate the IR enhancement in the one-loop term and have to always retain the whole finite difference of the wiggly power spectrum $P_w(|\mathbf{k} + \mathbf{q}|) - P_w(k)$ in (3.2). This is precisely what is meant by ‘incompleteness’ of IR cancellation in the presence of the BAO feature.

In this Chapter we identify the IR-enhanced contributions for all Γ_n vertices, and establish a power counting scheme to compute corrections to the most enhanced terms. The leading contributions to the oscillatory part of the power spectrum are given by a set of ‘daisy’ diagrams, and their resummation is represented diagrammatically in the following form (see Sec. 3.3 for details),

$$\begin{aligned}
 P_w^{IR\text{res},LO}(\eta; k) = & \text{wavy line} + \text{diagram } \bar{\Gamma}_4^w \\
 & + \text{diagram } \bar{\Gamma}_6^w + \text{diagram } \bar{\Gamma}_8^w + \text{diagram } \dots
 \end{aligned} \tag{3.3}$$

This diagrammatic representation is straightforwardly extended to IR-enhanced contributions into higher correlation functions.

At leading order (LO) for the power spectrum the resummation reproduces the

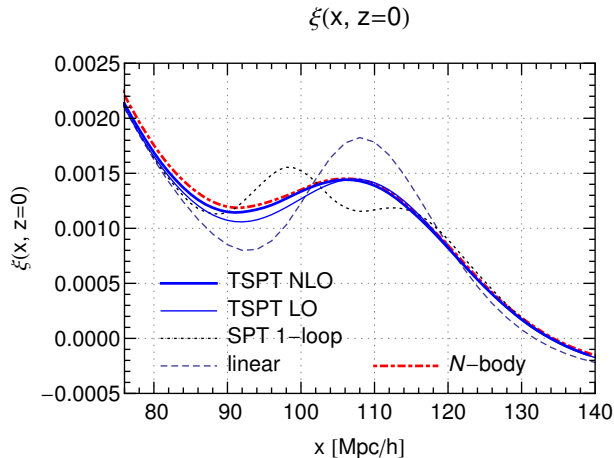


FIGURE 3.1: Matter two-point correlation function $\xi(x)$ at redshift $z = 0$. The thin (thick) blue solid line shows the infrared-resummed result obtained in TSPT at leading order (next-to-leading order). At BAO scales the perturbative expansion within the TSPT framework converges well and agrees with N -body results from large-scale numerical simulations [101] (red dot-dashed line). For comparison, we also show the linear (black dashed) and SPT 1-loop (black dotted) results.

result found in [29], which consists in a broadening of the BAO peak. Using TSPT we systematically compute next-to leading order (NLO) corrections. Apart from being quantitatively important in order to achieve good agreement with the results of large-scale N -body simulations at BAO scales, these NLO contributions are crucial for a reliable determination of the shift of the BAO peak. Furthermore, they are sensitive to the non-dipole corrections and consequently capture deviations from the Zel’dovich approximation (ZA). This may also be helpful to assess potential biases introduced in BAO reconstruction, which often uses the Zel’dovich approximation for backwards evolution. Our numerical results for the matter correlation function $\xi(x)$ at redshift $z = 0$ are summarized in Fig. 3.1, where we compare the TSPT results at LO and NLO with N -body data, and also show the naive SPT 1-loop result for comparison. It is worth noting that the results are obtained from first principles without adjusting any free parameters.

3.1 TSPT and wiggly-smooth decomposition

In this section we first briefly remind the basic elements of the TSPT approach to large-scale structure formation (see [1] for a detailed presentation) and then

discuss our strategy to identify IR enhanced effects on the BAO peak by decomposing the matter power spectrum as well as the TSPT vertices into smooth and oscillatory components.

3.1.1 TSPT in terms of wiggly and smooth elements

The initial power spectrum that sources the different elements of TSPT can be decomposed into a *smooth (non-wiggly)* part (with the maximum at $k = k_{eq} \sim 0.02 h/\text{Mpc}$ corresponding to the matter-radiation equality) and an oscillatory part (or *wiggly power spectrum*) that describes the impact of the BAO,

$$P_{\text{in}}(\eta, k) = g(\eta)^2 \bar{P}(k) = g(\eta)^2 (\bar{P}_{nw}(k) + \lambda \bar{P}_w(k)) . \quad (3.4)$$

Here we have factored out the time-dependence given by the growth factor $g = D(z)$ and introduced a book-keeping parameter λ to count the powers of \bar{P}_w in various expressions. As for the vertices, the bar denotes the time-independent power spectra. The amplitude of the wiggly power spectrum is suppressed compared to that of the smooth power spectrum in a realistic cosmological model. Its value can be estimated as [102] (see also [103]),

$$\frac{\bar{P}_w}{\bar{P}_{nw}} = O\left(e^{-(\eta_{\text{rec}} - \eta_{\text{eq}})} \frac{\Omega_b}{\Omega_m}\right) \sim 0.05 . \quad (3.5)$$

The wiggly power spectrum \bar{P}_w can be parametrized as [102, 103],

$$\bar{P}_w(k) \propto \sin(k/k_{\text{osc}}) \exp[-(k/k_{\text{Silk}})^2] T(k) , \quad (3.6)$$

where $1/k_{\text{osc}} \simeq 110 \text{ Mpc}/h$, the Silk damping scale is $k_{\text{Silk}} \sim 0.2 h/\text{Mpc}$ and $T(k)$ is the dark matter transfer function which is slowly varying¹ with k . For our numerical analysis we do not use (3.6), but extract the wiggly part by fitting a smooth multi-parameter template to the linear power spectrum for a given cosmological model. The details of this procedure are outlined in Appendix B of [3]. The corresponding (time-independent) ratio P_w/P_{nw} is shown by the solid curve in Fig. 3.2 for the case of the reference cosmological model used later on. Notice that this ratio vanishes both at low and high wavenumbers.

To check that the results do not depend on the precise prescription for separating the total power spectrum into smooth and wiggly components, we have also used an alternative decomposition with P_w/P_{nw} depicted by the dashed curve in Fig. 3.2. This decomposition was obtained by constructing splines that smoothly

¹It tends to 1 at $k < k_{\text{eq}}$ and behaves as $\ln k/k^2$ at higher k .

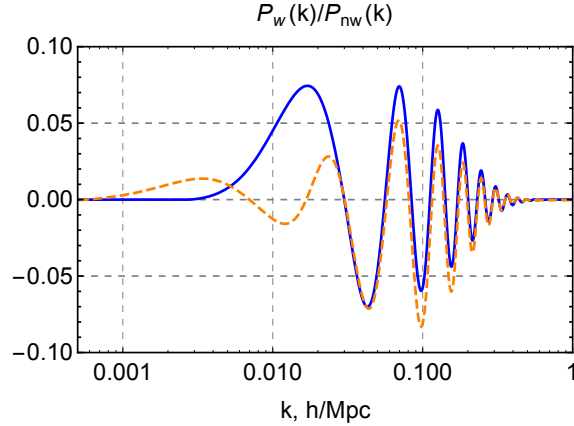


FIGURE 3.2: Ratio of oscillatory (wiggly) part P_w of the linear power spectrum to the smooth part P_{nw} obtained using two separation prescriptions. The Λ CDM cosmological parameters have been chosen as in [101]. The solid curve corresponds to the decomposition used in numerical computations in Sec. 3.6. The alternative decomposition (dashed curve) is used for cross-checks.

interpolate the linear power spectrum in between the BAO wiggles. We find that the difference in the final results for the total power spectrum and the correlation function obtained using the two forms of P_w are at the sub-percent level, below the uncertainties introduced by other approximations. This is to be expected: the ambiguity in the wiggly-smooth decomposition is relevant at large scales, $k \lesssim 0.03 h/\text{Mpc}$, which are essentially unaffected by the non-linear IR dynamics. As will become clear later, in the physical observables at these scales the smooth and wiggly components are simply summed back, and the ambiguity disappears. Similarly, an overall vertical off-set between the two curves in Fig. 3.2 at $k \gtrsim 0.1 h/\text{Mpc}$ does not contribute into the BAO feature.

The decomposition (3.4) can be extended to all the $\bar{\Gamma}_n$ vertices, since they are functionals of the initial power spectrum. Let us start with $\bar{\Gamma}_2$ from (2.17a),

$$\begin{aligned} \bar{\Gamma}'_2(\mathbf{k}, -\mathbf{k}) &= \frac{1}{\bar{P}(k)} = \frac{1}{\bar{P}_{nw}(k)} - \lambda \frac{\bar{P}_w(k)}{\bar{P}_{nw}^2(k)} + O(\lambda^2) \\ &\equiv \bar{\Gamma}_2^{nw}(\mathbf{k}, -\mathbf{k}) + \lambda \bar{\Gamma}_2^{w}(\mathbf{k}, -\mathbf{k}) + O(\lambda^2). \end{aligned} \quad (3.7)$$

Given that the vertex $\bar{\Gamma}'_2$ generates all the higher vertices by the recursion relation (2.17b), one can introduce a similar decomposition for all the $\bar{\Gamma}'_n$ vertices

$$\bar{\Gamma}'_n = \bar{\Gamma}_n^{nw} + \lambda \bar{\Gamma}_n^{w} + O(\lambda^2). \quad (3.8)$$

The $\bar{\Gamma}_n^{w}$ ($\bar{\Gamma}_n^{nw}$) vertices are computed using $\bar{\Gamma}'_2$ ($\bar{\Gamma}_2^{nw}$) as an input in (2.17b).

The decomposition (3.8) can be introduced back in the partition function (2.13).

$$\begin{aligned}
 \text{wiggly line } \mathbf{k} &= g^2(\eta)\bar{P}_w(k), & \text{wiggly vertex } (\mathbf{k}_1, \mathbf{k}_2, \mathbf{k}_3) &= -\frac{g^{-2}(\eta)}{3!}\bar{\Gamma}_3^w(\mathbf{k}_1, \mathbf{k}_2, \mathbf{k}_3), \\
 \text{straight line } \mathbf{k} &= g^2(\eta)\bar{P}_{nw}(k), & \text{smooth vertex } (\mathbf{k}_1, \mathbf{k}_2, \mathbf{k}_3) &= -\frac{g^{-2}(\eta)}{3!}\bar{\Gamma}_3^{nw}(\mathbf{k}_1, \mathbf{k}_2, \mathbf{k}_3).
 \end{aligned}$$

FIGURE 3.3: Example of Feynman rules for wiggly and smooth elements.

Since the C_n and K_n kernels are not functionals of the linear power spectrum [1] (see also Appendix B.1), they are not subject to the wiggly-smooth decomposition. The leading order $O(\lambda^0)$ corresponds to the *smooth* correlation functions. The $O(\lambda)$ results include the *wiggly* contribution. In terms of diagrams, they can be summarized in the form of a new wiggly propagator $g^2 P_w$ (represented by a wiggly line) and by wiggly vertices Γ_n^w (represented by a dashed circle), see Fig. 3.3. We use small dots to depict the smooth vertices and straight lines to represent the smooth power spectrum. The terms $O(\lambda^2)$ are quadratic in P_w and will be neglected.

The graphs with the wiggly elements are loosely referred to as wiggly graphs. For instance, the tree-level wiggly bispectrum is given by the following four wiggly graphs²,

$$\langle \Theta_\eta(\mathbf{k}_1)\Theta_\eta(\mathbf{k}_2)\Theta_\eta(\mathbf{k}_3) \rangle_w^{\text{tree}} = \text{diagram 1} + \text{diagram 2} + \text{diagram 3} + \text{diagram 4} \quad (3.10)$$

$$= -\lambda g^4(\eta) \left(\prod_{i=1}^3 \bar{P}_{nw}(k_i) \bar{\Gamma}_3^w(\mathbf{k}_1, \mathbf{k}_2, \mathbf{k}_3) + \sum_{j=1}^3 \bar{P}_w(k_j) \prod_{\substack{i=1, \\ i \neq j}}^3 \bar{P}_{nw}(k_i) \bar{\Gamma}_3^{nw}(\mathbf{k}_1, \mathbf{k}_2, \mathbf{k}_3) \right).$$

² In terms of SPT kernels the result of (3.10) can be rewritten as

$$\begin{aligned}
 &\langle \Theta(\mathbf{k}_1)\Theta(\mathbf{k}_2)\Theta(\mathbf{k}_3) \rangle_w^{\text{tree}} \\
 &= 2\lambda g^4(\eta) G_2(\mathbf{k}_1, \mathbf{k}_2) (\bar{P}_w(k_1)\bar{P}_{nw}(k_2) + \bar{P}_w(k_2)\bar{P}_{nw}(k_1)) + \text{permutations}. \quad (3.9)
 \end{aligned}$$

To obtain the matter density bispectrum one has to add to the previous expression six more graphs with the vertex K_2 ,

$$\begin{aligned} \Delta\langle\delta(\mathbf{k}_1)\delta(\mathbf{k}_2)\delta(\mathbf{k}_3)\rangle_w^{\text{tree}} &= \text{[Diagram: a central black dot with a wavy line on the left, a straight line on the right, and a triangle pointing down from the dot]} + \text{permutations} \quad (3.11) \\ &= -\lambda g^A(\eta) \sum_{i<j=1}^3 (\bar{P}_w(k_j)\bar{P}_{nw}(k_i) + \bar{P}_{nw}(k_j)\bar{P}_w(k_i)) K_2(\mathbf{k}_i, \mathbf{k}_j) (2\pi)^3 \delta_D^{(3)}\left(\sum_l \mathbf{k}_l\right). \end{aligned}$$

In what follows we set $\lambda = 1$ whenever there is no possible confusion.

3.2 IR enhanced diagrams and power counting

One of the advantages of the TSPT approach is that all of its building blocks are free of spurious infrared enhancements. In particular, the $\bar{\Gamma}_n$ vertices are finite in the limit $\{q\} \rightarrow 0$, where $\{q\}$ is any subset of the arguments of $\bar{\Gamma}_n$ [1]. In contrast, within SPT individual vertices have poles in q which cancel only after summing all contributions at a given order. Nevertheless, as mentioned previously, for a linear power spectrum with an oscillatory behavior the cancellation of enhanced terms is incomplete for $q \gtrsim k_{osc}$. In this section we show how to extract these enhanced contributions within TSPT and then discuss power counting rules. These are helpful to organize the resummation of enhanced contributions, and later on to develop a perturbative expansion for taking sub-leading corrections to the resummed result into account.

3.2.1 IR enhanced vertices

We consider a TSPT n -point vertex $\bar{\Gamma}_n(\mathbf{k}_1, \dots, \mathbf{k}_n)$ evaluated with arguments \mathbf{k}_i that have magnitudes given schematically by two different scales: a hard scale denoted by k and a soft scale denoted by q , with

$$q/k \ll 1. \quad (3.12)$$

Let us first analyze the three-point vertex $\bar{\Gamma}_3^{nw}$. Using (2.17b) we find,

$$\bar{\Gamma}_3^{nw}(\mathbf{k}, -\mathbf{k}-\mathbf{q}, \mathbf{q}) = I_2(\mathbf{k}, \mathbf{q}) \frac{\bar{P}_w(|\mathbf{k}+\mathbf{q}|)}{\bar{P}_{nw}^2(|\mathbf{k}+\mathbf{q}|)} + I_2(-\mathbf{k}-\mathbf{q}, \mathbf{q}) \frac{\bar{P}_w(k)}{\bar{P}_{nw}^2(k)} + I_2(-\mathbf{k}-\mathbf{q}, \mathbf{k}) \frac{\bar{P}_w(q)}{\bar{P}_{nw}^2(q)}, \quad (3.13)$$

where I_2 is given in (2.10b). In the limit (3.12) the rightmost term in (3.13) is smaller than $O(q/k)$ and will be neglected in what follows. The other terms

provide an expression of the form

$$\bar{\Gamma}_3'^w(\mathbf{k}, -\mathbf{k} - \mathbf{q}, \mathbf{q}) = \frac{\mathbf{k} \cdot \mathbf{q}}{q^2} \left(\frac{\bar{P}_w(|\mathbf{k} + \mathbf{q}|) - \bar{P}_w(k)}{\bar{P}_{nw}(k)^2} \right) + O((q/k)^0), \quad (3.14)$$

where we have used that the derivatives of the smooth component scale as $1/k$ and expanded $\bar{P}_{nw}(|\mathbf{k} + \mathbf{q}|) = \bar{P}_{nw}(k) + O(q/k)$. In contrast, we kept the finite difference for the wiggly component that varies substantially for $q \gtrsim k_{osc}$.

It is convenient to use compact notations by introducing the linear operator

$$\mathcal{D}_{\mathbf{q}}[\bar{P}_w(k)] = \frac{\mathbf{k} \cdot \mathbf{q}}{q^2} \left(\bar{P}_w(|\mathbf{k} + \mathbf{q}|) - \bar{P}_w(k) \right) = \frac{\mathbf{k} \cdot \mathbf{q}}{q^2} (e^{\mathbf{q} \cdot \nabla_{\mathbf{k}'}} - 1) \bar{P}_w(k') \Big|_{k'=k}. \quad (3.15)$$

This operator will play a central role in the following, and therefore we elaborate on some of its properties. Consider first its action on a purely oscillatory function $e^{ik/k_{osc}}$, where we are interested in the case $k \gg k_{osc}$. Expanding the exponent in the small parameter q/k we obtain,

$$\mathcal{D}_{\mathbf{q}}[e^{ik/k_{osc}}] \approx \frac{\mathbf{k} \cdot \mathbf{q}}{q^2} \left(e^{iq \cos(\mathbf{k}, \mathbf{q})/k_{osc}} - 1 \right) e^{ik/k_{osc}}, \quad (3.16)$$

where we introduced $\cos(\mathbf{k}, \mathbf{q}) = \frac{\mathbf{k} \cdot \mathbf{q}}{kq}$. For $q \gtrsim k_{osc}$ the expression in the brackets is of order one, whereas the prefactor is enhanced by k/q . On the other hand, if $q \ll k_{osc}$, Eq. (3.16) reduces to

$$\mathcal{D}_{\mathbf{q}}[e^{ik/k_{osc}}] \approx \frac{ik}{k_{osc}} \cos^2(\mathbf{k}, \mathbf{q}) e^{ik/k_{osc}}, \quad (3.17)$$

so that the enhancement is given by k/k_{osc} . In a more realistic case the wiggly power spectrum can be viewed as an oscillating function that is modulated by a smooth envelope, $P_w(k) \sim f_{env}(k)e^{i(k/k_{osc} + \varphi)} + \text{c.c.}$ with³ $\nabla f_{env}(k) \sim O(1/k)f_{env}(k)$. For example, the parametrization (3.6) is of this form. Inserting this parameterization into (3.15) one observes that the derivatives acting on the envelope are suppressed compared to those acting on the oscillating part. They must be taken into account only when looking at the sub-leading corrections. We conclude that

$$\mathcal{D}_{\mathbf{q}}[\bar{P}_w(k)] \sim O(\varepsilon^{-1})\bar{P}_w(k), \quad (3.18)$$

³Strictly speaking, due to existence of the Silk damping, $\nabla f_{env}(k) \sim O(\max(1/k, 1/k_{Silk}))f_{env}(k)$. However, we use the simpler estimate from above since in practice we do not consider values of k that are parametrically larger than k_{Silk} .

where we introduced the small parameter

$$\varepsilon \equiv \max(q/k, k_{osc}/k). \quad (3.19)$$

As we are going to see shortly, the enhancement by $1/\varepsilon$ is the reason why the naive SPT loop expansion breaks down for the BAO. The sub-leading corrections coming from the derivatives of the envelope and higher terms in the expansion of the oscillating part correspond to contributions of order ε^0 (or higher powers of ε) that are suppressed relative to the leading $1/\varepsilon$ enhancement. This will be important to establish systematic power counting rules.

It turns out to be useful to extend the action of $\mathcal{D}_{\mathbf{q}}$ to any wiggly element. This is done by recalling that the latter are linear expressions in P_w with smooth k -dependent coefficients. Then, by definition, $\mathcal{D}_{\mathbf{q}}$ acts on any occurrence of P_w according to (3.15), leaving the smooth coefficients intact. For example,

$$\mathcal{D}_{\mathbf{q}}[\bar{\Gamma}'_3(\mathbf{k}_1, \mathbf{k}_2, \mathbf{k}_3)] \Big|_{\mathbf{k}_3 = -\mathbf{k}_1 - \mathbf{k}_2} \equiv \left(\frac{\mathcal{D}_{\mathbf{q}}[\bar{P}_w(k_1)]}{\bar{P}_{nw}^2(k_1)} I_2(\mathbf{k}_2, \mathbf{k}_3) + \text{perm.} \right) \Big|_{\mathbf{k}_3 = -\mathbf{k}_1 - \mathbf{k}_2}, \quad (3.20)$$

and similarly for other $\bar{\Gamma}'_n$. Note that an immediate consequence of this definition is that $\mathcal{D}_{\mathbf{q}}$ commutes with itself,

$$\mathcal{D}_{\mathbf{q}_1} \mathcal{D}_{\mathbf{q}_2} \bar{\Gamma}'_n = \mathcal{D}_{\mathbf{q}_2} \mathcal{D}_{\mathbf{q}_1} \bar{\Gamma}'_n \quad (3.21)$$

The result (3.14) for the 3-point vertex can be generalized by induction to arbitrary n -point vertices with m hard wavenumbers \mathbf{k}_i and $n - m$ wavenumbers \mathbf{q}_j going uniformly to zero. In Appendix B we prove the following formula,

$$\bar{\Gamma}'_n(\mathbf{k}_1, \dots, \mathbf{k}_m - \sum_{j=1}^{n-m} \mathbf{q}_j, \mathbf{q}_1, \dots, \mathbf{q}_{n-m}) = (-1)^{n-m} \left(\prod_{j=1}^{n-m} \mathcal{D}_{\mathbf{q}_j} \right) [\bar{\Gamma}'_m(\mathbf{k}_1, \dots, \mathbf{k}_m)] \times (1 + O(\varepsilon)), \quad (3.22)$$

where $\mathbf{k}_m = -\sum_{i=1}^{m-1} \mathbf{k}_i$ due to momentum conservation. Note that the leading IR enhancement $\propto (1/\varepsilon)^{n-m}$ is equal to the number of soft arguments. The maximal enhancement happens for the case of $n - 2$ soft wavenumbers where we have

$$\begin{aligned} \bar{\Gamma}'_n(\mathbf{k}, -\mathbf{k} - \sum_{i=1}^{n-2} \mathbf{q}_i, \mathbf{q}_1, \dots, \mathbf{q}_{n-2}) &= (-1)^{n-2} \left(\prod_{i=1}^{n-2} \mathcal{D}_{\mathbf{q}_i} \right) [\bar{\Gamma}'_2(\mathbf{k}, -\mathbf{k})] \times (1 + O(\varepsilon)) \\ &= (-1)^{n-1} \left[\prod_{i=1}^{n-2} \frac{(\mathbf{k} \cdot \mathbf{q}_i)}{q_i^2} (e^{\mathbf{q}_i \cdot \nabla_{\mathbf{k}'}} - 1) \right] \frac{\bar{P}_w(k')}{\bar{P}_{nw}^2(k)} \Big|_{\mathbf{k}' = \mathbf{k}} \times (1 + O(\varepsilon)), \end{aligned} \quad (3.23)$$

which scales as $O(\varepsilon^{-n+2})$. Clearly, the sensitivity of the vertices $\bar{\Gamma}_n^w$ to the large parameter $1/\varepsilon$ grows with n . In the subsequent sections we show how these large enhancement factors can be resummed within a systematic approach.

3.2.2 Leading diagrams and power counting rules

Consider a loop diagram containing a wiggly TSPT vertex Γ_n^w with m external legs and $(n - m)$ legs attached to the loops. As we saw above, this vertex is enhanced by powers $1/\varepsilon$ in the limit where its arguments \mathbf{q}_j flowing in the loops become soft compared to the external wavenumbers \mathbf{k}_i . In order to extract the corresponding enhancement of the loop diagrams, we split all loop integrations into a soft part with $q < k_S$ and a hard part with $q > k_S$. The scale k_S is in principle arbitrary, and observables do not depend on it when computed exactly. Nevertheless, this splitting allows us to separately treat the IR and UV parts of loop integrations, and resum the large IR loops. Any residual dependence on k_S should be taken as an estimate of the theoretical uncertainty, that should become smaller and smaller when computing at higher orders. In practice, the BAO feature is mostly affected by the modes with q between k_{osc} and k_{Silk} , so the range $k_{osc} < k_S < k_{Silk}$ can be expected to lead to good convergence properties. We will return to the choice of k_S in Sec. 3.6.

To account for the IR enhancement, we identify the expansion parameter with (cf. (3.19))

$$\varepsilon = \frac{\langle q \rangle}{k}, \quad (3.24)$$

where $k_{osc} < \langle q \rangle < k_S$ is the characteristic scale giving the dominant contributions into the IR loop integrals. As will become clear below by inspection of the eventual expressions (3.29), (3.71) for the IR enhanced loops, the integrand in them peaks roughly at the maximum of the smooth power spectrum implying $\langle q \rangle \sim k_{eq}$.

In addition to ε , the relevant parameter that controls the loop expansion is given by the variance of the input linear power spectrum. The latter is dominated by the smooth component P_{nw} . Due to the splitting into an IR ('soft') and UV ('hard') parts we can discriminate two variances

$$\sigma_S^2 \equiv g^2 \int_{q < k_S} \frac{d^3 q}{(2\pi)^3} \bar{P}_{nw}(q), \quad (3.25)$$

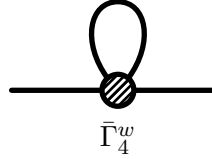
$$\sigma_h^2 \equiv g^2 \int_{q > k_S} \frac{d^3 q}{(2\pi)^3} \bar{P}_{nw}(q). \quad (3.26)$$

For example, for a realistic Λ CDM model one has $\sigma_S^2 \sim 0.16g^2$ (recall that $g \equiv D(z)$) for the choice $k_S = 0.1h/\text{Mpc}$, whereas σ_h^2 is formally UV divergent. In practice, the hard part of the loop corrections remains finite due to additional suppression of the actual integrands in the UV. Still, these corrections are UV dominated and their reliable calculation requires proper renormalization of the contribution due to very short modes. On the other hand, while the importance of the UV counterterms increases for high wavenumbers and at higher orders of the perturbation theory, they contribute only at a percent level to the hard one-loop corrections to the power spectrum at the BAO performed in this Chapter. The latter corrections are well-behaved and are of order $\text{few} \times 10\%$ at $z = 0$. We postpone the study of the UV counterterms in TSPT for future work and focus in this Chapter on the IR loops. σ_h^2 will be used in what follows as a formal counting parameter for the number of hard loops.

Although σ_S^2 seems to be rather small, we will now argue that soft loops are enhanced by a factor $1/\varepsilon^2 \sim O(10)$ for the wiggly observables. Therefore they are proportional to the product $\sigma_S^2 \times 1/\varepsilon^2$ which is $O(1)$ at low redshift, implying that the corresponding soft loops need to be resummed. Consider, for example, 1-loop corrections to the wiggly $\Theta\Theta$ power spectrum, given by the following TSPT diagrams,

$$\begin{aligned}
P_{w,\Theta\Theta}^{1-loop}(\eta; k) = & \bar{\Gamma}_3^{nw} \text{ (loop) } \bar{\Gamma}_3^{nw} + \bar{\Gamma}_4^{nw} \text{ (loop) } + \bar{\Gamma}_3^{nw} \text{ (loop) } \bar{\Gamma}_3^{nw} + \bar{\Gamma}_4^{nw} \text{ (loop) } \\
& + \bar{\Gamma}_3^w \text{ (loop) } \bar{\Gamma}_3^{nw} + \bar{\Gamma}_4^w \text{ (loop) } . \tag{3.27}
\end{aligned}$$

The loop integration in each diagram can be either hard, $q > k_S$, in which case the diagrams are counted at order σ_h^2 , or soft, $q < k_S$, and are of order σ_S^2 . Only the soft contributions can be IR enhanced, so we focus on them for the moment. The diagrams in the first line of (3.27) are never IR-enhanced, *i.e.* they are at most of order $\varepsilon^0 \times \sigma_S^2$, because they do not contain a wiggly vertex. On the other hand, the diagrams with the wiggly vertices do receive any IR enhancement. The first diagram in the second line contains $\bar{\Gamma}_3^w$ and is according to (3.23), (3.18) of order $1/\varepsilon \times \sigma_S^2$. The last diagram contains $\bar{\Gamma}_4^w$, and using (3.23), (3.18) we find that it is of order $1/\varepsilon^2 \times \sigma_S^2$ and thus is the most IR-enhanced one-loop diagram. At leading order in ε it is given by



The diagram shows a horizontal line with a shaded circular vertex. A loop is attached to this vertex, consisting of a vertical line segment going up, a curved line forming a semi-circle at the top, and another vertical line segment going down back to the vertex. Below the vertex is the label $\bar{\Gamma}_4^w$.

$$= \frac{g^2}{2} \int_{|\mathbf{q}| \leq k_S} \bar{P}_{nw}(q) \mathcal{D}_{\mathbf{q}} \mathcal{D}_{-\mathbf{q}} P_w(\eta; k) \equiv -g^2 \mathcal{S} P_w(\eta; k), \quad (3.28)$$

where in the last step we defined the operator \mathcal{S} which can be written as

$$\mathcal{S} P_w(\eta; k) = \int_{|\mathbf{q}| \leq k_S} \bar{P}_{nw}(q) \frac{(\mathbf{k} \cdot \mathbf{q})^2}{q^4} (1 - \cosh(\mathbf{q} \cdot \nabla_{k'})) P_w(\eta; k') \Big|_{k'=k} \quad (3.29)$$

In terms of our power counting

$$\mathcal{S} P_w(\eta; k) \sim O(1/\varepsilon^2 \times \sigma_S^2) P_w(\eta; k). \quad (3.30)$$

As discussed previously, the product $1/\varepsilon^2 \times \sigma_S^2$ can be of $O(1)$ at low redshift and therefore this one-loop contribution can be comparable to the linear wiggly spectrum.

In order to identify and eventually resum such terms we now discuss how to determine the order of an arbitrary L -loop diagram in our power counting. This is valid for any n -point correlation function, with external wavenumbers k_i around the BAO scale, $k_{Silk} \gtrsim k_i \gg k_S, k_{osc}$. Given a TSPT diagram with L loops (*i.e.* scaling as g^{2L}), one must

1. choose for each propagator and each vertex whether it is smooth or wiggly. Since we are interested in diagrams that contain one power of P_w , at most one element (either propagator or vertex) can be wiggly. To obtain the full answer, one eventually needs to sum over all possibilities to choose a vertex or propagator to be the wiggly one.
2. assign each loop to be either hard ($q > k_S$) or soft ($q < k_S$). Formally, this can be done by splitting the linear input spectrum into two parts as $P_{lin}(q) = \theta(q - k_S)P_{lin}(q) + \theta(k_S - q)P_{lin}(q)$, and calling a loop hard if all propagators and vertices along the loop contain only power spectra of the former type⁴. The number of hard loops is denoted by L_h and the number of soft loops by L_s . Trivially $L = L_h + L_s$, and the diagram contributes at order $(\sigma_S^2)^{L_s} \times (\sigma_h^2)^{L_h}$. Again, to obtain the full answer, one needs to sum over all assignments eventually.
3. count the *number of soft lines that are attached to the wiggly vertex*. We call this number l . According to (3.23), the IR-enhancement is $1/\varepsilon^l$.

⁴ Strictly speaking, the splitting into hard and soft contributions is only necessary for the loops that contain a wiggly vertex. For other loops, since $\sigma_S^2 + \sigma_h^2 \approx \sigma_h^2$ in a realistic case, it is effectively irrelevant whether we make this split or not.

The order in our power counting of a contribution characterized by the numbers (L_h, L_s, l) is therefore given by⁵

$$O\left((\sigma_S^2)^{L_s} \times (\sigma_h^2)^{L_h} \times 1/\varepsilon^l\right). \quad (3.31)$$

If a diagram contains no wiggly vertex then $l = 0$ and no IR-enhancement occurs. The most IR-enhanced contributions have the largest value of l . As a single loop cannot contain more than two lines attached to the same vertex, we have the inequality $l \leq 2L_s$. This means that the most IR enhanced contributions are of order $(\sigma_S^2/\varepsilon^2)^{L_s} \times (\sigma_h^2)^{L_h}$. As argued before σ_S^2/ε^2 is $O(1)$ at low redshift and therefore it is desirable to resum all diagrams with the maximal enhancement $l = 2L_s$. This is the subject of the next section.

3.3 Resummation of leading infrared effects

Here we perform the resummation of dominant IR enhanced diagrams contributing into wiggly observables. We start with the power spectrum, then consider the bispectrum and outline the generalization to higher n -point functions. We work at the order $(\sigma_h^2)^0$, i.e. neglecting the hard loop corrections. The task of taking them into account is postponed till Sec. 3.4.

3.3.1 Power spectrum

The most IR-enhanced contributions correspond to diagrams with $l = 2L_s$ and $L_h = 0$, *i.e.* all loops are soft and they contain a wiggly vertex to which $l = 2L_s$ soft lines are attached. At one-loop, the most IR enhanced diagram is the tadpole diagram (3.28) with $L_s = 1$ soft loop and $l = 2$ soft lines attached to $\bar{\Gamma}_4^w$ (the two lines that belong to the loop). At two-loop, $L_s = 2$, the most IR-enhanced diagram should contain a wiggly vertex with $l = 4$ soft lines attached to it. In addition, the IR enhancement can only occur if also a hard momentum flows through the wiggly vertex. For $L_h = 0$ this can only be the external momentum. Therefore, the most IR-enhanced diagram has to contain a wiggly vertex $\bar{\Gamma}_6^w$ with four soft arguments attached to loops and two hard arguments that correspond to the two external legs. The only possibility that remains is a single diagram, given by a double-tadpole. Analogously, at higher loop orders, the most IR-enhanced diagrams are obtained by attaching more and more loops to the wiggly

⁵To be more precise, this provides an upper estimate for the magnitude of the contribution. Specific terms can be further suppressed, as will be seen below.

vertex in the center. The first few diagrams that contribute to the wiggly part of the power spectrum are shown in Eq. (3.3). It is natural to call them *daisy* diagrams. Note that the leading IR-enhanced contributions are the same for the density and velocity power spectra. Indeed, within TSPT the δ power spectrum is obtained from that of Θ by adding diagrams with the kernels K_n (see Sec. 2). These kernels do not depend on the wiggly power spectrum and are therefore not subject to IR enhancement. Consequently, diagrams involving K_n kernels give subdominant contributions at each loop order.

The daisy diagram with L loops, all of which are soft (*i.e.* $L_s = L$), is given by

$$P_w^{L-loop,LO}(\eta; k) = -\frac{1}{(2L+2)!} \cdot (2L+2)(2L+1)(2L-1)!! \\ \times \prod_{i=1}^L \left[\int_{|\mathbf{q}_i| \leq k_S} g^2 \bar{P}_{nw}(q_i) \right] g^4 \bar{P}_{nw}(k)^2 g^{-2} \bar{\Gamma}_{2L+2}^{nw,LO}(\mathbf{k}, -\mathbf{k}, \mathbf{q}_1, -\mathbf{q}_1, \dots, \mathbf{q}_L, -\mathbf{q}_L). \quad (3.32)$$

The symmetry factor in this formula arises as follows: there are $(2L+2)(2L+1)$ ways to choose the two external legs, and $(2L-1) \cdot (2L-3) \cdot \dots \cdot 1$ ways to connect all the remaining lines into the loops. Making use of (3.23), one obtains

$$P_w^{L-loop,LO}(\eta; k) = \frac{1}{L!} \prod_{i=1}^L \left[\frac{g^2}{2} \int_{|\mathbf{q}_i| \leq k_S} \bar{P}_{nw}(q_i) \mathcal{D}_{\mathbf{q}_i} \mathcal{D}_{-\mathbf{q}_i} \right] P_w(\eta; k) \\ = \frac{(-g^2(\eta)\mathcal{S})^L}{L!} P_w(\eta; k), \quad (3.33)$$

where the operator \mathcal{S} has been defined in (3.28). The sum over all daisy graphs gives the leading-order IR-resummed wiggly power spectrum

$$P_w^{IR\ res,LO}(\eta, k) = \sum_{L=0}^{\infty} P_w^{L-loop,LO}(\eta; k) = e^{-g^2(\eta)\mathcal{S}} P_w(\eta; k). \quad (3.34)$$

We see that the operator \mathcal{S} exponentiates.

The total power spectrum is obtained by adding the smooth part which, to the required order of accuracy, can be taken at tree level. This yields,

$$P^{IR\ res,LO} = P_{nw}(\eta; k) + e^{-g^2(\eta)\mathcal{S}} P_w(\eta; k). \quad (3.35)$$

Let us stress again that this expression holds both for the density and velocity divergence power spectra. Moreover, it is the same in the full hydrodynamics (called ‘exact dynamics (ED)’ in the LSS literature) and ZA as the expansion (3.23) used in the derivation is valid in both cases. The difference between ED

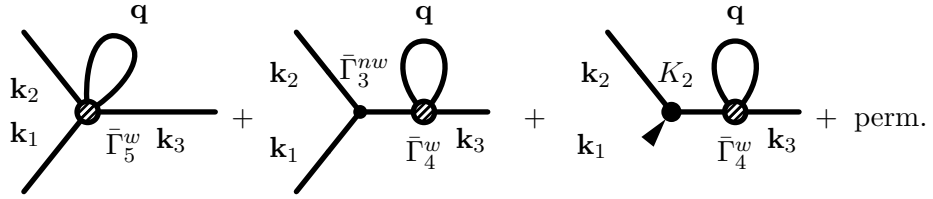
and ZA and between δ and Θ appears for higher correlators and for the power spectrum beyond the leading order.

3.3.2 Bispectrum and other n -point correlation functions

In this section we extend the resummation procedure of the IR-enhanced loop contributions to the wiggly part of higher order correlation functions. We first discuss the bispectrum and then general n -point correlation functions.

The wiggly part of the tree-level bispectrum for the velocity divergence field is given by the four graphs (3.10), whereas for the density bispectrum one has to add the graphs (3.11). At one loop order, and assuming all external wavenumbers are hard, the most IR-enhanced contributions are obtained by ‘dressing’ the wiggly vertices and propagators in (3.10), (3.11) with a soft loop ($q < k_S$) attached to the wiggly vertex,

$$B_{w,\delta\delta\delta}^{1-loop,LO}(\eta; \mathbf{k}_1, \mathbf{k}_2, \mathbf{k}_3) = \quad (3.36)$$



Within our power counting, these diagrams contribute at order $\sigma_L^2 \times 1/\varepsilon^2$ compared to the tree-level bispectrum. Using a similar reasoning as for the power spectrum, one finds that at higher loop orders the most IR-enhanced corrections are given by daisy diagrams obtained by attaching more soft loops to the wiggly vertices appearing in each diagram in (3.36). Parametrically, these L -loop diagrams scale as

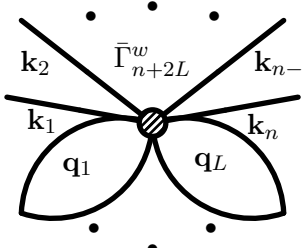
$$B_{w,\delta\delta\delta}^{L-loop,LO} \sim (\sigma_L^2/\varepsilon^2)^L B_{w,\delta\delta\delta}^{tree}, \quad (3.37)$$

and thus need to be resummed.

The daisy diagrams centered on the propagator (like the second and third terms in (3.36)) are essentially the same as those appearing in the calculation of the power spectrum from the previous subsection. They are evaluated using Eq. (3.32) and their resummation leads to the replacement of the external wiggly propagators in the tree level expression,

$$\bar{P}_w \mapsto e^{-g^2 S} \bar{P}_w. \quad (3.38)$$

A new type of contributions comes from one-particle-irreducible (1PI) diagrams with soft loops dressing the 3-point vertex (like the first diagram in (3.36)). In view of future uses, let us consider the general case of a wiggly vertex with n hard wavenumbers dressed by L soft loops,

$$\begin{aligned}
V_{w,n}^{L-loop} &= \text{Diagram} \\
&= \frac{1}{(n+2L)!} \cdot (2L+n)\dots(2L+1) \cdot (2L-1)!! \\
&\quad \times \prod_{i=1}^L \left[\int_{|\mathbf{q}_i| \leq k_S} g^2 \bar{P}_{nw}(q_i) \right] g^{-2} \bar{\Gamma}_{n+2L}^{nw}(\mathbf{k}_1, \dots, \mathbf{k}_n, \mathbf{q}_1, -\mathbf{q}_1, \dots, \mathbf{q}_L, -\mathbf{q}_L)
\end{aligned} \tag{3.39}$$


Using Eq. (3.22) we obtain for the leading IR-enhanced part,

$$V_{w,n}^{L-loop,LO} = \frac{(-g^2 \mathcal{S})^L}{L!} g^{-2} \bar{\Gamma}_n^{nw}(\mathbf{k}_1, \dots, \mathbf{k}_n). \tag{3.40}$$

Clearly, resummation of these diagrams results in the substitution of the wiggly vertex,

$$\bar{\Gamma}_n^{nw}(\mathbf{k}_1, \dots, \mathbf{k}_n) \mapsto \exp\{-g^2 \mathcal{S}\} \bar{\Gamma}_n^{nw}(\mathbf{k}_1, \dots, \mathbf{k}_n). \tag{3.41}$$

Combining all terms together, one obtains the resummed bispectrum,

$$\begin{aligned}
B_{w,\delta\delta\delta}^{IR\ res,LO}(\eta; \mathbf{k}_1, \mathbf{k}_2, \mathbf{k}_3) &= -g^4(\eta) \delta^{(3)}\left(\sum_l \mathbf{k}_l\right) \left[\prod_{i=1}^3 \bar{P}_{nw}(k_i) e^{-g^2(\eta)\mathcal{S}} \bar{\Gamma}_3^{nw}(\mathbf{k}_1, \mathbf{k}_2, \mathbf{k}_3) \right. \\
&\quad + \sum_{j=1}^3 e^{-g^2(\eta)\mathcal{S}} \bar{P}_w(k_j) \prod_{\substack{i=1 \\ i \neq j}}^3 \bar{P}_{nw}(k_i) \bar{\Gamma}_3^{nw}(\mathbf{k}_1, \mathbf{k}_2, \mathbf{k}_3) \\
&\quad \left. + \sum_{i < j=1}^3 e^{-g^2(\eta)\mathcal{S}} (\bar{P}_w(k_j) \bar{P}_{nw}(k_i) + \bar{P}_{nw}(k_j) \bar{P}_w(k_i)) K_2(\mathbf{k}_i, \mathbf{k}_j) \right] \\
&= e^{-g^2(\eta)\mathcal{S}} B_{w,\delta\delta\delta}^{tree}(\eta; \mathbf{k}_1, \mathbf{k}_2, \mathbf{k}_3).
\end{aligned} \tag{3.42}$$

Recall that in the last expression the operator $e^{-g^2 \mathcal{S}}$ should be understood as acting on every occurrence of P_w in the tree-level expression for the bispectrum. In terms of the SPT kernels, Eq. (3.42) can be rearranged into a somewhat

simpler form,

$$B_{w,\delta\delta\delta}^{IR\ res,LO}(\eta; \mathbf{k}_1, \mathbf{k}_2, \mathbf{k}_3) = 2 \sum_{i<j=1}^3 F_2(\mathbf{k}_i, \mathbf{k}_j) e^{-g^2(\eta)\mathcal{S}} (P_w(\eta; k_j) P_{nw}(\eta; k_i) + i \leftrightarrow j) . \quad (3.43)$$

The total bispectrum is obtained by adding to this expression the smooth tree-level part.

The above result extends to any equal-time n -point correlation functions $\mathfrak{C}_n(\mathbf{k}_1, \dots, \mathbf{k}_n)$ of δ or Θ with hard external legs. Namely, the IR resummation at LO amounts to simply substituting the wiggly part of the linear spectrum, P_w , that enters via wiggly vertices and propagators within the TSPT tree-level calculation, by the resummed expression $e^{-g^2\mathcal{S}}P_w$. This can be summarized in the following compact form,

$$\mathfrak{C}_n^{IR\ res,LO}(\mathbf{k}_1, \dots, \mathbf{k}_n) = \mathfrak{C}_n^{tree} [P_{nw} + e^{-g^2\mathcal{S}}P_w](\mathbf{k}_1, \dots, \mathbf{k}_n) , \quad (3.44)$$

where \mathfrak{C}_n^{tree} is understood as a functional of the linear power spectrum. Note that, since the tree-level n -point correlation functions, when summed over all perturbative contributions, coincide in SPT and in TSPT, one can equivalently use the replacement (3.38) in the usual SPT computations. However, the clear diagrammatic representation as daisy resummation is only possible within TSPT. In addition, TSPT allows to systematically compute corrections to the LO resummation presented above.

3.4 Taking into account hard loops

So far, we have considered and resummed the contributions that in the power-counting scheme of Sec. 3.2.2 are of order $(\sigma_h^2)^0 \times (\sigma_S^2 \times 1/\varepsilon^2)^{L_s}$. We now discuss corrections to this result. One can discriminate two types of corrections:

- (1) Soft diagrams with non-maximal IR enhancement, characterized by $l = 2L_s - 1$ (see Eq. (3.31)), as well as the subleading terms in the diagrams considered in Sec. 3.3. These contributions are suppressed by one power of ε relative to the leading order.
- (2) Diagrams with one hard loop, $L_h = 1$, and otherwise maximal IR enhancement $l = 2L_s$. These diagrams are suppressed by one factor of σ_h^2 relative to the leading order.

We refer to these two types of contributions as NLO_s and NLO_h , respectively. When combined, they constitute the total NLO correction. In this section we analyze the contributions of the second type, while NLO_s corrections will be included in the next section.

We start from the ‘hard’ 1-loop contribution to the wiggly matter power spectrum⁶,

$$\begin{aligned}
 P_{w,\delta\delta}^{1-loop}(\eta; k) \Big|_{hard} = & \text{Diagram 1} + \text{Diagram 2} + \text{Diagram 3} \\
 & + \text{Diagram 4} + \text{Diagram 5} \\
 & + \text{Diagram 6} + \text{Diagram 7} \\
 & + \text{Diagram 8} + \text{Diagram 9} + \text{Diagram 10} \\
 & + \text{Diagram 11} + \text{Diagram 12} + \text{Diagram 13}
 \end{aligned}
 \tag{3.45}$$

where the wavenumber \mathbf{p} running in the loop is taken to be above the separation scale k_S , $p > k_S$. Note the appearance of a diagram with the counterterm C_2 in the second line. Similarly to the case of the tree-level bispectrum, all wiggly elements in these graphs can be dressed with soft daisies producing contributions of order

$$\sigma_h^2 \times (\sigma_S^2 \times 1/\varepsilon^2)^{L_s} .
 \tag{3.46}$$

Resummation of these contributions proceeds in a straightforward manner using the general expressions (3.39), (3.40) and yields,

$$P_{w,\delta\delta}^{IR\ res.,NLO_h}(\eta; k) = e^{-g^2(\eta)\mathcal{S}} P_{w,\delta\delta}^{1-loop}(\eta; k) \Big|_{hard},
 \tag{3.47}$$

where the r.h.s stands for the 1-loop diagrams (3.45) computed using the wiggly power spectrum $e^{-g^2\mathcal{S}}P_w$ instead of the linear power spectrum P_w as an input.

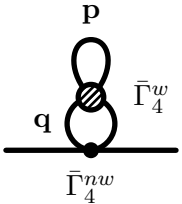
⁶For the Θ power spectrum one simply omits the diagrams containing the kernels K_n .

Two comments are in order. First, the diagrams in the third and fourth lines in (3.45), as well as their descendants obtained by dressing with daisies, contain a wiggly element inside the loop. This implies that the integrand of the corresponding loop integral is oscillating leading to cancellation between positive and negative contributions. As a result, the corresponding diagrams are further suppressed compared to the naive estimate (3.46). In fact, the suppression is formally exponential, as follows from the general formula for the Fourier transform of a smooth function,

$$\int [dp] \sin(p/k_{osc}) f_{smooth}(p/k) \sim e^{-k/k_{osc}} \sim e^{-1/\epsilon} .$$

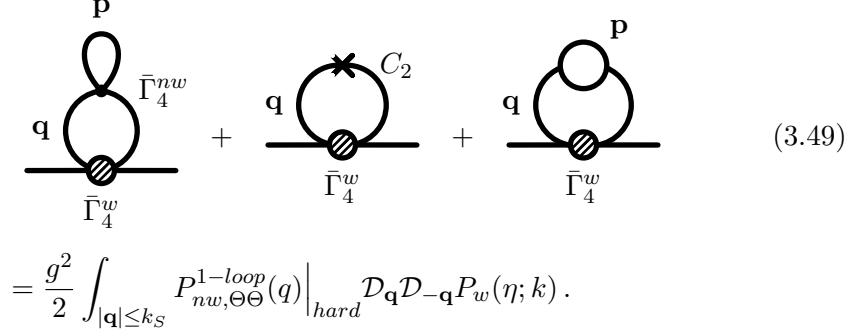
From the viewpoint of our power-counting scheme, these contributions are ‘non-perturbative’ and can be included or neglected without changing the accuracy of the perturbative calculation. We prefer to keep them as it allows us to write the result of IR resummation in the compact form (3.47).

Second, a careful reader might have noticed that the contributions discussed so far, namely those obtained by the daisy dressing of (3.45), do not exhaust all possible diagrams that formally would be of order (3.46) by the power-counting rules of Sec. 3.2.2. The remaining diagrams fall into two categories. First, there are diagrams where a hard line closes on a wiggly vertex, which is in its turn attached to the external legs via a soft loop; a two-loop example is given by



$$(3.48)$$

However, these diagrams necessarily contain a wiggly vertex inside a hard loop and thus, according to the previous discussion, are exponentially suppressed. They can be safely neglected. Another set of extra diagrams is given by the graphs where a hard loop is attached to a smooth propagator that belongs itself to a soft loop. For example, at two-loop order these are



$$\begin{aligned}
& \text{Diagram 1} + \text{Diagram 2} + \text{Diagram 3} \quad (3.49) \\
&= \frac{g^2}{2} \int_{|\mathbf{q}| \leq k_S} P_{nw, \Theta\Theta}^{1-loop}(q) \Big|_{hard} \mathcal{D}_{\mathbf{q}} \mathcal{D}_{-\mathbf{q}} P_w(\eta; k).
\end{aligned}$$

The subdiagrams attached to the soft loop combine into the hard part of the one-loop correction to the smooth velocity divergence power spectrum $P_{nw, \Theta\Theta}^{1-loop}(\eta; q)$, see [1]. As before, the ‘hard part’ means that the loop integration in $P_{nw, \Theta\Theta}^{1-loop}(q)$ is restricted to $p > k_S$. This correction could be viewed as a loop-correction to the operator \mathcal{S} suggesting to substitute the smooth power spectrum in \mathcal{S} by $P_s \mapsto P_{nw} + P_{nw, \Theta\Theta}^{1-loop} \Big|_{hard}$. While it is tempting to do this replacement, we refrain from this step for two reasons. First, this would correspond to a partial resummation of *hard* loops, and therefore goes against the rigorous expansion in our power counting parameters. Second, and more importantly, the hard loop corrections to the power spectrum are universally suppressed as q^2/k_S^2 at soft momenta $q \ll k_S$ due to the well-known decoupling of long and short modes [104, 105] (see also [106]). This suppression essentially removes the IR enhancement of the operator $\mathcal{D}_{\mathbf{q}} \mathcal{D}_{-\mathbf{q}}$ in (3.49), so that the term (3.49) is suppressed by $\langle q \rangle^2/k_S^2$ compared to the contributions resummed in (3.47). Here $\langle q \rangle$ is the characteristic IR scale which, as discussed in Sec. 3.2.2, is of order k_{eq} . Therefore, the contribution (3.49) is small as long as $k_{eq} \ll k_S$. In the real universe the hierarchy between k_S and k_{eq} cannot be too large. Nevertheless, we have checked numerically that for the standard Λ CDM and the realistic range of values $k_S \sim O(0.1h/\text{Mpc})$, the contribution (3.49) is quantitatively unimportant. In what follows we neglect the diagrams with hard loops inside soft ones.

The expression (3.47) can be cast in a more convenient form by the following steps. Let us add and subtract the soft part of the one-loop diagrams,

$$\begin{aligned}
P_{w, \delta\delta}^{IR res, NLO_h} &= e^{-g^2 \mathcal{S}} P_{w, \delta\delta}^{1-loop} \Big|_{hard} + e^{-g^2 \mathcal{S}} P_{w, \delta\delta}^{1-loop} \Big|_{soft} - e^{-g^2 \mathcal{S}} P_{w, \delta\delta}^{1-loop} \Big|_{soft} \\
&= e^{-g^2 \mathcal{S}} P_{w, \delta\delta}^{1-loop} + e^{-g^2 \mathcal{S}} g^2 \mathcal{S} P_w,
\end{aligned} \quad (3.50)$$

where in the last line $P_{w, \delta\delta}^{1-loop}$ stands for the *total* one-loop correction and we used Eq. (3.28) to express the leading soft-loop contribution. Combining this with the one-loop correction to the smooth power spectrum and the LO expression (3.35)

we obtain the final expression for the power spectrum with NLO_h corrections included,

$$P_{\delta\delta}^{IR\ res, LO+NLO_h} = P_{nw} + (1 + g^2 \mathcal{S}) e^{-g^2 \mathcal{S}} P_w + P_{\delta\delta}^{1-loop} [P_{nw} + e^{-g^2 \mathcal{S}} P_w] . \quad (3.51)$$

Here $P_{\delta\delta}^{1-loop}$ is understood as the functional of the input linear power spectrum; the latter has been modified by the IR resummation. Note the appearance of the term $g^2 \mathcal{S} e^{-g^2 \mathcal{S}} P_w$ in the ‘tree-level’ part of the expression (3.51) that is important to avoid double counting of the soft contributions.

The formula (3.51) can be straightforwardly generalized to other n -point functions, both of density and velocity divergence. We give here the final result without derivation,

$$\mathfrak{C}_n^{IR\ res, LO+NLO_h} = \mathfrak{C}_n^{tree} [P_{nw} + (1 + g^2 \mathcal{S}) e^{-g^2 \mathcal{S}} P_w] + \mathfrak{C}_n^{1-loop} [P_{nw} + e^{-g^2 \mathcal{S}} P_w] . \quad (3.52)$$

Moreover, it is possible to include higher hard loops, i.e. corrections of order $\sigma_h^{2L_h}$ with $L_h \geq 2$. Let us do it for the power spectrum⁷. Repeating the arguments that led to Eq. (3.47), one finds at the $NNLO_h$ order,

$$P_w^{IR\ res, NNLO_h} = e^{-g^2 \mathcal{S}} P_w^{2-loop} \Big|_{hh} , \quad (3.53)$$

where the 2-loop contribution on the r.h.s. is ‘double-hard’, i.e. the integration in both loops run over $p > k_S$. This is equivalently written in the form,

$$P_w^{IR\ res, NNLO_h} = e^{-g^2 \mathcal{S}} P_w^{2-loop} - e^{-g^2 \mathcal{S}} P_w^{2-loop} \Big|_{hs} - e^{-g^2 \mathcal{S}} P_w^{2-loop} \Big|_{ss} , \quad (3.54)$$

where the first term contains the total 2-loop contribution, whereas the second and third terms are ‘hard-soft’ and ‘soft-soft’ respectively. Next, we use the relations valid at the leading soft order,

$$P_w^{2-loop} \Big|_{ss} = \frac{g^4 \mathcal{S}^2}{2} P_w , \quad (3.55a)$$

$$P_w^{2-loop} \Big|_{hs} = -g^2 \mathcal{S} P_w^{1-loop} \Big|_h = -g^2 \mathcal{S} P_w^{1-loop} - g^4 \mathcal{S}^2 P_w , \quad (3.55b)$$

where to obtain the last expression in (3.55b) we have again added and subtracted the soft one-loop contribution. Combining everything together and with the

⁷The derivation does not depend on the type of the power spectrum ($\delta\delta$, $\Theta\Theta$ or $\Theta\delta$) so we do not specify it explicitly.

NLO_h expression (3.51) we arrive at a compact formula,

$$\begin{aligned}
P^{IR\ res, LO+NLO_h+NNLO_h} = & P_{nw} + \left(1 + g^2\mathcal{S} + \frac{g^4\mathcal{S}^2}{2}\right) e^{-g^2\mathcal{S}} P_w \\
& + P^{1-loop} [P_{nw} + (1 + g^2\mathcal{S})e^{-g^2\mathcal{S}} P_w] + P^{2-loop} [P_{nw} + e^{-g^2\mathcal{S}} P_w].
\end{aligned}
\tag{3.56}$$

Its extension to other correlation functions and to higher orders in hard loops can be done by proceeding analogously.

The expressions (3.51), (3.52), (3.56) do not take into account subleading soft corrections. These are formally of order ε and thus can be expected to be significant as in the real universe the latter parameter is not small, $\varepsilon \sim 0.2 \div 0.3$. Therefore the next section is devoted to a detailed computation of these corrections. Notably, we will find that the dominant NLO_s corrections are already captured by the one-loop term in (3.51) for the power spectrum, such that it works remarkably well. Still, it is important to properly assess the NLO_s contributions because they are required for a reliable determination of the shift of the BAO peak, as discussed in Sec. 3.6.4.

3.5 Resummation of infrared effects at next-to leading order

Here we discuss corrections to the power spectrum that are suppressed by one power of ε relative to the leading order IR resummed results discussed previously. There are two possibilities to obtain such corrections: (a) On the one hand, one can consider the same daisy diagrams, *i.e.* with maximal IR enhancement $l = 2L_s$, but take into account the first sub-leading correction in the expansion of the wiggly vertex (3.23). (b) On the other hand, one can consider new diagrams with $l = 2L_s - 1$. All diagrams that contribute at $O(\varepsilon)$ to the velocity divergence power spectrum at increasing number of loops are given by

$$\begin{aligned}
 P_{w,\Theta\Theta}^{IR\,res,LO+NLO_s}(\eta; k) = & \text{wavy line } \mathbf{k} + \text{fish diagram } \bar{\Gamma}_4^w + \text{fish diagram } \bar{\Gamma}_3^w + \text{fish diagram } \bar{\Gamma}_3^{nw} \\
 & + \text{fish diagram } \bar{\Gamma}_6^w + \text{fish diagram } \bar{\Gamma}_5^w + \text{fish diagram } \bar{\Gamma}_3^{nw} + \text{fish diagram } \bar{\Gamma}_5^w \\
 & + \text{fish diagram } \bar{\Gamma}_8^w + \text{fish diagram } \bar{\Gamma}_7^w + \text{fish diagram } \bar{\Gamma}_3^{nw} + \text{fish diagram } \bar{\Gamma}_7^w + \dots
 \end{aligned}
 \tag{3.57}$$

Here all loops are soft, *i.e.* integrated over wavenumbers below k_S . The daisy diagrams containing the vertices $\bar{\Gamma}_4^w, \bar{\Gamma}_6^w, \bar{\Gamma}_8^w \dots$ at 1, 2, 3-loop, and so on, belong to the category (a). The diagrams containing $\bar{\Gamma}_3^w, \bar{\Gamma}_5^w, \bar{\Gamma}_7^w \dots$ at 1, 2, 3-loop, and so on, have $l = 1, 3, 5, \dots$, and therefore belong to category (b). All diagrams in category (b) are related to two new diagrams: the *fish* (last diagram in the first line) and *oyster* (last diagram in the second line). All higher-loop diagrams of type (b) are obtained by dressing the wiggly vertex contained in these diagrams with daisy loops, such as *e.g.* the middle diagram in the second line and the last two diagrams in the last line. The matter power spectrum includes in addition at $O(\varepsilon)$ the dressed fish diagram with the vertex K_2 ,

$$\begin{aligned}
 P_{w,\delta\delta}^{IR\,res,LO+NLO_s}(\eta, k) = & P_{w,\Theta\Theta}^{IR\,res,LO+NLO_s}(\eta, k) \\
 & + \text{fish diagram } \bar{\Gamma}_3^w + \text{fish diagram } \bar{\Gamma}_5^w + \dots
 \end{aligned}
 \tag{3.58}$$

We first consider the diagrams of type (b). Dressing of the fish diagrams simply leads to the already familiar replacement (3.38). We do not need these contributions explicitly, as our eventual goal is to combine them with the hard corrections (3.47) to form the total fish diagrams evaluated using the modified wiggly power spectrum (3.38).

For the oyster diagram, a straightforward evaluation using the expansion (3.22) for $\bar{\Gamma}_5^w$ and the exact expression for $\bar{\Gamma}_3^{nw}$ yields,

$$\delta P_{w,oyster}^{1-loop} \Big|_{soft} \equiv \left(\text{Diagram: a horizontal line with a loop on top, labeled } \bar{\Gamma}_3^{nw} \text{ above and } \bar{\Gamma}_5^w \text{ below} \right) \Big|_{soft} = g^6 (\mathcal{S}^a + 2\kappa \mathcal{S}^b) \bar{P}_w(k), \quad (3.59)$$

where we introduced the operators,

$$\mathcal{S}^a \bar{P}_w(k) = 2 \int_{|\mathbf{q}|, |\mathbf{q}'| \leq k_S} \bar{P}_{nw}(q) \bar{P}_{nw}(q') \frac{(\mathbf{k} \cdot \mathbf{q})^2 (\mathbf{k} \cdot \mathbf{q}') (\mathbf{q} \cdot \mathbf{q}')}{q^4 q'^4} \sinh(\mathbf{q} \cdot \nabla) (1 - \cosh(\mathbf{q}' \cdot \nabla)) \bar{P}_w(k), \quad (3.60a)$$

$$\begin{aligned} \mathcal{S}^b \bar{P}_w(k) &= \frac{6}{7} \int_{|\mathbf{q}|, |\mathbf{q}'| \leq k_S} \bar{P}_{nw}(q) \bar{P}_{nw}(q') \sin^2(\mathbf{q}, \mathbf{q}') \\ &\times \frac{(\mathbf{k} \cdot \mathbf{q}) (\mathbf{k} \cdot \mathbf{q}') (\mathbf{k} \cdot (\mathbf{q} + \mathbf{q}'))}{q^2 q'^2 (\mathbf{q} + \mathbf{q}')^2} \sinh(\mathbf{q} \cdot \nabla) (1 - \cosh(\mathbf{q}' \cdot \nabla)) \bar{P}_w(k), \end{aligned} \quad (3.60b)$$

and $\kappa = 1$ ($\kappa = 0$) in ED (ZA). The dressing of the wiggly vertex by daisies again leads to the replacement (3.38) in this formula,

$$\delta P_{w,oyster}^{IR res, NLO_s} = g^6 (\mathcal{S}^a + 2\kappa \mathcal{S}^b) e^{-g^2 \mathcal{S}} \bar{P}_w(k). \quad (3.61)$$

Next, we turn to the contributions of type (a), i.e. daisy diagrams expanded to the NLO_s order. Remarkably, these also can be resummed. To see this, we need the first corrections in ε to Eq. (3.23). The latter are derived in Appendix B.3 with the result,

$$\begin{aligned} \bar{\Gamma}_n^{nw, LO+NLO} \left(\mathbf{k}, -\mathbf{k} - \sum_{i=1}^{n-2} \mathbf{q}_i, \mathbf{q}_1, \dots, \mathbf{q}_{n-2} \right) \\ = (-1)^{n-1} \left[\prod_{i=1}^{n-2} \mathcal{D}_{\mathbf{q}_i} + \sum_{j=1}^{n-2} \mathcal{E}_{\mathbf{q}_j} \prod_{\substack{i=1 \\ i \neq j}}^{n-2} \mathcal{D}_{\mathbf{q}_i} + \sum_{\substack{j_1, j_2=1 \\ j_1 < j_2}}^{n-2} \mathcal{F}_{\mathbf{q}_{j_1} \mathbf{q}_{j_2}} \prod_{\substack{i=1 \\ i \neq j_1, j_2}}^{n-2} \mathcal{D}_{\mathbf{q}_i} \right] \frac{\bar{P}_w(k)}{\bar{P}_{nw}^2(k)}, \end{aligned} \quad (3.62)$$

where $\mathcal{E}_{\mathbf{q}}$ and $\mathcal{F}_{\mathbf{q}_1 \mathbf{q}_2}$ are new finite-difference operators acting on \bar{P}_w that are defined in (B.18) and (B.21). Inserting this expression into Eq. (3.32) and summing over the number of loops L we obtain,

$$\delta P_{w,daisy}^{IR res, LO+NLO_s} = (g^2 + g^4 \mathcal{S}^c - g^6 \mathcal{S}^a - g^6 \kappa \mathcal{S}^b) e^{-g^2 \mathcal{S}} \bar{P}_w(k), \quad (3.63)$$

where

$$\mathcal{S}^c \bar{P}_w(k) = \frac{1}{2} \int_{|\mathbf{q}| \leq k_S} \bar{P}_{nw}(q) (\mathcal{E}_{\mathbf{q}} \mathcal{D}_{-\mathbf{q}} + \mathcal{E}_{-\mathbf{q}} \mathcal{D}_{\mathbf{q}} + \mathcal{F}_{\mathbf{q}, -\mathbf{q}}) \bar{P}_w(k), \quad (3.64)$$

and we used the relation

$$\frac{1}{2} \int_{|\mathbf{q}|, |\mathbf{q}'| \leq k_S} \bar{P}_{nw}(q) \bar{P}_{nw}(q') \mathcal{F}_{\mathbf{q}, \mathbf{q}'} \mathcal{D}_{-\mathbf{q}} \mathcal{D}_{-\mathbf{q}'} = -(\mathcal{S}^a + \varkappa \mathcal{S}^b). \quad (3.65)$$

It is desirable to connect the expression (3.63) to the one-loop daisy graph computed using the modified linear power spectrum,

$$\delta P_{w, daisy}^{1-loop, LO+NLO_s} [P_{nw} + e^{-g^2 \mathcal{S}} P_w]. \quad (3.66)$$

One may be tempted to compute this by simply making the replacement (3.38) in the NLO expression (B.20) for the vertex function $\bar{\Gamma}_4^w$. However, this would produce a mistake at the NLO_s order. The reason is that the operator \mathcal{S} depends on the hard wavenumber \mathbf{k} (see Eq. (3.29)). When $\bar{\Gamma}_4^w$ is evaluated with the new wiggly power spectrum $e^{-g^2 \mathcal{S}} \bar{P}_w$, the operator \mathcal{S} gets shifted,

$$\mathcal{S}|_{\mathbf{k}} \mapsto \mathcal{S}|_{\mathbf{k} \pm \mathbf{q}} = \mathcal{S}|_{\mathbf{k}} \pm \Delta \mathcal{S}|_{\mathbf{q}}.$$

The correct expression for the vertex taking this shift into account is derived in Appendix B.3, see Eq. (B.29). Using it to evaluate the loop we obtain,

$$\delta P_{w, daisy}^{1-loop, LO+NLO_s} [P_{nw} + e^{-g^2 \mathcal{S}} P_w] \Big|_{soft} = (-g^4 \mathcal{S} + g^4 \mathcal{S}^c - g^6 \mathcal{S}^a) e^{-g^2 \mathcal{S}} \bar{P}_w(k). \quad (3.67)$$

This should be compared with (3.63). We have

$$\begin{aligned} \delta P_{w, daisy}^{IR res, LO+NLO_s} &= g^2 (1 + g^2 \mathcal{S}) e^{-g^2 \mathcal{S}} \bar{P}_w + \delta P_{w, daisy}^{1-loop, LO+NLO_s} [P_{nw} + e^{-g^2 \mathcal{S}} P_w] \Big|_{soft} \\ &\quad - g^6 \varkappa \mathcal{S}^b e^{-g^2 \mathcal{S}} \bar{P}_w. \end{aligned} \quad (3.68)$$

Notice that the operators \mathcal{S}^a , \mathcal{S}^c have dropped out of this relation.

We are now ready to combine all NLO contributions together. These include the resummed hard loops (3.47), soft fish diagrams, the contribution of the soft oyster diagram (3.61), and the resummed daisies (3.68). Adding to them the

smooth part we obtain,

$$P_w^{IR\ res, LO+NLO} = P_{nw} + (1 + g^2 \mathcal{S}) e^{-g^2 \mathcal{S}} P_w + P^{1-loop} [P_{nw} + e^{-g^2 \mathcal{S}} P_w] + g^4 (\mathcal{S}^a + \varkappa \mathcal{S}^b) e^{-g^2 \mathcal{S}} P_w. \quad (3.69)$$

This is our final result for the full NLO power spectrum. At face value, it differs from the NLO_h formula (3.51) only by the last term. However, we emphasize that now all subleading IR corrections have been consistently included. In particular, the one-loop contribution differs for ZA and ED as well as for density and velocity correlators at the NLO_s order. The last term scales as g^4 compared to the leading piece. This reflects that it receives contributions only starting from 2-loops. Nevertheless, at face value this term is of order $O(\varepsilon)$ in our power counting and therefore must be retained. Still, we will find below that it accidentally happens to be numerically small due to the specific shape of the matter power spectrum in our universe.

3.6 Practical implementation and comparison with other methods

In this section we first discuss how the IR resummed power spectrum obtained in TSPT can be evaluated in practice, and then compare to other analytic approaches as well as to N -body data. In the last part we discuss the predictions for the shift of the BAO peak.

3.6.1 Evaluation of IR resummed power spectrum

After decomposing the linear power spectrum $P^{lin}(z, k) = D(z)^2 (P_{nw}(k) + P_w(k))$ into smooth and oscillating (wiggly) contributions⁸, we need to evaluate the derivative operator \mathcal{S} defined in (3.29), that describes the IR enhancement. This is done using

$$\nabla_{\alpha_1} \cdots \nabla_{\alpha_{2n}} P_w(k) = (-1)^n \frac{\hat{k}_{\alpha_1} \cdots \hat{k}_{\alpha_{2n}}}{k_{osc}^{2n}} P_w(k) (1 + O(\varepsilon)),$$

where ε is the small expansion parameter related to IR enhancement defined in (3.19) and $\hat{\mathbf{k}} = \mathbf{k}/k$. Recall that $k_{osc} = h/(110 \text{ Mpc})$ is the scale setting the

⁸ In this section we adopt the conventional notations and denote the growth factor $g \mapsto D(z)$ and the linear power spectra at $z = 0$ simply by $\bar{P}_{s(w)}(k) \mapsto P_{s(w)}(k)$.

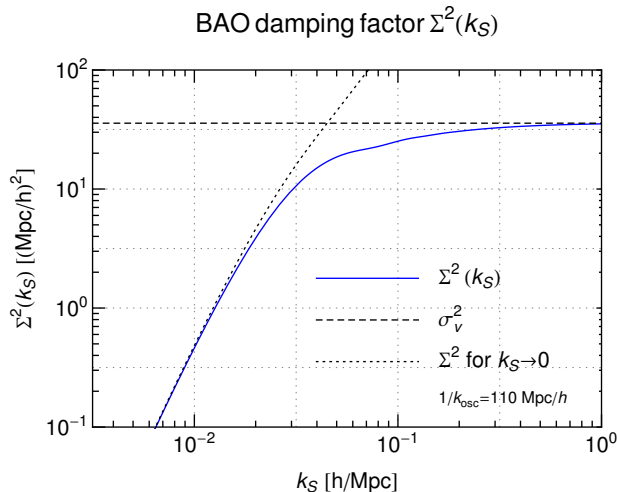


FIGURE 3.4: Dependence of the BAO damping factor Σ^2 on the separation scale k_S . Dashed curves show the limiting cases discussed in the text.

period of the BAO oscillations. A straightforward computation yields

$$\mathcal{S}P_w(k) = k^2 \Sigma^2 P_w(k) \times (1 + O(\varepsilon)), \quad (3.70)$$

with

$$\Sigma^2 \equiv \frac{4\pi}{3} \int_0^{k_S} \frac{dq}{(2\pi)^3} P_{nw}(q) \left[1 - j_0\left(\frac{q}{k_{osc}}\right) + 2j_2\left(\frac{q}{k_{osc}}\right) \right], \quad (3.71)$$

where j_n are spherical Bessel functions and k_S is the (a priori arbitrary) separation scale of long and short modes, that has been introduced in order to treat the perturbative expansion in the two regimes separately. Since the exact result for the power spectrum and other observables is independent of k_S , any residual dependence on it can be taken as an estimate of the perturbative uncertainty. The IR resummed power spectrum at leading order following from (3.35) is given by

$$P^{IR\ res, LO}(z, k) = D(z)^2 \left(P_{nw}(k) + e^{-k^2 D(z)^2 \Sigma^2} P_w(z) \right), \quad (3.72)$$

where the first term corresponds to the smooth part of the linear spectrum. The leading effect of IR enhanced loop contributions is an exponential damping of the oscillatory part of the spectrum.

Let us now discuss the choice of k_S . By inspection of the integrand in (3.71) we find that it peaks at $q \sim 0.03h/\text{Mpc}$, but gives significant contribution into the integral up to wavenumbers $q \sim 0.2h/\text{Mpc}$. This is corroborated by the numerical evaluation of the damping factor Σ^2 as a function of k_S ; the result is shown in Fig. 3.4 for a realistic ΛCDM model. For very small

values of the IR separation scale $k_S \lesssim k_{osc}$ it approaches the limiting form $\Sigma^2 \rightarrow 2\pi/5 \int_0^{k_S} dq q^2 P_{nw}(q)/k_{osc}^2/(2\pi)^3$, while for large $k_S \gg k_{osc}$ it asymptotes to a constant $\Sigma^2 \rightarrow \sigma_v^2 \equiv 4\pi/3 \int_0^\infty dq P_{nw}(q)/(2\pi)^3$. It is desirable to take k_S as large as possible to include more IR contributions and minimize the dependence of the damping factor on k_S . On the other hand, k_S cannot be taken too large as the previous analysis relies on the IR expansions which are valid for $q \ll k$. As a compromise, we consider several values of k_S around the BAO scale $k_{BAO} \sim 0.1h/\text{Mpc}$. We are going to see that the dependence of our results on the precise choice of k_S in this range is very mild.

At NLO, the IR resummed power spectrum (3.69) can be written in the form⁹

$$\begin{aligned} P^{IR\ res, LO+NLO}(z, k) &= D(z)^2 \left(P_s(k) + (1 + k^2 D(z)^2 \Sigma^2) e^{-k^2 D(z)^2 \Sigma^2} P_w(k) \right) \\ &\quad + D(z)^4 P^{1-loop} [P_{nw} + e^{-k^2 D(z)^2 \Sigma^2} P_w] \\ &\quad + D(z)^6 e^{-k^2 D(z)^2 \Sigma^2} (\mathcal{S}^a + \varkappa \mathcal{S}^b) P_w(k), \end{aligned} \tag{3.73}$$

where $\varkappa = 1$ in ED ($\varkappa = 0$ in ZA). The first term in the second line of (3.73) corresponds to the standard one-loop result, but computed with the LO IR resummed power spectrum, instead of the linear one. As was demonstrated in [1], the sum over all one-loop diagrams in TSPT agrees with the SPT result. Therefore, in practice, one can use the usual expression $P^{1-loop} = P_{22} + 2P_{13}$, however evaluating the loop integrals P_{22} and P_{13} with the input spectrum (3.72) instead of the linear spectrum.

Finally, the finite-difference operators in the last term can be evaluated similarly to \mathcal{S} . After somewhat lengthy but straightforward calculation, we obtain

$$\begin{aligned} \mathcal{S}^a P_w(k) &= \frac{8\pi}{5} k_{osc} k^3 \Sigma^2 \int_0^{k_S} \frac{qdq}{(2\pi)^3} P_{nw}(q) \left[3j_1\left(\frac{q}{k_{osc}}\right) - 2j_3\left(\frac{q}{k_{osc}}\right) \right] \frac{dP_w(k)}{dk} \\ &\equiv k^3 \Sigma_a^2 \frac{dP_w(k)}{dk}, \end{aligned} \tag{3.74a}$$

$$\begin{aligned} \mathcal{S}^b P_w(k) &= - (4\pi)^2 k_{osc}^2 k^3 \int_0^{k_S} \frac{dqdq'}{(2\pi)^6} P_{nw}(q) P_{nw}(q') h\left(\frac{q'}{k_{osc}}, \frac{q}{k_{osc}}\right) \frac{dP_w(k)}{dk} \\ &\equiv k^3 \Sigma_b^2 \frac{dP_w(k)}{dk}, \end{aligned} \tag{3.74b}$$

⁹ Since we are keeping NLO terms, one should in principle keep also the first sub-leading corrections in the evaluation of the derivative operator in (3.70). However, it turns out that this correction cancels in (3.73) at NLO precision. The simplest way to see this is to go back to Eqs. (3.63), (3.67) and substitute in them the expansion (3.70) keeping track of the $O(\varepsilon)$ terms. By comparing the resulting expressions one finds that the relation (3.68) holds with NLO precision if \mathcal{S} is everywhere replaced by $k^2 \Sigma^2$. As all other contributions comprising (3.69) do not contain an $O(1)$ part, the replacement $\mathcal{S} \mapsto k^2 \Sigma^2$ in them is also justified leading to (3.73).

with

$$h(x, y) = \frac{3}{7}(h_1(x, y) + h_2(x, y) + h_2(y, x)). \quad (3.75)$$

The functions $h_{1,2}(x, y)$ are given in App. C. The result (3.73) is valid for both density, velocity and cross power spectra when using the appropriate expressions for the one-loop correction. In addition, one can obtain the result in ZA by using the corresponding one-loop expression with kernels computed in ZA and setting $\varkappa = 0$.

An important comment is in order. Naively, we expected the corrections NLO soft corrections to scale as

$$\varepsilon \times (\sigma_S^2 \times 1/\varepsilon^2)^{L_s}, \quad (3.76)$$

in which case they should have $O(\varepsilon) \sim k_{eq}/k \sim 10\%$ effect. However, in contradiction to this expectation, a direct numerical evaluation of contributions (3.74) shows that they only have a sub-percent effect at the BAO scales. We now argue that the smallness of the NLO soft corrections is a consequence of the specific shape of the linear power spectrum in the Λ CDM cosmology. From Eq. (3.74) one observes that the integrands of the LO and NLO soft contributions are different, so that the estimate (3.76) should be properly written as

$$(\sigma_{S,\text{NLO}}^2 \times 1/\varepsilon) \times (\sigma_{S,\text{LO}}^2 \times 1/\varepsilon^2)^{L_s-1}. \quad (3.77)$$

Here $\sigma_{S,\text{LO}}^2$ receives contributions from momenta $k_{osc} \lesssim q \lesssim k_S$ and is saturated in the vicinity of the maximum of the power spectrum at $q \sim k_{eq} > k_{osc}$. It is indeed of the order¹⁰ (3.25). On the other hand, the integrand in the subleading soft loop corrections (c.f. (D.7)) schematically has the form,

$$\begin{aligned} (\sigma_{S,\text{NLO}}^2 \times 1/\varepsilon) &\propto g^2 \int_{q < k_S} \frac{d^3 q}{(2\pi)^3} \frac{(\mathbf{q} \cdot \mathbf{k})}{q^2} \bar{P}_{nw}(q) (1 - e^{i \frac{\mathbf{q} \cdot \mathbf{k}}{k_{osc}}}) \\ &\sim g^2 k \int_0^{k_S} \frac{dq}{(2\pi)^3} q \bar{P}_{nw}(q) \left[j_1 \left(\frac{q}{k_{osc}} \right) \right], \end{aligned} \quad (3.78)$$

where j_1 is the spherical Bessel function. The integral is effectively cut at $q \sim k_{osc}$, before the linear power spectrum reaches its maximum. Recalling that in this region the Λ CDM power spectrum behaves as $\bar{P}_{nw}(q) \propto q$, we find that

$$\sigma_{S,\text{NLO}}^2 / \sigma_{S,\text{LO}}^2 \sim (k_{osc}/k_{eq})^3 \sim 0.1. \quad (3.79)$$

¹⁰Essentially, $\sigma_{S,\text{LO}}^2$ coincides with $k_{eq}^2 \Sigma^2$, where Σ^2 is the BAO damping factor given in Eq. (3.71). Its numerical value is plotted in Fig. 3.4.

This leads to additional numerical suppression of the NLO soft corrections.

Qualitatively, the result (3.79) can be understood as follows. The NLO soft corrections are responsible for the shift of the BAO peak. This shift can be seen as shrinking of the BAO scale in an overdense region that locally behaves as a universe with positive spatial curvature [107]. Hence, the shift is sensitive only to the curvature of this “universe”, which is generated by modes with wavelengths bigger than r_{BAO} . Thus, the NLO soft contributions should be saturated at k_{osc} . On the other hand, the damping of the BAO feature (which is produced by LO soft corrections) is affected by modes with wavelengths down to the width of the BAO peak [29]. Thus, the LO soft corrections should include contributions from wavenumbers $q \gg k_{osc}$.

Note that in a hypothetical universe with $k_{eq} \ll k_{osc}$ the situation would be different, with $\sigma_{S,NLO}^2$ being of the same order as $\sigma_{S,LO}^2$. The power-counting rules of Sec. 3.2.2 are formulated in full generality and do not rely on the precise shape of the linear power spectrum.

The upshot of our discussion is that in the Λ CDM cosmology the soft NLO corrections are numerically suppressed and can be neglected for many purposes, e.g. if one is interested in the full-shape measurements of the power spectrum or the 2-point correlation function. On the other hand, we will see shortly that the NLO soft corrections are important for an accurate determination of the shift of the BAO peak.

Finally, the IR resummed result for the bispectrum is given at leading order in ε and σ_h^2 by (see Eq. (3.43))

$$B_{\delta\delta\delta}^{IR\ res;LO}(z; \mathbf{k}_1, \mathbf{k}_2, \mathbf{k}_3) = B_{s,\delta\delta\delta}^{tree}(z; \mathbf{k}_1, \mathbf{k}_2, \mathbf{k}_3) + 2D(z)^4 \sum_{i<j=1}^3 F_2(\mathbf{k}_i, \mathbf{k}_j) \left(e^{-k_j^2 D(z)^2 \Sigma^2} P_w(k_j) P_s(k_i) + i \leftrightarrow j \right), \quad (3.80)$$

where $B_{s,\delta\delta\delta}^{tree}(z; \mathbf{k}_1, \mathbf{k}_2, \mathbf{k}_3)$ is the tree-level result for the smooth part, as obtained also in SPT, and $F_2(\mathbf{k}_i, \mathbf{k}_j)$ is the usual SPT kernel [15]. IR resummation again corresponds to a damping of the oscillating contributions.

3.6.2 Comparison with other approaches

Let us now compare our results to other approaches existing in the literature. From a phenomenological viewpoint, it is well-known that an exponential damping factor applied to the oscillating component of the power spectrum gives a reasonable description of the BAO peak in the measured two- and also three-point correlation functions, see e.g. [44] and references therein. Therefore, the aim of perturbative descriptions is to derive this behavior from first principles, identify effects that go beyond a simple damping, and give a definite quantitative prediction as well as an estimate of the theoretical error.

There exist many schemes to derive non-linear corrections to the BAO peak within cosmological perturbation theory, here we focus on a few of them. In [27], the RPT formalism [62] was used to obtain a formula of the form.

$$P(z, k) = G^2(z, k)P_{\text{lin}}(k) + P_{MC}(z, k), \quad (3.81)$$

where $G(z, k)$ is the propagator and P_{MC} is the part due to the mode coupling. The propagator describes how a perturbation evolves over time and is not a Galilean invariant quantity. As such, it contains IR enhanced contributions corresponding to the translation of inhomogeneities by large-scale flows. When resummed at the leading order, these contributions produce an exponential damping factor at high k ,

$$G^2(z, k) = D(z)^2 \exp[-k^2 D(z)^2 \sigma_v^2], \quad (3.82)$$

with

$$\sigma_v^2 \equiv 4\pi/3 \int_0^\infty dq P_{\text{lin}}(q)/(2\pi)^3 \quad (3.83)$$

In the RPT-based approach this form of the propagator is substituted into (3.81). A similar result is derived in the Lagrangian picture in [63, 108]. Notice that the exponential damping in this case applies to the whole linear power spectrum, including both wiggly and smooth parts. Further developments of this idea have been proposed in [109].

While being successful on a phenomenological level, this approach is quite different from ours. In RPT, there is no clear parametric dependence that would single out the resummed set of contributions. In particular, for a *smooth* power spectrum the contributions resummed in (3.82) are of the same order as those comprising P_{MC} , and actually cancel with them [17, 18, 20, 22–24] as required

by the equivalence principle. On the other hand, our approach is based on well-defined power-counting rules formulated directly for the perturbative expansion of equal-time correlation functions. As a result, we obtain a damping only of the oscillating part of the power spectrum, in line with the expected cancellation of IR enhancement for the smooth part. A simple modification of (3.82) that fixes this issue can be obtained by applying the exponential damping only on the wiggly power spectrum,

$$P(z, k) = P_{nw}(k) + e^{-k^2 D^2(z) \sigma_v^2} P_w(k). \quad (3.84)$$

However, the damping factor from our expression (3.71) has a different structure from the rms velocity displacement (3.83). The latter is enhanced at very low q , whereas the modes with $q \ll k_{osc}$ should not affect the BAO feature as dictated by the equivalence principle.

Another model for the non-linear damping was put forward in Refs. [26, 103],

$$P(z, k) = P_{nw}(k) + e^{-k^2 D^2(z) \Sigma_\infty^2} P_w(k), \quad (3.85)$$

$$\Sigma_\infty^2 \equiv \frac{4\pi}{3} \int_0^\infty \frac{dq}{(2\pi)^3} P(q) \left[1 - j_0\left(\frac{q}{k_{osc}}\right) + 2j_2\left(\frac{q}{k_{osc}}\right) \right].$$

This model explicitly takes into account the fact that bulk flows significantly affect only the wiggly part of the power spectrum. On the other hand, the damping factor in (3.85) is slightly different from ours, see Eq. (3.71). Although both factors (3.71) and (3.85) have the same integrand, the integral in (3.85) is evaluated up to $k_S = \infty$. In contrast to the RPT-based models discussed above, the integrand of (3.85) tends to zero in the IR, which is consistent with the physical expectations based on the equivalence principle. On the other hand, the choice of $k_S = \infty$ contradicts the logic that only long-wavelength modes have to be resummed and should be contrasted with our expressions which explicitly reflect this argument. Indeed, only for the soft modes with $q \ll k$ the mode coupling affecting the BAO is enhanced.

As shown in Fig. 3.4, the numerical value of our damping factor appears to be quite close to both (3.83) and (3.85) for the Λ CDM cosmology. It was already pointed out in [29] that if our universe had more power at large scales, $q \lesssim k_{osc}$, the damping factor (3.71) would be notably different¹¹ from σ_v^2 . On the other hand, if there were more power at short scales, using (3.85) one would significantly overdamp the BAO signal.

¹¹ It would be interesting to understand if this can account for the discrepancy between σ_v^2 and the actual damping factor found in simulations of a toy cosmological model with a bigger k_{osc} in [110].

To conclude on the comparison with approaches (3.82) and (3.85), we emphasize that when taking the NLO corrections into account our result (3.73) cannot be described anymore by a simple exponential damping of the overall power spectrum or its wiggly part.

Ref. [29] proposed a description of the IR enhanced effects on the BAO peak motivated by consistency relations between the bispectrum and the power spectrum based on the equivalence principle. This approach is related to the earlier perturbative framework developed in [28]. At leading order, our result (3.72) coincides with the results of [29] when choosing $k_S = k/2$. The agreement essentially extends to the corrections produced by hard loops (see Sec. 3.4). Subleading soft corrections were not considered in [29]. TSPT gives a simple diagrammatic description of IR enhancement and provides a tool to systematically derive, scrutinize and extend the results found in [29]. In particular, the subleading soft corrections computed in the present work and entering in (3.73) capture the shift of the BAO peak, as we will see below, and the power counting allows in principle to go beyond NLO in a systematic way. Furthermore, the IR resummation in TSPT readily generalizes beyond the power spectra and applies to any n -point correlation functions.

3.6.3 Comparison with N -body data

We consider a Λ CDM model with cosmological parameters matching those of the Horizon simulation [101]. The linear power spectrum is obtained from the CLASS code [111] and decomposed into smooth and oscillating components as described in Sec. 3.1.1.

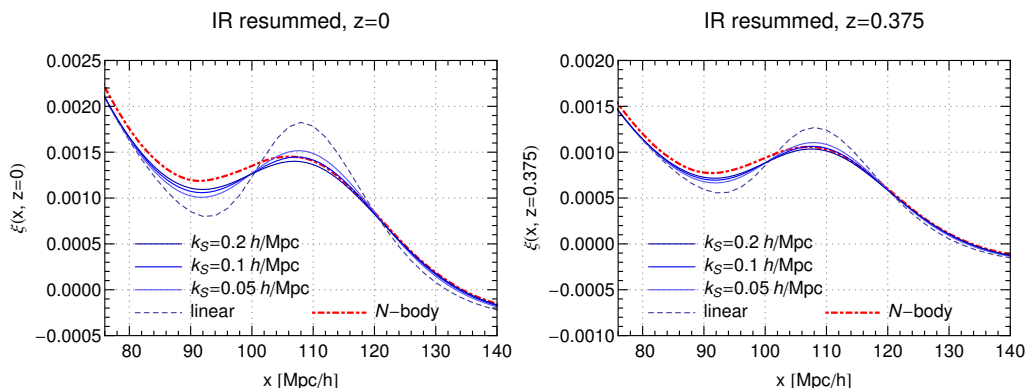


FIGURE 3.5: Infra-red resummed matter correlation function at LO obtained in TSPT for three different values of the IR separation scale k_S , and two different redshifts (left: $z = 0$, right: $z = 0.375$). Also shown is the linear result (dashed) and the result of the Horizon Run 2 large-scale N -body simulation [101]. We use $1/k_{osc} = 110 \text{ Mpc}/h$.

In the following we show results for the correlation function, because it exhibits a clear separation between the BAO peak and the small-distance part of the correlations, and allows to visualize the effects on the BAO feature in a transparent way. The matter correlation function is related to the power spectrum as

$$\xi(x, z) = \frac{4\pi}{x} \int_0^\infty \frac{dk}{(2\pi)^3} kP(k, z) \sin(kx). \quad (3.86)$$

In Fig. 3.5, we show the leading-order IR resummed result for three different choices of k_S (blue solid lines). The damping of the BAO oscillations described by Σ corresponds to a broadening of the BAO peak in real space and gives already a relatively good description of the N -body result shown by the red dashed line [101], especially when compared to the linear prediction (thin dashed line). Nevertheless, there are some differences, and the dependence on k_S is not negligible.

We now turn to the NLO result. The comparison of the matter correlation function obtained using (3.73) with the N -body data is shown in Fig. 3.6. One observes that the agreement is considerably improved compared to the LO. Furthermore, the dependence on the separation scale k_S is reduced. This is an important consistency check, because the dependence on k_S vanishes in principle in the exact result. Thus, any residual dependence on k_S can be taken as an estimate of the perturbative uncertainty, and it is reassuring that this uncertainty is reduced when going from LO to NLO.

We conclude that the systematic IR resummation gives a very accurate description of the correlation function at BAO scales. The residual discrepancies at shorter distances visible in Fig. 3.6 are expected due to several effects. The variance due to the finite boxsize, and the finite resolution of the N -body data leads to an uncertainty of several percent¹². In addition, the correlation function is sensitive to the UV physics which has been left beyond the scope of our present study.

In Fig. 3.7 we show the ratio of the NLO result to the correlation function obtained in the Zel'dovich approximation¹³. The differences are around 5% in the

¹²Ref. [101] does not give error bars for the simulation data points. An estimate of the statistical variance using the number of available modes in the simulation as well as the finite resolution suggests that the uncertainty is at the few percent level in the range of scales relevant for BAO. This level of accuracy is also consistent with the difference between the correlation function extracted from Horizon Run 2 ($L = 7.2\text{Gpc}/h$, $N = 6000^3$) versus Horizon Run 3 ($L = 10.8\text{Gpc}/h$, $N = 7210^3$) data presented in [101].

¹³Here by the Zel'dovich approximation we mean the leading order of Lagrangian perturbation theory. The 2-point correlation function in ZA was computed with the publicly available code ZelCa [112].

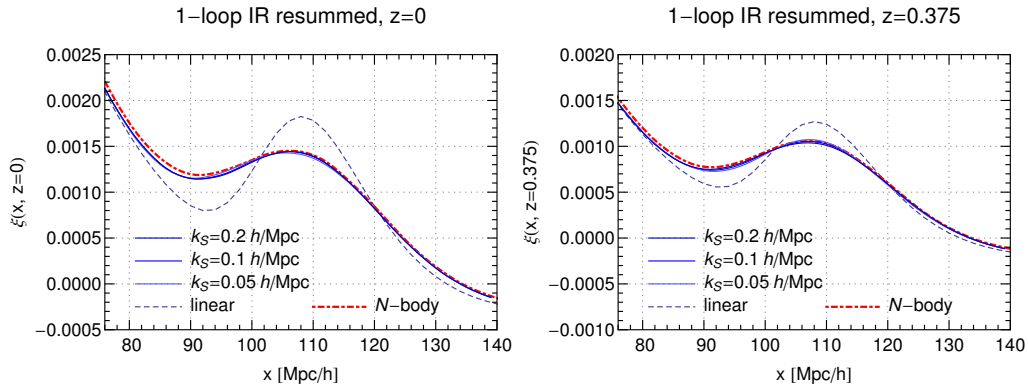


FIGURE 3.6: Same as Fig. 3.5, but showing the infra-red resummed matter correlation function obtained in TSPT at next-to-leading order (blue lines) compared to the Horizon Run 2 N -body data (red line). Note that the three lines for the three values of k_S are almost indistinguishable.

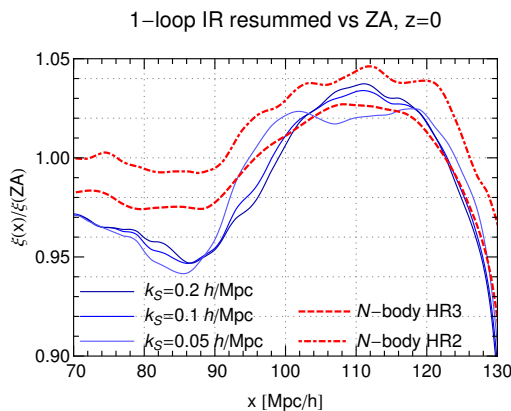


FIGURE 3.7: The correlation function computed in TSPT at NLO normalized to the correlation function in the Zel'dovich approximation (blue curves). We also show the correlation functions of the Horizon Run 2 and 3 [101] divided by the Zel'dovich approximation (red curves).

BAO range, and therefore our results are broadly consistent with ZA, as expected. Nevertheless, the differences are larger than the ultimate precision that is desired to match future surveys. The ratio between the N -body correlation function and the one obtained in ZA is also shown on the same plot by the red line. The TSPT result agrees with the N -body data somewhat better than ZA in the BAO peak region, though the error range of the N -body data does not allow at the moment to clearly discriminate between the two. As discussed before, the TSPT framework can be systematically extended to NNLO, and further corrections from UV modes can be incorporated, which is left for future work.

Finally, we have compared the results for the correlation function computed using the full NLO formula (3.73) and its reduced version without the last term containing the operators \mathcal{S}^a , \mathcal{S}^b . The relative difference $\Delta\xi/\xi$ at $z=0$ does not

exceed 0.5%. Given the strong dependence of the omitted term on the growth factor and hence its quick decrease with redshift, one concludes that this term is negligible for all practical purposes.

3.6.4 Shift of the BAO peak

A valuable piece of information provided by the BAO peak is its position as a function of redshift that can be used as a standard ruler to infer cosmological parameters and probe possible alternatives to Λ CDM (see [113] for a recent discussion in the context of modified gravity). The upcoming surveys aim at measuring this quantity with sub-percent accuracy [114]. Therefore, it is important to assess how non-linear dynamics offsets the BAO peak as compared to the linear prediction.

For concreteness we focus on the position of the maximum of the BAO peak which we denote by x_{BAO} . There are two effects that contribute to its shift with respect to the linear result x_{BAO}^{lin} . First, the damping of the wiggly component in the power spectrum, which occurs already at leading order of the IR resummation, shifts the maximum because the correlation function $\xi(x)$ is not symmetric. Second, at NLO the interactions of the modes in the BAO region with soft modes shift the phase of the BAO. This, in turn, translates into an additional shift of the peak in position space. Let us discuss these two contributions one by one.

It is convenient to decompose the correlation function into a smooth component and a component that describes the BAO peak,

$$\xi(x) = \xi_{nw}(x) + \xi_w(x), \quad (3.87)$$

that are inherited from the decomposition of the power spectrum into smooth and wiggly parts. In the region of the peak these two contributions are of the same order with ξ_w being a factor of a few larger than ξ_{nw} . At the linear level, the condition for the maximum of the peak reads,

$$0 = \int dk k^2 P_w(k) \cos(kx_{BAO}^{lin}) - \frac{1}{x_{BAO}^{lin}} \int dk k P_w(k) \sin(kx_{BAO}^{lin}) + \frac{x_{BAO}^{lin}}{4\pi} \xi'_{nw}(x_{BAO}^{lin}). \quad (3.88)$$

To obtain analytic estimates we represent the wiggly power spectrum as a product of the oscillating part and a smooth envelope (cf. Eq. (3.6)),

$$P_w(k) = f_{env}(k) \sin(k/k_{osc}). \quad (3.89)$$

This implies that the position of the peak is close to $x_{BAO}^{lin} \approx k_{osc}^{-1}$. In what follows we seek the corrections to this relation. Writing

$$x_{BAO}^{lin} = k_{osc}^{-1} + \delta x^{lin}$$

and treating the product $k \delta x^{lin}$ as small we obtain from (3.88)

$$\delta x^{lin} = -k_{osc} \frac{\int dk k f_{env}(k) - (2\pi k_{osc}^2)^{-1} \xi'_{nw}(k_{osc}^{-1})}{\int dk k^3 f_{env}(k)}, \quad (3.90)$$

where we have neglected the integrals of rapidly oscillating functions. In particular, we have used the relation

$$\int dk k f_{env} \sin^2(k/k_{osc}) = \int dk k f_{env} \frac{1 - \cos(k/k_{osc})}{2} \approx \frac{1}{2} \int dk k f_{env}(k).$$

If instead of the linear power spectrum, we consider the LO expression (3.72) with damped wiggly component, we obtain the position of the corresponding peak as

$$x_{BAO}^{LO} = k_{osc}^{-1} + \delta x^{LO},$$

where δx^{LO} is given by the expression (3.90), but with f_{env} replaced by $f_{env}(k)e^{-k^2 D(z)^2 \Sigma^2}$. One concludes that the shift of the LO peak relative to the linear one is

$$\begin{aligned} \frac{\Delta x^{LO}}{x_{BAO}} \equiv \frac{\delta x^{LO} - \delta x^{lin}}{x_{BAO}} = & k_{osc}^2 \left[\frac{\int dk k f_{env}(k)}{\int dk k^3 f_{env}(k)} - \frac{\int dk k f_{env}(k) e^{-k^2 D(z)^2 \Sigma^2}}{\int dk k^3 f_{env}(k) e^{-k^2 D(z)^2 \Sigma^2}} \right] \\ & - \frac{\xi'_{nw}(k_{osc}^{-1})}{2\pi} \left[\frac{1}{\int dk k^3 f_{env}(k)} - \frac{1}{\int dk k^3 f_{env}(k) e^{-k^2 D(z)^2 \Sigma^2}} \right]. \end{aligned} \quad (3.91)$$

The two contributions in this formula are of the same order $(k_{osc}/k)^2$, where $k \sim 0.1h/\text{Mpc}$ is the characteristic range of wavenumbers corresponding to BAO. At $z = 0$ we have

$$\frac{\Delta x^{LO}}{x_{BAO}} \sim -1\%. \quad (3.92)$$

We see that this LO shift is quite significant. It is worth emphasizing that it is exclusively due to the damping of BAO by large IR effects. The damping is the same in ED and ZA. Therefore Δx^{LO} is expected to be removed by the BAO reconstruction procedure which essentially uses the ZA to evolve the density field backward in time. To understand if this procedure can leave any residual shift we have to go to the next-to-leading order.

Writing the correlation function as $\xi = \xi^{LO} + \xi^{NLO}$ one easily derives the additional shift of the peak induced by the second term,

$$\frac{\Delta x^{NLO}}{x_{BAO}} = - \left. \frac{(\xi^{NLO})'}{x(\xi^{LO})''} \right|_{x=x_{BAO}}. \quad (3.93)$$

One can check that the contribution of the smooth correlation function into this expression is negligible, so that one can safely replace in it $\xi \mapsto \xi_w$.

We evaluate the LO and NLO contributions into the correlation function numerically using Eqs. (3.72), (3.73) for the power spectrum. The shift of the peak is then computed either directly by comparing the full correlation function to that at LO, or using (3.93). The results of this evaluation are presented in Table 3.1 (second and third columns). We consider three choices of the separation scale k_S bounding the IR region. Modulo some scatter introduced by the k_S dependence,

$k_S, h/\text{Mpc}$	$\Delta x^{NLO}/x_{BAO}$		
	Full	Eq. (3.93)	Eq. (3.98)
0.05	-0.38%	-0.43%	-0.46%
0.1	-0.41%	-0.45%	-0.40%
0.2	-0.45%	-0.50%	-0.32%

TABLE 3.1: Shift of the BAO peak at redshift $z = 0$ for three values of the separation scale k_S . First column: full NLO result. Second column: evaluation using Eq. (3.93). Third column: analytic estimate Eq. (3.99).

our estimate for the NLO shift is around 0.4%. This lies in the ballpark of the estimates obtained using different approaches [27, 107, 110, 115, 116] and agrees well with the value of the so-called ‘physical’ shift [27, 115] measured in the simulations [48, 116, 117]. While we expect that the NLO shift considered here agrees essentially with the ‘physical’ shift, the precise relation is not completely clear to us and we leave the task of understanding it for future work.

It is instructive to derive an analytic estimate for Δx^{NLO} . It is shown in Appendix D that the NLO wiggly power spectrum has the form,

$$P_w^{IR\ res,NLO}(z, k) = D(z)^4 e^{-k^2 D(z)^2 \Sigma^2} \left(H(k) P_w(k) + S(z, k) \frac{dP_w(k)}{dk} \right). \quad (3.94)$$

The first term in brackets receives contributions both from hard and soft modes, whereas the second term is exclusively due to soft modes with wavenumbers $q \lesssim k_{osc}$. It describes a phase shift of the wiggly component of the power spectrum. The precise form of the function $H(k)$ is not relevant to us; it is only

important that it depends smoothly on its argument. For $S(z, k)$ we find,

$$S(z, k) = s k + (\Sigma_{Silk}^2 + \varkappa D(z)^2 \Sigma_b^2) k^3, \quad (3.95)$$

where Σ_b^2 is defined in (3.74b). The other two coefficients are related to the density variance at the scale k_{osc} ,

$$s \sim \sigma^2(k_{osc}) \equiv \int_0^{k_{osc}} \frac{dq}{(2\pi)^3} q^2 P_s(q), \quad \Sigma_{Silk}^2 \sim \sigma^2(k_{osc})/k_{Silk}^2, \quad (3.96)$$

where in the last formula $k_{Silk} \sim 0.2 h/\text{Mpc}$ is the Silk damping scale. The detailed expressions are given in Appendix D. It is worth to point out that the formula for s is different in ED and ZA, as well as for the density and velocity divergence power spectra. Notice also the presence of the coefficient \varkappa in (3.95) that discriminates between ZA ($\varkappa = 0$) and ED ($\varkappa = 1$).

Next, we substitute (3.94) into (3.93) which yields,

$$\frac{\Delta x^{NLO}}{x_{BAO}} = k_{osc} D(z)^2 \frac{\int dk k^2 \cos(k/k_{osc}) [H(k) P_w(k) + S(z, k) \frac{dP_w}{dk}] e^{-k^2 D(z)^2 \Sigma^2}}{\int dk k^3 \sin(k/k_{osc}) P_w(k) e^{-k^2 D(z)^2 \Sigma^2}}. \quad (3.97)$$

Recalling the form (3.89) of P_w one observes that the integral involving the first term in the numerator contains a rapidly oscillating function and thus gives a negligible contribution. In the second term we integrate by parts. Neglecting again integrals of rapidly oscillating functions and using (3.95) we arrive at

$$\frac{\Delta x^{NLO}}{x_{BAO}} = D(z)^2 s + D(z)^2 (\Sigma_{Silk}^2 + \varkappa D(z)^2 \Sigma_b^2) \frac{\int dk k^5 P_w e^{-k^2 D(z)^2 \Sigma^2} \sin(k/k_{osc})}{\int dk k^3 P_w e^{-k^2 D(z)^2 \Sigma^2} \sin(k/k_{osc})}. \quad (3.98)$$

For realistic power spectra the ratio of integrals in the second term is of order $0.02 [h/\text{Mpc}]^2$ at $z = 0$. It is worth noting that numerically the second term gives a subdominant contribution, so approximately one can write,

$$\frac{\Delta x^{NLO}}{x_{BAO}} \approx D(z)^2 s. \quad (3.99)$$

Still, we prefer to use the complete expression (3.98). Evaluating various contributions entering into it using the expressions from Appendix D and Eq. (3.74b) we obtain the estimates for the shift listed in the fourth column of Table 3.1. They are in reasonable agreement with the values obtained by the direct numerical evaluation of the correlation function.

As already mentioned before, the values of s and \varkappa are different in ED and ZA. Consequently, the BAO shift computed in ZA is somewhat lower than in ED:

$$(\Delta x^{NLO}/x_{BAO})^{ZA} \simeq -(0.28 \div 0.22)\% ,$$

depending on the choice of k_S . Thus, while the ZA gives a rather accurate description of the BAO broadening, it underestimates the BAO shift. The difference is expected since the terms responsible for the BAO shift originate from the non-dipole parts of the interaction vertices, which are different in ZA and in ED. One concludes that, in principle, the BAO reconstruction based on ZA is expected to leave a small residual shift of order 0.1%. However, this discrepancy is likely to be too small to have any significant effect on the determination of the BAO peak position.

Let us make a cautious remark. Although the above analysis provides a qualitative understanding of the origin of the BAO shift, as well as a trustable estimate of its order of magnitude, the concrete numbers listed in Table 3.1 should be taken with a grain of salt. They are smaller than the typical percent accuracy of our calculations, which calls for a re-assessment of various approximations made in their derivation. Also a realistic calculation of the BAO shift must include the effect of the bias [107, 110, 118], which makes a $O(1)$ correction to the leading result and hence is more important than the two-loop contributions that we kept in (3.98). We leave the study of these issues for future work.

Before closing this section, let us mention that the term proportional to k^3 in (3.95) generates also a *distortion* of the BAO peak that tends to make it more asymmetric. However, in Λ CDM this effect is subdominant compared to the initial asymmetry of the peak present already at the linear level and amplified by various other terms in the NLO power spectrum. Still, the different contributions are not completely degenerate and it would be interesting to understand the impact of non-linear distortion on an accurate description of the BAO data.

3.7 Conclusions and outlook

In this work we have developed a systematic approach to describe the non-linear evolution of the feature imprinted in the matter correlation functions by baryon acoustic oscillations. We have provided a theoretical framework to efficiently resum corrections arising from non-linear interactions with long-wavelength modes that are particularly enhanced for the baryon acoustic feature.

Our approach is based on the framework of TSPT, that provides a perturbative description of structure formation manifestly free from spurious infrared divergences. Besides, it is based on an Eulerian description and therefore its practical implementation does not suffer from the complications arising in Lagrangian perturbation theory. These features make TSPT a convenient framework to discuss the effect of bulk flows on the BAO feature. We have first developed a formalism to isolate IR enhanced effects by splitting the TSPT propagators and vertices into smooth and oscillating (wiggly) contributions. Next, we identified the IR enhanced loop contributions, taking modes below an (a priori arbitrary) separation scale k_S into account. These have a simple diagrammatic representation, with the dominant diagrams corresponding to daisy graphs. Finally, we have shown that within TSPT one can develop a modified perturbative expansion in which the large IR effects are resummed to all orders, and we computed next-to-leading corrections including loops with hard wavenumbers as well as subleading contributions of the soft loops. Our leading IR resummed result agrees with that obtained in [29] using the symmetry arguments. TSPT provides a useful framework to systematically extend this result to higher n -point functions and compute relevant corrections in a controlled way.

Our analysis provides a simple prescription for practical evaluation of the resummed correlation functions. At the leading order, it amounts to replacing the linear power spectrum in all calculations by the spectrum with damped wiggly component. This essentially remains true upon inclusion of hard loops, whereas the subleading soft loops introduce new terms. Our result for the IR resummed power spectrum with inclusion of all next-to-leading corrections is given in (3.73). It describes the non-linear evolution of the BAO peak with sub-percent accuracy, when compared to large-scale N -body simulations. Although we found that the soft NLO corrections are rather small, they are important to capture the shift in the position of the peak maximum.

The residual dependence of our results on the artificial separation scale k_S provides an estimate of the theoretical error, similar to analogous scale-dependencies in quantum field theory computations. At LO our result for the two-point correlation function close to the BAO peak exhibits a dependence on this scale at the level of several percent, when varying k_S in the plausible range $(0.05 \div 0.2)h/\text{Mpc}$. As expected, the scale-dependence is reduced in the NLO result and is well below the percent level close to the BAO peak. The theoretical error estimated in this way is consistent with the agreement with N -body data, except for short scales sensitive to the UV effects that were not considered in this Chapter.

Our results suggest several directions for future research. First, one can use the systematic TSPT approach to investigate the effects on the BAO peak in cosmological models beyond Λ CDM. As examples we mention inclusion of neutrino masses or modifications of gravity. In particular, the NLO corrections affecting the BAO shift are sensitive to non-dipole corrections to the non-linear evolution that are not protected by the equivalence principle, and therefore can be particularly sensitive to modifications of the dynamics. Second, it will be very interesting to study in detail the BAO feature in the three-point function. Finally, the TSPT framework can also be used to address the contributions of UV modes that influence correlation functions at shorter distances.

Chapter 4

IR resummation in redshift space

4.1 Review of standard redshift space mapping

Peculiar velocities alter the apparent picture of clustering along the line-of-sight and lead to the so-called redshift-space distortions (RSD) [119–122]. RSD break the full rotation symmetry of cosmological correlation functions down to a little group of azimuthal rotations along the line-of-sight. Qualitatively, one can distinguish two main effects. At large scales, galaxies in redshift space appear to be closer along-the-line of sight due to mutually directed infall velocities, which is observed as an enhancement of the amplitude of fluctuations in this direction. At small scales, the velocity dispersion in virialized halos elongate structures along the line-of-sight, which is known as the “fingers of God” effect [119, 120, 123]. This elongation washes out observed structures and results in a suppression of apparent short-scale power in the line-of-sight direction.

In what follows we will work in the plane-parallel (flat sky) approximation valid for separations between points in redshift space much smaller than the distances from these points to the observer. This approximation is justified for mildly non-linear scales $\sim 100 \text{ Mpc}/h$ typical for perturbation theory considerations.

In the plane-parallel regime the relation between the real space coordinate \mathbf{x} and the redshift space coordinate \mathbf{s} is inferred using Hubble’s law,

$$\mathbf{s} = \mathbf{x} + \hat{\mathbf{z}} \frac{v_z^{(r)}(\tau, \mathbf{x})}{\mathcal{H}}, \quad (4.1)$$

where \mathcal{H} is the conformal Hubble parameter, $\hat{\mathbf{z}}$ is the unit vector along the line-of-sight, $v_z^{(r)}(\tau, \mathbf{x})$ is the projection of the peculiar velocity field on the line-of-sight and τ is conformal time. Following the standard convention, we will denote real space quantities by the superscript (r) , whereas their redshift space counterparts will be denoted by (s) .

The redshift space matter density in the Eulerian picture is obtained via

$$(1 + \delta^{(s)}(\tau, \mathbf{s}))d^3s = (1 + \delta^{(r)}(\tau, \mathbf{x}))d^3x, \quad (4.2)$$

which is dictated by the conservation of mass. In Fourier space the above equation can be rewritten as

$$\delta^{(s)}(\tau, \mathbf{k}) = \delta^{(r)}(\tau, \mathbf{k}) + \int d^3x e^{-i\mathbf{k}\cdot\mathbf{x}} \left(e^{-ik_z v_z^{(r)}(\tau, \mathbf{x})/\mathcal{H}} - 1 \right) (1 + \delta^{(r)}(\tau, \mathbf{x})). \quad (4.3)$$

In the Eulerian standard perturbation theory (SPT) [15] the velocity field is fully characterized by its suitably normalized divergence $\Theta^{(r)}$,

$$v_i^{(r)} = -f\mathcal{H} \frac{\partial_i \Theta^{(r)}}{\Delta}, \quad (4.4)$$

where we introduced the logarithmic growth rate f defined as

$$f(\tau) = \frac{d \ln D}{d \ln a}, \quad (4.5)$$

$D(\tau)$ is the linear theory growth factor and $a(\tau)$ is the scale factor. In what follows we will also use the rescaled time variable $\eta \equiv \ln D$.

Working within SPT, one Taylor expands the exponent containing the velocity field in Eq. (4.3). Next, one uses the SPT expansion for the real space density

$$\delta^{(r)}(\eta, \mathbf{k}) = \sum_{n=1}^{\infty} D(\eta)^n \int_{\mathbf{q}_1, \dots, \mathbf{q}_n} (2\pi)^3 \delta_D^{(3)}(\mathbf{k} - \mathbf{q}_{1\dots n}) F_n(\mathbf{q}_1, \dots, \mathbf{q}_n) \delta_0(\mathbf{q}_1) \dots \delta_0(\mathbf{q}_n), \quad (4.6)$$

and an analogous expansion for the velocity divergence $\Theta^{(r)}$ with the G_n kernels, instead of F_n . This allows one to obtain the formal expression

$$\delta^{(s)}(\eta, \mathbf{k}) = \sum_{n=1}^{\infty} D(\eta)^n \int_{\mathbf{q}_1, \dots, \mathbf{q}_n} (2\pi)^3 \delta_D^{(3)}(\mathbf{k} - \mathbf{q}_{1\dots n}) Z_n(\mathbf{q}_1, \dots, \mathbf{q}_n) \delta_0(\mathbf{q}_1) \dots \delta_0(\mathbf{q}_n), \quad (4.7)$$

where Z_n kernels now contain RSD contributions. Expressions for a first few of them are given in Appendix E. Various correlators of the redshift density field are

computed using the statistical distribution of the initial density field δ_0 , which is typically assumed to be Gaussian.

In a matter dominated universe, the linear growth factor coincides with the scale factor, $D(\tau) = a(\tau)$, so that $f(\tau) = 1$ and the kernels F_n in (4.6) are time-independent. This is no longer true in the presence of cosmological constant or dark energy. Still, it is known that the use of (4.6) with the time-independent kernels F_n together with the correct growth factor $D(\tau)$ provides an accurate approximation to the exact SPT expression for the density in the real space [124]. This is known as the Einstein–de Sitter (EdS) approximation. Following the common practice, we will adopt it in this dissertation; corrections to it can, in principle, be taken into account perturbatively. Notice that we do not assume any simplifications in the redshift space mapping (4.3), so that the redshift space kernels Z_n explicitly contain the factors $f(\tau)$ with the full time dependence.

A notorious drawback of SPT is spurious IR sensitivity that arises due to homogeneous translations of small-scale density fluctuations by soft modes. Technically, the sensitivity of the density field to large-scale translations is encoded in the poles of the kernels F_n, G_n at low momenta. The presence of these poles translates into an IR divergence of SPT loop diagrams composed out of F_n or G_n kernels.

The situation becomes worse in redshift space. The exponent of the velocity field in Eq. (4.3) produces new poles compared to those already present in real space, which brings in new spurious IR enhanced terms and further complicates the calculations. The way to avoid these difficulties is to work directly in terms of equal-time correlation functions which are protected from IR divergences by the equivalence principle. This is precisely the core idea of TSPT. In order to realize this program and explicitly retain IR-safety in redshift space one has to perform a mapping from real to redshift space at the level of equal-time correlation functions. We introduce such a mapping in the next section.

4.2 Redshift space transformation as a 1D fluid flow

In this section we present a new mapping procedure that allows us to obtain redshift space correlators directly from real space ones. The core observation is that Eq. (4.1) can be equivalently rewritten in the form

$$\mathbf{s} = \mathbf{x} + \hat{\mathbf{z}} v_z^{(r)}(\mathbf{x}) \mathcal{T}, \quad (4.8)$$

where $\mathcal{T} \equiv 1/\mathcal{H}$. Now assume that the parameter \mathcal{T} ranges from 0 to $1/\mathcal{H}$. Then Eq. (4.8) turns into an equation describing a flow of particles with Lagrangian coordinates \mathbf{x} along the z -axis with initial velocity $v_z^{(r)}(\mathbf{x})$. The parameter \mathcal{T} plays a role of time in the fictitious dynamics described by Eq. (4.8). This fictitious dynamics can be described in the Eulerian picture upon introducing the density $\delta^{(s)}$ and velocity $\mathbf{v}^{(s)}$ of this flow. If we set the initial conditions

$$\begin{aligned} \mathbf{v}^{(s)} \Big|_{\mathcal{T}=0} &= \mathbf{v}^{(r)}(\eta, \mathbf{x}), \\ \delta^{(s)} \Big|_{\mathcal{T}=0} &= \delta^{(r)}(\eta, \mathbf{x}), \end{aligned} \quad (4.9)$$

then the value of $\delta^{(s)}$ at $\mathcal{T} = 1/\mathcal{H}$ will give us the redshift space density, while $\mathbf{v}^{(s)}(\mathcal{T} = 1/\mathcal{H}, \mathbf{s})$ will have the meaning of the fluid velocity at a given position in redshift space. Note that only orthogonal to the line-of-sight components of this velocity can, in principle, be observed, so the physical relevance of this quantity is not clear. However, it appears convenient to use this variable in intermediate steps when computing the density correlators.

There are no external forces in our fictitious evolution, thus the velocity is conserved along the flow:

$$\frac{Dv^{(s),i}}{D\mathcal{T}} = \partial_{\mathcal{T}}v^{(s),i} + v_z^{(s)}\partial_z v^{(s),i} = 0. \quad (4.10)$$

This equation conserves vorticity. In real-space Eulerian perturbation theory the velocity field is longitudinal. Then the initial conditions (4.9) imply that $v^{(s)}$ is longitudinal as well, i.e.

$$v_i^{(s)} = -f\mathcal{H} \frac{\partial_i \Theta^{(s)}}{\Delta}. \quad (4.11)$$

It is convenient to rescale our auxiliary time as

$$\mathcal{T} \rightarrow \mathcal{F} = f\mathcal{T}\mathcal{H} \quad \text{with} \quad \mathcal{F} \in [0, f]. \quad (4.12)$$

In this case the equation of motion for the velocity divergence obtained from (4.10) takes a very simple form independent of cosmology,

$$\partial_{\mathcal{F}}\Theta^{(s)}(\mathcal{F}, \mathbf{s}; \mathbf{e}) = \partial_i \left(\frac{\partial_i \partial_z \Theta^{(s)}}{\Delta} \frac{\partial_z \Theta^{(s)}}{\Delta} \right), \quad (4.13)$$

where we have emphasized that in this equation $\Theta^{(s)}$ depends parametrically on the cosmic time \mathbf{e} .

Since Eq. (4.8) describes a simple Lagrangian flow of particles, its density current

$$\mathbf{j}^{(s)} = (1 + \delta^{(s)})\mathbf{v}^{(s)}$$

is conserved, which implies the continuity equation:

$$\partial_{\mathcal{T}}\delta^{(s)} + \partial_z[v_z^{(s)}(1 + \delta^{(s)})] = 0. \quad (4.14)$$

Collecting together Eqs. (4.13) and (4.14) and switching to Fourier space we obtain the final system

$$\begin{aligned} \partial_{\mathcal{F}}\delta_{\mathbf{k}}^{(s)} - \frac{k_z^2}{k^2}\Theta_{\mathbf{k}}^{(s)} &= \int_{\mathbf{q}_1, \mathbf{q}_2} \delta^{(3)}(\mathbf{k} - \mathbf{q}_{12})\alpha^{(s)}(\mathbf{q}_1, \mathbf{q}_2)\Theta_{\mathbf{q}_1}^{(s)}\delta_{\mathbf{q}_2}^{(s)}, \\ \partial_{\mathcal{F}}\Theta_{\mathbf{k}}^{(s)} &= \int_{\mathbf{q}_1, \mathbf{q}_2} \delta^{(3)}(\mathbf{k} - \mathbf{q}_{12})\beta^{(s)}(\mathbf{q}_1, \mathbf{q}_2)\Theta_{\mathbf{q}_1}^{(s)}\Theta_{\mathbf{q}_2}^{(s)}, \end{aligned} \quad (4.15)$$

where

$$\alpha^{(s)}(\mathbf{q}_1, \mathbf{q}_2) \equiv \frac{q_{1,z}(q_{1,z} + q_{2,z})}{q_1^2}, \quad \beta^{(s)}(\mathbf{q}_1, \mathbf{q}_2) \equiv \frac{(\mathbf{q}_1 + \mathbf{q}_2)^2 q_{1z} q_{2z}}{2q_1^2 q_2^2}. \quad (4.16)$$

Note that the system of equations (4.15) contains a closed equation for the velocity divergence field and in this respect is quite similar to the Zel'dovich approximation in the Eulerian picture.

4.3 TSPT partition function and vertices

Our next step is to build a generating functional which produces the correlation functions of the $\Theta^{(s)}$ field¹. This can be done by applying the ideas of TSPT to the system (4.15). A detailed description of the TSPT framework is given in Ref. [1] for a generic system, here we only outline the main steps. Some details on the TSPT in real space are given in 2.

The PDF of the velocity divergence field undergoes certain evolution in the auxiliary time \mathcal{F} . The initial distribution is given by the PDF in real space and the final one corresponds to the PDF in redshift space that we are looking for. In order to describe this evolution, consider the TSPT generating functional at a finite slice of the redshift time \mathcal{F} :

$$Z[J; \mathcal{F}] = \int \mathcal{D}\Theta^{(s)} \mathcal{P}[\Theta^{(s)}; \mathcal{F}] \exp \left\{ \int_{\mathbf{k}} \Theta_{\mathbf{k}}^{(s)} J(-\mathbf{k}) \right\}, \quad (4.17)$$

¹We will discuss the density field $\delta^{(s)}$ in the next subsection.

where the PDF \mathcal{P} is perturbatively expanded as

$$\mathcal{P}[\Theta^{(s)}; \mathcal{F}] = \exp \left\{ - \sum_{n=1}^{\infty} \frac{1}{n!} \int_{\mathbf{q}_1, \dots, \mathbf{q}_n} \Gamma_n^{(s) \text{ tot}}(\mathcal{F}; \mathbf{k}_1, \dots, \mathbf{k}_n) \prod_{j=1}^n \Theta_{\mathbf{q}_j}^{(s)} \right\} \quad (4.18)$$

Conservation of probability under the change of redshift time implies

$$\mathcal{D}[\Theta^{(s)} + \delta\Theta^{(s)}] \mathcal{P}[\Theta^{(s)} + \delta\Theta^{(s)}; \mathcal{F} + \delta\mathcal{F}] = \mathcal{D}[\Theta^{(s)}] \mathcal{P}[\Theta^{(s)}; \mathcal{F}]. \quad (4.19)$$

This leads to the following evolution equations for the TSPT vertices $\Gamma_n^{(s)}$:

$$\begin{aligned} & \partial_{\mathcal{F}} \Gamma_n^{(s) \text{ tot}}(\mathcal{F}; \mathbf{k}_1, \dots, \mathbf{k}_n) \\ & + \sum_{m=1}^n \frac{1}{(n-m)!m!} \sum_{\sigma} I_m^{(s)}(\mathbf{k}_{\sigma(1)}, \dots, \mathbf{k}_{\sigma(m)}) \Gamma_{n-m+1}^{(s) \text{ tot}} \left(\mathcal{F}; \sum_{l=1}^m \mathbf{k}_{\sigma(l)}, \mathbf{k}_{\sigma(m+1)}, \dots, \mathbf{k}_{\sigma(n)} \right) \\ & = (2\pi)^3 \delta_{\text{D}}^{(3)} \left(\sum_{i=1}^n \mathbf{k}_i \right) \int_{\mathbf{p}} I_{n+1}^{(s)}(\mathcal{F}; \mathbf{p}, \mathbf{k}_1, \dots, \mathbf{k}_n), \end{aligned} \quad (4.20)$$

where in the second line the sum runs over all permutations σ of n indices and $I_m^{(s)}$ are the kernels determining the dynamical evolution of field $\Theta^{(s)}$:

$$\partial_{\mathcal{F}} \Theta_{\mathbf{k}}^{(s)} = \sum_{n=1}^{\infty} \frac{1}{n!} \int_{\mathbf{q}_1, \dots, \mathbf{q}_n} (2\pi)^3 \delta_{\text{D}}^{(3)}(\mathbf{k} - \mathbf{q}_1 \dots \mathbf{q}_n) I_n^{(s)}(\mathbf{q}_1, \dots, \mathbf{q}_n) \Theta_{\mathbf{q}_1}^{(s)} \dots \Theta_{\mathbf{q}_n}^{(s)}. \quad (4.21)$$

In the case of the system (4.15) we simply have $I_2^{(s)} = 2\beta_z$ with all other kernels vanishing. In particular, $I_1^{(s)} = 0$, in contrast to $I_1^{(r)} = 1$ in real space, which makes the structure of solution to (4.20) somewhat different from the case of real-space TSPT [1] (see also Chapter 2).

It is convenient to split the solution of Eq. (4.20) into the solution of the homogeneous equation $\Gamma_n^{(s)}$ and ‘counterterms’ $C_n^{(s)}$ sourced by the singular r.h.s. The corresponding initial conditions are

$$\Gamma_n^{(s)} \Big|_{\mathcal{F}=0} = \Gamma_n^{(r)}, \quad C_n^{(s)} \Big|_{\mathcal{F}=0} = C_n^{(r)}, \quad (4.22)$$

where $\Gamma_n^{(r)}$ and $C_n^{(r)}$ are TSPT vertices in real space. Their structure is discussed in Chapter 2. In particular, for Gaussian initial conditions and in Einstein-de Sitter approximation (which we adopt in this Chapter), the counterterms $C_n^{(r)}$ are time independent, whereas the time dependence of $\Gamma_n^{(r)}$ factorizes (here we

are talking about the dependence on the physical time e),

$$\Gamma_n^{(r)} = \frac{\bar{\Gamma}_n^{(r)}}{g^2(\eta)}. \quad (4.23)$$

In this expression $g(\eta)$ is the linear growth factor as defined in Eq. (2.3).

The equations for the $\Gamma_n^{(s)}$ vertices take the following form:

$$\partial_{\mathcal{F}} \Gamma_n^{(s)}(\mathcal{F}; \mathbf{k}_1, \dots, \mathbf{k}_n) + \sum_{i < j}^n I_2^{(s)}(\mathbf{k}_i, \mathbf{k}_j) \Gamma_{n-1}^{(s)}(\mathcal{F}; \mathbf{k}_1, \dots, \check{\mathbf{k}}_i, \dots, \check{\mathbf{k}}_j, \dots, \mathbf{k}_i + \mathbf{k}_j) = 0, \quad (4.24)$$

where $\check{\mathbf{k}}_j$ means that \mathbf{k}_j is *not* included in the arguments of $\Gamma_{n-1}^{(s)}$. Let us start with the first non-trivial vertex Γ_2 . We have:

$$\partial_{\mathcal{F}} \Gamma_2^{(s)} = 0, \quad \Rightarrow \quad \Gamma_2^{(s)} = \Gamma_2^{(r)} = (2\pi)^3 \frac{\delta_D^{(3)}(\mathbf{k}' + \mathbf{k})}{g^2 \bar{P}(k)}, \quad (4.25)$$

where $\bar{P}(k)$ is the linear power spectrum at $e = 0$ and we have used Eq. (2.17a) in the last equality. Note that the inverse of $\Gamma_2^{(s)}$ gives the linear power spectrum of $\Theta^{(s)}$. From (4.25) we conclude that the latter coincides with the linear power spectrum of matter overdensities $g^2(\eta) \bar{P}(k)$. For $n \geq 3$ we consider the Ansatz,

$$\Gamma_n^{(s)} = \sum_{l=0}^{n-2} \Gamma_{n,l}^{(s)} \mathcal{F}^l. \quad (4.26)$$

Plugging it into Eq. (4.24) leads to the following recursion relation

$$\Gamma_{n,l}^{(s)} = -\frac{1}{l} \sum_{i < j}^n I_2^{(s)}(\mathbf{k}_i, \mathbf{k}_j) \Gamma_{n-1,l-1}^{(s)}(\mathbf{k}_1, \dots, \check{\mathbf{k}}_i, \dots, \check{\mathbf{k}}_j, \dots, \mathbf{k}_i + \mathbf{k}_j), \quad (4.27)$$

with the initial condition for $l = 0$,

$$\Gamma_{n,0}^{(s)} = \Gamma_n^{(r)}. \quad (4.28)$$

The recursion relation (4.27) allows us to obtain all redshift space velocity vertices from the real space ones (given in Chapter 2). Since the redshift space vertices are sourced by the real space ones through the linear recursion relation Eq. (4.27), in the case of Gaussian initial conditions they inherit factorized dependence on the coupling constant $g(\eta)$ given by (4.23). Another important property of the RSD vertices is that they are IR safe. The proof essentially repeats the proof of IR safety of the standard TSPT vertices given in Ref. [1] and we do not present it here.

The singular counterterms $C_n^{(s)}$ satisfy the following equations,

$$\begin{aligned} \partial_{\mathcal{F}} C_1^{(s)}(\mathcal{F}; \mathbf{k}) &= (2\pi)^3 \delta^{(3)}(\mathbf{k}) \int_{\mathbf{p}} I_2^{(s)}(\mathbf{p}, \mathbf{k}), \\ \partial_{\mathcal{F}} C_n^{(s)}(\mathcal{F}; \mathbf{k}_1, \dots, \mathbf{k}_n) + \sum_{i < j} I_2^{(s)}(\mathbf{k}_i, \mathbf{k}_j) C_{n-1}^{(s)}(\mathcal{F}; \mathbf{k}_1, \dots, \check{\mathbf{k}}_i, \dots, \check{\mathbf{k}}_j, \dots, \mathbf{k}_i + \mathbf{k}_j) &= 0, \quad n > 1. \end{aligned} \quad (4.29)$$

Using the Ansatz $C_n^{(s)} = \sum_{l=0}^n C_{n,l}^{(s)} \mathcal{F}^l$, we find the recursion relations similar to Eq. (4.27),

$$\begin{aligned} C_{1,1}^{(s)} &= (2\pi)^3 \delta^{(3)}(\mathbf{k}) \int_{\mathbf{p}} I_2^{(s)}(\mathbf{p}, \mathbf{k}), \\ C_{n,l}^{(s)} &= -\frac{1}{l} \sum_{i < j} I_2^{(s)}(\mathbf{k}_i, \mathbf{k}_j) C_{n-1, l-1}^{(s)}(\mathbf{k}_1, \dots, \check{\mathbf{k}}_i, \dots, \check{\mathbf{k}}_j, \dots, \mathbf{k}_i + \mathbf{k}_j), \quad n > 1, \end{aligned} \quad (4.30)$$

with $C_{n,0}^{(s)} = C_n^{(r)}$. Note that the C_n counterterms appear already in the perfect fluid description. Their structure is totally fixed by the relevant equations of motion.

4.3.1 Density field as a composite operator

In cosmological perturbation theory with adiabatic initial conditions there is only one statistically independent field which can appear as the integration variable in the generating functional. For studies of the IR structure it appears convenient to choose the velocity field, as we did above. In this subsection we express the redshift density field in terms of $\Theta^{(s)}$ as a composite operator. We focus on the matter density for the time being. Biased tracers will be studied in Sec. 4.5. We introduce the Ansatz,

$$\delta_{\mathbf{k}}^{(s)} = \sum_{n=1}^{\infty} \frac{1}{n!} \int_{\mathbf{q}_1, \dots, \mathbf{q}_n} (2\pi)^3 \delta_{\mathbf{D}}^{(3)}(\mathbf{k} - \mathbf{q}_{1\dots n}) K_n^{(s)}(\mathcal{F}; \mathbf{q}_1, \dots, \mathbf{q}_n) \Theta_{\mathbf{q}_1}^{(s)} \dots \Theta_{\mathbf{q}_n}^{(s)}. \quad (4.31)$$

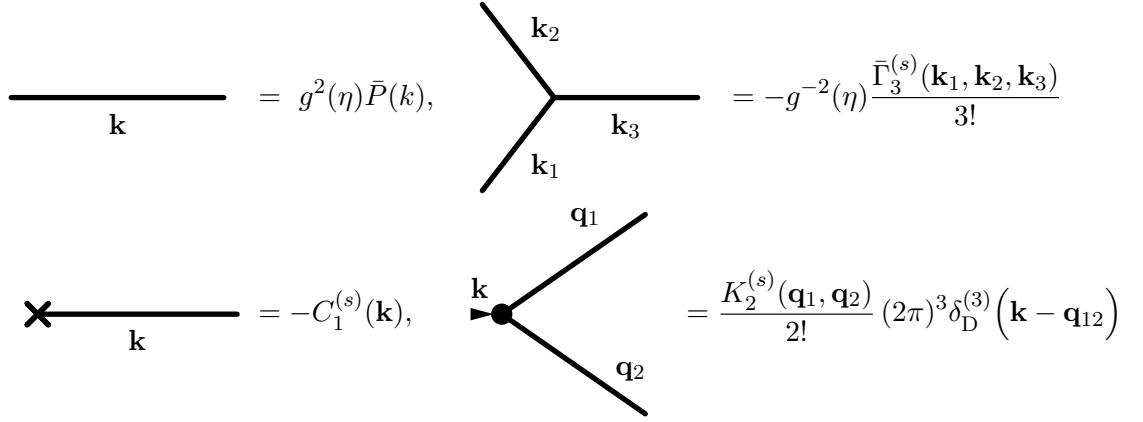


FIGURE 4.1: Examples of TSPT Feynman rules in redshift space.

Plugging (4.31) into the equations of motion (4.15), we obtain

$$\begin{aligned} \partial_{\mathcal{F}} K_1^{(s)}(\mathbf{k}_1) &= \frac{k_z^2}{k^2}, \\ \partial_{\mathcal{F}} K_n^{(s)}(\mathbf{k}_1, \dots, \mathbf{k}_n) &= \sum_{i=1}^n K_{n-1}^{(s)}(\mathbf{k}_1, \dots, \check{\mathbf{k}}_i, \dots, \mathbf{k}_n) \alpha^{(s)} \left(\mathbf{k}_i, \sum_{j \neq i} \mathbf{k}_j \right) \\ &\quad - 2 \sum_{i < j}^n K_{n-1}^{(s)}(\mathbf{k}_1, \dots, \check{\mathbf{k}}_i, \dots, \check{\mathbf{k}}_j, \dots, \mathbf{k}_n, \mathbf{k}_i + \mathbf{k}_j) \beta^{(s)}(\mathbf{k}_i, \mathbf{k}_j), \quad n > 1. \end{aligned} \quad (4.32)$$

The kernels $K_n^{(s)}$ satisfy the following initial conditions:

$$K_n^{(s)} \Big|_{\mathcal{F}=0} = K_n^{(r)}, \quad (4.33)$$

where $K_n^{(r)}$ are TSPT kernels relating the density and velocity field in real space (see Chapter 2). The first two kernels read,

$$\begin{aligned} K_1^{(s)}(\mathbf{k}_1) &= 1 + \frac{k_z^2}{k^2} f, \\ K_2^{(s)}(\mathbf{k}_1, \mathbf{k}_2) &= K_2^{(r)}(\mathbf{k}_1, \mathbf{k}_2) + \left\{ \frac{k_{1z}^2}{k_1^2} + \frac{k_{2z}^2}{k_2^2} - 2 \frac{(\mathbf{k}_1 \cdot \mathbf{k}_2) k_{1z} k_{2z}}{k_1^2 k_2^2} \right\} f, \end{aligned} \quad (4.34)$$

where we have made the substitution $\mathcal{F} \rightarrow f$ in the final expressions. Proceeding along the lines of Ref. [1] one can easily prove that the kernels $K_n^{(s)}$ are IR safe.

4.3.2 Feynman rules

The TSPT perturbative expansion is produced by expanding the PDF \mathcal{P} in the generating functional (4.17) over its Gaussian part, which is equivalent to an expansion in the coupling constant $g(\eta)$. This calculation can be represented as a sum of Feynman diagrams. Our redshift space mapping does not produce new diagrammatic elements, thus we can use the same Feynman rules as in real space, see Ref. [1]. The first elements of the perturbative expansion in redshift space are shown in Fig. 4.1: the linear power spectrum (inverse of $\Gamma_2^{(s)}$) is represented by a line (propagator), the different elements $\Gamma_n^{(s)}$ (with $n > 2$) and $C_n^{(s)}$ correspond to vertices, and $K_n^{(s)}$ are depicted as vertices with an extra arrow. To compute an n -point correlation function of the velocity divergence $\Theta^{(s)}$ one needs to draw all diagrams with n external legs. For the correlators of the density field $\delta^{(s)}$ one has to add diagrams with external arrows (composite operators) and multiply each external line with momentum \mathbf{k} by a factor $K_1^{(s)}(\mathbf{k})$. For instance, at linear order we have the following expression for the correlator of the $\delta^{(s)}$ field,

$$P_{mm}^{(s)}(\eta; k) = \begin{array}{c} \text{---} \text{---} \text{---} \\ \leftarrow \quad \rightarrow \\ K_1^{(s)} \quad K_1^{(s)} \end{array} = (K_1^{(s)}(\mathbf{k}))^2 g^2 \bar{P}(k) = \left(1 + f(\eta) \frac{k_z^2}{k^2}\right)^2 g^2(\eta) \bar{P}(k), \quad (4.35)$$

which reproduces the famous Kaiser formula [121].

4.4 IR resummation

The absence of spurious IR enhancement of loop integrals in TSPT allows one to easily extract the physical IR effects responsible for deforming the BAO pattern in redshift space. In this section we work out the ingredients necessary for systematic IR resummation along the lines of Chapter 3: perform the decomposition of the redshift space vertices into ‘wiggly’ and ‘smooth’ parts, introduce power counting rules, identify the leading IR contributions, and resum them. In this section we will be discussing only the redshift space quantities and omit the superscript (s) on TSPT vertices to simplify notations. In all vertices and kernels we set $\mathcal{F} \rightarrow f$. We also introduce primed notations for quantities stripped of the momentum delta functions, e.g.,

$$\Gamma_n^{(s)}(\mathbf{k}_1, \dots, \mathbf{k}_n) = (2\pi)^3 \delta_D^{(3)}(\mathbf{k}_{1\dots n}) \Gamma_n^{\prime(s)}(\mathbf{k}_1, \dots, \mathbf{k}_n). \quad (4.36)$$

4.4.1 Wiggly-smooth decomposition

As in the previous Chapter, we decompose the linear matter power spectrum into an oscillating (wiggly) component corresponding to BAO and a smooth (non-wiggly) part,

$$\bar{P}(k) = \bar{P}_{nw}(k) + \bar{P}_w(k). \quad (4.37)$$

The period of oscillations of \bar{P}_w is set by $k_{osc} = r_{BAO}^{-1} \sim 9 \cdot 10^{-3} h/\text{Mpc}$. Interaction with long-wavelength modes differently affects these two components leading to exponential damping of the wiggly part in the non-linear power spectrum. In principle, the decomposition (4.37) is not unique; two possible algorithms are described above. In practice, the two algorithms lead to essentially identical results in real space and we expect this to be true also with inclusion of RSD.

Since the TSPT vertices $\bar{\Gamma}_n$ depend on the linear power spectrum, the decomposition (4.37) produces a similar decomposition of vertices,

$$\bar{\Gamma}_n = \bar{\Gamma}_n^{nw} + \bar{\Gamma}_n^w. \quad (4.38)$$

Here $\bar{\Gamma}_n^w$ is of order $O(\bar{P}_w/\bar{P}_{nw})$ and one can neglect terms $O(\bar{P}_w^2/\bar{P}_{nw}^2)$ as they produce sub-percent corrections. The counterterms C_n and kernels K_n are not subject to wiggly-smooth decomposition as they are not functionals of the initial power spectrum. Their momentum dependence is purely smooth. Throughout this Chapter we will use the same graphic representation for the redshift-space propagators and vertices as in Chapter 3, see Fig. 3.3.

4.4.2 IR-enhanced diagrams and power counting

Consider a TSPT n -point vertex $\bar{\Gamma}_n(\mathbf{k}_1, \dots, \mathbf{k}_n)$ whose arguments \mathbf{k}_i may belong to two different domains: either the soft one, denoted by q , or the hard one, denoted by k , with

$$q \ll k. \quad (4.39)$$

Let us first take a look at the wiggly three-point vertex $\bar{\Gamma}_3^{'w}(\mathbf{k}_1, \mathbf{k}_2, \mathbf{k}_3)$. From Eq. (4.27) it is found to be

$$\bar{\Gamma}_3^{'w}(\mathbf{k}, \mathbf{q}, -\mathbf{k}-\mathbf{q}) = J_2(\mathbf{k}, \mathbf{q}) \frac{\bar{P}_w(|\mathbf{k}+\mathbf{q}|)}{\bar{P}_{nw}^2(|\mathbf{k}+\mathbf{q}|)} + J_2(-\mathbf{k}-\mathbf{q}, \mathbf{q}) \frac{\bar{P}_w(k)}{\bar{P}_{nw}^2(k)} + J_2(\mathbf{k}, -\mathbf{k}-\mathbf{q}) \frac{\bar{P}_w(q)}{\bar{P}_{nw}^2(q)}, \quad (4.40)$$

where we have defined

$$J_2(\mathbf{k}_1, \mathbf{k}_2) \equiv \frac{(\mathbf{k}_1 + \mathbf{k}_2)^2}{k_1^2 k_2^2} ((\mathbf{k}_1 \cdot \mathbf{k}_2) + f k_{1,z} k_{2,z}). \quad (4.41)$$

In the limit (4.39) the rightmost term in Eq. (4.40) is negligibly small, while the other two terms yield the expression

$$\bar{\Gamma}_3^{nw}(\mathbf{k}, \mathbf{q}, -\mathbf{k} - \mathbf{q}) = \frac{(\mathbf{k} \cdot \mathbf{q}) + f k_z q_z}{q^2} \frac{\bar{P}_w(|\mathbf{k} + \mathbf{q}|) - \bar{P}_w(k)}{\bar{P}_{nw}^2(k)} + O(1). \quad (4.42)$$

Here we have Taylor expanded the smooth power spectrum $\bar{P}_{nw}(|\mathbf{k} + \mathbf{q}|) = \bar{P}_{nw}(k) + O(q/k)$. We observe that at

$$k_{osc} < q \ll k \quad (4.43)$$

the first term is enhanced by $O(k/q)$. For yet softer $q \ll k_{osc}$, one can write,

$$\bar{P}_w(|\mathbf{k} + \mathbf{q}|) - \bar{P}_w(k) \approx \frac{(\mathbf{k} \cdot \mathbf{q})}{k} \frac{d\bar{P}_w}{dk}. \quad (4.44)$$

Taking into account that $d\bar{P}_w/dk \sim \bar{P}_w/k_{osc}$, we see that the enhancement of (4.42) becomes $O(k/k_{osc})$. Note that despite the enhancement, the vertex (4.42) remains finite in the limit $q \rightarrow 0$, in line with the IR safety of the TSPT expansion discussed in Sec. 4.3. The situation here is completely analogous to the one we had in real space: for general values of q in the range (4.43) the expansion (4.44) does not provide a good approximation to the finite difference on the l.h.s. Indeed, the latter oscillates with the period $q \sim 2\pi k_{osc}$, whereas the r.h.s. of (4.44) is linear in q . As we want to include the range (4.43) in our analysis, we work in what follows with the representation (4.42), where the finite difference of the wiggly power spectra is kept explicitly.

The enhanced contribution (4.42) can be written in a compact form by introducing a linear operator $\mathcal{D}_{\mathbf{q}}^{(s)}$ acting on the wiggly power spectrum,

$$\begin{aligned} \mathcal{D}_{\mathbf{q}}^{(s)}[\bar{P}_w(k)] &= \frac{(\mathbf{k} \cdot \mathbf{q}) + f k_z q_z}{q^2} (\bar{P}_w(|\mathbf{k} + \mathbf{q}|) - \bar{P}_w(k)) \\ &= \frac{\mathcal{P}_{ab} k^a q^b}{q^2} (e^{\mathbf{q} \cdot \nabla_{\mathbf{k}'}} - 1) \bar{P}_w(k') \Big|_{k'=k}, \end{aligned} \quad (4.45)$$

where

$$\mathcal{P}_{ab} \equiv \delta_{ab} + f \hat{z}_a \hat{z}_b. \quad (4.46)$$

This operator has the following properties. First, it scales as

$$\mathcal{D}_{\mathbf{q}}^{(s)}[\bar{P}_w] = O(1/\varepsilon)\bar{P}_w, \quad (4.47)$$

where $\varepsilon \sim q/k$. Second, this operator commutes with itself and in any expression acts only on occurrences of \bar{P}_w , leaving the smooth components intact. It is a simple generalization of the operator $\mathcal{D}_{\mathbf{q}}^{(r)}$ which controls the IR enhancement in real space and is obtained from $\mathcal{D}_{\mathbf{q}}^{(s)}$ by replacing \mathcal{P}_{ab} with the Kronecker symbol δ_{ab} (see Chapter 2).

In Appendix B.4 we prove that the expression (4.42) generalizes to an arbitrary n -point vertex with m hard momenta \mathbf{k}_i and $n - m$ soft momenta \mathbf{q}_j uniformly going to zero,

$$\begin{aligned} \bar{\Gamma}_n'^w(\mathbf{k}_1, \dots, \mathbf{k}_m - \sum_{i=1}^{n-m} \mathbf{q}_i, \mathbf{q}_1, \dots, \mathbf{q}_{n-m}) \\ = (-1)^{n-m} \left(\prod_{j=1}^{n-m} \mathcal{D}_{\mathbf{q}_j}^{(s)} \right) [\bar{\Gamma}_m'^w(\mathbf{k}_1, \dots, \mathbf{k}_m)] (1 + O(\varepsilon)). \end{aligned} \quad (4.48)$$

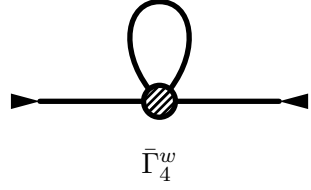
The leading IR enhancement of this vertex is $O(\varepsilon^{-n+m})$, and the maximum is achieved for $n - 2$ soft wavenumbers,

$$\begin{aligned} \bar{\Gamma}_n'^w(\mathbf{k}, -\mathbf{k} - \sum_{i=1}^{n-2} \mathbf{q}_i, \mathbf{q}_1, \dots, \mathbf{q}_{n-2}) = (-1)^{n-2} \left(\prod_{j=1}^{n-2} \mathcal{D}_{\mathbf{q}_j}^{(s)} \right) \bar{\Gamma}_2'^w(\mathbf{k}, -\mathbf{k})(1 + O(\varepsilon)) \\ = (-1)^{n-1} \left(\prod_{j=1}^{n-2} \frac{\mathcal{P}_{ab} k^a q_j^b}{q_j^2} (e^{\mathbf{q}_j \cdot \nabla_{\mathbf{k}}} - 1) \right) \left. \frac{\bar{P}_w(k')}{\bar{P}_{nw}^2(k)} \right|_{k'=k} (1 + O(\varepsilon)). \end{aligned} \quad (4.49)$$

On the other hand, it is straightforward to verify that the smooth vertices do not receive IR enhancements as their arguments go to zero, in line with the fact that bulk flows have significant effect only on wiggly correlation functions.

We now discuss the power counting rules that will help us identify IR enhanced diagrams. These rules are completely similar to those discussed in Section 3.2, where the reader can find further details. Owing to Eq. (4.48), the resummation procedure is totally analogous to the one discussed in Chapter 3, with the only difference that we have to substitute the real-space operator $\mathcal{D}_{\mathbf{q}}^{(r)}$, kernels and vertices with their redshift-space counterparts.

It is instructive to consider the leading IR correction to the matter power spectrum at one loop. It is given by the following graph:



The diagram shows a horizontal line with arrows at both ends, representing a propagator. A vertical line connects this horizontal line to a circular loop. The vertex where the vertical line meets the horizontal line is shaded with diagonal lines. Below the horizontal line is the label $\bar{\Gamma}_4^w$.

$$= \frac{g^4}{2} K_1^2(\mathbf{k}) \int_{|\mathbf{q}| < k_S} \bar{P}_{nw}(q) \mathcal{D}_{\mathbf{q}}^{(s)} \mathcal{D}_{-\mathbf{q}}^{(s)} \bar{P}_w(k) \equiv -g^4 K_1^2 \mathcal{S}^{(s)}[\bar{P}_w], \quad (4.50)$$

where in the last equality we defined a new linear operator $\mathcal{S}^{(s)}$ acting on the wiggly power spectrum,

$$\mathcal{S}^{(s)}[\bar{P}_w] = \mathcal{P}_{ab} \mathcal{P}_{cd} k^a k^c \int_{|\mathbf{q}| < k_S} \bar{P}_{nw}(q) \frac{q^b q^d}{q^4} (1 - \cosh(\mathbf{q} \cdot \nabla_{k'})) \bar{P}_w(k') \Big|_{k'=k}. \quad (4.51)$$

Within our power counting rules,

$$g^2 \mathcal{S}^{(s)}[\bar{P}_w] \sim O(1/\varepsilon^2 \times \sigma_S^2) \bar{P}_w. \quad (4.52)$$

As discussed previously, the product $1/\varepsilon^2 \times \sigma_S^2$ is $O(1)$ at low redshifts and therefore this one-loop contribution is of the same order as the linear wiggly power spectrum, which points to the need for IR resummation.

The key observation is that the structure of IR enhancement in redshift space vertices is same as that of the real space ones. Hence, in the case of redshift space one can use exactly the same power counting rules as in real space, see Sec. 3.2.2.

4.4.3 IR resummation at leading order

Let us first consider the density power spectrum. The leading-order derivation will be analogous to the real space one, yet we present it here for the sake of self-containment of this Chapter. As in the case of real space, the most IR-enhanced contributions correspond to $l = 2L$ and $L_h = 0$. Resummation of these *daisy*

diagrams is graphically represented as follows,

$$P_{mm,w}^{(s)\text{IR res,LO}}(\eta; \mathbf{k}) = \text{wavy line} + \text{loop diagram} \quad (4.53)$$

$$+ \text{2-loop diagram} + \text{3-loop diagram} + \text{4-loop diagram} + \dots$$

Using Eq. (4.48) we find that the L -th contribution here has the form,

$$\begin{aligned} & g^2 K_1^2(\mathbf{k}) \bar{P}_{nw}^2(k) \frac{1}{L!} \left[\frac{g^2}{2} \int_{|\mathbf{q}| < k_S} \bar{P}_{nw}(q) \mathcal{D}_{\mathbf{q}}^{(s)} \mathcal{D}_{-\mathbf{q}}^{(s)} \right]^L \bar{\Gamma}_2^{nw}(\mathbf{k}, -\mathbf{k}) \\ & = g^2 K_1^2(\mathbf{k}) \cdot \frac{1}{L!} (-g^2 \mathcal{S}^{(s)})^L \bar{P}_w(k), \end{aligned} \quad (4.54)$$

up to ε -suppressed corrections. As we have already shown, summing the series (4.53) leads to the exponentiation of the operator (4.51), which we have already encountered at one loop order, i.e.

$$P_{mm}^{(s)\text{IR res,LO}}(\eta; \mathbf{k}) = g^2 K_1^2 (\bar{P}_{nw} + e^{-g^2 \mathcal{S}^{(s)}} \bar{P}_w), \quad (4.55)$$

where we have also added the smooth part which is unaffected by IR resummation. The time dependence of the resummed power spectrum comes from its explicit dependence on $g(\eta)$, as well as implicitly through the dependence of the kernel K_1 and the operator $\mathcal{S}^{(s)}$ on $f(\eta)$. The practical method to evaluate the exponential operator appearing in (4.55) will be discussed in Sec. 4.6.

Similarly, one can show by following the arguments of Chapter 3 that IR resummation of an arbitrary n -point function at the leading order (LO) amounts to simply substituting the wiggly part of the linear spectrum, \bar{P}_w by its resummed version $e^{-g^2 \mathcal{S}^{(s)}} \bar{P}_w$ in all tree-level diagrams. This can be summarized in the following compact form,

$$\mathfrak{C}_n^{(s)\text{IR res,LO}}(\mathbf{k}_1, \dots, \mathbf{k}_n) = \mathfrak{C}_n^{(s)\text{tree}}[\bar{P}_{nw} + e^{-g^2 \mathcal{S}^{(s)}} \bar{P}_w](\mathbf{k}_1, \dots, \mathbf{k}_n), \quad (4.56)$$

where $\mathfrak{C}_n^{(s)\text{tree}}$ should be understood as a functional of the linear power spectrum. Note that the leading IR-enhanced contributions are essentially the same for

velocity and density correlators.

4.4.4 Next-to-leading order corrections and hard loops

There are two different types of next-to-leading order corrections to the above results:

- (1) Soft diagrams with non-maximal IR enhancement, characterized by $l = 2L_s - 1$ (see Eq. (3.31)), as well as subleading terms in the daisy diagrams considered above. Formally, these contributions are suppressed by one power of ε relative to the leading order.
- (2) Diagrams with one hard loop, $L_h = 1$, and otherwise maximal IR enhancement $l = 2L_s$. These diagrams are suppressed by one factor of σ_h^2 relative to the leading order.

Let us first discuss the corrections of the first type. Their resummation for the matter power spectrum in real space was performed in Chapter 3, where it was shown that they have only a sub percent effect. We argued that this is a consequence of the specific shape of the matter power spectrum. The same should be true for redshift space, as our argument only appealed to the shape of the Λ CDM power spectrum and the structure of mode coupling which is similar in real and redshift spaces. We leave the analysis of the modifications due to redshift space and bias for future work. We point out that, albeit small, these corrections are necessary for a robust estimation of the shift of the BAO peak.

We now focus on contributions with one hard loop and maximal IR enhancement. These contributions scale as

$$\sigma_h^2 \times (\sigma_S^2 \times 1/\varepsilon^2)^{L_s} \quad (4.57)$$

and their resummation proceeds in a straightforward manner along the lines of Chapter 3. The key observation is that due to Eq. (4.48) the redshift space vertices have the same factorization property as the real space vertices, see Eq. (3.39). Thus, dressing hard-loop diagrams with soft loops results in the simple replacement of the wiggly power spectrum appearing in propagators and vertices with its resummed version. For instance, the IR-resummed matter power spectrum at NLO reads

$$P_{mm}^{(s) \text{ IR res, LO+NLO}} = g^2 K_1^2 [\bar{P}_{nw} + (1 + g^2 \mathcal{S}^{(s)}) e^{-g^2 \mathcal{S}^{(s)}} \bar{P}_w] + P_{mm}^{(s) 1-loop} [\bar{P}_{nw} + e^{-g^2 \mathcal{S}^{(s)}} \bar{P}_w], \quad (4.58)$$

where $P_{mm}^{(s)1-loop}$ is the one-loop contribution understood as a functional of the linear power spectrum². The above formula has a simple meaning: one has to use the leading order IR-resummed linear power spectrum as an input in the 1-loop calculation and correct the tree-level result in order to avoid double-counting. We emphasize that Eq. (4.58) is not a phenomenological model but an outcome of the rigorous resummation of IR-enhanced corrections at order (4.57). The result (4.58) can be easily generalized to higher-order statistics, i.e. for an arbitrary n -point function one obtains

$$\mathfrak{C}_n^{(s)\text{IR res, LO+NLO}} = \mathfrak{C}_n^{(s)\text{tree}} [\bar{P}_{nw} + (1 + g^2 \mathcal{S}^{(s)}) e^{-g^2 \mathcal{S}^{(s)}} \bar{P}_w] + \mathfrak{C}_n^{(s)1-loop} [\bar{P}_{nw} + e^{-g^2 \mathcal{S}^{(s)}} \bar{P}_w]. \quad (4.59)$$

Further, it is possible to include higher order hard loop corrections, i.e. to resum the graphs that scale as $(\sigma_h^2)^2 \times (\sigma_S^2 \times 1/\varepsilon^2)^{L_s}$. For the power spectrum the net result reads

$$\begin{aligned} P_{mm}^{(s),\text{IR res, LO+NLO+NNLO}} &= g^2 K_1^2 \left[\bar{P}_{nw} + \left(1 + g^2 \mathcal{S}^{(s)} + \frac{1}{2} (g^2 \mathcal{S}^{(s)})^2 \right) e^{-g^2 \mathcal{S}^{(s)}} \bar{P}_w \right] \\ &+ P_{mm}^{(s)1-loop} [\bar{P}_{nw} + (1 + g^2 \mathcal{S}^{(s)}) e^{-g^2 \mathcal{S}^{(s)}} \bar{P}_w] + P_{mm}^{(s)2-loop} [\bar{P}_{nw} + e^{-g^2 \mathcal{S}^{(s)}} \bar{P}_w]. \end{aligned} \quad (4.60)$$

Generalization to other correlation functions and higher hard-loop orders is straightforward.

4.5 Bias

Bias is the relation between the density of observed tracers (e.g. galaxies, halos, etc.) and the density of the underlying matter field [125–130], see [131] for a recent comprehensive review. This relation can be written involving the matter density field at the initial (Lagrangian biasing) or final (Eulerian biasing) time slice. As TSPT is formulated in terms of Eulerian fields at a finite time slice, in what follows we adopt the Eulerian biasing scheme. As long as perturbative treatment is valid, it is possible to describe *deterministic* bias as a local in time and space operator expansion [129, 131],

$$\delta_h^{(r)}(\tau, \mathbf{x}) = \sum_n \sum_{\mathcal{O}^{(n)}} b_{\mathcal{O}^{(n)}}(\tau) \mathcal{O}^{(n)}(\tau, \mathbf{x}) \quad (4.61)$$

²Formally, $P_{mm}^{(s)1-loop}$ should contain only the hard part of the loop. However, it is convenient to extend it to include soft momenta. This introduces a difference of order of soft NLO corrections which, as we argued, are numerically small.

where $\delta_h^{(r)}$ stands for the density contrast of biased tracers in real space and $\mathcal{O}^{(n)}$ are operators constructed out of the density field to the n 'th power, i.e. $\mathcal{O}^{(n)} \sim O(\delta^n)$. The coefficients $b_{\mathcal{O}^{(n)}}$ are called bias parameters; in general, they are functions of time. The first sum runs over orders in perturbation theory, and the second sum runs over all independent operators at a given order. Note that in general the bias expansion should also include stochastic (noise) contributions, generated by small-scale fluctuations that are uncorrelated with the long-wavelength density field. The formal inclusion of stochastic terms into TSPT is straightforward. However, we defer the detailed treatment of these contributions for two reasons. First, the effect of stochastic bias is expected to be negligibly small at the BAO scales. Second, noise terms clearly have a UV origin and thus should be treated on the same footing as the UV counterterms, which are left beyond the scope of this Chapter.

Due to the equivalence principle, the density of tracers cannot depend on the value of the Newtonian potential and its first derivatives. Thus, the operators $\mathcal{O}^{(n)}$ must be constructed using the tidal tensor

$$\Pi_{ij}^{[1]} = \partial_i \partial_j \Phi \quad (4.62)$$

and its derivatives. Here Φ is the suitably normalized gravitational potential related to the standard Newtonian potential ϕ via $\Phi \equiv 2\phi/(3\Omega_m \mathcal{H}^2)$. A convenient basis is constructed as follows. One introduces a sequence of tensors,

$$\Pi_{ij}^{[1]} = \partial_i \partial_j \Phi, \quad (4.63a)$$

$$\Pi_{ij}^{[n]} = \frac{1}{(n-1)!} \left[\frac{1}{f\mathcal{H}} \frac{D}{D\tau} \Pi_{ij}^{[n-1]} - (n-1) \Pi_{ij}^{[n-1]} \right], \quad (4.63b)$$

where $D/D\tau$ is the convective derivative,

$$\frac{D}{D\tau} = \frac{\partial}{\partial\tau} + v^i \partial_i = \frac{\partial}{\partial\tau} - f\mathcal{H} \frac{\partial_i \Theta^{(r)}}{\Delta} \partial_i, \quad (4.64)$$

and in passing to the last equality we used that only the longitudinal component of the peculiar velocity is present in perturbation theory. The use of convective derivative accounts for the fact that the evolution of tracers is determined by the physical conditions along the fluid flow [131]. The second term in (4.63b) is adjusted to subtract $O(\delta^{n-1})$ contributions, so that $\Pi_{ij}^{[n]}$ has homogeneous dependence on δ of order $O(\delta^n)$. Despite the fact that the tensors (4.63b) contain partial time derivatives, it is always possible to eliminate them by using the equations of motion for matter.

The bias operators at n 'th order are given by all possible contractions of the tensors (4.63) with total order n , e.g.

$$\begin{aligned}
& \text{1st} \quad \text{Tr}[\Pi^{[1]}], \\
& \text{2nd} \quad \text{Tr}[(\Pi^{[1]})^2], \quad (\text{Tr}[\Pi^{[1]})]^2, \\
& \text{3rd} \quad \text{Tr}[(\Pi^{[1]})^3], \quad \text{Tr}[(\Pi^{[1]})^2]\text{Tr}[\Pi^{[1]}], \quad (\text{Tr}[\Pi^{[1]})]^3, \quad \text{Tr}[\Pi^{[1]}\text{Tr}[\Pi^{[2]}], \\
& \dots
\end{aligned} \tag{4.65}$$

Note that the terms $\text{Tr}[\Pi^{[n]}]$ are excluded at the n 'th order (except $n = 1$) as they are degenerate with other operators in the basis. The basis (4.63) does not contain higher-derivative terms. In principle, they can always be added by applying derivatives to the tidal tensor and making all possible contractions analogous to (4.65). As the bias expansion preserves the equivalence principle [129], it contains no IR poles. We give explicit expressions for a few first bias operators relevant for one-loop computations in Appendix E.

All in all, the bias expansion takes the following form:

$$\delta_h^{(r)}(\tau, \mathbf{k}) = \sum_{n=1}^{\infty} \frac{1}{n!} \int_{\mathbf{q}_1, \dots, \mathbf{q}_n} (2\pi)^3 \delta_D^{(3)}(\mathbf{k} - \mathbf{q}_{1\dots n}) \tilde{M}_n(\tau; \mathbf{q}_1, \dots, \mathbf{q}_n) \prod_{i=1}^n \delta^{(r)}(\tau, \mathbf{q}_i). \tag{4.66}$$

In order to incorporate bias into TSPT, it is convenient to rewrite (4.66) in terms of the velocity divergence field. Using that the matter density field can be expressed in perturbation theory through the velocity divergence via (2.8), the relation (4.66) can be rearranged in the desired form:

$$\delta_h^{(r)}(\tau, \mathbf{k}) = \sum_{n=1}^{\infty} \frac{1}{n!} \int_{\mathbf{q}_1, \dots, \mathbf{q}_n} (2\pi)^3 \delta_D^{(3)}(\mathbf{k} - \mathbf{q}_{1\dots n}) M_n^{(r)}(\tau; \mathbf{q}_1, \dots, \mathbf{q}_n) \prod_{i=1}^n \Theta^{(r)}(\tau, \mathbf{q}_i). \tag{4.67}$$

The kernels $M_n^{(r)}$ relevant for the 1-loop calculation are given in Appendix E. In principle, the $M_n^{(r)}$ kernels may have arbitrary time-dependence, that is why we will not treat them as functions of the coupling constant g in the TSPT perturbative expansion. The bias parameters are expected to evolve slowly, with the rate comparable to that of the growth of matter. Note that the bias parameters are subject to UV renormalization [129, 132]. This issue will be addressed elsewhere.

The tracers' velocity field can, in principle, also be biased, so within the validity of perturbation theory it will be expressed as a power series in $\Theta^{(r)}$,

$$\Theta_h^{(r)}(\tau, \mathbf{k}) = \sum_{n=1}^{\infty} \frac{1}{n!} \int_{\mathbf{q}_1, \dots, \mathbf{q}_n} (2\pi)^3 \delta_D^{(3)}(\mathbf{k} - \mathbf{q}_{1\dots n}) V_n(\eta; \mathbf{q}_1, \dots, \mathbf{q}_n) \prod_{i=1}^n \Theta^{(r)}(\tau, \mathbf{q}_i). \quad (4.68)$$

However, as long as the effect of relative velocities between different matter components can be neglected, the velocity bias will be absent at the lowest order in spatial derivatives. The difference of $\Theta_h^{(r)}$ from $\Theta^{(r)}$ will appear only at higher derivatives. For example,

$$V_1(\tau; \mathbf{k}) = 1 + b_{\nabla^2 \mathbf{v}}(\tau) k^2. \quad (4.69)$$

We conclude that the velocity bias has the same order in the derivative expansion as the UV counterterms, and thus its treatment goes beyond the scope of this thesis. In what follows we will neglect all the effects related to velocity bias.

4.5.1 IR resummation for biased tracers in real and redshift space

The goal of this section is to incorporate bias into TSPT and perform IR resummation for correlation functions of biased tracers in real and redshift space.

We start by discussing real space. In this case Eq. (4.67) describes the density of biased tracers as a composite operator analogous to the density of matter. Thus, we can use the technique developed in [1] by simply using the kernels M_n instead of K_n in the relevant Feynman diagrams. Since the bias vertices are IR safe, they do not produce additional contributions to be resummed. IR resummation thus goes in full analogy with the IR resummation of the density correlators in real space, see Chapter 3. The result of this procedure in real space is very simple: one has to substitute the linear power spectrum by its IR-resummed version in all expressions for the correlation functions of biased tracers.

Generalization to the case of redshift space is straightforward. The redshift coordinate of the tracer is related to the real-space one by means of the tracer's velocity $\mathbf{v}_h^{(r)}(\mathbf{x})$,

$$\mathbf{s}_h = \mathbf{x} + \hat{\mathbf{z}} \frac{v_{h,z}^{(r)}(\mathbf{x})}{\mathcal{H}}. \quad (4.70)$$

As pointed out before, we do not consider velocity bias in this thesis, thus in the rest of it we will assume that tracers are comoving with matter and simply

replace

$$\mathbf{v}_h^{(r)} \rightarrow \mathbf{v}^{(r)} \quad (4.71)$$

in Eq. (4.70). In order to transform the bias kernels $M_n^{(r)}$ into redshift space we use the same trick of introducing a fictitious 1D flow described in Sec. 4.2. In this way we obtain the same equations of motion as (4.15), but with $\delta^{(s)}$ replaced by $\delta_h^{(s)}$. At the next step we use these equations to derive the kernels relating the tracer density field with the redshift space velocity $\Theta^{(s)}$. We obtain

$$\delta_h^{(s)}(\mathcal{F}; \tau, \mathbf{k}) = \sum_{n=1}^{\infty} \frac{1}{n!} \int [dq]^n M_n^{(s)}(\mathcal{F}; \mathbf{q}_1, \dots, \mathbf{q}_n) \Theta_{\mathbf{q}_1}^{(s)} \dots \Theta_{\mathbf{q}_n}^{(s)}, \quad (4.72)$$

with $M_n^{(s)}$'s satisfying the same equations of motion as (4.32) with an obvious change in the initial conditions,

$$M_n^{(s)} \Big|_{\mathcal{F}=0} = M_n^{(r)}. \quad (4.73)$$

This procedure allows us to unambiguously map the real space bias parameters to redshift space ones. It should be noted that some tracers (e.g. Ly α forest, 21 cm intensity) may have additional biases in redshift space [131, 133, 134]. In this case one has to supplement (4.72) with relevant extra bias operators.

An immediate consequence of the above construction is that the kernels $M_n^{(s)}$ are IR-safe and are not functionals of the initial power spectra. Thus, they do not receive any IR enhancement which, as before, affects solely the vertices $\bar{\Gamma}_n^{w(s)}$. The diagrams involving these vertices are resummed, as has been shown in the previous sections. The net result at leading order is that one has to use the ‘‘dressed’’ power spectrum

$$\bar{P}_{nw} + e^{-g^2 \mathcal{S}^{(s)}} \bar{P}_w, \quad (4.74)$$

instead of the linear one in all tree-level calculations. At first order in hard loops one has to use the power spectrum (4.74) in the loop diagrams and correct the tree-level result for double-counting. At higher loop order this procedure iterates, as illustrated by Eq. (4.60).

4.6 Practical implementation and comparison with other methods

In this section we formulate the practical prescription to evaluate the IR-resummed power spectra and bispectra. We then compare our results with other analytic approaches. While our results have been derived within the TSPT framework, they can be easily reformulated in the language of the standard perturbation theory [15], which may be convenient for implementation within existing numerical codes, e.g. FAST-PT [135, 136] or FnFast [137].

4.6.1 The power spectrum and bispectrum at leading order

In order to simplify notations in this section we drop the explicit time dependence of the power spectra and use the shorthand

$$P(k) \equiv D^2(z) \bar{P}(k). \quad (4.75)$$

Having decomposed the linear power spectrum into wiggly and smooth parts, e.g. using one of the methods described in [3], we have to evaluate the derivative operator acting on the wiggly part. Since P_w is a function oscillating with the period $k_{osc} = h/(110 \text{ Mpc})$, we have

$$\nabla_{\alpha_1} \cdots \nabla_{\alpha_{2n}} P_w(k) = (-1)^n \frac{\hat{k}_{\alpha_1} \cdots \hat{k}_{\alpha_{2n}}}{k_{osc}^{2n}} P_w(k) (1 + O(\varepsilon)), \quad (4.76)$$

where $\varepsilon \simeq k_{eq}/k$ is the small expansion parameter controlling the IR enhancement and $\hat{\mathbf{k}} = \mathbf{k}/k$. Then the action of the operator $\mathcal{S}^{(s)}$ (Eq. (4.51)) at leading order in ε reads,

$$g^2 \mathcal{S}^{(s)}[P_w(k)] = \mathcal{P}_{ab} \mathcal{P}_{cd} k^a k^c \int_{|\mathbf{q}| < k_S} P_{nw}(q) \frac{q^b q^d}{q^4} \left[1 - \cos\left(\frac{(\mathbf{q} \cdot \hat{\mathbf{k}})}{k_{osc}}\right) \right] P_w(k), \quad (4.77)$$

which reduces to a \mathbf{k} -dependent multiplicative factor. Evaluating the integral we obtain,

$$g^2 \mathcal{S}^{(s)}[P_w(k)] = k^2 [(1 + f\mu^2(2 + f))\Sigma^2 + f^2\mu^2(\mu^2 - 1)\delta\Sigma^2] P_w(k) \times (1 + O(\varepsilon)), \quad (4.78)$$

with $\mu \equiv k_z/k$ and

$$\Sigma^2 \equiv \frac{4\pi}{3} \int_0^{k_S} \frac{dq}{(2\pi)^3} P_{nw}(q) \left[1 - j_0\left(\frac{q}{k_{osc}}\right) + 2j_2\left(\frac{q}{k_{osc}}\right) \right], \quad (4.79a)$$

$$\delta\Sigma^2 \equiv 4\pi \int_0^{k_S} \frac{dq}{(2\pi)^3} P_{nw}(q) j_2\left(\frac{q}{k_{osc}}\right). \quad (4.79b)$$

Here j_n are spherical Bessel functions and k_S is the separation scale of long and short modes in the loop integrals. Thus, the LO IR-resummed power spectrum of biased tracers (say, halos) in redshift space is given by

$$P_{hh}^{(s)\text{IR res,LO}}(k, \mu) = (b_1 + f\mu^2)^2 \left(P_{nw}(k) + e^{-k^2 \Sigma_{\text{tot}}^2(\mu; k_S)} P_w(k) \right), \quad (4.80)$$

where

$$\Sigma_{\text{tot}}^2(\mu; k_S) \equiv (1 + f\mu^2(2 + f))\Sigma^2 + f^2\mu^2(\mu^2 - 1)\delta\Sigma^2. \quad (4.81)$$

Note that the damping factor Σ^2 has already appeared as a result of IR resummation in real space [3, 29], while $\delta\Sigma^2$ is a new contribution. The form of the first term in (4.81) has a simple physical meaning: one has to keep the perpendicular (real space) rms displacement Σ of soft modes intact while multiplying the rms displacements along the line-of-sight by a factor $(1 + f)$, as prescribed by the Kaiser formula, i.e.

$$k_{\parallel}^2(1 + f)^2\Sigma^2 + k_{\perp}^2\Sigma^2 = \Sigma^2(1 + f\mu^2(2 + f)), \quad (4.82)$$

where $k_{\parallel} = k_z$, $k_{\perp} = \sqrt{k^2 - k_z^2}$. Note that the contribution proportional to $\delta\Sigma^2$ is negative and thus it somewhat reduces the BAO damping compared to the simple formula (4.82). The form of exponential damping (4.81) does not depend on bias parameters. This is consistent with physical intuition, as the degradation of the BAO feature in the statistics of biased tracers is caused by displacements of underlying matter, in agreement with the equivalence principle [131].

We plot the dependence of the damping factors Σ^2 and $\delta\Sigma^2$ on the choice of k_S in the left panel of Fig. 4.2. At small $k_S \ll k_{osc}$ the damping functions have the following asymptotic behavior:

$$\Sigma^2(k_S) \rightarrow \frac{2\pi}{5} \int_0^{k_S} \frac{dq}{(2\pi)^3} \frac{q^2}{k_{osc}^2} P_{nw}(q), \quad \delta\Sigma^2(k_S) \rightarrow \frac{4\pi}{15} \int_0^{k_S} \frac{dq}{(2\pi)^3} \frac{q^2}{k_{osc}^2} P_{nw}(q). \quad (4.83)$$

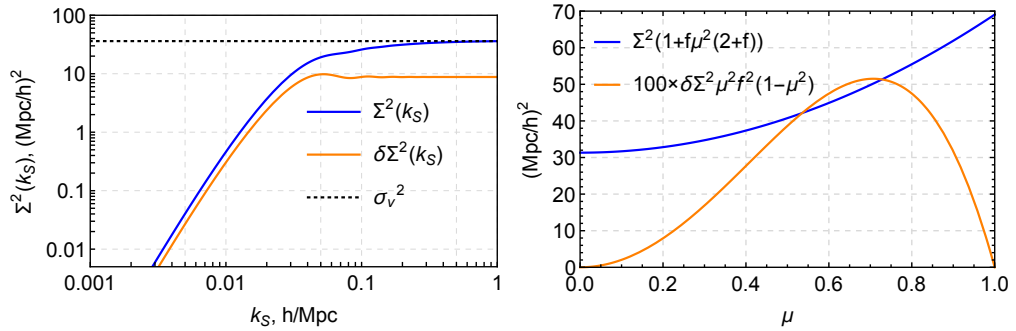


FIGURE 4.2: Left panel: the dependence of the BAO damping factors Σ^2 and $\delta\Sigma^2$ on the separation scale k_S at redshift zero (in the cosmological model of [138], $f = 0.483$). Right panel: the dependence of two contributions to the damping factor on the angle μ between the Fourier wavevector and the line-of-sight; k_S is fixed to $0.2 h/\text{Mpc}$.

The integral in $\delta\Sigma^2(k_S)$ is cut off at k_{osc} by the Bessel function and becomes a constant equal to

$$\delta\Sigma^2(k_{osc}) \simeq \frac{4\pi}{15k_{osc}^2} \int_{|\mathbf{q}| \lesssim k_{osc}} \frac{dq}{(2\pi)^3} q^2 P_{nw}(q), \quad (4.84)$$

whereas $\Sigma^2(k_S)$ keeps growing up to $q \sim 0.2 h/\text{Mpc}$ where it approaches its asymptotic value $\sigma_v^2 \equiv 4\pi \int dq P_{nw}(q)/3$. The integral in $\Sigma^2(k_S)$ receives the dominant contribution from $q \gtrsim k_{eq}$ and is significantly bigger than $\delta\Sigma^2(k_S)$. This numerical hierarchy is due to the specific shape of the ΛCDM power spectrum which is strongly suppressed at $q \lesssim k_{osc}$; if the power spectrum peaked at momenta smaller than k_{osc} , the damping factors $\Sigma^2(k_S)$ and $\delta\Sigma^2(k_S)$ would have comparable magnitudes.

As discussed in Sec. 4.4.2, the scale k_S should be chosen high enough to include the contributions of all relevant soft modes. At the same time, it should be smaller than the momentum k of interest. In the numerical calculations below we will vary k_S in the range $(0.05 \div 0.2) h/\text{Mpc}$. The dependence of the final result on the precise choice of k_S should be considered as a measure of theoretical uncertainty.

In order to understand the effect of damping in redshift space let us rewrite the expression (4.81) as $\Sigma_{\text{tot}}^2 = \Sigma_1^2 + \Sigma_2^2$ with

$$\begin{aligned} \Sigma_1^2(\mu; k_S) &\equiv (1 + f\mu^2(2+f))\Sigma^2, \\ \Sigma_2^2(\mu; k_S) &\equiv f^2\mu^2(\mu^2 - 1)\delta\Sigma^2. \end{aligned} \quad (4.85)$$

Σ_1^2 and Σ_2^2 as functions of μ are plotted in the right panel of Fig. 4.2. We fix

$k_S = 0.2 h/\text{Mpc}$. For visualization purposes we multiply Σ_2^2 by factor 100 and flip its sign. We observe that Σ_2^2 is much smaller than Σ_1^2 for all wavevector directions. Its relative effect somewhat increases at high redshifts where the suppression by factor f^2 is mitigated. As for the Σ_1^2 contribution, we see that it grows monotonically with μ and thus, as expected, the BAO signal is more suppressed for the wavevectors aligned with the line-of-sight.

The IR-resummed bispectrum at leading order is easily obtained from the general formula (4.56). Making use of the well-known SPT result we get,

$$B_{hhh}^{(s)\text{IR res,LO}}(\mathbf{k}_1, \mathbf{k}_2, \mathbf{k}_3) = 2 \sum_{1 \leq i < j \leq 3} (b_1 + f\mu_i^2)(b_1 + f\mu_j^2) Z_2(\mathbf{k}_i, \mathbf{k}_j) \\ \times \left(P_{nw}(k_j)P_{nw}(k_i) + e^{-k_j^2 \Sigma_{\text{tot}}^2(\mu_j)} P_w(k_j)P_{nw}(k_i) + e^{-k_i^2 \Sigma_{\text{tot}}^2(\mu_i)} P_w(k_i)P_{nw}(k_j) \right), \quad (4.86)$$

where $\mu_j \equiv \hat{\mathbf{k}}_j \cdot \hat{\mathbf{z}}$. As everywhere else in the Chapter, we have retained only linear terms in P_w . The expression for the SPT kernel Z_2 is given in Appendix E.

4.6.2 The power spectrum and bispectrum at next-to-leading order

At NLO the IR-resummed power spectrum can be written as

$$P_{hh}^{(s)\text{IR res,LO+NLO}}(k, \mu) = (b_1 + f\mu^2)^2 \left(P_{nw}(k) + (1 + k^2 \Sigma_{\text{tot}}^2(\mu)) e^{-k^2 \Sigma_{\text{tot}}^2(\mu)} P_w(k) \right) \\ + P_{hh}^{(s)1\text{-loop}} [P_{nw} + e^{-k^2 \Sigma_{\text{tot}}^2(\mu)} P_w]. \quad (4.87)$$

Note that the power spectrum that must be used as an input in the loop contribution is anisotropic due to the angular dependence of the damping factor. This complicates evaluation of the loop integral, as it prevents from using the standard procedure of integrating over the azimuthal angle and reducing $P_{hh}^{(s)1\text{-loop}}$ to a finite series in μ^2 . To cast (4.87) in a more convenient form, we isolate the wiggly terms,

$$P_{hh,w}^{(s)1\text{-loop}} = 6Z_1(\mathbf{k}) e^{-k^2 \Sigma_{\text{tot}}^2(\mu)} P_w(k) \int_{\mathbf{p}} Z_3(\mathbf{k}, \mathbf{p}, -\mathbf{p}) P_{nw}(p) \\ + 6Z_1(\mathbf{k}) P_{nw}(k) \int_{\mathbf{p}} Z_3(\mathbf{k}, \mathbf{p}, -\mathbf{p}) P_w(p) e^{-p^2 \Sigma_{\text{tot}}^2(\mu_{\mathbf{p}})} \\ + 4 \int_{\mathbf{p}} (Z_2(\mathbf{p}, \mathbf{k} - \mathbf{p}))^2 P_{nw}(|\mathbf{k} - \mathbf{p}|) P_w(p) e^{-p^2 \Sigma_{\text{tot}}^2(\mu_{\mathbf{p}})}, \quad (4.88)$$

where $\mu_{\mathbf{p}} \equiv (\hat{\mathbf{p}} \cdot \hat{\mathbf{z}})$. The first term contains an integral of the isotropic smooth power spectrum and its evaluation does not pose any problem. The second term is an integral of a quickly oscillating function and is exponentially suppressed within our power counting. Indeed, approximating P_w with the sine we have³,

$$\int_{\mathbf{p}} \sin(p/k_{osc}) f_{smooth}(p/k) \sim e^{-k/k_{osc}} \sim e^{-1/\varepsilon}. \quad (4.89)$$

Similarly, the hard part of the third integral, i.e. the contribution from $|\mathbf{p} - \mathbf{k}| > k_S$, is also exponentially suppressed. On the other hand, in the vicinity $|\mathbf{p} - \mathbf{k}| < k_S$ the damping factor can be approximated as

$$e^{-p^2 \Sigma_{tot}^2(\mu_{\mathbf{p}})} = e^{-k^2 \Sigma_{tot}^2(\mu)} (1 + O(\varepsilon)). \quad (4.90)$$

The difference pertains to NLO soft corrections which we neglect in this Chapter. We conclude that the damping factor can be pulled out of the loop integrals without changing the order of approximation in our power counting. This allows us to rewrite the IR-resummed power spectrum in the form involving only integration over the isotropic initial power spectrum,

$$\begin{aligned} P_{hh}^{(s) \text{ IR res, LO+NLO}}(k, \mu) = & (b_1 + f\mu^2)^2 \left(P_{nw}(k) + (1 + k^2 \Sigma_{tot}^2(\mu)) e^{-k^2 \Sigma_{tot}^2(\mu)} P_w(k) \right) \\ & + P_{hh}^{(s) 1-loop} [P_{nw}] + e^{-k^2 \Sigma_{tot}^2(\mu)} P_{hh,w}^{(s) 1-loop}, \end{aligned} \quad (4.91)$$

where $P_{hh}^{(s) 1-loop} [P_{nw}]$ is evaluated on the smooth power spectrum only and

$$\begin{aligned} P_{hh,w}^{(s) 1-loop} = & 6P_w(k) Z_1(\mathbf{k}) \int_{\mathbf{p}} Z_3(\mathbf{p}, -\mathbf{p}, \mathbf{k}) P_{nw}(p) \\ & + 4 \int_{\mathbf{p}} (Z_2(\mathbf{p}, \mathbf{k} - \mathbf{p}))^2 P_{nw}(|\mathbf{k} - \mathbf{p}|) P_w(p). \end{aligned} \quad (4.92)$$

An expression similar to (4.91) was obtained for the 1-loop IR resummed real-space power spectrum in Ref. [29].

For higher-point correlation functions the ‘‘isotropisation’’ of the IR resummed loop integrands is in general impossible. However, some partial contributions to the total result may still be simplified. Thus, in Appendix F we show that the

³The kernel $Z_3(\mathbf{k}, \mathbf{p}, -\mathbf{p})$ is not regular at $\mathbf{p} \rightarrow 0$. However, this singularity does not contribute because $P_w(p)$ vanishes at the origin.

1-loop bispectrum in redshift space can be written in the following form,

$$\begin{aligned}
B^{(s)\text{ IR res, LO+NLO}} &= B^{(s)\text{ tree}} [P_{nw} + (1+k^2\Sigma_{\text{tot}}^2)e^{-k^2\Sigma_{\text{tot}}^2}P_w] + B^{(s)\text{ 1-loop}} [P_{nw} + e^{-k^2\Sigma_{\text{tot}}^2}P_w] \\
&\approx B^{(s)\text{ tree}} [P_{nw} + (1+k^2\Sigma_{\text{tot}}^2)e^{-k^2\Sigma_{\text{tot}}^2}P_w] + B^{(s)\text{ 1-loop}} [P_{nw}] \\
&\quad + \tilde{B}_{411,w}^{(s)} + \tilde{B}_{321-I,w}^{(s)} + \tilde{B}_{321-II,w}^{(s)} + \tilde{B}_{222,w}^{(s)},
\end{aligned} \tag{4.93}$$

where all terms except $\tilde{B}_{222,w}^{(s)}$ involve isotropic power spectra inside the momentum integrals. The ‘approximately equal’ sign between the first and second lines means that the two expressions are equal up to NLO soft correction. The formulae for $\tilde{B}_{411,w}^{(s)}$, $\tilde{B}_{321-I,w}^{(s)}$, $\tilde{B}_{321-II,w}^{(s)}$ and $\tilde{B}_{222,w}^{(s)}$ are given in Eqs. (F.5) of Appendix F.

4.6.3 Comparison with other approaches

Let us compare our results to other methods. At the phenomenological level the suppression of the BAO feature in redshift space is well described by a μ -dependent exponential damping acting on the wiggly part of the linear power spectrum. The aim of analytic approaches is to derive this result from first principles and consistently generalize it to higher orders in perturbation theory, where the effects beyond this simple damping are relevant. In this section we will focus on a few methods to describe the BAO peak which are most common in the literature.

The simplest model describing the suppression of the BAO peak in redshift space is given by

$$P^{(s)}(k, \mu) = (b_1 + f\mu^2)^2 (P_{nw}(k) + e^{-k^2 D^2(z) A^2 (1+f\mu^2(2+f))} P_w(k)), \tag{4.94}$$

with two possible choices of the damping factor A :

$$A^2 = \sigma_v^2 \equiv \frac{4\pi}{3} \int_0^\infty \frac{dq}{(2\pi)^3} P(q), \quad \text{following [62, 63]}, \tag{4.95a}$$

$$A^2 = \Sigma_\infty^2 \equiv \frac{4\pi}{3} \int_0^\infty \frac{dq}{(2\pi)^3} P(q) \left[1 - j_0\left(\frac{q}{k_{\text{osc}}}\right) + 2j_2\left(\frac{q}{k_{\text{osc}}}\right) \right], \quad \text{following [26, 103]}. \tag{4.95b}$$

These models are, essentially, the generalizations of the real space models discussed in detail in Section 3.6.2. Although they are quite successful at the phenomenological level, we emphasize that most of its success is merely a numerical

coincidence that happens due to a particular shape of the linear power spectrum in Λ CDM. Also note that the models (4.95) do not take into account the $\delta\Sigma^2$ contribution, which, albeit small in the Λ CDM cosmology, could be sizable if k_{eq} were smaller than k_{osc} .

The leading order IR-resummed power spectrum (4.80) coincides with the expression found in Ref. [139]. The approach used in [139] is related to the framework developed in Refs. [140, 141]. We point out that the accurate description of the BAO feature requires including loop corrections and thus goes beyond the simple exponential damping prescribed by (4.94).

Our results for the power spectrum are consistent with those obtained within the effective field theory of large scale structure [28, 64–66, 69, 142, 143]. Our expressions (4.58) and (4.60) agree, up to higher order corrections⁴, with those obtained in Ref. [142]. We emphasize that TSPT gives a simple diagrammatic description of IR resummation and provides a tool to examine and extend the results found in Ref. [142]. IR resummation in TSPT readily generalizes beyond the power spectrum and applies to any n -point correlation functions with an arbitrary number of hard loops. The power counting, outlined in this Chapter, allows one to go beyond next-to-leading order in a systematic way. In particular, TSPT allows one to systematically compute the subleading soft corrections relevant for the shift of the BAO peak. We leave their detailed study for future work.

4.7 Numerical results and comparison with N-body data

In this section we show the results for the 2-point correlation function and the power spectrum of matter in redshift space, although our analysis can be easily extended to biased tracers. We will first discuss the 2-point correlation function, which allows us to clearly illustrate the effect of IR resummation on the BAO feature due to a better separation between the BAO peak and short scales. Then we compare our predictions for the IR-resummed power spectrum at one loop against N-body data. To the best of our knowledge, there are no publicly available data on the 2-point correlation function in redshift space. That is why

⁴Note that [142] essentially applies the operator $e^{-g^2 S^{(s)}}$ to the whole power spectrum, including its smooth part. This is equivalent to a partial resummation of IR corrections to the smooth power spectrum. These corrections are not enhanced and therefore their resummation is not legitimate within our power-counting rules.

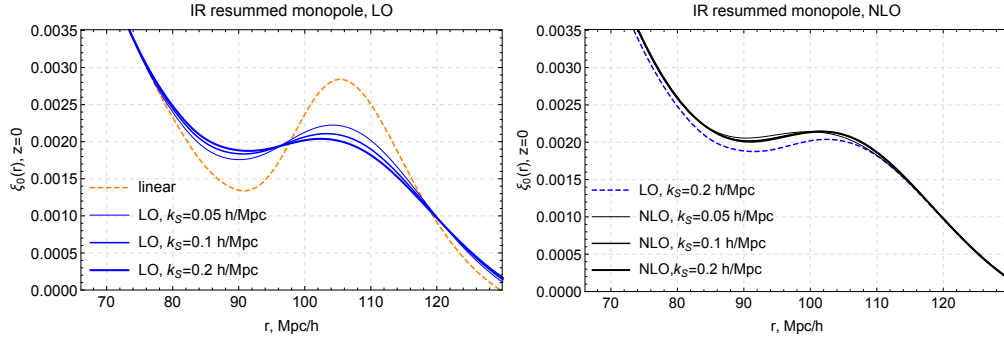


FIGURE 4.3: The monopole ($\ell = 0$) moment of the 2-point correlation function of matter in redshift space at $z = 0$. *Left panel:* linear theory (orange, dashed) vs leading order (LO) IR resummed results for several choices of k_S (blue). *Right panel:* LO for $k_S = 0.2h/\text{Mpc}$ (blue, dashed) vs next-to-leading order (NLO) IR resummed results (black).

in this Chapter we limit the comparison to the power spectrum, even though it is not optimal for the visualization of the BAO.

As common in redshift space analysis, we will study Legendre multipoles of the power spectrum and the 2-point correlation function, defined via

$$\begin{aligned}
 P_\ell(k) &= \frac{2\ell + 1}{2} \int_{-1}^1 L_\ell(\mu) P^{(s)}(k, \mu) d\mu, \\
 \xi_\ell(r) &= 4\pi i^\ell \int P_\ell(k) j_\ell(kr) \frac{k^2 dk}{(2\pi)^3},
 \end{aligned}
 \tag{4.96}$$

where L_ℓ is the Legendre polynomial of order ℓ . We will focus on the monopole, quadrupole and hexadecapole moments ($\ell = 0, 2, 4$), which fully characterize the linear correlation function in redshift space.

We consider the cosmological model corresponding to the N-body simulations performed in [138]. The linear power spectrum is produced with the Boltzmann code CLASS [111] and then decomposed into the wiggly and non-wiggly components using the spline approximation of the broadband power spectrum [3]. The redshift space one-loop integrals are evaluated using the FFTLog algorithm [144, 145]. A similar technique is used to compute the correlation function multipoles from those of the power spectrum.

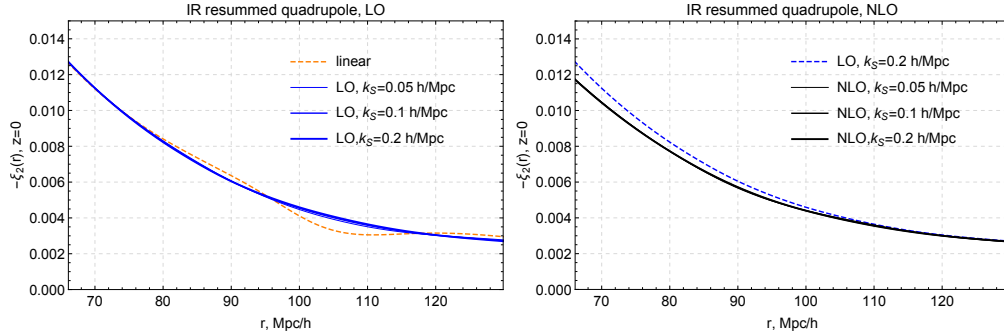


FIGURE 4.4: The quadrupole ($\ell = 2$) moment of the 2-point correlation function of matter in redshift space at $z = 0$. *Left panel:* linear theory (orange, dashed) vs LO IR resummed results for several choices of k_S (blue). *Right panel:* LO for $k_S = 0.2h/\text{Mpc}$ (blue, dashed) vs NLO IR resummed results (black). The three NLO curves are virtually indistinguishable.

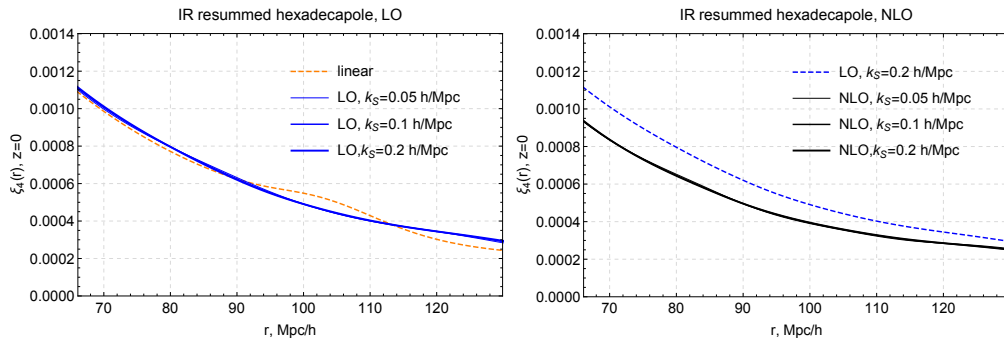


FIGURE 4.5: The hexadecapole ($\ell = 4$) moment of the 2-point correlation function of matter in redshift space at $z = 0$. *Left panel:* linear theory (orange, dashed) vs LO IR resummed results for several choices of k_S (blue). *Right panel:* LO for $k_S = 0.2h/\text{Mpc}$ (blue, dashed) vs NLO IR resummed results (black). Note that different choices of k_S lead to virtually identical curves.

4.7.1 2-point correlation function: quantitative study

In the left panel of Fig. 4.3 we show the leading-order IR resummed monopole correlation function for three different values⁵ of k_S . For comparison we also show the prediction of linear theory. As expected, the damping of the BAO described by a simple exponential suppression of the wiggly component translates into a suppression of the BAO peak. On the other hand, the scatter induced by the choice of k_S is quite sizable at leading order. To reduce this uncertainty one has to go to next-to-leading order. The corresponding correlation function is displayed in the right panel of Fig. 4.3. For comparison we also show the LO result for $k_S = 0.2h/\text{Mpc}$. We observe that the 1-loop contribution slightly

⁵ Alternatively, one could consider a k -dependent separation scale [29] to account for the fact that the enhancement only takes place for modes with $k \gg q$. In order to avoid the uncertainty related to the precise form of k -dependence, we prefer to keep k_S as a free parameter that allows us to control the theoretical error of our method.

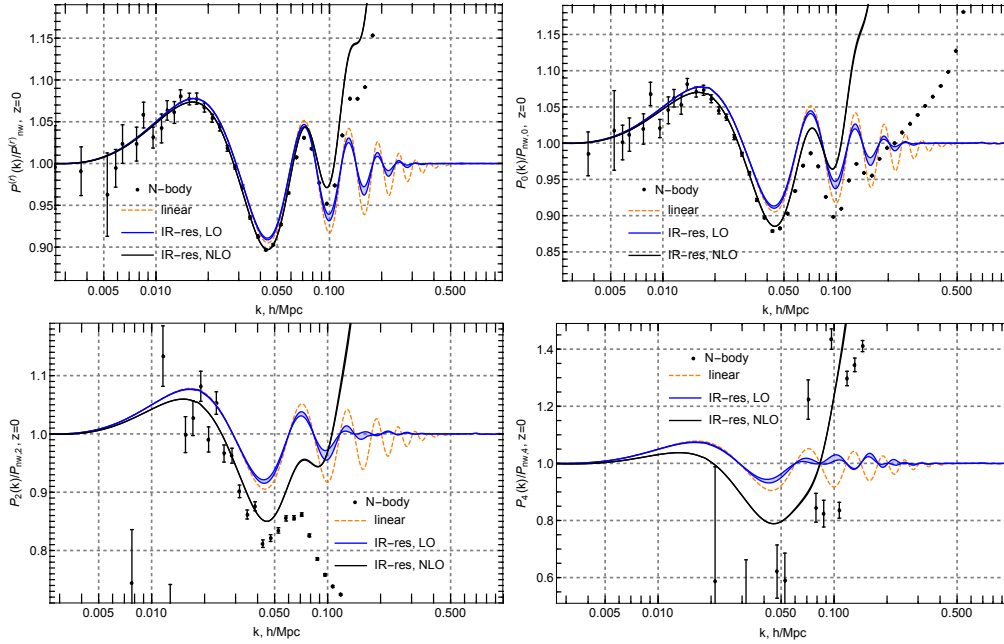


FIGURE 4.6: Matter power spectrum in real space (upper left panel) and power spectrum multipoles in redshift space: monopole (upper right panel), quadrupole (lower left panel), and hexadecapole (lower right panel), normalized to the corresponding linear non-wiggly power spectra. Bands show variation of the IR-resummed results when k_S changes between 0.05 and 0.2 h/Mpc . For NLO results the bands are barely visible. All results are shown for $z = 0$, $f = 0.483$.

lifts the correlation function at short scales. The NLO predictions have a very mild (sub-percent) dependence on the separation scale k_S which indicates the convergence of our resummation scheme.

Fig. 4.4 shows the result for the quadrupole, $\ell = 2$. In the left panel we plot the correlation function in linear theory and at the leading order of IR resummation for three choices of k_S . Since the quadrupole contribution is proportional to the derivatives of the real-space correlation function [122], instead of a single peak we observe an oscillating pattern at the BAO scales in linear theory. After IR resummation this pattern becomes almost invisible. This happens because the broadband part of the quadrupole has a significant amplitude at the BAO scale, which makes it difficult to distinguish a much smaller BAO contribution. We note that the dependence on the separation scale is quite mild both at leading (left panel) and next-to-leading order (right panel). We also observe the relative impact of the one-loop contribution becomes more sizable as compared to the monopole.

Fig. 4.5 shows the result for the hexadecapole, $\ell = 4$. Similarly to the previous case, we observe that the oscillating pattern corresponding to the BAO is strongly

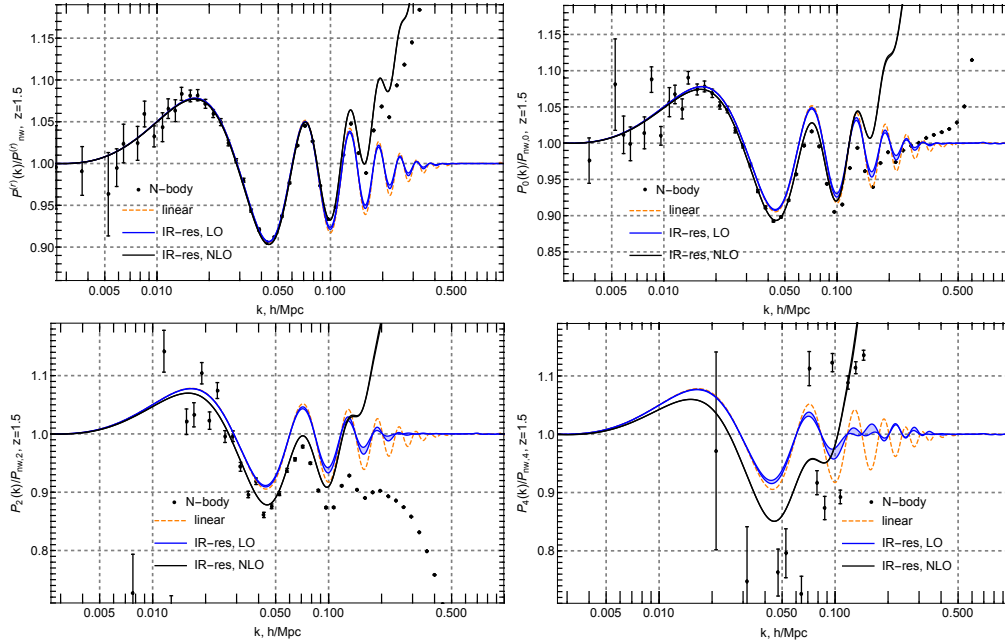


FIGURE 4.7: Matter power spectrum in real space (upper left panel) and power spectrum multipoles in redshift space: monopole (upper right panel), quadrupole (lower left panel), and hexadecapole (lower right panel), normalized to the corresponding linear non-wiggly power spectra. Bands show variation of the IR-resummed results when k_S changes between 0.05 and 0.2 h/Mpc . For NLO results the bands are barely visible. All results are shown for $z = 1.5$, $f = 0.916$.

suppressed after the IR resummation. The dependence on the separation scale is mild both at LO and NLO. We observe that the broadband part is significantly altered by the one-loop correction to the smooth power spectrum.

4.7.2 Matter power spectrum: comparison with N-body data

In this section we compare our predictions for the power spectrum and its multipoles at LO and NLO with the N-body simulations performed in [138]. The results of this section should be taken with a grain of salt as they do not take into account UV counterterms whose inclusion is necessary for a consistent description of the short-scale dynamics. The analysis including UV counterterms will be reported elsewhere.

Fig. 4.6 shows the results for the power spectrum in real space at $z = 0$ (upper left panel) and the power spectrum multipoles: monopole (upper right panel), quadrupole (lower left panel), and hexadecapole (lower right panel) divided by the corresponding linear non-wiggly power spectra. We show the predictions of linear theory (orange, dashed), leading order (blue) and next-to-leading order

(black) IR resummation models. For IR resummed power spectra we show bands corresponding to the theoretical uncertainty caused by variation of k_S in the range $(0.05 \div 0.2) h/\text{Mpc}$. Note that for the NLO spectra this band is barely visible. The error bars correspond to variance drawn from 160 realizations of volume $(2.4\text{Gpc}/h)^3$ each. They do not take into account systematic errors due to discreteness effects, which become big for higher-order power spectrum multipoles at large scales. In particular, we observe that the fluctuations in the measured hexadecapole power spectrum are very large even at mildly non-linear scales.

Qualitatively, we observe that the LO result does not improve much over linear theory as it misses the correct broadband information, while upon including the 1-loop corrections at NLO the agreement between the data and the theory improves. The monopole and quadrupole moments clearly exhibit the finger-of-God suppression at short scales. It reduces the range of agreement between the data and the theory as compared to real space and implies that UV counterterms should play a significant role in redshift space [65, 143].

In Fig. 4.7 we demonstrate the results for $z = 1.5$, which display an improvement in the agreement between the data and the theory over a wider range of scales in line with the suppression of non-linearities at large redshifts.

4.8 Summary and outlook

In this Chapter we embedded redshift space distortions and bias in time-sliced perturbation theory. We developed a manifestly IR-safe framework which allows us to perturbatively compute non-linear equal-time correlation functions of biased tracers in redshift space. The key observation is that the coordinate transformation from real to redshift space can be viewed as a fictitious 1D fluid flow, which maps real space correlation functions to the redshift space ones. Once this mapping is done, one can systematically resum the enhanced IR corrections affecting the BAO feature. The IR resummation of cosmological correlators proceeds in a straightforward manner along the lines of [3]. IR resummation in TSPT is based on physically motivated power counting rules and has a clear diagrammatic representation, which allows to compute the relevant corrections in a systematic and controllable way.

Our analysis gives a simple prescription for the numerical evaluation of the IR-resummed cosmological correlation functions. First, one has to isolate the oscillating part of the power spectrum as only this contribution is susceptible to non-linear damping due to bulk flows. IR resummation at leading order amounts to replacing the usual linear power spectrum by the “improved” one,

$$P(k) \rightarrow P_{nw}(k) + e^{-k^2 \Sigma_{\text{tot}}^2(\mu; k_S)} P_w(k), \quad (4.97)$$

where μ is the cosine of the angle between the wavevector \mathbf{k} and the line-of-sight, k_S is the separation scale defining the range of modes which are resummed, and the damping factor Σ_{tot}^2 is given in (3.71). Applying this prescription we obtained the explicit expressions for the IR-resummed power spectrum (4.80) and bispectrum (4.86) of biased tracers in redshift space.

At first order in hard loops IR resummation amounts to computing loop diagrams using the IR-resummed power spectrum (4.97) as an input. This must be accompanied by modification of the input power spectrum in the tree-level part to avoid double counting. The general formula for n -point IR-resummed redshift-space correlator reads,

$$\begin{aligned} \mathfrak{C}_n^{(s) \text{ IR res, LO+NLO}}(\mathbf{k}_1, \dots, \mathbf{k}_n) = & \mathfrak{C}_n^{(s) \text{ tree}} [P_{nw} + (1 + k^2 \Sigma_{\text{tot}}^2) e^{-k^2 \Sigma_{\text{tot}}^2} P_w](\mathbf{k}_1, \dots, \mathbf{k}_n) \\ & + \mathfrak{C}_n^{(s) \text{ 1-loop}} [P_{nw} + e^{-k^2 \Sigma_{\text{tot}}^2} P_w](\mathbf{k}_1, \dots, \mathbf{k}_n), \end{aligned} \quad (4.98)$$

where $\mathfrak{C}_n^{(s) \text{ tree}}$ and $\mathfrak{C}_n^{(s) \text{ 1-loop}}$ are the tree-level and 1-loop contributions understood as functionals of the input power spectrum. Equation (4.98) applies both to the density and velocity correlators, as well as to biased tracers. It also admits a straightforward generalization to higher orders in hard loops.

The angular dependence of the damping factor Σ_{tot}^2 in (4.98) reduces the symmetry of one-loop integrands and complicates the numerical evaluation. We have shown that for the one-loop power spectrum it is possible to rearrange our result in an equivalent form, Eq. (4.91), suitable for numerical implementation using standard algorithms. We also derived a simplified expression for the redshift-space 1-loop bispectrum, see Eq. (4.93).

The separation scale k_S is *a priori* arbitrary and any dependence on it should be considered as part of the theoretical uncertainty. We show that the scatter of our results w.r.t variations of this scale in the reasonable range $(0.05 \div 0.2) h/\text{Mpc}$ is not negligible at LO, but substantially reduces when including NLO corrections. This testifies the convergence of our resummation procedure.

We compared our results with available N-body data on the power spectrum of matter in redshift space and found that IR resummation at NLO significantly improves the range of agreement between theory and data compared to linear theory and LO IR resummation. The results of our comparison are preliminary at the moment as we have not included into calculation the UV-counterterms. Taking into account these counterterms is expected to further improve the agreement. We leave this task for future study.

Our results suggest several directions for future research. On one hand, one can accurately assess the shift of the BAO peak in redshift space and for biased tracers. Although the expression (4.91) already contains some contributions into the shift, its precise value must be validated by computing full NLO soft corrections. On the other hand, our results may be useful for elucidating systematic uncertainties of the reconstruction algorithms, see Ref. [57] for a recent work in this direction. Finally, our theoretical template may be used for analyzing the data from full-shape measurements of galaxy clustering without reconstruction. Note that in that case proper UV counterterms must be added to our expressions (4.80) and (4.86).

Part II

Non-perturbative probability distribution function of spherically-averaged matter density field

Chapter 5

Path integral derivation from first principles

5.1 Path integral for counts-in-cells PDF

In this chapter we introduce a general formalism to describe the counts in cells statistics, compute the 1-point PDF and discuss its main ingredients.

5.1.1 Spherical collapse saddle point

Consider the density contrast averaged over a spherical cell of radius r_* ,

$$\bar{\delta}_W = \int \frac{d^3x}{r_*^3} \tilde{W}(r/r_*) \delta(\mathbf{x}) = \int_{\mathbf{k}} W(kr_*) \delta(\mathbf{k}), \quad (5.1)$$

where $\delta(\mathbf{x}) \equiv \frac{\delta\rho(\mathbf{x})}{\rho_{\text{univ}}}$, $\tilde{W}(r/r_*)$ is a window function, $W(kr_*)$ is its Fourier transform, and we have introduced the notation $\int_{\mathbf{k}} \equiv \int \frac{d^3k}{(2\pi)^3}$. We will soon specify the window function to be top-hat in the position space, which is the standard choice for counts-in-cells statistics. However, it is instructive to see how far one can proceed without making any specific assumptions about \tilde{W} , apart from it being spherically symmetric. The window function is normalized as

$$\int \frac{d^3x}{r_*^3} \tilde{W}(r/r_*) = 1. \quad (5.2)$$

We are interested in the 1-point PDF $\mathcal{P}(\delta_*)$ describing the probability that the random variable $\bar{\delta}_W$ takes a given value δ_* . Due to translational invariance, the

1-point statistics do not depend on the position of the cell. Thus, without loss of generality we center the cell at the origin, $\mathbf{x} = 0$.

We assume that the initial conditions for the density perturbations at some large redshift z_i are adiabatic and Gaussian, so that their statistical properties are fully determined by the 2-point cumulant,¹

$$\langle \delta_i(\mathbf{k})\delta_i(\mathbf{k}') \rangle = (2\pi)^3 \delta_D^{(3)}(\mathbf{k} + \mathbf{k}') g^2(z_i) P(k), \quad (5.3)$$

where $\delta_D^{(3)}$ is the 3-dimensional Dirac delta-function. Here $P(k)$ is the *linear* power spectrum at redshift zero and $g(z)$ is the linear growth factor². The latter is normalized to be 1 at $z = 0$. Nevertheless, it is convenient to keep g^2 explicitly in the formulas and treat it as a small free parameter. The rationale behind this approach is to use g^2 as a book-keeping parameter that characterizes the overall amplitude of the power spectrum and thereby controls the saddle-point evaluation of the PDF, just like a coupling constant controls the semiclassical expansion in QFT (cf. [1]). The true physical expansion parameter in our case is the smoothed density variance at the scale r_* , as will become clear shortly.

Instead of working directly with the initial density field δ_i , it is customary to rescale it to redshift z using the linear growth factor,

$$\delta_L(\mathbf{k}, z) = \frac{g(z)}{g(z_i)} \delta_i(\mathbf{k}). \quad (5.4)$$

We will refer to δ_L as the ‘linear density field’ in what follows and will omit the explicit z -dependence to simplify notations.

The desired PDF is given by the following path integral [85, 97],

$$\mathcal{P}(\delta_*) = \mathcal{N}^{-1} \int \mathcal{D}\delta_L \exp \left\{ - \int_{\mathbf{k}} \frac{|\delta_L(\mathbf{k})|^2}{2g^2 P(k)} \right\} \delta_D^{(1)}(\delta_* - \bar{\delta}_W[\delta_L]), \quad (5.5)$$

where different linear density perturbations are weighted with the appropriate Gaussian weight. The Dirac delta-function ensures that only the configurations that produce the average density contrast δ_* are retained in the integration. Note that we have written $\bar{\delta}_W$ as a functional of the linear density field, $\bar{\delta}_W[\delta_L]$. In general, this functional is complicated and its evaluation requires knowing non-linear dynamics that map initial linear perturbations onto the final non-linear

¹From now on we will use $P(k)$ to denote the linear matter power spectrum at redshift zero. There will be no other power spectra discussed.

²The growth factor is commonly denoted by $D(z)$ in the LSS literature. We prefer the notation $g(z)$ to emphasize the analogy with a coupling constant in QFT.

density field $\delta(\mathbf{x})$. The normalization factor in (5.5) is

$$\mathcal{N} = \int \mathcal{D}\delta_L \exp \left\{ - \int_{\mathbf{k}} \frac{|\delta_L(\mathbf{k})|^2}{2g^2 P(k)} \right\}. \quad (5.6)$$

It is convenient to rewrite the delta-function constraint using the inverse Laplace transform,

$$\mathcal{P}(\delta_*) = \mathcal{N}^{-1} \int_{-i\infty}^{i\infty} \frac{d\lambda}{2\pi i g^2} \int \mathcal{D}\delta_L \exp \left\{ - \frac{1}{g^2} \left[\int_{\mathbf{k}} \frac{|\delta_L(\mathbf{k})|^2}{2P(k)} - \lambda(\delta_* - \bar{\delta}_W[\delta_L]) \right] \right\}, \quad (5.7)$$

where we introduced the Lagrange multiplier λ . Our goal is to compute the above integral by the steepest-descent method. We expect the result to take the form,

$$\mathcal{P}(\delta_*) = \exp \left\{ - \frac{1}{g^2} (\alpha_0 + \alpha_1 g^2 + \alpha_2 g^4 + \dots) \right\}. \quad (5.8)$$

The leading term α_0 corresponds to the exponent of the integrand in (5.7) evaluated on the saddle-point configuration. The first correction $\alpha_1 g^2$ stems from the Gaussian integral around the saddle point. It gives rise to a g -independent prefactor³ in the PDF. As we discuss below, the evaluation of α_1 corresponds to a one-loop calculation in the saddle-point background. Higher loops give further corrections $\alpha_2 g^4$ etc., which can be rewritten as $O(g^2)$ corrections to the prefactor. We will not consider them in this dissertation.

We are looking for a saddle point of the integral (5.7) in the limit $g^2 \rightarrow 0$. Taking variations of the expression in the exponent w.r.t. δ_L and λ , we obtain the equations for the saddle-point configuration⁴,

$$\frac{\delta_L(\mathbf{k})}{P(k)} + \lambda \frac{\partial \bar{\delta}_W}{\partial \delta_L(\mathbf{k})} = 0, \quad (5.9a)$$

$$\bar{\delta}_W[\delta_L] = \delta_*. \quad (5.9b)$$

Now comes a crucial observation: a spherically symmetric Ansatz for $\delta_L(\mathbf{k})$ goes through these equations. Let us prove this. The check is non-trivial only for Eq. (5.9a). Clearly, if the linear field is spherically symmetric, the first term in (5.9a) depends only on the absolute value k of the momentum. We need to show that this is also the case for the second term. To this end, expand the variational derivative,

$$\frac{\partial \bar{\delta}_W}{\partial \delta_L(\mathbf{k})} = \int \frac{d^3 x}{r_*^3} \tilde{W}(r/r_*) \frac{\partial \delta(\mathbf{x})}{\partial \delta_L(\mathbf{k})}. \quad (5.10)$$

³In fact, we will see that α_1 also has a term $\sim \ln g$ which introduces an overall factor $1/g$ in the PDF.

⁴We write the variational derivatives w.r.t. the linear density field as an ordinary partial derivative $\partial/\partial \delta_L(\mathbf{k})$ to avoid proliferation of deltas.

Due to rotational invariance of dynamics, the derivative $\partial\delta(\mathbf{x})/\partial\delta_L(\mathbf{k})$, evaluated on a spherically symmetric linear density configuration, is a rotationally invariant function of the vectors \mathbf{x} and \mathbf{k} . Thus, it depends only on the lengths x , k and the scalar product $(\mathbf{k}\mathbf{x})$. Upon integration with a spherically symmetric window function \tilde{W} , only the dependence on the absolute value of the momentum k survives. This completes the proof.

The previous observation greatly simplifies the solution of the saddle-point equations (5.9). It implies that we can search for the saddle point among spherically symmetric configurations. For such configurations there exists a simple mapping between the linear and non-linear density fields prior to shell-crossing, see Appendix G. This mapping relates the non-linear density contrast averaged over a cell of radius r ,

$$\bar{\delta}(r) \equiv \frac{3}{r^3} \int_0^r dr_1 r_1^2 \delta(r_1) , \quad (5.11)$$

with the linear averaged density

$$\bar{\delta}_L(R) \equiv \frac{3}{R^3} \int_0^R dR_1 R_1^2 \delta_L(R_1) \quad (5.12)$$

at the radius

$$R = r(1 + \bar{\delta}(r))^{1/3} . \quad (5.13)$$

In the last expression one recognizes the Lagrangian radius of the matter shell whose Eulerian radius is r . The mapping then gives $\bar{\delta}_L(R)$ as a function of $\bar{\delta}(r)$ and vice versa,

$$\bar{\delta}_L(R) = F(\bar{\delta}(r)) \quad \iff \quad \bar{\delta}(r) = f(\bar{\delta}_L(R)) . \quad (5.14)$$

Evaluation of the functions F or f requires an inversion of an elementary analytic function (in EdS cosmology) or solution of a first-order ordinary differential equation (in Λ CDM). Both operations are easily performed using standard computer packages. Curiously, the mapping (5.14) is almost independent of cosmology (EdS vs. Λ CDM)⁵.

The existence of the mapping (5.14) allows us to compute the variational derivative in Eq. (5.9a) explicitly for spherically symmetric⁶ $\delta_L(k)$. Assuming that the non-linear density field $\delta(r)$ has not undergone shell-crossing, we transform the

⁵At sub-percent level, see Fig. 5.1 and the discussion in the next subsection.

⁶To avoid confusion, let us stress that we do not intend to restrict the path integral (5.7) to spherical configurations. This restriction is used only to find the saddle point.

expression for $\bar{\delta}_W$ as follows,

$$\begin{aligned}\bar{\delta}_W &= \frac{4\pi}{r_*^3} \int dr r^2 \tilde{W}(r/r_*) (1 + \delta(r)) - 1 \\ &= \frac{4\pi}{r_*^3} \int dR R^2 \tilde{W} \left(R(1 + f(\bar{\delta}_L(R)))^{-1/3}/r_* \right) - 1.\end{aligned}\quad (5.15)$$

Taking into account that

$$\bar{\delta}_L(R) = \int_{\mathbf{k}} \frac{3j_1(kR)}{kR} \delta_L(k), \quad (5.16)$$

where j_1 is the spherical Bessel function (see Appendix A for conventions), we obtain,

$$\frac{\partial \bar{\delta}_W}{\partial \delta_L(k)} = -\frac{4\pi}{r_*^4 k} \int dR R^2 \tilde{W}'(R(1+f)^{-1/3}/r_*) \frac{f'}{(1+f)^{4/3}} j_1(kR), \quad (5.17)$$

where primes denote differentiation of the functions w.r.t. their arguments. Here f and f' are functions of $\bar{\delta}_L(R)$ and hence functionals of $\delta_L(k)$. Substituting this expression into (5.9a) we obtain,

$$\delta_L(k) = \lambda P(k) \frac{4\pi}{r_*^4 k} \int dR R^2 \frac{\tilde{W}'(R(1+f)^{-1/3}/r_*) f' j_1(kR)}{(1+f)^{4/3}}. \quad (5.18)$$

This is a non-linear integral equation for $\delta_L(k)$ which can, in principle, be solved numerically. Together with Eq. (5.9b) that fixes the value of the Lagrange multiplier λ through the overall normalization of $\delta_L(k)$, they form a complete system of equations determining the saddle-point linear density. For a generic window function \tilde{W} the solution of this system appears challenging. We are now going to see that Eq. (5.18) gets drastically simplified for top-hat \tilde{W} .

5.1.2 Leading exponent for top-hat window function

From now on we specify to the case of a top-hat window function in position space,

$$\tilde{W}_{\text{th}}(r/r_*) = \frac{3}{4\pi} \Theta_{\text{H}} \left(1 - \frac{r}{r_*} \right) \iff W_{\text{th}}(kr_*) = \frac{3j_1(kr_*)}{kr_*}, \quad (5.19)$$

where Θ_{H} stands for the Heaviside theta-function. As the derivative of \tilde{W}_{th} is proportional to the Dirac delta-function, the integral in (5.18) localizes to $R = R_*$, where

$$R_* = r_*(1 + \delta_*)^{1/3}. \quad (5.20)$$

After a straightforward calculation Eq. (5.18) simplifies to

$$\delta_L(k) = -\frac{\lambda}{C} P(k) W_{\text{th}}(kR_*) \quad (5.21)$$

with

$$C = F'(\delta_*) + \frac{\bar{\delta}_L(R_*) - \delta_L(R_*)}{1 + \delta_*}. \quad (5.22)$$

Here F is the spherical-collapse mapping function introduced in (5.14) and in deriving (5.21), (5.22) we have used the relation,

$$F'(\delta_*) = \frac{1}{f'(\bar{\delta}_L(R_*))}.$$

One observes that (5.21) fixes the k -dependence of the saddle-point configuration. We now use Eq. (5.9b) where we act with the function F on both sides. This yields,

$$\bar{\delta}_L(R_*) = F(\delta_*). \quad (5.23)$$

Combining it with Eqs. (5.21), (5.16) gives an equation for the Lagrange multiplier,

$$\lambda = -\frac{F(\delta_*)}{\sigma_{R_*}^2} C, \quad (5.24)$$

where

$$\sigma_{R_*}^2 \equiv \int_{\mathbf{k}} P(k) |W_{\text{th}}(kR_*)|^2 \quad (5.25)$$

is the linear density variance filtered at the scale R_* . Note that it depends on δ_* through the corresponding dependence of R_* , see Eq. (5.20).

Substituting (5.24) back into (5.21) we arrive at the final expression for the saddle-point linear density, which will be denoted with an overhat,

$$\hat{\delta}_L(k) = \frac{F(\delta_*)}{\sigma_{R_*}^2} P(k) W_{\text{th}}(kR_*). \quad (5.26)$$

In Lagrangian position space the linear density reads,

$$\hat{\delta}_L(R) = \frac{F(\delta_*)}{\sigma_{R_*}^2} \hat{\xi}(R). \quad (5.27)$$

where we introduced the profile function

$$\hat{\xi}(R) \equiv \frac{1}{2\pi^2} \int dk k^2 \frac{\sin(kR)}{kR} W_{\text{th}}(kR_*) P(k). \quad (5.28)$$

Note that it coincides with the 2-point correlation function smeared with the top-hat filter. In what follows we will also need the saddle-point value of the

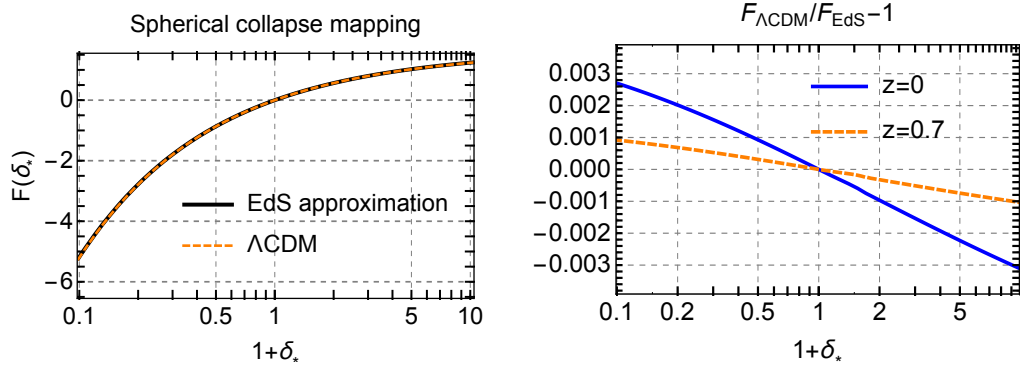


FIGURE 5.1: Left panel: the function F mapping spherically-averaged non-linear density contrast into its linear counterpart within the spherical collapse dynamics. The results are shown for an EdS universe and Λ CDM cosmology at $z = 0$. The two curves practically coincide. Right panel: the relative difference between $F_{\Lambda\text{CDM}}$ and F_{EdS} at two values of the redshift.

Lagrange multiplier. This is obtained by substituting (5.26) into (5.22), (5.24). The result is,

$$\hat{\lambda} = -\frac{F(\delta_*)}{\sigma_{R_*}^2} \hat{C}, \quad \hat{C}(\delta_*) = F'(\delta_*) + \frac{F(\delta_*)}{1 + \delta_*} \left(1 - \frac{\xi_{R_*}}{\sigma_{R_*}^2} \right), \quad (5.29)$$

where we have denoted $\xi_{R_*} \equiv \hat{\xi}(R_*)$. Finally, substituting the saddle-point configuration into the expression (5.7) for the PDF we obtain the leading exponential behavior,

$$\mathcal{P}(\delta_*) \propto \exp \left\{ -\frac{F^2(\delta_*)}{2g^2\sigma_{R_*}^2} \right\}. \quad (5.30)$$

We observe that the PDF exhibits a characteristic ‘semiclassical’ scaling in the limit $g^2 \rightarrow 0$.

Let us take a closer look at the various ingredients that define the saddle-point configuration. We start with the function $F(\delta_*)$. It is determined exclusively by the dynamics of spherical collapse and does not depend at all on the statistical properties of the perturbations. We have computed it using the procedure described in Appendix G for the cases of an EdS universe ($\Omega_m = 1, \Omega_\Lambda = 0$) and the reference Λ CDM cosmology ($\Omega_m = 0.26, \Omega_\Lambda = 0.74$). The results are shown in Fig. 5.1, left panel. The dependence on cosmology is very weak, so that the curves essentially overlay. In the EdS case the mapping is redshift-independent. Its behavior for small values of the argument is,

$$F_{\text{EdS}}(\delta_*) = \delta_* - \frac{17}{21}\delta_*^2 + \frac{2815}{3969}\delta_*^3 + \mathcal{O}(\delta_*^4), \quad (5.31a)$$

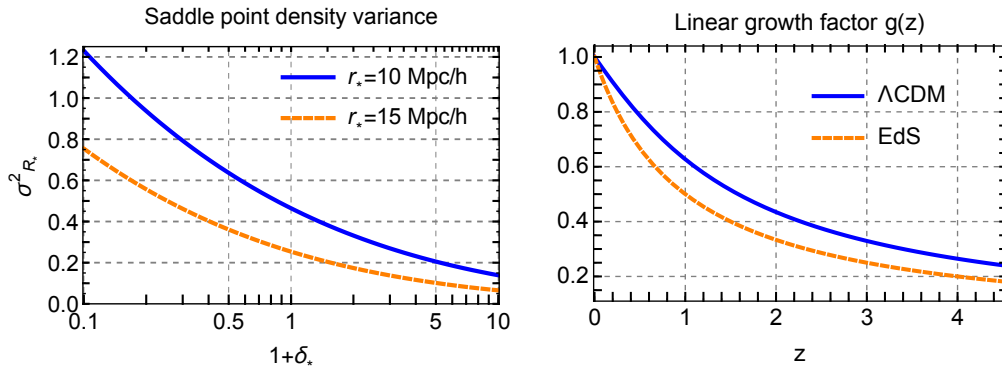


FIGURE 5.2: Left panel: the saddle point linear density variance as a function of the final density in the cell at $z = 0$ for comoving cell radii 10 Mpc/h and 15 Mpc/h. Right panel: the dependence of the linear growth factor on redshift in Λ CDM and EdS cosmologies. In the latter case, it is equal to $(1+z)^{-1}$.

whereas its asymptotics at large over/underdensities are

$$F_{\text{EdS}} \rightarrow 1.686 \quad \text{at } \delta_* \rightarrow \infty, \quad (5.31b)$$

$$F_{\text{EdS}} \sim -(1 + \delta_*)^{-3/2} \quad \text{at } \delta_* \rightarrow -1. \quad (5.31c)$$

For Λ CDM this function has a very mild redshift dependence illustrated in the right panel of Fig. 5.1, which shows the relative difference between $F_{\Lambda\text{CDM}}$ and F_{EdS} . This difference is maximal for $z = 0$, where it reaches a few per mil at the edges of the considered range of δ_* . However, F enters in the exponent of the PDF (see (5.30)) and a few per mil inaccuracy in it would generate a few percent relative error at the tails of the PDF. For these reasons we will use the exact Λ CDM mapping whenever the function F appears in the leading exponent. In all other instances the EdS approximation provides sufficient accuracy.

The second ingredient is the linear density variance at redshift zero $\sigma_{R_*}^2$. In contrast to F , it is determined only by the linear power spectrum and is independent of the non-linear dynamics. As already pointed out, it depends on the argument δ_* of the PDF through the Lagrangian radius R_* . This dependence is shown in the left panel of Fig. 5.2 for two different cell radii. By definition, $\sigma_{R_*}^2$ is independent of the redshift. The redshift dependence of the PDF comes through the linear growth factor g , shown as a function of z in the right panel of Fig. 5.2. From the way g^2 and $\sigma_{R_*}^2$ enter the leading exponent (5.30) it is clear that the physical expansion parameter controlling the validity of the saddle-point approximation is the z -dependent linear variance $g^2(z)\sigma_{R_*}^2$. One expects the semiclassical expansion to work as long as $g^2\sigma_{R_*}^2 \lesssim 1$. The numerical values of the linear density variance for $\delta_* = 0$ are given in Table 5.1.

	$r_* = 10 \text{ Mpc}/h$	$r_* = 15 \text{ Mpc}/h$
$z=0$	0.464	0.254
$z=0.7$	0.238	0.130
$z=4$	0.0325	0.0177

TABLE 5.1: The filtered density variance $g^2\sigma_{r_*}^2$ for various redshifts and cell radii.

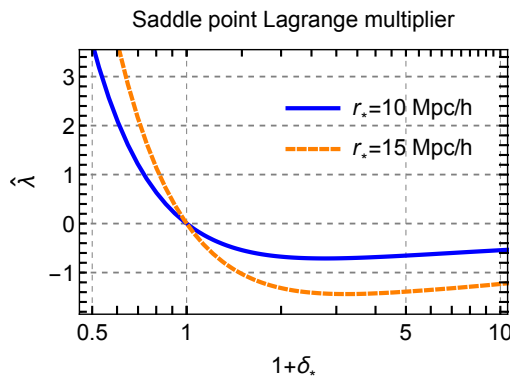


FIGURE 5.3: The saddle-point Lagrange multiplier, Eq. (5.29), as a function of δ_* . The computation is performed in the EdS approximation.

The Lagrange multiplier $\hat{\lambda}$ does not appear in the leading exponent of the PDF. However, we will see below that it enters the prefactor. So, it is instructive to plot its dependence on δ_* , see Fig. 5.3. Note that it is positive (negative) for under- (over-) densities. It quickly grows at $\delta_* < 0$.

For completeness, we also present in Fig. 5.4 the saddle-point linear density profiles for several values of δ_* . For $\delta_* \gtrsim 7$ the density profile in the central region exceeds the critical value⁷ 1.674, and therefore the innermost part of the profile experiences shell-crossing. Conservatively, one would expect a breakdown of our saddle-point expansion for such large overdensities. However, we will see shortly that the available data are consistent with the semiclassical scaling even for $\delta_* \gtrsim 7$. This robustness of the semiclassical approach may be explained by the fact that the averaged density at R_* is still less than the critical value even when the central regions undergo shell-crossing. Since the velocities of matter particles are rather low, it takes a significant amount of time for the information about shell-crossing to propagate to the boundary R_* . Until this happens, the dynamics of the boundary remain the same as if no shell-crossing occurred, so that the spherical collapse mapping used in the derivation of (5.30) still applies.

⁷ We give the critical value at $z = 0$ for our reference Λ CDM cosmology. It is somewhat lower than the well-known EdS value $\delta_c = 1.686$.

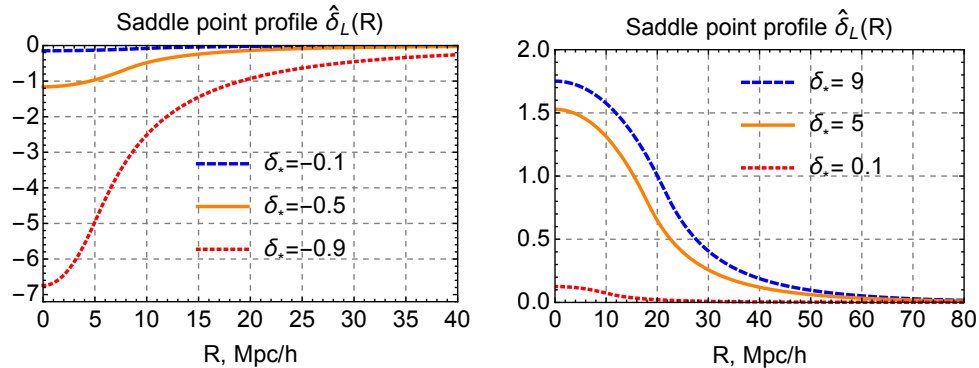


FIGURE 5.4: The saddle point linear density profiles in Lagrangian position space for several values of δ_* corresponding to underdensities (left panel) and overdensities (right panel). The results are shown for the cell radius $r_* = 10$ Mpc/h.

It should be stressed that having a spherical collapse saddle point does not mean that an exact spherical collapse happens inside each cell. Recall that in the case of tunneling in quantum mechanics the saddle-point solution, by itself, has measure zero in the space of all possible trajectories in the path integral, and thus is never realized precisely (see e.g. [146, 147]). What makes the tunneling amplitude finite are small perturbations around the saddle point solution that add up coherently and eventually contribute to the prefactor. From this argument it is clear that fluctuations around the saddle point are crucial for the consistency of our path integral calculation. If the saddle-point approximation works, the actual dynamics of the density field inside each cell is spherical collapse perturbed by aspherical fluctuations.

5.1.3 Prefactor from fluctuations

We now consider small fluctuations around the spherical collapse saddle point found in the previous subsection. To leading order in g^2 , the path integral over these fluctuations is Gaussian and produces the prefactor in front of the leading exponent (5.30), as was pointed out in Refs. [85, 148]. It is natural to expand the fluctuations of the linear density field in spherical harmonics. We write,

$$\delta_L(\mathbf{k}) = \hat{\delta}_L(k) + \delta_{L,0}^{(1)}(k) + \sum_{\ell>0} \sum_{m=-\ell}^{\ell} (-i)^\ell \delta_{L,\ell m}^{(1)}(k) Y_{\ell m}(\mathbf{k}/k), \quad (5.32a)$$

$$\lambda = \hat{\lambda} + \lambda^{(1)}, \quad (5.32b)$$

where we have singled out the monopole fluctuation $\delta_{L,0}^{(1)}$. Note that due to our convention for the spherical harmonics (see Appendix A), the reality condition

$(\delta_L(\mathbf{k}))^* = \delta_L(-\mathbf{k})$ translates into the conditions

$$(\delta_{L,0}^{(1)}(k))^* = \delta_{L,0}^{(1)}(k), \quad (\delta_{L,\ell m}^{(1)}(k))^* = \delta_{L,\ell,-m}^{(1)}(k). \quad (5.33)$$

Fluctuations give rise to a perturbation of the averaged density contrast which up to second order can be written as,

$$\begin{aligned} \bar{\delta}_W = & \delta_* + \int [dk] 4\pi S(k) \delta_{L,0}^{(1)}(k) + \int [dk]^2 4\pi Q_0(k_1, k_2) \delta_{L,0}^{(1)}(k_1) \delta_{L,0}^{(1)}(k_2) \\ & + \sum_{\ell>0, m} \int [dk]^2 Q_\ell(k_1, k_2) \delta_{L,\ell m}^{(1)}(k_1) \delta_{L,\ell,-m}^{(1)}(k_2), \end{aligned} \quad (5.34)$$

where we introduced the notation,

$$[dk]^n \equiv \prod_{i=1}^n \frac{k_i^2 dk_i}{(2\pi)^3}, \quad (5.35)$$

and S , Q_0 , Q_ℓ are some kernels. Below we will refer to Q_0 , Q_ℓ as *response matrices*. Note the factor 4π that we included in the definition of S and Q_0 ; it reflects the difference in our normalization of spherical harmonics in the monopole and higher multipole sectors, see Eq. (A.10). In the expression (5.34) we have used the fact that non-monopole fluctuations can contribute only at quadratic order due to spherical symmetry. For the same reason, the kernels Q_ℓ do not depend on the azimuthal number m .

Substituting (5.32a) and (5.34) into the path integral (5.7), after a straightforward calculation, we find that the Gaussian integrals over fluctuations with different multipole numbers ℓ factorize. This leads to the following representation for the PDF,

$$\mathcal{P}(\delta_*) = \mathcal{A}_0 \cdot \prod_{\ell>0} \mathcal{A}_\ell(\delta_*) \cdot \exp \left\{ -\frac{F^2(\delta_*)}{2g^2 \sigma_{R_*}^2} \right\}, \quad (5.36)$$

where

$$\begin{aligned} \mathcal{A}_0 = & \mathcal{N}_0^{-1} \int_{-i\infty}^{i\infty} \frac{d\lambda^{(1)}}{2\pi i g^2} \int \mathcal{D}\delta_{L,0}^{(1)} \exp \left\{ -\frac{4\pi}{g^2} \left[\int \frac{[dk]}{2P(k)} (\delta_{L,0}^{(1)}(k))^2 \right. \right. \\ & \left. \left. + \lambda^{(1)} \int [dk] S(k) \delta_{L,0}^{(1)}(k) + \hat{\lambda} \int [dk]^2 Q_0(k_1, k_2) \delta_{L,0}^{(1)}(k_1) \delta_{L,0}^{(1)}(k_2) \right] \right\}, \end{aligned} \quad (5.37)$$

$$\begin{aligned} \mathcal{A}_\ell = & \mathcal{N}_\ell^{-1} \int [\mathcal{D}\delta_{L,\ell m}^{(1)}] \exp \left\{ -\frac{1}{g^2} \sum_m \left[\int \frac{[dk]}{2P(k)} \delta_{L,\ell m}^{(1)}(k) \delta_{L,\ell,-m}^{(1)}(k) \right. \right. \\ & \left. \left. + \hat{\lambda} \int [dk]^2 Q_\ell(k_1, k_2) \delta_{L,\ell m}^{(1)}(k_1) \delta_{L,\ell,-m}^{(1)}(k_2) \right] \right\}. \end{aligned} \quad (5.38)$$

The integration measure in the last expression is $[\mathcal{D}\delta_{L,lm}^{(1)}] = \prod_{m=-l}^l \mathcal{D}\delta_{L,lm}^{(1)}$, whereas the normalization factors are,

$$\mathcal{N}_0 = \int \mathcal{D}\delta_{L,0} \exp \left\{ -\frac{4\pi}{g^2} \int \frac{[dk]}{2P(k)} (\delta_{L,0}(k))^2 \right\}, \quad (5.39)$$

$$\mathcal{N}_\ell = \int [\mathcal{D}\delta_{L,lm}] \exp \left\{ -\frac{1}{g^2} \sum_m \int \frac{[dk]}{2P(k)} \delta_{L,\ell m}(k) \delta_{L,\ell,-m}(k) \right\}. \quad (5.40)$$

Despite appearing more complicated, the monopole prefactor \mathcal{A}_0 can be evaluated analytically. This is not surprising, since the dynamics in the monopole sector is known exactly. We postpone this analysis to the next section and focus here on the prefactor stemming from higher multipoles.

The quadratic form in the exponent of Eq. (5.38) is a convolution of the vector $\delta_{L,\ell m}^{(1)}$ with the matrix

$$\frac{1}{g^2} \left(\mathbb{1} \cdot \frac{1}{P(k)} + 2\hat{\lambda}Q_\ell \right) \delta_{m,-m},$$

where $\mathbb{1}$ is the unit operator in k -space whose kernel with respect to the measure (5.35) is,

$$\mathbb{1}(k, k') = (2\pi)^3 k^{-2} \delta_{\mathbb{D}}^{(1)}(k - k'), \quad (5.41)$$

and $\delta_{m,-m}$ is the Kronecker symbol. The Gaussian integral over $\delta_{L,\ell m}^{(1)}$ is inversely proportional to the square root of the determinant of this matrix. To get \mathcal{A}_ℓ , this determinant must be divided by the determinant of the corresponding matrix in the normalization factor (5.40) which is simply

$$\frac{1}{g^2} \left(\mathbb{1} \cdot \frac{1}{P(k)} \right) \delta_{m,-m}.$$

In this way we obtain

$$\mathcal{A}_\ell = \mathcal{D}_\ell^{-(\ell+1/2)}, \quad (5.42)$$

where

$$\mathcal{D}_\ell = \det \left(\mathbb{1} + 2\hat{\lambda}\sqrt{P}Q_\ell\sqrt{P} \right), \quad (5.43)$$

is the ℓ th *aspherical fluctuation determinant*. The second term in \mathcal{D}_ℓ denotes an operator with the kernel $\sqrt{P(k)}Q_\ell(k, k')\sqrt{P(k')}$. It is convenient to introduce the *aspherical prefactor* that aggregates contributions of all multipoles with strictly positive ℓ ,

$$\mathcal{A}_{\text{ASP}} \equiv \prod_{\ell>0} \mathcal{A}_\ell = \prod_{\ell>0} \mathcal{D}_\ell^{-(\ell+1/2)}. \quad (5.44)$$

We see that its computation requires knowledge of the aspherical response matrices Q_ℓ .

Let us make an important remark. The growth factor g has dropped out of the expression for the fluctuation determinants (5.43). Also, it can be shown that the response matrices Q_ℓ do not depend on the redshift⁸ (see Sec. 6.2). This implies that the aspherical prefactor is redshift-independent. We are going to see in the next section that this theoretical expectation is confirmed by the N-body data.

The redshift-independence of \mathcal{A}_{ASP} may be somewhat puzzling. Indeed, being a non-trivial function of δ_* , the aspherical prefactor affects the shape of PDF even at early times, when the distribution must be Gaussian. To resolve this apparent paradox, we notice that at high redshifts (in the limit $g^2 \rightarrow 0$) the distribution (5.36) approaches the delta-function centered at $\delta_* = 0$. On the other hand, recall that $\hat{\lambda}$ vanishes at δ_* (see Fig. 5.3) and hence $\mathcal{D}_\ell(\delta_* = 0) = 1$ for all ℓ . This implies $\mathcal{A}_{\text{ASP}}(\delta_* = 0) = 1$ and in the limit $g^2 \rightarrow 0$ the whole aspherical prefactor reduces to unity. One concludes that the role of the aspherical prefactor decreases as the distribution becomes sharper towards high redshifts.

5.2 Closer look at the prefactor

In this section we explicitly compute the monopole prefactor \mathcal{A}_0 from the spherical collapse dynamics. We then use N-body data to extract the aspherical prefactor \mathcal{A}_{ASP} and discuss its main properties.

5.2.1 Monopole

The factorization property (5.36) implies that in the computation of the monopole prefactor all aspherical perturbations can be set to zero. Thereby it is convenient to consider the path integral over the spherically symmetric sector as a whole, without splitting the density field into the saddle-point configuration and fluctuations. In this way we arrive at what can be called ‘spherical PDF’,

$$\mathcal{P}_{\text{SP}}(\delta_*) = \mathcal{N}_0^{-1} \int \mathcal{D}\delta_{L,0} \exp \left\{ -\frac{4\pi}{g^2} \int \frac{[dk]}{2P(k)} (\delta_{L,0}(k))^2 \right\} \delta_D^{(1)}(\delta_* - \bar{\delta}_W[\delta_{L,0}]), \quad (5.45)$$

⁸Strictly speaking, this statement is true only in the EdS universe. However, the response matrices computed in the exact Λ CDM cosmology coincide with the EdS approximation better than at a per cent level. Another source of a weak z -dependence is a UV counterterm in the prefactor, required to renormalize the short-distance contributions, see Sec. 6.5.2.

with the normalization factor given in Eq. (5.39). We stress that \mathcal{P}_{SP} is *not* equal to the true PDF, as it restricts the original path integral (5.5) to spherically symmetric configurations only, and thus misses the contribution of aspherical modes.

Due to the existence of the spherical collapse mapping (5.14), the condition $\delta_* = \bar{\delta}_W[\delta_{L,0}]$ is equivalent to the condition $F(\delta_*) = \bar{\delta}_{L,0}(R_*)$. Thus, the delta-function in (5.45) is proportional to the delta-function of the argument $F(\delta_*) - \bar{\delta}_{L,0}(R_*)$,

$$\delta_D^{(1)}(\delta_* - \bar{\delta}_W[\delta_{L,0}]) = C[\delta_{L,0}] \cdot \delta_D^{(1)}(F(\delta_*) - \bar{\delta}_{L,0}(R_*)). \quad (5.46)$$

The proportionality coefficient C is given in Eq. (5.22); it is fixed by the requirement that the integral of both sides of (5.46) over δ_* produces unity. Substituting this relation into Eq. (5.45) and using the integral representation for the delta-function we obtain,

$$\begin{aligned} \mathcal{P}_{\text{SP}}(\delta_*) = & \mathcal{N}_0^{-1} \int_{-i\infty}^{i\infty} \frac{d\lambda}{2\pi i g^2} e^{\lambda F/g^2} \int \mathcal{D}\delta_{L,0} C[\delta_{L,0}] \\ & \times \exp \left\{ -\frac{4\pi}{g^2} \left[\int \frac{[dk]}{2P(k)} (\delta_{L,0}(k))^2 + \lambda \int [dk] W_{\text{th}}(kR_*) \delta_{L,0}(k) \right] \right\}. \end{aligned} \quad (5.47)$$

It is now straightforward to evaluate this integral by the saddle point method, which yields⁹,

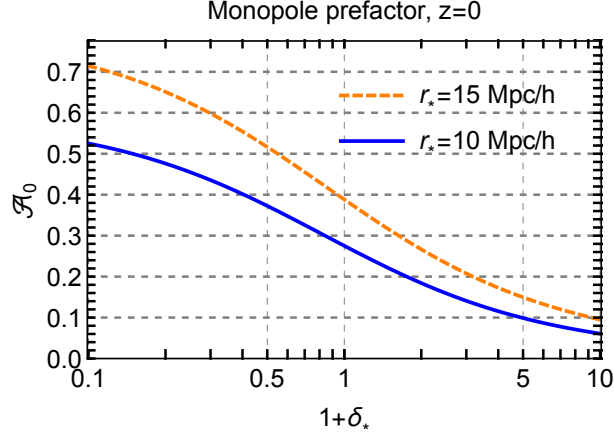
$$\mathcal{P}_{\text{SP}}(\delta_*) = \frac{\hat{C}(\delta_*)}{\sqrt{2\pi g^2 \sigma_{R_*}^2}} \exp \left(-\frac{F^2(\delta_*)}{2g^2 \sigma_{R_*}^2} \right), \quad (5.48)$$

where \hat{C} is defined in (5.29). From this expression we infer the monopole prefactor,

$$\mathcal{A}_0(\delta_*) = \frac{\hat{C}(\delta_*)}{\sqrt{2\pi g^2 \sigma_{R_*}^2}}. \quad (5.49)$$

We plot its dependence on the density contrast in Fig. 5.5. It varies roughly by an order of magnitude in the range $\delta_* = [-0.9, 9]$. Since it is inversely proportional to the r.m.s density contrast $g\sigma_{R_*}$, it significantly varies with the window function radius and redshift. For illustration purposes we show the results for $z = 0$. The curves for other redshifts are qualitatively similar and can be obtained upon rescaling by an appropriate growth factor (shown in the right panel of Fig. 5.2).

⁹This result is actually exact as $C[\delta_{L,0}]$ is a linear functional of $\delta_{L,0}$, and for this type of integrals there are no corrections to the saddle-point approximation.


 FIGURE 5.5: The monopole prefactor at $z = 0$.

By construction, the spherical PDF (5.45) is normalized to unity,

$$\int_{-1}^{\infty} d\delta_* \mathcal{P}_{\text{SP}}(\delta_*) = 1. \quad (5.50)$$

However, it does not reproduce the correct zero mean value of the density contrast,

$$\langle \delta_* \rangle_{\text{SP}} \equiv \int_{-1}^{\infty} d\delta_* \mathcal{P}_{\text{SP}}(\delta_*) \delta_* \neq 0. \quad (5.51)$$

To see this, we define the variable $\nu = F/\sigma_{R_*}$ and rewrite (5.48) as

$$\mathcal{P}_{\text{SP}} = \frac{1}{\sqrt{2\pi g^2}} \frac{d\nu}{d\delta_*} e^{-\frac{\nu^2}{2g^2}}. \quad (5.52)$$

The expectation value (5.51) becomes,

$$\langle \delta_* \rangle_{\text{SP}} = \int_{-\infty}^{\infty} \frac{d\nu}{\sqrt{2\pi g^2}} \delta_*(\nu) e^{-\frac{\nu^2}{2g^2}} = \frac{g^2}{2} \frac{d^2 \delta_*}{d\nu^2} \Big|_{\nu=0}, \quad (5.53)$$

where we have evaluated the integral at leading order in g^2 . It is straightforward to compute the second derivative appearing in the above equation. One finds,

$$\frac{d^2 \delta_*}{d\nu^2} \Big|_{\nu=0} = -\sigma_{r_*}^2 \left[F''(0) + 2 \left(1 - \frac{\xi_{r_*}}{\sigma_{r_*}^2} \right) \right]. \quad (5.54)$$

Using also the Taylor expansion (5.31a) for the function F one obtains,

$$\langle \delta_* \rangle_{\text{SP}} = -g^2 \sigma_{r_*}^2 a_1, \quad \text{where } a_1 = \frac{4}{21} - \frac{\xi_{r_*}}{\sigma_{r_*}^2}. \quad (5.55)$$

The numerical values of a_1 for different cell radii are given in Table 5.2 in the next subsection.

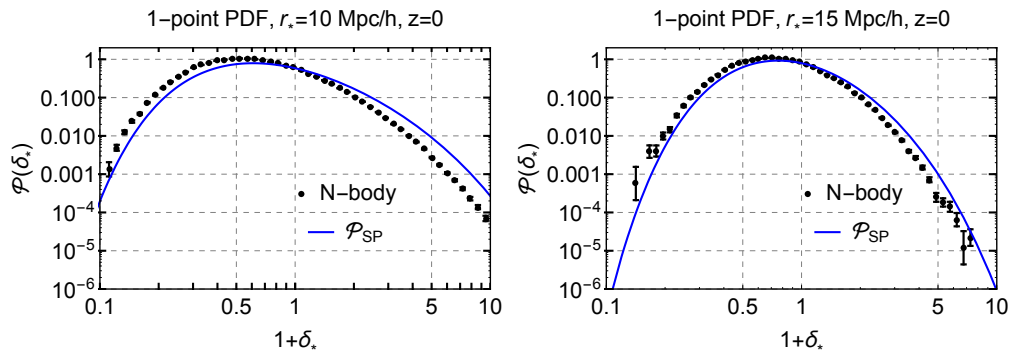


FIGURE 5.6: 1-point PDF of the smoothed density field at redshift $z = 0$ for $r_* = 10 \text{ Mpc}/h$ (left panel) and $r_* = 15 \text{ Mpc}/h$ (right panel): the spherical PDF given by Eq. (5.48) (blue line) against the N-body data (black dots). Error-bars on the data points show the statistical uncertainty.

At a first glance, the fact that the spherical PDF fails to reproduce the zero mean value of δ_* may seem surprising. However, it becomes less so once we realize that vanishing of $\langle \delta_* \rangle$ is related to translational invariance. Indeed, it is implied by the vanishing of $\langle \delta(\mathbf{x}) \rangle$, the mean density contrast at each space point. The latter, in turn, involves two ingredients: (i) the constraint $\int d^3x \delta(\mathbf{x}) = 0$ which follows trivially from the definition of the density contrast, and (ii) the fact that, due to translational invariance, $\langle \delta(\mathbf{x}) \rangle$ is the same at all points. But the translational invariance has been explicitly broken by the reduction of the path integral to the spherically symmetric sector that singles out the origin as a preferred point in space. The correct identity $\langle \delta_* \rangle = 0$ will be restored once we take into account the aspherical prefactor generated by fluctuations beyond the monopole sector.

5.2.2 Aspherical prefactor from N-body data

Before delving into the calculation of the aspherical prefactor, let us verify the semiclassical factorization formula (5.36) against the N-body data. To this end, we have run a suite of N-body simulations using the `FastPM` code [100] and obtained the counts-in-cells statistics for a total of 518400 cells with radius $r_* = 10 \text{ Mpc}/h$ and 153600 cells with $r_* = 15 \text{ Mpc}/h$. The details of our simulations are presented in Appendix B of Ref. [9]. Figure 5.6 shows the data points together with the spherical PDF \mathcal{P}_{SP} . The results are shown for redshift $z = 0$. The PDFs for other redshifts are qualitatively similar and will be discussed shortly. From Fig. 5.6 we see that although the spherical PDF correctly captures the exponential falloff of the data points at large over-/under-densities, it is clearly off-set from the data even at $\delta_* = 0$. According to (5.36), this off-set should be

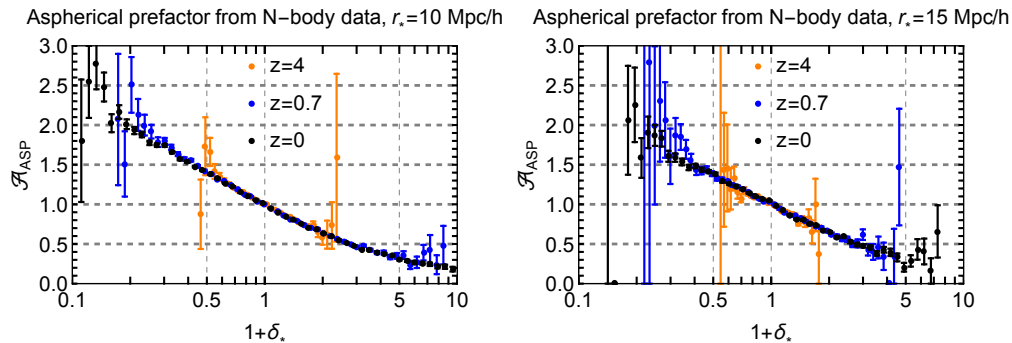


FIGURE 5.7: The aspherical prefactor $\mathcal{A}_{\text{ASP}} = \mathcal{P}_{\text{data}}/\mathcal{P}_{\text{SP}}$ extracted from the simulations. The results are shown for the cell radii 10 Mpc/h (left panel) and 15 Mpc/h (right panel).

compensated by the aspherical prefactor \mathcal{A}_{ASP} . Using the full PDF $\mathcal{P}_{\text{data}}(\delta_*)$ measured from the data, we can extract the aspherical prefactor as

$$\mathcal{A}_{\text{ASP}}(\delta_*) = \frac{\mathcal{P}_{\text{data}}(\delta_*)}{\mathcal{P}_{\text{SP}}(\delta_*)}. \quad (5.56)$$

The result is shown in Fig. 5.7 for various redshifts and cell radii. At higher redshifts the distribution becomes sharper, which increases the measurement errors away from the origin. This is especially visible in the case $z = 4$ where the available δ_* -range in the data significantly shrinks compared to $z = 0$. The errorbars shown in the plots represent the statistical uncertainty of our data. It is worth noting that the bins at the tails of the distribution are expected to contain also a systematic error comparable to the statistical one, see the discussion in Appendix B of [9].

The spherical PDF has an exponential sensitivity to the density variance, which changes by an order of magnitude across the considered redshifts, see Tab. 5.1. Similarly, the measured PDF's at different redshifts and cell radii are exponentially different. Nevertheless, we observe that the results of their division by the spherical PDF's depend very weakly on the redshift and the size of the window function. This is a strong confirmation of the validity of the semiclassical scaling (5.36). In particular, we conclude that the spherical collapse saddle point indeed dominates the probability: if it were not the case, one would expect exponentially large difference between $\mathcal{P}_{\text{data}}$ and \mathcal{P}_{SP} . Moreover, the data are clearly consistent with the redshift-independence of \mathcal{A}_{ASP} , as predicted by the theory (see Sec. 5.1.3). Note that the aspherical prefactor is a very smooth function that varies only by an order of magnitude within the density range where the whole PDF varies by six-seven orders of magnitude.

In complete agreement with the theoretical expectation (recall the discussion at the end of Sec. 5.1.3), we see that $\mathcal{A}_{\text{ASP}}|_{\delta_*=0} = 1$. Note that this ensures the correct normalization of the full PDF $\mathcal{P} = \mathcal{A}_{\text{ASP}}\mathcal{P}_{\text{SP}}$ in the leading semiclassical approximation. Indeed, in this approximation the PDF is concentrated around $\delta_* = 0$ and we have,

$$\int d\delta_* \mathcal{A}_{\text{ASP}}(\delta_*)\mathcal{P}_{\text{SP}}(\delta_*) = \mathcal{A}_{\text{ASP}}|_{\delta_*=0} \int d\delta_* \mathcal{P}_{\text{SP}}(\delta_*) = \mathcal{A}_{\text{ASP}}|_{\delta_*=0}.$$

Let us now see how inclusion of the aspherical prefactor restores the zero expectation value of the density contrast. To this end, we introduce the variable ν as in (5.52) and write,

$$\begin{aligned} \langle \delta_* \rangle &= \int_{-1}^{\infty} d\delta_* \mathcal{A}_{\text{ASP}}(\delta_*)\mathcal{P}_{\text{SP}}(\delta_*) \delta_* = \int_{-\infty}^{\infty} \frac{d\nu}{\sqrt{2\pi g^2}} \mathcal{A}_{\text{ASP}}(\nu) \delta_*(\nu) e^{-\frac{\nu^2}{2g^2}} \\ &= g^2 \left(\frac{d\mathcal{A}_{\text{ASP}}}{d\nu} \cdot \frac{d\delta_*}{d\nu} + \frac{1}{2} \frac{d^2\delta_*}{d\nu^2} \right) \Big|_{\nu=0}, \end{aligned} \quad (5.57)$$

where in the last equality we evaluated the integral at leading order in g^2 . For $\langle \delta_* \rangle$ to vanish, the first derivative of \mathcal{A}_{ASP} at $\delta_* = 0$ must satisfy,

$$\frac{d\mathcal{A}_{\text{ASP}}}{d\delta_*} \Big|_{\delta_*=0} = -\frac{1}{2} \left(\frac{d\delta_*}{d\nu} \right)^{-2} \frac{d^2\delta_*}{d\nu^2} \Big|_{\nu=0}.$$

Comparing with Eq. (5.54) we obtain the condition

$$\frac{d\mathcal{A}_{\text{ASP}}}{d\delta_*} \Big|_{\delta_*=0} = a_1, \quad (5.58)$$

where a_1 has been defined in (5.55).

We have checked that the N-body data are fully consistent with this requirement. Namely, we fit the dependence $\mathcal{A}_{\text{ASP}}(\delta_*)$ extracted from the data with the formula

$$\mathcal{A}_{\text{ASP}} = 1 + a_1 \ln(1 + \delta_*) + a_2 \ln^2(1 + \delta_*) + a_3 \ln^3(1 + \delta_*), \quad (5.59)$$

where we fix a_1 to the numerical values predicted by Eq. (5.55), whereas a_2 and a_3 are treated as free parameters of the fit. The results of the fit are shown in Fig. 5.8 and the parameters are summarized in Table 5.2. We observe that the expression (5.59) accurately describes the data throughout the whole available range of densities. In particular, there is a perfect match between the slopes of the fitting curve and the data at the origin. Note that the precise values of the coefficients a_2, a_3 listed in Table 5.2 should be taken with a grain of salt as they

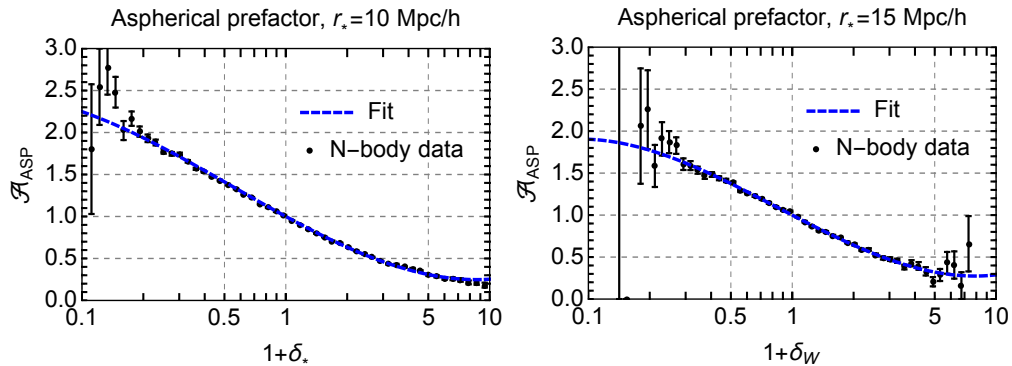


FIGURE 5.8: The fitting formula for the aspherical prefactor (5.59) against the N-body data for $r_* = 10 \text{ Mpc}/h$ (left panel) and $r_* = 15 \text{ Mpc}/h$ (right panel). All results are shown for $z = 0$.

are determined by the tails of the measured distribution, which are subject to systematic errors.

	a_1	a_2	a_3
$r_* = 10 \text{ Mpc}/h$	-0.575	0.047	0.027
$r_* = 15 \text{ Mpc}/h$	-0.546	0.018	0.037

TABLE 5.2: Parameters of the fitting formula (5.59) for the aspherical prefactor for two different cell radii. The parameter a_1 is computed from Eq. (5.55), and *is not* fitted from the data.

We have seen that the aspherical prefactor is independent of the linear growth factor. We also observe that the prefactor depends rather weakly on the size of the window function. The leading response of the PDF to a change in the cosmological model (such as e.g. variation of the cosmological parameters or beyond- Λ CDM physics) will clearly enter through the exponent of the spherical part \mathcal{P}_{SP} . The modification of the PDF due to the change of \mathcal{A}_{ASP} is expected to be subdominant. Hence, for practical applications of the 1-point PDF to constraining the cosmological parameters or exploring new physics one can, in principle, proceed with the simple fitting formula (5.59) with the parameters extracted from N-body simulations of a fiducial Λ CDM cosmology. Nevertheless, from the theoretical perspective, it is highly instructive to perform the full first-principle calculation of the aspherical prefactor. The rest of this thesis is devoted to this task. In the four subsequent sections we derive and analyze the relevant equations.

Chapter 6

Accurate calculation of aspherical prefactor

6.1 Perturbative calculation at small density contrast

In this section we compute the aspherical prefactor treating the saddle point configuration perturbatively. This approximation is valid at small contrasts $|\delta_*| \ll 1$. We will work at quadratic order in δ_* which, as we will see shortly, corresponds to the 1-loop order of standard perturbation theory. We first consider standard cosmological perturbation theory (SPT) [15] and then discuss its extension, the effective field theory (EFT) of large scale structure [30, 31]. Eventually, we are interested in large averaged density contrasts $|\delta_*| \sim 1$ where perturbation theory does not apply. Still, it will serve us to grasp important features of a fully non-linear calculation.

It is convenient to introduce an alternative representation of the aspherical prefactor. Let us multiply and divide the expression (5.44) by the square root of the monopole fluctuation determinant

$$\mathcal{D}_0 = \det \left[\mathbb{1} + 2\hat{\lambda}\sqrt{P}Q_0\sqrt{P} \right], \quad (6.1)$$

where Q_0 is the monopole response matrix introduced in (5.34). Next we observe that

$$\prod_{\ell=0}^{\infty} \mathcal{D}_\ell^{-(\ell+1/2)} = \mathcal{N}^{-1} \int \mathcal{D}\delta_L^{(1)} \exp \left\{ -\frac{1}{g^2} \left[\int_{\mathbf{k}} \frac{(\delta_L^{(1)}(\mathbf{k}))^2}{2P(k)} + \hat{\lambda} \int_{\mathbf{k}_1} \int_{\mathbf{k}_2} Q_{tot}(\mathbf{k}_1, \mathbf{k}_2) \delta_L^{(1)}(\mathbf{k}_1) \delta_L^{(1)}(\mathbf{k}_2) \right] \right\}, \quad (6.2)$$

where

$$Q_{tot}(\mathbf{k}_1, \mathbf{k}_2) = \frac{1}{2} \frac{\partial^2 \bar{\delta}_W}{\partial \delta_L(\mathbf{k}_1) \partial \delta_L(\mathbf{k}_2)} \quad (6.3)$$

is the *total quadratic response operator*. Note that it is defined in the space of functions depending on the full 3-dimensional wavevectors \mathbf{k} , unlike the partial multipole operators Q_ℓ defined in the space of functions of the radial wavenumber k . The expression on the r.h.s. of (6.2) is the inverse square root of the *total fluctuation determinant*,

$$\mathcal{D}_{tot} = \det[\mathbb{1} + 2\hat{\lambda}\sqrt{P}Q_{tot}\sqrt{P}]. \quad (6.4)$$

In this way we obtain the following formula for the aspherical prefactor,

$$\mathcal{A}_{ASP} = \sqrt{\frac{\mathcal{D}_0}{\mathcal{D}_{tot}}}. \quad (6.5)$$

The monopole determinant \mathcal{D}_0 can be computed analytically for any value of δ_* , see Appendix G.3. Note that, by itself, it does not have any physical meaning as the quadratic monopole fluctuations are already taken into account in the monopole prefactor \mathcal{A}_0 . The introduction of the monopole determinant is just a useful trick to simplify the calculation, \mathcal{D}_{tot} being more convenient to treat in perturbation theory than the determinants in separate multipole sectors.

6.1.1 Fluctuation determinant in standard perturbation theory

In order to find the response matrix we use the SPT solution [15] for the mildly non-linear density field,

$$\delta(\mathbf{k}) = \delta_L(\mathbf{k}) + \sum_{n=2}^{\infty} \int_{\mathbf{k}_1} \dots \int_{\mathbf{k}_n} (2\pi)^3 \delta_D^{(3)}\left(\mathbf{k} - \sum_i \mathbf{k}_i\right) F_n(\mathbf{k}_1, \dots, \mathbf{k}_n) \prod_{i=1}^n \delta_L(\mathbf{k}_i). \quad (6.6)$$

We work in the EdS approximation, where the SPT kernels F_n are redshift-independent, e.g.

$$F_2(\mathbf{k}_1, \mathbf{k}_2) = \frac{17}{21} + (\mathbf{k}_1 \cdot \mathbf{k}_2) \left(\frac{1}{2k_1^2} + \frac{1}{2k_2^2} \right) + \frac{2}{7} \left(\frac{(\mathbf{k}_1 \cdot \mathbf{k}_2)^2}{k_1^2 k_2^2} - \frac{1}{3} \right). \quad (6.7)$$

We will discuss the EFT corrections later on. Using (6.6) we obtain

$$Q_{tot}(\mathbf{k}_1, \mathbf{k}_2) = \sum_{n=2}^{\infty} \frac{n(n-1)}{2} \int_{\mathbf{q}_1} \dots \int_{\mathbf{q}_{n-2}} F_n(\mathbf{k}_1, \mathbf{k}_2, \mathbf{q}_1, \dots, \mathbf{q}_{n-2}) \\ \times W_{th}(|\mathbf{k}_{12} + \mathbf{q}_{1\dots n-2}|r_*) \prod_{i=1}^{n-2} \hat{\delta}_L(\mathbf{q}_i), \quad (6.8)$$

where $\mathbf{q}_{1\dots m} \equiv \mathbf{q}_1 + \dots + \mathbf{q}_m$. We will keep only the first two terms in the expansion (6.8):

$$Q_{tot}(\mathbf{k}_1, \mathbf{k}_2) = F_2(\mathbf{k}_1, \mathbf{k}_2) W_{th}(|\mathbf{k}_{12}|r_*) + 3 \int_{\mathbf{q}} F_3(\mathbf{k}_1, \mathbf{k}_2, \mathbf{q}) W_{th}(|\mathbf{k}_{12} + \mathbf{q}|r_*) \hat{\delta}_L(\mathbf{q}). \quad (6.9)$$

An important comment is in order. The SPT kernels $F_n(\mathbf{k}_1, \dots, \mathbf{k}_n)$ are known to contain poles when one or several momenta vanish, see e.g. the second term in (6.7). These lead to the so-called¹ ‘IR divergence’ in the individual SPT loop integrals that cancel in the final results for the correlation functions [18]. Equation (6.9) implies that the response matrix has IR poles when \mathbf{k}_1 or \mathbf{k}_2 (or both) tend to zero. Nevertheless, we are going to see that the IR divergences associated with these poles cancel in the determinant \mathcal{D}_{tot} . In other words, the aspherical prefactor, and hence the full 1-point PDF, is IR safe. In Sec. 6.3.1 this property will be related to the equivalence principle.

To compute the determinant \mathcal{D}_{tot} , we make use of the trace formula,

$$\mathcal{D}_{tot} = \exp \left\{ \text{Tr} \ln \left(\mathbb{1} + 2\hat{\lambda} \sqrt{P} Q_{tot} \sqrt{P} \right) \right\} \\ \approx \exp \left\{ \left[-2 \frac{\delta_*^2}{s_{r_*}^2} + 6 \frac{\delta_*^2}{\sigma_{r_*}^2} \left(-\frac{4}{21} + \frac{\xi_{r_*}}{\sigma_{r_*}^2} \right) \right] \text{Tr}(P Q_{tot}) - 2 \frac{\delta_*^2}{s_{r_*}^4} \text{Tr}(P Q_{tot} P Q_{tot}) \right\}, \quad (6.10)$$

where in the second line we perturbatively expanded the Lagrange multiplier $\hat{\lambda}$ and kept only the terms that can contribute at order δ_*^2 . Let us first compute the leading-order contribution $O(\delta_*)$. From Eq. (6.9) it is proportional to

$$\text{Tr}(Q_{tot} P)_{LO} = W_{th}(0) \int_{\mathbf{k}} F_2(\mathbf{k}, -\mathbf{k}) P(k). \quad (6.11)$$

But this vanishes due to $F_2(\mathbf{k}, -\mathbf{k}) = 0$. Note that this property can be traced back to the translational invariance. Indeed, the latter implies conservation of momentum, so that at quadratic order of SPT around homogeneous background

¹For the realistic power spectrum there are no true divergences, but rather spurious enhanced contributions of soft modes.

one has,

$$\delta(\mathbf{k}) = \delta_L(\mathbf{k}) + \int_{\mathbf{q}} F_2(\mathbf{k} - \mathbf{q}, \mathbf{q}) \delta_L(\mathbf{k} - \mathbf{q}) \delta_L(\mathbf{q}).$$

Averaging over the Gaussian initial conditions and recalling that $\langle \delta(\mathbf{k}) \rangle = \langle \delta_L(\mathbf{k}) \rangle = 0$ by construction, one obtains that the integral entering (6.11) must vanish. As this should be true for any power spectrum, one further infers vanishing of $F_2(\mathbf{k}, -\mathbf{k})$.

At next-to-leading order one has,

$$\text{Tr}(Q_{tot}P)_{\text{NLO}} = 3 \frac{\delta_*^2}{\sigma_{r_*}^2} \int_{\mathbf{k}} \int_{\mathbf{q}} F_3(\mathbf{q}, -\mathbf{q}, \mathbf{k}) P(k) P(q) |W_{\text{th}}(kr_*)|^2. \quad (6.12)$$

This term is similar to the P_{13} -contribution to the filtered density variance in SPT. It is known to contain a spurious IR-enhancement, which cancels upon adding the P_{22} contribution, whose counterpart in our calculation is the right-most term in (6.10),

$$\text{Tr}(Q_{tot}PQ_{tot}P) = \int_{\mathbf{k}_1} \int_{\mathbf{k}_2} F_2^2(\mathbf{k}_1, \mathbf{k}_2) P(k_1) P(k_2) |W_{\text{th}}(|\mathbf{k}_1 + \mathbf{k}_2|r_*)|^2. \quad (6.13)$$

The net expression for the prefactor generated by total fluctuations reads:

$$\mathcal{A}_{tot} \equiv \mathcal{D}_{tot}^{-1/2} \approx \exp \left\{ \frac{\delta_*^2 \sigma_{1\text{-loop}}^2}{2 \sigma_{r_*}^4} \right\}, \quad (6.14)$$

where we defined the filtered 1-loop density variance:

$$\sigma_{1\text{-loop}}^2 = \int_{\mathbf{k}} P_{1\text{-loop}}(k) |W_{\text{th}}(kr_*)|^2, \quad (6.15a)$$

$$P_{1\text{-loop}}(k) = \int_{\mathbf{q}} \left(2F_2^2(\mathbf{k} - \mathbf{q}, \mathbf{q}) P(q) P(|\mathbf{k} - \mathbf{q}|) + 6F_3(\mathbf{k}, -\mathbf{q}, \mathbf{q}) P(q) P(k) \right). \quad (6.15b)$$

This result has an intuitive interpretation. Expression (6.14) is precisely the factor which appears if we use the full 1-loop corrected power spectrum instead of the linear one in the variance entering the saddle-point exponent (5.30):

$$\exp \left\{ -\frac{\delta_*^2}{2g^2(\sigma_{r_*}^2 + g^2\sigma_{1\text{-loop}}^2)} \right\} \approx \exp \left\{ -\frac{\delta_*^2}{2g^2\sigma_{r_*}^2} + \frac{\delta_*^2 \sigma_{1\text{-loop}}^2}{2 \sigma_{r_*}^4} \right\}. \quad (6.16)$$

The replacement of the linear variance by the 1-loop expression in (6.16) is reminiscent of the coupling constant renormalization due to radiative corrections in instanton calculations in QFT (see e.g. [149]).

6.1.2 Effective field theory corrections

SPT does not capture correctly the effect of very short modes that become deeply non-linear by $z = 0$. This problem is addressed in EFT of LSS. The latter augments the pressureless hydrodynamics equations solved in SPT by the effective stress tensor, which is treated within a gradient expansion [30, 31, 150]. At the leading (1-loop) order it produces the following correction (counterterm) to the density contrast,

$$\delta_{\text{ctr}}(\mathbf{k}) = -\gamma(z)k^2\delta_L(\mathbf{k}), \quad (6.17)$$

which must be added to the SPT expression (6.6). Here $\gamma(z)$ is a z -dependent coefficient with the dimension of $(\text{length})^2$ whose value and scaling with $g(z)$ will be discussed below. Note that this contribution is linear in δ_L . However, it has the same order of magnitude as the one-loop correction because the combination γk^2 is assumed to be small according to the rules of gradient expansion.

Addition of the term (6.17) to the relation between linear and non-linear density contrasts slightly modifies the saddle-point solution. To find this correction we observe that, at the order we are working, the final smoothed density contrast is related to the linear density field as,

$$\bar{\delta}_W = \int_{\mathbf{k}} W_{\text{th}}(kr_*) \delta_L(\mathbf{k}) (1 - \gamma k^2). \quad (6.18)$$

Substituting this into the saddle-point equations (5.9) we obtain,

$$\hat{\delta}_L = \frac{\delta_*}{\sigma_{r_*}^2} \left(1 + \frac{2\gamma\Sigma_{r_*}^2}{\sigma_{r_*}^2} \right) P(k)W_{\text{th}}(kr_*)(1 - \gamma k^2), \quad (6.19)$$

where

$$\Sigma_{r_*}^2 = \int_{\mathbf{k}} |W_{\text{th}}(kr_*)|^2 P(k) k^2. \quad (6.20)$$

The modification of the saddle point produces a shift in the leading exponent of the PDF and results in the following counterterm prefactor:

$$\mathcal{A}_{\text{ctr}} = \exp \left(-\delta_*^2 \frac{\gamma(z)}{g^2(z)} \frac{\Sigma_{r_*}^2}{\sigma_{r_*}^4} \right). \quad (6.21)$$

It is instructive to derive this result in an alternative way. One recalls that the 1-loop SPT correction to the power spectrum (6.15b) receives a large contribution

from short modes that has the form (see e.g. [150]),

$$g^2 P_{1\text{-loop, UV}}(k) = \left(-\frac{61}{630\pi^2} \int_{q \gg k} dq P(q) \right) g^2 k^2 P(k). \quad (6.22)$$

This contribution would be divergent for a universe where the spectrum $P(q)$ falls slower than q^{-1} at $q \rightarrow \infty$. In EFT of LSS it is renormalized by the counterterm $-2\gamma k^2 P(k)$ coming from the correction (6.17). Performing the renormalization inside the filtered 1-loop density variance we obtain the expression,

$$\sigma_{1\text{-loop, ren}}^2 = \sigma_{1\text{-loop}}^2 - \frac{2\gamma}{g^2} \Sigma_{r_*}^2, \quad (6.23)$$

which translates into the multiplication of the 1-loop prefactor \mathcal{A}_{tot} by the counterterm (6.21).

We obtain the value of the EFT coefficient $\gamma(z=0)$ by fitting the dark matter power spectrum of the simulations² at $z=0$ to the 1-loop IR-resummed theoretical template of Chapter 3. We follow Ref. [151] to include the theoretical error in our analysis, which yields the following result:

$$\gamma_0 \equiv \gamma|_{z=0} = 1.51 \pm 0.07 \quad (\text{Mpc}/h)^2. \quad (6.24)$$

In general, the redshift dependence of γ should be also fitted from the power spectrum in different redshift bins. In our analysis we use a simplified model of a scaling universe [152]. In the range of wavenumbers $k \sim 0.1 h/\text{Mpc}$ relevant for the EFT considerations the broad-band part of the power spectrum can be approximated as a power law [153, 154],

$$P(k) \sim \frac{2\pi^2}{k_{NL}^3} \left(\frac{k}{k_{NL}} \right)^n, \quad (6.25)$$

where k_{NL} is the non-linear scale and the spectral index is estimated in the range $n \simeq -(1.5 \div 1.7)$. In a universe with such spectrum, the EFT coefficient is expected to scale as $\gamma \propto k_{NL}^{-2}$, whereas k_{NL} depends on the growth factor as $k_{NL} \propto (g(z))^{\frac{n+3}{2}}$. This gives the dependence,

$$\gamma(z) = \gamma_0 (g(z))^{\frac{4}{n+3}}. \quad (6.26)$$

It has been found consistent with the results of N-body simulations [150, 155]. For numerical estimates we will adopt the value $n = -3/2$ and the corresponding

²For the fit we use the power spectrum of the Horizon Run 2 [101] that has the same cosmology as assumed in this Chapter. This gives a better precision than our own simulations performed in relatively small boxes and contaminated by systematic errors at large scales.

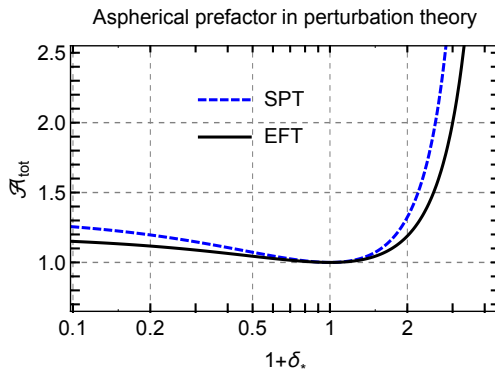


FIGURE 6.1: The prefactor \mathcal{A}_{tot} due to quadratic fluctuations in perturbation theory computed at 1-loop order in SPT and EFT. The results are shown at $z = 0$. Perturbation theory is strictly applicable in the neighborhood of $\delta_* = 0$.

scaling $\gamma(z) = \gamma_0 (g(z))^{8/3}$.

In Fig. 6.1 we compare the numerical results for \mathcal{A}_{tot} at $z = 0$ computed in SPT and upon inclusion of the EFT correction (we use the value $\gamma_0 = 1.5 (\text{Mpc}/h)^2$). We see that the EFT correction has a sizable effect on the prefactor, and somewhat reduces its value.

6.1.3 Aspherical prefactor at second order in background density

In order to compute the full aspherical prefactor we have to combine the total determinant with the spherical one, see Eq. (G.34). Unlike the total determinant, the spherical determinant differs from unity at leading order in δ_* and yields

$$\mathcal{A}_{\text{ASP}}^{\text{LO}} = \mathcal{D}_0^{1/2} = \exp \left\{ \delta_* \left(\frac{4}{21} - \frac{\xi_{r_*}}{\sigma_{r_*}^2} \right) \right\}. \quad (6.27)$$

Remarkably, the aspherical prefactor at order $O(\delta_*)$ is fully controlled by translation invariance which forces the corresponding terms in \mathcal{A}_{tot} to vanish. Thus, the slope of the aspherical prefactor at the origin is encoded in the spherical collapse dynamics. Note that this slope has precisely the value necessary to restore the zero mean of the density contrast, Eqs. (5.58), (5.55). This is an important consistency check of our approach.

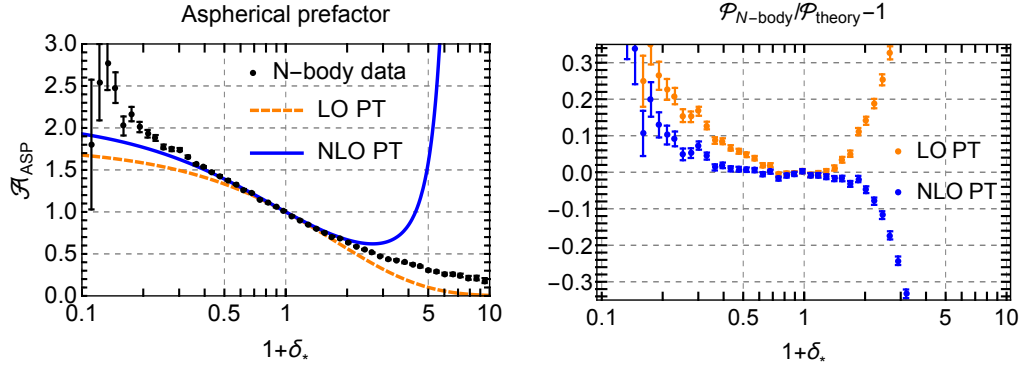


FIGURE 6.2: Left panel: the aspherical prefactor in perturbation theory at leading (LO) and next-to-leading (NLO) orders shown against the N-body data for cell radius $r_* = 10 \text{ Mpc}/h$ at $z = 0$. Right panel: the corresponding residuals.

Expanding the monopole determinant, one finds at the next-to-leading order:

$$\mathcal{A}_{\text{ASP}}^{\text{NLO}} = \exp \left\{ \delta_* \left(\frac{4}{21} - \frac{\xi_{r_*}}{\sigma_{r_*}^2} \right) + \frac{\delta_*^2 \sigma_{1\text{-loop, ren}}^2}{2 \sigma_{r_*}^4} + \frac{\delta_*^2}{2} \left(-\frac{1180}{1323} + \frac{40\xi_{r_*}}{21\sigma_{r_*}^2} + \frac{r_*^2 \Sigma_{r_*}^2}{3\sigma_{r_*}^2} + \frac{\xi_{r_*}^2}{\sigma_{r_*}^4} - \frac{3\sigma_{1r_*}^2}{\sigma_{r_*}^2} \right) \right\}, \quad (6.28)$$

where $\Sigma_{r_*}^2$ is defined in (6.20) and

$$\sigma_{1r_*}^2 = \int_{\mathbf{k}} \left(\frac{\sin(kr_*)}{kr_*} \right)^2 P(k). \quad (6.29)$$

In the left panel of Fig. 6.2 we show the aspherical prefactor evaluated at leading and next-to-leading orders in perturbation theory. We observe that the LO result works surprisingly well and does not deviate from the data by more than 10% in the range $\delta_* \approx [-0.5, 1]$, while the NLO results extends the agreement up to $\delta_* \approx [-0.8, 1.5]$. In the right panel of Fig. 6.2 we show the residuals for the perturbation theory PDF. One sees that the NLO corrections reduce the residuals close to the origin, but quickly blow up towards large overdensities.

One takes four main lessons from the perturbative calculation:

1. The response matrix contains spurious IR enhanced terms that cancel in the determinant.
2. Including the aspherical corrections amounts, in part, to replacing the linear density variance by its non-linear version.

3. The short-scale contributions should be renormalized by appropriate EFT counterterms.
4. The slope of the aspherical prefactor at the origin is dictated by translational invariance and is such that the mean value $\langle \delta_* \rangle$ vanishes.

6.2 Aspherical prefactor at large density contrasts: main equations

In Sec. 5.1.3 we expressed the aspherical prefactor as the product of fluctuation determinants in different multipole sectors. Calculation of these determinants requires knowledge of the aspherical response matrices Q_ℓ . In this and the subsequent section we set up the equations for the determination of Q_ℓ that we will solve numerically afterwards. For simplicity, we work in the EdS approximation. The equations for Λ CDM cosmology are summarized in Appendix E of Ref. [9]. We have checked that the difference in the final answers for the prefactor in Λ CDM and in EdS does not exceed 1%. Thus, the EdS approximation is vastly sufficient for our purposes.

6.2.1 Linearized fluctuations with $\ell > 0$

We first derive the evolution equations for linearized aspherical perturbations in the background of the saddle-point solution. We start from the standard pressureless Euler–Poisson equations for the density, peculiar velocity, and the Newtonian gravitational potential in an EdS universe,

$$\frac{\partial \delta}{\partial t} + \partial_i((1 + \delta)u_i) = 0, \quad (6.30a)$$

$$\frac{\partial u_i}{\partial t} + \mathcal{H}u_i + (u_j \partial_j)u_i = -\partial_i \Phi, \quad (6.30b)$$

$$\Delta \Phi = \frac{3\mathcal{H}^2}{2} \delta, \quad (6.30c)$$

where t is conformal time, $\mathcal{H} = \partial_t a/a = 2/t$ is the conformal Hubble parameter and a is the scale factor. We expand all quantities into background and first-order perturbations, $\delta = \hat{\delta} + \delta^{(1)}$, etc. Next, we take the divergence of (6.30b) and introduce the velocity potential Ψ :

$$u_i^{(1)} = -\mathcal{H} \partial_i \Psi^{(1)}, \quad \partial_i u_i^{(1)} = -\mathcal{H} \Theta^{(1)}. \quad (6.31)$$

From now on we also switch to a new time variable

$$\eta \equiv \ln a(t), \quad (6.32)$$

To linear order in perturbations, the system (6.30) takes the form,

$$\dot{\delta}^{(1)} - \Theta^{(1)} + \mathcal{H}^{-1} \hat{u}_i \partial_i \delta^{(1)} + \mathcal{H}^{-1} \partial_i \hat{u}_i \delta^{(1)} - \partial_i \hat{\delta} \partial_i \Psi^{(1)} - \hat{\delta} \Theta^{(1)} = 0, \quad (6.33a)$$

$$\dot{\Theta}^{(1)} + \frac{1}{2} \Theta^{(1)} - \frac{3}{2} \delta^{(1)} + \mathcal{H}^{-1} \hat{u}_i \partial_i \Theta^{(1)} + \mathcal{H}^{-1} \partial_i \partial_j \hat{u}_j \partial_i \Psi^{(1)} + 2\mathcal{H}^{-1} \partial_i \hat{u}_j \partial_i \partial_j \Psi^{(1)} = 0, \quad (6.33b)$$

$$\Delta \Psi^{(1)} = \Theta^{(1)}, \quad (6.33c)$$

where dot denotes the derivative with respect to η . Note that the background quantities have only radial dependence and the velocity \hat{u}_i has only the radial component, so that

$$\mathcal{H}^{-1} \partial_i \hat{u}_j = -\partial_i \partial_j \hat{\Psi} = \frac{x_i x_j}{r^2} \partial_r^2 \hat{\Psi} + \left(\delta_{ij} - \frac{x_i x_j}{r^2} \right) \frac{\partial_r \hat{\Psi}}{r}. \quad (6.34)$$

We now expand the perturbations in spherical harmonics,

$$\delta^{(1)}(\mathbf{x}) = \sum_{\ell > 0} \sum_{m=-\ell}^{\ell} Y_{\ell m}(\mathbf{x}/r) \delta_{\ell m}(r), \quad (6.35)$$

and similarly for the other fields. To simplify notations, we have omitted the superscript ‘(1)’ on the multipole components of the fluctuations. In what follows we will also omit the azimuthal quantum number m as it does not appear explicitly in the equations. Substituting the expansion into Eqs. (6.33) we obtain,

$$\dot{\delta}_\ell - \Theta_\ell - \partial_r \hat{\Psi} \partial_r \delta_\ell - \hat{\Theta} \delta_\ell - \partial_r \hat{\delta} \partial_r \Psi_\ell - \hat{\delta} \Theta_\ell = 0, \quad (6.36a)$$

$$\begin{aligned} \dot{\Theta}_\ell + \frac{1}{2} \Theta_\ell - \frac{3}{2} \delta_\ell - \partial_r \hat{\Psi} \partial_r \Theta_\ell - \partial_r \hat{\Theta} \partial_r \Psi_\ell - 2\partial_r^2 \hat{\Psi} \Theta_\ell \\ + 2 \left(\partial_r^2 \hat{\Psi} - \frac{\partial_r \hat{\Psi}}{r} \right) \left(\frac{2}{r} \partial_r \Psi_\ell - \frac{\ell(\ell+1)}{r^2} \Psi_\ell \right) = 0, \end{aligned} \quad (6.36b)$$

$$\partial_r^2 \Psi_\ell + \frac{2}{r} \partial_r \Psi_\ell - \frac{\ell(\ell+1)}{r^2} \Psi_\ell = \Theta_\ell. \quad (6.36c)$$

This is a system of (1+1)-dimensional partial differential equations for the set of functions $(\delta_\ell, \Theta_\ell, \Psi_\ell)$.

To determine the initial conditions, we reason as follows. At early times the saddle-point background vanishes and a solution to the previous system goes

into

$$\delta_\ell(r) \rightarrow e^\eta \delta_{L,\ell}(r) ,$$

where $\delta_{L,\ell}$ is a linear density field. Just like one decomposes linear perturbations over plane waves in 3-dimensional space, we need to choose a basis of functions on the half-line which are properly normalized w.r.t. to the radial integration measure,

$$\int_0^\infty dr r^2 \delta_{L,\ell,k}^*(r) \delta_{L,\ell,k'}(r) = (2\pi)^3 k^{-2} \delta_D^{(1)}(k - k') . \quad (6.37)$$

The expression on the r.h.s. is the radial delta-function compatible with the momentum-space measure $\int [dk]$, Eq. (A.4). A convenient basis with these properties is provided by the spherical Bessel functions (see Appendix A),

$$\delta_{L,\ell,k}(r) = 4\pi j_\ell(kr) .$$

We conclude that the relevant initial conditions are,

$$\delta_{\ell,k}(r) = \Theta_{\ell,k}(r) = e^\eta \cdot 4\pi j_\ell(kr) , \quad (6.38a)$$

$$\Psi_{\ell,k} = -e^\eta \cdot \frac{4\pi}{k^2} j_\ell(kr) \quad \text{at } \eta \rightarrow -\infty . \quad (6.38b)$$

In setting up the initial conditions for Ψ we have used that Bessel functions are eigenstates of the radial part of the Laplace operator, see Eq. (A.17).

6.2.2 Quadratic fluctuations in the monopole sector

To find the response matrix, we need the second-order monopole perturbation $\delta_0^{(2)}$ induced by a pair of first-order aspherical modes with a given ℓ . For simplicity, we will take the latter in the form,

$$\delta_k^{(1)}(r) = Y_{\ell,m=0}(\mathbf{x}/r) \delta_{\ell,k}(r) , \quad (6.39)$$

so that, according to (A.12), $\delta_{\ell,k}$ is real. Let us first focus on the diagonal elements of the response matrix, i.e. consider the case when the fluctuation $\delta_0^{(2)}$ is sourced by two linear modes with the same wavenumber k . Generalization to a pair with different wavenumbers will be discussed at the end of the subsection. For compactness we will omit this wavenumber in the subscript of $\delta_\ell, \Theta_\ell, \Psi_\ell$ in what follows.

Expanding the Euler–Poisson equations to the quadratic order and averaging over the angles we obtain,

$$\dot{\delta}_0^{(2)} - \Theta_0^{(2)} - \partial_r \hat{\Psi} \partial_r \delta_0^{(2)} - \hat{\Theta} \delta_0^{(2)} - \partial_r \hat{\delta} \partial_r \Psi_0^{(2)} - \hat{\delta} \Theta_0^{(2)} = \Xi_\delta, \quad (6.40a)$$

$$\dot{\Theta}_0^{(2)} + \frac{1}{2} \Theta_0^{(2)} - \frac{3}{2} \delta_0^{(2)} - \partial_r \hat{\Psi} \partial_r \Theta_0^{(2)} - \partial_r \hat{\Theta} \partial_r \Psi_0^{(2)} \quad (6.40b)$$

$$- 2 \partial_r^2 \hat{\Psi} \Theta_0^{(2)} + \frac{4}{r} \left(\partial_r^2 \hat{\Psi} - \frac{\partial_r \hat{\Psi}}{r} \right) \partial_r \Psi_0^{(2)} = \Xi_\Theta,$$

$$\partial_r^2 \Psi_0^{(2)} + \frac{2}{r} \partial_r \Psi_0^{(2)} = \Theta_0^{(2)}, \quad (6.40c)$$

where the sources on the r.h.s. are,

$$\Xi_\delta = -\frac{1}{\mathcal{H}} \int \frac{d\Omega}{4\pi} \partial_i (\delta^{(1)} u_i^{(1)}), \quad \Xi_\Theta = \frac{1}{\mathcal{H}^2} \int \frac{d\Omega}{4\pi} \partial_i (u_j^{(1)} \partial_j u_i^{(1)}). \quad (6.41)$$

Performing the angular integration and using the Poisson equation (6.36c) the sources can be cast in a suggestive form,

$$\Xi_\delta = \frac{1}{r^2} \partial_r (r^2 \Upsilon_\delta), \quad \Xi_\Theta = \frac{1}{r^2} \partial_r (r^2 \Upsilon_\Theta), \quad (6.42)$$

where

$$\Upsilon_\delta = \frac{1}{4\pi} \delta_\ell \partial_r \Psi_\ell, \quad (6.43a)$$

$$\Upsilon_\Theta = \frac{1}{4\pi} \left[\Theta_\ell \partial_r \Psi_\ell - \frac{2}{r} (\partial_r \Psi_\ell)^2 + \frac{2\ell(\ell+1)}{r^2} \Psi_\ell \partial_r \Psi_\ell - \frac{\ell(\ell+1)}{r^3} \Psi_\ell^2 \right]. \quad (6.43b)$$

Let us introduce a second-order overdensity integrated over a sphere of radius³ r_η ,

$$\mu^{(2)} = \int_0^{r_\eta} dr r^2 \delta_0^{(2)}(r), \quad (6.44)$$

where we allow r_η to be time dependent. We now show that if r_η satisfies an appropriate evolution equation, the system (6.40) reduces to an ordinary differential equation for $\mu^{(2)}$. It is convenient to work with the total quantities (background plus second order perturbations), $\delta_0 = \hat{\delta} + \delta_0^{(2)}$ etc. Then Eqs. (6.40) become,

$$\dot{\delta}_0 - \partial_r \Psi_0 \partial_r \delta_0 - (1 + \delta_0) \Theta_0 = \Xi_\delta, \quad (6.45a)$$

$$\dot{\Theta}_0 + \frac{1}{2} \Theta_0 - \frac{3}{2} \delta_0 - \partial_r \Psi_0 \partial_r \Theta_0 - \Theta_0^2 + \frac{2}{r^2} (\partial_r \Psi_0)^2 + \frac{4}{r} \partial_r^2 \Psi_0 \partial_r \Psi_0 = \Xi_\Theta, \quad (6.45b)$$

$$\partial_r (r^2 \partial_r \Psi_0) = r^2 \Theta_0. \quad (6.45c)$$

³Note that we do not divide by the volume of the sphere, so $\mu^{(2)}$ differs from the spherically averaged density contrast by a factor $r_\eta^3/3$.

Let us multiply the first equation by r^2 and integrate from 0 to r_η ,

$$\int_0^{r_\eta} dr r^2 \frac{\partial \delta_0}{\partial \eta} - \int_0^{r_\eta} dr r^2 \partial_r \Psi_0 \partial_r \delta_0 - \int_0^{r_\eta} dr r^2 (1 + \delta_0) \Theta_0 = \int_0^{r_\eta} dr r^2 \Xi_\delta . \quad (6.46)$$

The last two terms on the l.h.s. combine into a total derivative due to Eq. (6.45c). Also pulling the time derivative outside of the integral in the first term we obtain,

$$\frac{d}{d\eta} \int_0^{r_\eta} dr r^2 (1 + \delta_0(r)) - r_\eta^2 (1 + \delta_0(r_\eta)) (\dot{r}_\eta + \partial_r \Psi_0(r_\eta)) = r_\eta^2 \Upsilon_\delta(r_\eta) . \quad (6.47)$$

The boundary terms on the l.h.s. cancel if we choose the time-dependence of r_η in such a way that

$$\dot{r}_\eta = -\partial_r \Psi_0(r_\eta) . \quad (6.48)$$

In other words, we shall choose the boundary to be moving with the angular-averaged fluid velocity. Then Eq. (6.47) simplifies,

$$\dot{\mu} = r_\eta^2 \Upsilon_\delta(r_\eta) , \quad (6.49)$$

where we introduced⁴

$$\mu = \int_0^{r_\eta} dr r^2 (1 + \delta_0(r)) . \quad (6.50)$$

This equation has a clear physical interpretation. It tells us that the mass inside a spherical region comoving with the average spherical fluid flow changes due to the inflow through the boundary generated by aspherical modes.

Equation (6.49) allows us to determine μ once the time dependence of r_η is known. However, we still need an evolution equation for r_η in terms of r_η and μ to close the system⁵. This is obtained from (6.45b) by multiplying it with r^2 and integrating from 0 to r_η . Using (6.42) and (6.43b) we obtain,

$$r_\eta^2 \left(\frac{\partial}{\partial \eta} \partial_r \Psi_0 + \frac{1}{2} \partial_r \Psi_0 - \partial_r \Psi_0 \partial_r^2 \Psi_0 \right) \Big|_{r_\eta} - \frac{3}{2} \left(\mu - \frac{r_\eta^3}{3} \right) = r_\eta^2 \Upsilon_\Theta(r_\eta) . \quad (6.51)$$

It follows from (6.48) that

$$\ddot{r}_\eta = \left(-\frac{\partial}{\partial \eta} \partial_r \Psi_0 + \partial_r^2 \Psi_0 \partial_r \Psi_0 \right) \Big|_{r_\eta} . \quad (6.52)$$

Thus, we arrive at

$$\ddot{r}_\eta + \frac{\dot{r}_\eta}{2} - \frac{r_\eta}{2} + \frac{3\mu}{2r_\eta^2} = -\Upsilon_\Theta(r_\eta) . \quad (6.53)$$

⁴A careful reader might have noticed that we have run out of nice letters. Here μ should not be confused with the μ from Part I of this thesis.

⁵Equation (6.48) is not sufficient as it involves the monopole velocity potential Ψ_0 which is unknown.

There is again a transparent physical interpretation: the aspherical perturbations exert an effective force on the spherical flow that modifies its acceleration.

As a final step, we decompose μ and r_η into background values and second-order perturbations,

$$r_\eta = \hat{r}_\eta + r_\eta^{(2)}, \quad (6.54a)$$

$$\mu = \hat{\mu} + \mu^{(2)} + r_\eta^{(2)} \hat{r}_\eta^2 (1 + \hat{\delta}(\hat{r}_\eta)), \quad (6.54b)$$

where \hat{r}_η , $\hat{\mu}$ satisfy source-free Eqs. (6.49), (6.53). Subtracting the background contributions from the evolution equations we obtain,

$$\dot{\mu}^{(2)} + \dot{\hat{r}}_\eta^{(2)} \hat{r}_\eta^2 (1 + \hat{\delta}(\hat{r}_\eta)) + r_\eta^{(2)} \frac{d}{d\eta} \left(\hat{r}_\eta^2 (1 + \hat{\delta}(\hat{r}_\eta)) \right) = \hat{r}_\eta^2 \Upsilon_\delta(\hat{r}_\eta) \quad (6.55a)$$

$$\ddot{r}_\eta^{(2)} + \frac{\dot{\hat{r}}_\eta^{(2)}}{2} + \left(1 + \frac{3}{2} \hat{\delta}(\hat{r}_\eta) - \frac{R_*^3}{\hat{r}_\eta^3} \right) r_\eta^{(2)} + \frac{3}{2 \hat{r}_\eta^2} \mu^{(2)} = -\Upsilon_\Theta(\hat{r}_\eta), \quad (6.55b)$$

where we have used the asymptotics $\hat{r}_\eta \rightarrow R_*$, $\hat{\mu} \rightarrow R_*^3/3$ at $\eta \rightarrow -\infty$. Equations (6.55) provide a closed system of linear ordinary differential equations for the variables $\mu_*^{(2)}$, $r_\eta^{(2)}$ once the sources $\Upsilon_{\delta,\Theta}$ are known.

We must supplement (6.55) by three boundary conditions. One of them is set at the final time and expresses the fact that we are interested in the overdensity within the fixed radius r_* , so that the final radius is not perturbed,

$$r_\eta^{(2)}|_{\eta=0} = 0. \quad (6.56a)$$

The conditions at the initial time $\eta \rightarrow -\infty$ are more subtle. The source-free Eqs. (6.55) admit solutions corresponding to first order monopole fluctuations, that can also change the mass within the cell. We need to eliminate such solutions. For this purpose, we observe that for the spurious solutions the fields δ_0 etc. behave as e^η at early times, whereas the second-order perturbations that we are interested in are proportional to $e^{2\eta}$. We conclude that we must require,

$$\mu^{(2)} \propto e^{2\eta}, \quad \text{at } \eta \rightarrow -\infty. \quad (6.56b)$$

As for $r_\eta^{(2)}$, it need not vanish in the beginning. Rather, it should approach a constant value in a specific way. Indeed, from Eqs. (6.49), (6.54b) and the fact that $\dot{\hat{\mu}}$ vanishes we conclude that the derivative of the combination $r_\eta^{(2)} \hat{r}_\eta^2 (1 + \hat{\delta}(\hat{r}_\eta))$ must fall off as $e^{2\eta}$. Thus, we obtain the third condition,

$$\dot{r}_\eta^{(2)} + r_\eta^{(2)} \frac{d}{d\eta} \ln [\hat{r}_\eta^2 (1 + \hat{\delta}(\hat{r}_\eta))] \propto e^{2\eta}, \quad \text{at } \eta \rightarrow -\infty. \quad (6.56c)$$

It is straightforward to generalize the above analysis to the case when the second-order perturbation is sourced by a pair of aspherical modes with different radial wavenumbers k and k' (but, of course, the same angular numbers ℓ and m). In that case the sources (6.43) are replaced by symmetric combinations constructed from the two modes,

$$\Upsilon_{\delta,kk'} = \frac{1}{8\pi} \delta_{\ell,k} \partial_r \Psi_{\ell,k'} + (k \longleftrightarrow k') , \quad (6.57a)$$

$$\begin{aligned} \Upsilon_{\Theta,kk'} = \frac{1}{8\pi} \left[\Theta_{\ell,k} \partial_r \Psi_{\ell,k'} - \frac{2}{r} \partial_r \Psi_{\ell,k} \partial_r \Psi_{\ell,k'} + \frac{2\ell(\ell+1)}{r^2} \Psi_{\ell,k} \partial_r \Psi_{\ell,k'} \right. \\ \left. - \frac{\ell(\ell+1)}{r^3} \Psi_{\ell,k} \Psi_{\ell,k'} \right] + (k \longleftrightarrow k') . \end{aligned} \quad (6.57b)$$

The rest of the derivation goes exactly the same as above, leading to Eqs. (6.55) with the new sources.

6.2.3 Summary of the algorithm

Summarizing the results of this section, one obtains the following algorithm to find the response matrix $Q_\ell(k, k')$ and the fluctuation determinant \mathcal{D}_ℓ :

1. One solves Eqs. (6.36) with the initial conditions (6.38) and finds the wavefunctions $\delta_\ell, \Theta_\ell, \Psi_\ell$ for each basis function from a set of $N + 1$ momenta $\{k_0, \dots, k_N\}$.
2. One uses these solutions to construct the sources (6.57) for a pair of wavevectors k_i and k_j .
3. One solves (6.55) with the initial conditions (6.56). The final variation in the averaged overdensity gives the element of Q_ℓ ,

$$Q_\ell(k_i, k_j) = \frac{3}{r_*^3} \mu^{(2)}(\eta = 0) . \quad (6.58)$$

4. One repeats the above procedure for all different pairs of wavenumbers (k_i, k_j) , construct the operator $\mathbb{1} + 2\hat{\lambda}\sqrt{P}Q_\ell\sqrt{P}$ and evaluates its determinant.

The implementation of this algorithm on a discrete grid is described in Appendix G of [9].

The algorithm requires a modification in the dipole sector ($\ell = 1$) due to the IR sensitivity of the matrix Q_1 . We now focus on this issue.

6.3 Removing IR divergences in the dipole contribution

A complication arises in the dipole sector ($\ell = 1$). The initial conditions (6.38b) imply that the velocity potential $\Psi_{1,k} \propto e^{\eta \cdot r}/k$ has a $1/k$ pole⁶ at $kr \sim kr_* \ll 1$. Substitution of these expressions into equations of motion (6.36a), (6.36b) leads to further $1/k$ contributions in $\delta_{1,k}$ and $\Theta_{1,k}$ proportional to the derivatives of the background configuration $\partial_r \hat{\delta}$, $\partial_r \hat{\Theta}$. Thus, the linear solution $(\delta_1, \Theta_1, \Psi_1)$ contains singular $1/k$ terms which translate into first- and second-order poles in the matrix $Q_1(k, k')$ at $k, k' \ll 1/r_*$. As we discuss below, these infrared (IR) enhanced contribution must cancel in the determinant \mathcal{D}_1 entering the prefactor (5.44), which is IR-safe⁷. However, the presence of the ‘IR-divergent’⁸ terms makes a straightforward numerical evaluation of the determinant unfeasible. The purpose of this section is to show that the IR-enhanced contributions can be isolated and the IR-divergences can be removed, whereby reducing the task to numerical evaluation of IR-safe quantities only.

6.3.1 IR safety of the prefactor

We start by showing that the aspherical prefactor (5.44) is IR safe. We first give a heuristic argument and then a more direct proof. Let us assume that the mapping from the linear to non-linear density fields is invertible⁹. Then the counts-in-cells PDF can be written in the schematic form,

$$\mathcal{P}(\delta_*) = \mathcal{N}^{-1} \int \mathcal{D}\delta \int \frac{d\lambda}{2\pi i g^2} \exp \left\{ -\frac{\Gamma[\delta]}{g^2} + \frac{\lambda}{g^2} (\delta_* - \bar{\delta}(r_*)) \right\}, \quad (6.59)$$

where the path integral runs over all density configurations at the final moment of time and $\Gamma[\delta]$ is a weighting functional obtained from the Gaussian weight using the map $\delta \mapsto \delta_L$. A perturbative expansion for the functional $\Gamma[\delta]$ was derived in [1] and it was shown that all coefficients in this expansion are IR-safe. Extrapolating this property to the non-perturbative level, one concludes that the

⁶This problem does not arise for higher multipoles. The Bessel functions behave at the origin as $(kr)^\ell$, and hence the corresponding velocity potential $\Psi_{\ell,k}$ is regular at $k \rightarrow 0$ for $\ell > 1$.

⁷We have already seen this cancellation in the perturbative calculation in Sec. 6.1.1.

⁸Here the term ‘divergence’ is used in the sense adopted in the perturbation theory literature, where it refers to the fact that loop integrals would be divergent in IR for power-law spectra $P(k) \propto k^n$ with $n \leq -1$. The Λ CDM power spectrum vanishes quickly at small k , so the loop integrals are actually convergent, albeit strongly enhanced.

⁹This would be true in the absence of shell-crossing, but in general is not correct.

matrix of second variational derivatives around the saddle-point solution

$$\left. \frac{\partial^2 \Gamma}{\partial \delta^{(1)}(\mathbf{x}) \partial \delta^{(1)}(\mathbf{x}')} \right|_{\delta = \hat{\delta}(\mathbf{x})} \quad (6.60)$$

is also IR-safe. The prefactor of the PDF is given by the determinant of this matrix, hence it is IR-safe as well.

We now give a more rigorous argument that does not require invertibility of the density mapping. We split the integration variables in the path integral (5.7) into soft ($k \ll 1/r_*$) and hard ($k \gtrsim 1/r_*$) modes. Omitting for clarity the normalization factors we obtain,

$$\mathcal{P}(\delta_*) = \int \mathcal{D}\delta_L^{\text{soft}} \exp \left\{ - \int_{\mathbf{k}} \frac{|\delta_L^{\text{soft}}(\mathbf{k})|^2}{2g^2 P(k)} \right\} \mathcal{P}[\delta_*; \delta_L^{\text{soft}}], \quad (6.61)$$

where

$$\mathcal{P}[\delta_*; \delta_L^{\text{soft}}] \equiv \int \mathcal{D}\delta_L^{\text{hard}} d\lambda \exp \left\{ - \frac{1}{g^2} \left[\int_{\mathbf{k}} \frac{|\delta_L^{\text{hard}}(\mathbf{k})|^2}{2P(k)} - \lambda (\delta_* - \bar{\delta}_W[\delta_L^{\text{hard}} + \delta_L^{\text{soft}}]) \right] \right\}, \quad (6.62)$$

has the physical meaning of the PDF for short-scale overdensities in the background of soft modes.

Now, the addition of a soft mode corresponds to immersion of the system into a large-scale flow. Due to the equivalence principle, the main effect of such flow is an overall translation of the hard modes by a distance proportional to the gradient of the Newtonian potential [19, 20, 23, 24, 156]. In other words,

$$\delta[\delta_L^{\text{hard}} + \delta_L^{\text{soft}}](\mathbf{x}, \eta) = \delta[\delta_L^{\text{hard}}] \left(\mathbf{x} - \frac{\nabla}{\Delta} \delta_L^{\text{soft}}(0, \eta), \eta \right) + \dots \quad (6.63)$$

The shift is enhanced for long-wavelength perturbations leading to $1/k_{\text{soft}}$ poles in the perturbative expansion of the expression (6.63) in δ_L^{soft} . On the other hand, the remaining terms represented by dots in (6.63) contain more derivatives acting on the Newtonian potential, and thus are regular in the limit when the soft momentum k_{soft} goes to zero.

The PDF (6.62) can be evaluated in the saddle-point approximation. The saddle-point solution is

$$\hat{\delta}_L[\delta_L^{\text{soft}}](\mathbf{x}) = \hat{\delta}_L \left(\mathbf{x} + \frac{\nabla}{\Delta} \delta_L^{\text{soft}}|_{\mathbf{x}=0} \right), \quad (6.64)$$

where $\hat{\delta}_L$ is the saddle-point configuration in the absence of soft modes. Likewise, the fluctuations around the solution (6.64) are obtained from those around $\hat{\delta}_L$ by the same translation, so that the integral over them does not contain any

poles. We conclude that $\mathcal{P}[\delta_*, \delta_L^{\text{soft}}]$ is IR-safe which implies the IR safety of the original PDF $\mathcal{P}(\delta_*)$.

6.3.2 Factorization of IR divergences

At $\ell = 1$ the equations (6.36) admit an exact solution

$$\delta_1 = \partial_r \hat{\delta} \cdot e^\eta, \quad \Theta_1 = \partial_r \hat{\Theta} \cdot e^\eta, \quad \Psi_1 = \partial_r \hat{\Psi} \cdot e^\eta + r \cdot e^\eta. \quad (6.65)$$

Notice that in the far past all contributions here vanish faster than e^η (actually, as $O(e^{2\eta})$), except for the last term in Ψ_1 . The latter corresponds to a uniform motion of all fluid elements¹⁰, i.e. to a large bulk flow. Existence of the solution (6.65) follows from the equivalence principle obeyed by the Euler-Poisson equations. Indeed, we can impose on any solution an infinitely large bulk flow that will sweep the original solution as a whole. The dipolar solution (6.65) precisely corresponds to imposing such a large bulk flow on the saddle-point configuration $(\hat{\delta}, \hat{\Theta}, \hat{\Psi})$.

The solution (6.65) can be added with an arbitrary coefficient to any other solution of eqs. (6.36). In particular, the perturbation with the initial conditions (6.38) for $\ell = 1$ can be written as,

$$\delta_{1,k} = \check{\delta}_k - \frac{4\pi}{3k} \partial_r \hat{\delta} e^\eta, \quad (6.66a)$$

$$\Theta_{1,k} = \check{\Theta}_k - \frac{4\pi}{3k} \partial_r \hat{\Theta} e^\eta, \quad (6.66b)$$

$$\Psi_{1,k} = \check{\Psi}_k - \frac{4\pi}{3k} \partial_r \hat{\Psi} e^\eta - \frac{4\pi r}{3k} e^\eta, \quad (6.66c)$$

where the triple $(\check{\delta}_k, \check{\Theta}_k, \check{\Psi}_k)$ is also a solution of eqs. (6.36) satisfying the same initial conditions (6.38a) for $\check{\delta}_k, \check{\Theta}_k$, but with modified initial condition for $\check{\Psi}_k$,

$$\check{\Psi}_k = \left[-\frac{4\pi}{k^2} j_1(kr) + \frac{4\pi r}{3k} \right] \cdot e^\eta. \quad (6.67)$$

Importantly, this modification eliminates the dangerous $1/k$ pole, so that the initial conditions for all functions $(\check{\delta}_k, \check{\Theta}_k, \check{\Psi}_k)$ are regular at $k \rightarrow 0$. In fact,

$$\check{\delta}_k, \check{\Theta}_k, \check{\Psi}_k = O(k). \quad (6.68)$$

Then, by linearity of eqs. (6.36), this property holds at all times.

¹⁰Recall that the gradient of Ψ is proportional to the fluid velocity, see eq. (6.31).

The next step is to isolate the IR divergences in the sources Υ_δ , Υ_Θ . Substituting (6.66) into (6.57), we obtain

$$\Upsilon_{\delta,kk'} = \frac{A_\delta}{kk'} + \frac{B_{\delta,k'}}{k} + \frac{B_{\delta,k}}{k'} + \check{\Upsilon}_{\delta,kk'} , \quad (6.69a)$$

$$\Upsilon_{\Theta,kk'} = \frac{A_\Theta}{kk'} + \frac{B_{\Theta,k'}}{k} + \frac{B_{\Theta,k}}{k'} + \check{\Upsilon}_{\Theta,kk'} , \quad (6.69b)$$

where

$$A_\delta = \frac{4\pi}{9} \partial_r \hat{\delta} (\partial_r^2 \hat{\Psi} + 1) e^{2\eta} , \quad (6.70a)$$

$$B_{\delta,k} = -\frac{1}{6} [(\partial_r^2 \hat{\Psi} + 1) \check{\delta}_k + \partial_r \hat{\delta} \partial_r \check{\Psi}_k] e^\eta , \quad (6.70b)$$

$$A_\Theta = \frac{4\pi}{9} \left[\partial_r \hat{\Theta} (\partial_r^2 \hat{\Psi} + 1) - \frac{2}{r} (\partial_r^2 \hat{\Psi})^2 + \frac{4}{r^2} \partial_r \hat{\Psi} \partial_r^2 \hat{\Psi} - \frac{2}{r^3} (\partial_r \hat{\Psi})^2 \right] e^{2\eta} , \quad (6.70c)$$

$$B_{\Theta,k} = -\frac{1}{6} \left[(\partial_r^2 \hat{\Psi} + 1) \check{\Theta}_k + \left(\partial_r \hat{\Theta} - \frac{4}{r} \partial_r^2 \hat{\Psi} + \frac{4}{r^2} \partial_r \hat{\Psi} \right) \partial_r \check{\Psi}_k + \left(\frac{4}{r^2} \partial_r^2 \hat{\Psi} - \frac{4}{r^3} \partial_r \hat{\Psi} \right) \check{\Psi}_k \right] e^\eta , \quad (6.70d)$$

and $\check{\Upsilon}_{\delta,kk'}$, $\check{\Upsilon}_{\Theta,kk'}$ are computed using the regular solutions $(\check{\delta}_k, \check{\Theta}_k, \check{\Psi}_k)$, $(\check{\delta}_{k'}, \check{\Theta}_{k'}, \check{\Psi}_{k'})$. Due to linearity of Eqs. (6.55), the pole structure of the sources (6.69) propagates into the pole structure of the matrix

$$Q_1(k, k') = \frac{A}{kk'} + \frac{B(k')}{k} + \frac{B(k)}{k'} + \check{Q}(k, k') , \quad (6.71)$$

where A , B , \check{Q} are found by solving Eqs. (6.55) with the sources (A_δ, A_Θ) , (B_δ, B_Θ) and $(\check{\Upsilon}_\delta, \check{\Upsilon}_\Theta)$ respectively. Due to the property (6.68) we have

$$B(k) = O(k) , \quad \check{Q}(k, k') = O(kk') \quad \text{at } k, k' \rightarrow 0 . \quad (6.72)$$

We now observe that the sought-for determinant has the form,

$$\mathcal{D}_1 = \det \left(\mathbb{1} + 2\hat{\lambda} \sqrt{P} \check{Q} \sqrt{P} + a(k)b(k') + b(k)a(k') \right) , \quad (6.73)$$

with

$$a(k) = \hat{\lambda} \frac{\sqrt{P(k)}}{k} , \quad b(k) = \left(\frac{A}{k} + 2B(k) \right) \sqrt{P(k)} . \quad (6.74)$$

Denoting

$$M(k, k') = (2\pi)^3 k^{-2} \delta_D^{(1)}(k - k') + 2\hat{\lambda} \sqrt{P(k)} \check{Q}(k, k') \sqrt{P(k')} \quad (6.75)$$

we write,

$$\mathcal{D}_1 = \det M \cdot \mathcal{D}^{IR} , \quad (6.76)$$

where all IR-sensitive contributions have been collected into

$$\mathcal{D}^{IR} = \det (\mathbb{1} + \tilde{a} \otimes \tilde{b} + \tilde{b} \otimes \tilde{a}) . \quad (6.77)$$

We have introduced $\tilde{a} = M^{-1/2}a$, $\tilde{b} = M^{-1/2}b$ and used the fact that the matrix M is symmetric.

The determinant (6.77) can be easily evaluated using Eq. (D.1) from Appendix D of Ref. [9],

$$\mathcal{D}^{IR} = 1 + 2(\tilde{a} \cdot \tilde{b}) + (\tilde{a} \cdot \tilde{b})^2 - \tilde{a}^2 \tilde{b}^2 . \quad (6.78)$$

Here dot denotes the scalar product,

$$\tilde{a} \cdot \tilde{b} = \int [dk] \tilde{a}(k) \tilde{b}(k) = \int [dk][dk'] a(k) M^{-1}(k, k') b(k') ,$$

and similarly for \tilde{a}^2 and \tilde{b}^2 . The inverse matrix M^{-1} has the form,

$$M^{-1} = \mathbb{1} - 2\hat{\lambda} \sqrt{P} \mathring{Q} \sqrt{P} \quad (6.79)$$

with

$$\mathring{Q}(k, k') = \check{Q}(k, k') + \dots = O(kk') \quad \text{at small } k, k' . \quad (6.80)$$

Using this property one isolates the ‘IR-divergences’ in the different terms¹¹ in (6.78),

$$2(\tilde{a} \cdot \tilde{b}) \ni 2\hat{\lambda} \int [dk] \frac{P(k)}{k^2} A \quad (6.81a)$$

$$\begin{aligned} (\tilde{a} \cdot \tilde{b})^2 - \tilde{a}^2 \tilde{b}^2 \ni & -4\hat{\lambda}^2 \int [dk]^2 \frac{P(k_1)}{k_1^2} P(k_2) (B(k_2))^2 \\ & + 8\hat{\lambda}^3 \int [dk]^3 \frac{P(k_1)}{k_1^2} P(k_2) P(k_3) \mathring{Q}(k_2, k_3) B(k_2) B(k_3) . \end{aligned} \quad (6.81b)$$

A necessary and sufficient condition for their cancellation in the determinant (6.78) is,

$$A = 2\hat{\lambda} \int [dk]^2 \sqrt{P(k_1)P(k_2)} B(k_1) M^{-1}(k_1, k_2) B(k_2) . \quad (6.82)$$

While we do not have a direct proof of this identity, the arguments of the previous subsection imply that it must be satisfied. We also checked it numerically and found that it is fulfilled in our computations within the accuracy of the numerical procedure.

¹¹ As in perturbation theory, for the realistic power spectrum these terms are finite, but still dangerously enhanced. They would be actually divergent if the power spectrum behaved as $P(k) \propto k^n$ with $n \leq -1$ at small k .

Using (6.82) we can simplify the expression (6.78). A straightforward calculation yields,

$$\mathcal{D}^{IR} = \left[1 + 2\hat{\lambda} \int [dk]^2 \sqrt{P(k_1)P(k_2)} \frac{1}{k_1} M^{-1}(k_1, k_2) B(k_2) \right]^2. \quad (6.83)$$

This is the final expression to be used in numerical evaluation. The algorithm for the computation of \mathcal{D}_1 consists of the following steps:

1. Solve the linear equations (6.36) with initial conditions (6.38a), (6.67) to find the functions $\check{\delta}_k, \check{\Theta}_k, \check{\Psi}_k$;
2. Find the matrix $\check{Q}(k, k')$ by solving Eqs. (6.55) with the sources $\check{\Upsilon}_{\delta, kk'}, \check{\Upsilon}_{\Theta, kk'}$;
3. Find the vector $B(k)$ by solving Eqs. (6.55) with the sources $B_{\delta, k}, B_{\Theta, k}$, Eqs. (6.70b), (6.70d);
4. Construct the matrix $M(k, k')$, Eq. (6.75), compute its determinant and inverse;
5. Use the inverse matrix $M^{-1}(k, k')$ and the vector $B(k)$ to compute the IR contribution (6.83);
6. Compute the full determinant in the dipole sector as a product of $\det M$ and \mathcal{D}^{IR} .

6.4 WKB approximation for high multipoles

In general the computation of the aspherical fluctuation determinant requires solving the system of linear partial differential equations (6.36) on a grid. However, in the sectors with large orbital numbers $\ell \gg 1$ one can use the Wentzel-Kramers-Brillouin (WKB) technique to simplify the problem and gain insights into the structure of the aspherical response matrix. Remarkably, in the WKB regime the system (6.36) reduces to a system of ordinary differential equations and can be easily solved, e.g. in *Mathematica*. The WKB analysis serves both to cross check the results of the full numerical integration of Eqs. (6.36) and to study the UV sensitivity of the aspherical prefactor in Sec. 6.5.2.

We start by noticing that the basis functions (6.38) are suppressed at $kr < \ell$ due to the centrifugal barrier. Indeed, at these values of r we obtain using

Eq. (10.19.3) from¹²,

$$j_\ell((\ell + 1/2)\varkappa r) \sim \frac{e^{-(\ell+1/2)\left(\operatorname{arcch}\frac{1}{\varkappa r} - \sqrt{1-(\varkappa r)^2}\right)}}{(2\ell + 1)\sqrt{\varkappa r}[1 - (\varkappa r)^2]^{1/4}}, \quad (6.84)$$

where we have introduced the ratio

$$\varkappa \equiv \frac{k}{\ell + 1/2} \quad (6.85)$$

which will be kept fixed in the limit $\ell \rightarrow \infty$. We see that $j_\ell(kr)$ is exponentially suppressed at $\varkappa r < 1$. Thus, if $kr_* \ll \ell$ the perturbation has support outside of the window function and does not contribute into the variation of the overdensity: $Q_\ell(k, k') \approx 0$ whenever k or k' is much smaller than ℓ/r_* . We conclude that the dominant contribution into the response matrix comes from the modes with

$$k \gtrsim \ell/r_* \gg 1/r_* . \quad (6.86)$$

These modes oscillate much faster than the background, so we can use the WKB technique to find their evolution.

We will see that we have to go up to the second order in the WKB expansion, hence we write the following Ansatz:

$$\begin{aligned} \delta_\ell &= (\delta_{\ell 1} + k^{-1}\delta_{\ell 2})e^{ikS_\ell} + \text{h.c.} , \\ \Theta_\ell &= (\Theta_{\ell 1} + k^{-1}\Theta_{\ell 2})e^{ikS_\ell} + \text{h.c.} , \\ \Psi_\ell &= (k^{-2}\Psi_{\ell 1} + k^{-3}\Psi_{\ell 2})e^{ikS_\ell} + \text{h.c.} \end{aligned} \quad (6.87)$$

where $\delta_{\ell 1}, \delta_{\ell 2}$ etc. are slowly varying functions. Note that Ψ_ℓ is suppressed by two powers of k compared to δ_ℓ and Θ_ℓ . From the Poisson equation (6.36c) we find at leading order

$$\Psi_{\ell 1} = -\frac{\Theta_{\ell 1}}{(S'_\ell)^2 + (\varkappa r)^{-2}} . \quad (6.88a)$$

The next-to-leading expansion yields,

$$\Psi_{\ell 2} = \frac{-\Theta_{\ell 2} + iS''_\ell\Psi_{\ell 1} + 2iS'_\ell\Psi'_{\ell 1} + \frac{2iS'_\ell}{r}\Psi_{\ell 1}}{(S'_\ell)^2 + (\varkappa r)^{-2}} . \quad (6.88b)$$

Further, we substitute the form (6.87) into the dynamical Eqs. (6.36a), (6.36b). At leading order $O(k)$ both equations reduce to

$$\dot{S}_\ell - \partial_r \hat{\Psi} S'_\ell = 0 . \quad (6.89)$$

¹²“Digital Library of Mathematical Functions,” <http://dlmf.nist.gov>.

In the combination on the l.h.s. one recognizes the time-derivative along the background flow, so one concludes that S_ℓ is conserved along the flow,

$$\left. \frac{dS_\ell}{d\eta} \right|_{\text{flow}} = 0. \quad (6.90)$$

In other words, $S_\ell(r, \eta) = S_\ell(R(r, \eta))$, where R is the Lagrangian coordinate of the spherical shell in the background solution. It is related to the Eulerian coordinate r and η by Eq. (5.13) where for the density contrast one takes the saddle-point profile $\hat{\delta}(r, \eta)$. At $\eta \rightarrow -\infty$ the Lagrangian and Eulerian coordinates coincide, $R = r$.

From the orders $O(1)$ and $O(1/k)$ of Eqs. (6.36a), (6.36b) we obtain the equations for the coefficient functions in the WKB Ansatz:

Next-to Leading Order,

$$\left. \frac{d\delta_{\ell 1}}{d\eta} \right|_{\text{flow}} - \hat{\Theta}\delta_{\ell 1} - (1 + \hat{\delta})\Theta_{\ell 1} = 0, \quad (6.91a)$$

$$\left. \frac{d\Theta_{\ell 1}}{d\eta} \right|_{\text{flow}} - \frac{3}{2}\delta_{\ell 1} + \left[\frac{1}{2} - \frac{2(\varkappa r S'_\ell)^2 \partial_r^2 \hat{\Psi}}{1 + (\varkappa r S'_\ell)^2} - \frac{2\partial_r \hat{\Psi}}{r(1 + (\varkappa r S'_\ell)^2)} \right] \Theta_{\ell 1} = 0. \quad (6.91b)$$

Next-to-Next-to-Leading Order,

$$\left. \frac{d\delta_{\ell 2}}{d\eta} \right|_{\text{flow}} - \hat{\Theta}\delta_{\ell 2} - (1 + \hat{\delta})\Theta_{\ell 2} = i\partial_r \hat{\delta} S'_\ell \Psi_{\ell 1}, \quad (6.92a)$$

$$\begin{aligned} \left. \frac{d\Theta_{\ell 2}}{d\eta} \right|_{\text{flow}} - \frac{3}{2}\delta_{\ell 2} + \left[\frac{1}{2} - \frac{2(\varkappa r S'_\ell)^2 \partial_r^2 \hat{\Psi}}{1 + (\varkappa r S'_\ell)^2} - \frac{2\partial_r \hat{\Psi}}{r(1 + (\varkappa r S'_\ell)^2)} \right] \Theta_{\ell 2} \\ = \frac{4iS'_\ell}{1 + (\varkappa r S'_\ell)^2} \left(\partial_r^2 \hat{\Psi} - \frac{\partial_r \hat{\Psi}}{r} \right) \Psi'_{\ell 1} \\ + \left[i\partial_r \hat{\Theta} S'_\ell + \frac{2i}{1 + (\varkappa r S'_\ell)^2} \left(S''_\ell - \frac{2S'_\ell (\varkappa r S'_\ell)^2}{r} \right) \left(\partial_r^2 \hat{\Psi} - \frac{\partial_r \hat{\Psi}}{r} \right) \right] \Psi_{\ell 1}. \end{aligned} \quad (6.92b)$$

We notice that Eqs. (6.91) do not contain spatial derivatives of $\delta_{\ell 1}, \Theta_{\ell 1}$, so that they form a system of ordinary differential equations for these functions. The same is true for Eqs. (6.92) with respect to the functions $\delta_{\ell 2}, \Theta_{\ell 2}$.

To set up the initial conditions we use the asymptotic expansion for the Bessel function at large order (Eq. (10.19.6) from¹³),

$$j_\ell \left(\frac{\ell + 1/2}{\cos \beta} \right) = \frac{\cos \beta}{(\ell + 1/2)\sqrt{\sin \beta}} \left(\cos \xi + \frac{1}{8(\ell + 1/2)} \left(\text{ctg } \beta + \frac{5}{3} (\text{ctg } \beta)^3 \right) \sin \xi + O(\ell^{-2}) \right), \quad (6.93)$$

¹³“Digital Library of Mathematical Functions,” <http://dlmf.nist.gov>.

where

$$\xi = (\ell + 1/2)(\text{tg } \beta - \beta) - \pi/4. \quad (6.94)$$

Substituting this into (6.38) and comparing with the WKB Ansatz (6.87) we find the initial conditions at $\eta \rightarrow -\infty$,

$$S_\ell = \frac{1}{\varkappa} \left[\sqrt{(\varkappa r)^2 - 1} - \arccos \frac{1}{\varkappa r} \right], \quad (6.95a)$$

$$\delta_{\ell 1} = \Theta_{\ell 1} = -\Psi_{\ell 1} = \frac{e^\eta}{\ell + 1/2} \cdot \frac{2\pi}{\sqrt{\varkappa r} [(\varkappa r)^2 - 1]^{1/4}} \cdot e^{-i\pi/4}, \quad (6.95b)$$

$$\delta_{\ell 2} = \Theta_{\ell 2} = -\Psi_{\ell 2} = \frac{e^\eta}{\ell + 1/2} \cdot \frac{\pi \varkappa}{4\sqrt{\varkappa r}} \left(\frac{1}{[(\varkappa r)^2 - 1]^{3/4}} + \frac{5}{3[(\varkappa r)^2 - 1]^{7/4}} \right) \cdot e^{-i3\pi/4}. \quad (6.95c)$$

Equation (6.90) with the initial conditions (6.95a) is readily solved giving

$$S_\ell = \frac{1}{\varkappa} \left[\sqrt{(\varkappa R)^2 - 1} - \arccos \frac{1}{\varkappa R} \right]. \quad (6.96)$$

We observe that in the large- ℓ limit the function S_ℓ becomes universal (ℓ -independent). The WKB approximation is valid as long as

$$S_\ell'' / (S_\ell')^2 \ll k \quad (6.97)$$

which is equivalent to

$$|\varkappa R - 1| \gg (\ell + 1/2)^{-2/3}. \quad (6.98)$$

Next, Eqs. (6.91) for the first-order WKB coefficients can be integrated numerically along the flow lines (i.e. at fixed R) starting from the initial conditions (6.95b). We will see shortly that the functions $\delta_{\ell 1}$, $\Theta_{\ell 1}$ need to be evaluated only in the vicinity of the flow line $R = R_*$ corresponding to the boundary of the spherical region that collapses to the cell of radius r_* at the final time. Knowing $\Theta_{\ell 1}$, one finds $\Psi_{\ell 1}$ by Eq. (6.88a) and inserts it in the r.h.s. of (6.92). Finally, Eqs. (6.92) are integrated at fixed R starting from the initial configuration (6.95c). Again, we will need $\delta_{\ell 2}$, $\Theta_{\ell 2}$ only at R_* . Notice that the r.h.s. of (6.92) involves the radial derivative $\Psi'_{\ell 1}$. Thus, evaluating the first-order functions precisely at R_* would be insufficient: one needs to know them in a small vicinity of this point¹⁴.

The factor $(\ell + 1/2)^{-1}$ in the initial conditions (6.95b), (6.95c) implies that the WKB solution is suppressed in the limit $\ell \rightarrow \infty$. This leads to a suppression of

¹⁴Alternatively, one can take radial derivatives of Eqs. (6.91) and in this way obtain a system of ordinary differential equations for $\delta'_{\ell 1}$, $\Theta'_{\ell 1}$. Then $\Psi'_{\ell 1}$ is computed from $\Theta'_{\ell 1}$ by using the radial derivative of Eq. (6.88a).

the sources $\Upsilon_{\delta,\Theta}$ appearing on the r.h.s. of Eqs. (6.55) and hence a suppression of the response matrix Q_ℓ . Then the fluctuation determinant can be approximated using the trace formula,

$$\mathcal{D}_\ell \approx \exp\left(2\hat{\lambda} \text{Tr}PQ_\ell\right), \quad (6.99)$$

and for its calculation it suffices to focus on the diagonal elements of the response matrix $Q_\ell(k, k)$. The sources for these elements are obtained by substituting the WKB solution with a single wavenumber k into (6.43). For the first source this yields,

$$\begin{aligned} \Upsilon_\delta = & \frac{1}{4\pi} \left[\frac{iS'_\ell}{k} \delta_{\ell 1} \Psi_{\ell 1} + \frac{1}{k^2} \left(\delta_{\ell 1} \Psi'_{\ell 1} + iS'_\ell \delta_{\ell 1} \Psi_{\ell 2} + iS'_\ell \delta_{\ell 2} \Psi_{\ell 1} \right) \right] e^{i2kS_\ell} \\ & + \frac{1}{4\pi k^2} \left(\delta_{\ell 1}^* \Psi'_{\ell 1} + iS'_\ell \delta_{\ell 1}^* \Psi_{\ell 2} + iS'_\ell \delta_{\ell 2}^* \Psi_{\ell 1} \right) + \text{h.c.} \end{aligned} \quad (6.100)$$

The term in the first line is quickly oscillating. In the eventual integral over k that appears in the Q_ℓ -trace it will average to zero. Neglecting it we get,

$$\overline{\Upsilon_\delta(\hat{r}_\eta)} = \frac{1}{2\pi k^2} \left[\tilde{\delta}_{\ell 1} \frac{\partial \tilde{\Psi}_{\ell 1}}{\partial R} + \frac{\partial S_\ell}{\partial R} (\tilde{\delta}_{\ell 1} \tilde{\Psi}_{\ell 2} - \tilde{\delta}_{\ell 2} \tilde{\Psi}_{\ell 1}) \right] \frac{\partial R}{\partial r} \Big|_{R_*}, \quad (6.101a)$$

where the overline means averaging over the oscillations. Here we denoted by tildes the functions with the complex phases stripped off¹⁵ and switched from the Eulerian to the Lagrangian radial coordinate R . Similarly, for the source Υ_Θ we have,

$$\begin{aligned} \overline{\Upsilon_\Theta(\hat{r}_\eta)} = & \frac{1}{2\pi k^2} \left\{ \left[\tilde{\Theta}_{\ell 1} \frac{\partial \tilde{\Psi}_{\ell 1}}{\partial R} + \frac{\partial S_\ell}{\partial R} (\tilde{\Theta}_{\ell 1} \tilde{\Psi}_{\ell 2} - \tilde{\Theta}_{\ell 2} \tilde{\Psi}_{\ell 1}) + \frac{2}{(\varkappa \hat{r}_\eta)^2} \tilde{\Psi}_{\ell 1} \frac{\partial \tilde{\Psi}_{\ell 1}}{\partial R} \right] \frac{\partial R}{\partial r} \right. \\ & \left. - \frac{2}{\hat{r}_\eta} \left(\frac{\partial S_\ell}{\partial R} \right)^2 \tilde{\Psi}_{\ell 1}^2 \left(\frac{\partial R}{\partial r} \right)^2 - \frac{1}{\varkappa^2 \hat{r}_\eta^3} \tilde{\Psi}_{\ell 1}^2 \right\} \Big|_{R_*}. \end{aligned} \quad (6.101b)$$

These relations allow us to extract the asymptotic dependence of the response matrix on ℓ and k . We first observe that k and ℓ appear in the dynamical equations (6.91), (6.92) only in the combination \varkappa . Together with the form (6.95) of the initial conditions this implies that the coefficient function $\delta_{\ell 1}$, $\delta_{\ell 2}$ etc. have a universal dependence on \varkappa , up to an overall factor $(\ell + 1/2)^{-1}$. This, in turn, implies that the sources (6.101) are functions of \varkappa times an overall factor $k^{-2}(\ell + 1/2)^{-2}$. On general grounds, the matrix elements of Q_ℓ are linear

¹⁵In other words, $\tilde{\delta}_{\ell 1} \equiv \delta_{\ell 1} e^{i\pi/4}$, $\tilde{\delta}_{\ell 2} \equiv \delta_{\ell 2} e^{i3\pi/4}$ and so on.

functionals of the sources,

$$Q_\ell(k, k) = \int_{-\infty}^0 d\eta \left(K_\delta(\eta) \Upsilon_\delta(\hat{r}_\eta, \eta; k, \ell) + K_\Theta(\eta) \Upsilon_\Theta(\hat{r}_\eta, \eta; k, \ell) \right), \quad (6.102)$$

with some kernels $K_{1,2}$ that do not depend on ℓ and k . This leads to the expression,

$$\overline{Q_\ell(k, k)} = k^{-2}(\ell + 1/2)^{-2} q(\varkappa), \quad (6.103)$$

where the function q depends only on the ratio (6.85).

We can now collect the contributions of all high- ℓ multipoles to the prefactor,

$$\begin{aligned} \mathcal{A}_{\text{high-}\ell} &= \exp \left[-2\hat{\lambda} \sum_{\ell} (\ell + 1/2) \text{Tr} Q_\ell P \right] \\ &= \exp \left[-2\hat{\lambda} \int d\varkappa q(\varkappa) \sum_{\ell} (2\pi)^{-3} P(\varkappa(\ell + 1/2)) \right]. \end{aligned} \quad (6.104)$$

The sum over ℓ converges as long as the power spectrum falls down faster than k^{-1} in the UV, which coincides with the condition for the convergence of the 1-loop corrections in the standard cosmological perturbation theory. One can show that $q(\varkappa) \propto \varkappa^{-2}$ at large values of \varkappa (see below), so the integral over \varkappa will converge as well. Still, the expression (6.104) receives large contributions from unphysical UV modes and must be renormalized just like the 1-loop correction to the power spectrum is renormalized in EFT of LSS. We will return to this issue in Sec. 6.5.2.

Let us discuss the lower limit of integration in (6.104). From the arguments of the beginning of this section we know that $q(\varkappa) = 0$ for $\varkappa R_* < 1$, so the integral in (6.104) should be taken from $\varkappa = R_*^{-1}$ to infinity. The WKB result for the function $q(\varkappa)$ and hence for the integral is valid at

$$\varkappa > (1 + \epsilon)/R_* , \quad \epsilon \gg \ell^{-2/3} . \quad (6.105)$$

One would like to extend the WKB expression for the integral down to $\varkappa = R_*^{-1}$ hoping that the error made in the region $1 < \varkappa R_* < 1 + \epsilon$ is small. However, here we encounter a problem. The expressions (6.95b), (6.95c) imply that the functions $\delta_{\ell 1}$, $\delta_{\ell 2}$, etc. have a singular behavior at $\varkappa \rightarrow R_*^{-1}$. Due to the locality of Eqs. (6.91), (6.92) this singularity survives the time evolution and gives rise to singular terms in the sources (6.101) behaving as $[(\varkappa R_*)^2 - 1]^{-3/2}$. Further, the representation (6.102) implies that the singularity is inherited by the function $q(\varkappa)$, so its integral actually diverges at the lower limit as $\epsilon^{-1/2}$. As shown in Appendix F of Ref. [9], this is an artifact of the WKB approximation and

the divergence is canceled by a boundary term produced by the integral over the interval $(1-\epsilon)/R_* < \varkappa < (1+\epsilon)/R_*$ which is not captured by the WKB method. The net result is that an integral of $q(\varkappa)$ with a smooth function $\varphi(\varkappa)$ should be understood as

$$\int d\varkappa q(\varkappa)\varphi(\varkappa) = \lim_{\epsilon \rightarrow 0} \left(\int_{(1+\epsilon)/R_*}^{\infty} d\varkappa q(\varkappa)\varphi(\varkappa) - \frac{2C}{\sqrt{\epsilon}} \right), \quad (6.106)$$

with

$$C = R_*^{-1}\varphi(R_*^{-1}) \lim_{\varkappa \rightarrow 1/R_*} [\varkappa R_* - 1]^{3/2} q(\varkappa). \quad (6.107)$$

A numerically efficient way to evaluate this integral is described in Appendix F of Ref. [9]. In the next section we will see that the WKB approximation becomes accurate for orbital numbers $\ell \geq 9$.

Before closing this section, let us discuss the limit $\varkappa \rightarrow \infty$, corresponding to $k \gg (\ell + 1/2)/r_*$. In this limit all the above formulas greatly simplify. From Eq. (6.96) we get $S_\ell = R$. Also \varkappa drops off the equations (6.91), (6.92) for the coefficient functions. In the initial conditions (6.95b), (6.95c) \varkappa factors out, so that all coefficient functions become simply proportional to $1/\varkappa$. This translates into the following asymptotics of the function $q(\varkappa)$,

$$q(\varkappa) = \frac{q_\infty}{\varkappa^2}, \quad \text{at } \varkappa \gg 1/R_*. \quad (6.108)$$

Alternatively, for the diagonal elements of the response matrix we obtain

$$\overline{Q_\ell(k, k)} = \frac{q_\infty}{k^4}, \quad \text{at } k \gg (\ell + 1/2)/R_*. \quad (6.109)$$

Note that this high- k asymptotics is ℓ -independent. Although it has been derived under the assumption of large ℓ , one can show that in fact it holds for any¹⁶ ℓ , including $\ell = 0$. Thus, we can determine q_∞ using the exact expression for the response matrix in the monopole sector. Comparing (6.109) to (G.33) we get,

$$q_\infty = \frac{6\pi}{R_*^4} \left(-\frac{3\hat{E}}{\hat{C}^3} + \frac{1}{\hat{C}^2(1 + \delta_*)} \right), \quad (6.110)$$

where \hat{C} , \hat{E} are defined in (5.29), (G.32) respectively. We have verified that the numerically computed function $q(\varkappa)$ satisfies the asymptotics (6.108) with q_∞ from (6.110) with very high precision.

¹⁶To obtain (6.109) at arbitrary fixed ℓ and $k \rightarrow \infty$, one can use a slightly modified version of the WKB expansion based on the asymptotics of Bessel functions at large arguments.

6.5 Aspherical prefactor: results

6.5.1 Evaluation of fluctuation determinants

In this section we present the results obtained by a fully-nonlinear numerical calculation of the aspherical prefactor. We follow the algorithm discussed in Sec. 6.2.3: compute the linear aspherical fluctuations on the grid, use them to build the sources $\Upsilon_{\Theta,\delta}$, solve the ODE's governing the time evolution of the response matrix, and finally compute the fluctuation determinants. For the dipole sector we have implemented the IR safe algorithm discussed in Sec. 6.3.2. The details of our numerical procedure are presented in Appendix H. We have evaluated the aspherical prefactor both in the EdS approximation and for the exact Λ CDM cosmology and found that the results agree within one percent accuracy. This is consistent with the fact that the departures from EdS appear only at late times. However, at this stage the coupling of the fluctuations to the local spherical collapse background already dominates the effect of the cosmological expansion, so the effect of the cosmological constant is suppressed. In what follows we display the results obtained within the EdS approximation.

Figure 6.3 shows individual contributions of different multipoles to the aspherical prefactor. We fix the cell size to $r_* = 10 \text{ Mpc}/h$; the results for $r_* = 15 \text{ Mpc}/h$ are similar. The most significant contribution comes from the dipole sector and is shown in the upper left panel. We observe that it is a decreasing convex function that changes by a factor ~ 0.2 between $\delta_* = -0.9$ and $\delta_* = 9$. At large δ_* the curve flattens out. The contributions of the multipoles with $2 \leq \ell \leq 5$ and $6 \leq \ell \leq 9$ are shown in the upper right and lower left panels respectively. These curves are quite different from the dipole: their deviation from unity in the explored δ_* -range is only $\sim 40\%$ for the quadrupole and even less ($\lesssim 10\%$) for the higher multipoles. The variation of \mathcal{A}_ℓ decreases with the multipole number. Note that in the case of overdensities ($\delta_* > 0$) all \mathcal{A}_ℓ are less than 1 which is consistent with the expectation that any aspherical fluctuation makes collapse less efficient. On the other hand, at underdensities the partial contributions \mathcal{A}_ℓ can be both larger or smaller than unity, depending on the value of ℓ .

The aggregate contribution of all sectors with $\ell > 9$ is shown in the lower right panel of Fig. 6.3. It has been evaluated using the WKB formula (6.104). We test the validity of the WKB approximation by comparing it to the results of the full numerical routine in Fig. 6.4. The comparison is performed for $\ell = 5$ (left panel) and $\ell = 9$ (right panel). For $\ell = 5$ there is a significant difference between the full

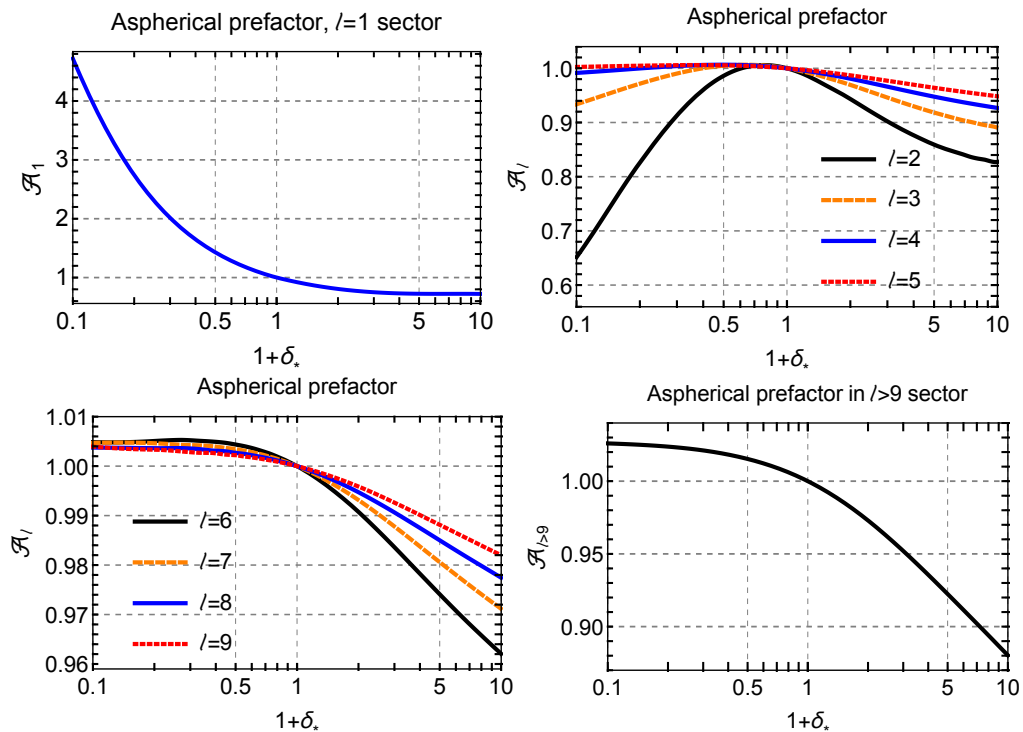


FIGURE 6.3: The prefactor of aspherical fluctuations in different orbital sectors. Upper left panel: the dipole ($\ell = 1$) sector. Upper right panel: $\ell = 2, 3, 4, 5$ sectors. Lower left panel: $\ell = 6, 7, 8, 9$ sectors. Lower right panel: the cumulative prefactor for orbital numbers $\ell > 9$ computed in the WKB approximation. All results are shown for $r_* = 10 \text{ Mpc}/h$.

calculation and the WKB approximation at strong underdensities. At overdensities the WKB approximation exhibits spurious wiggles that can be traced back to the baryon acoustic oscillations in the power spectrum¹⁷. However, already for $\ell = 9$ the WKB approximation is in perfect agreement with the full result. We have checked that the relative error introduced in the aggregate contribution of $\ell > 9$ by the use of the WKB approximation does not exceed 10^{-3} . Given that this contribution itself is small compared to that of lower multipoles, the error in the whole prefactor is negligible.

The total result for the aspherical prefactor obtained upon multiplying the contributions of all $\ell \geq 1$ is shown in Fig. 6.5, where it is compared with the prefactor extracted from the N-body data (see Sec. 5.2.2). One observes a good qualitative agreement between the theoretical curve and the data. However, there is a clear quantitative discrepancy which grows towards the edges of the δ_* -interval. The discrepancy is somewhat bigger for $r_* = 10 \text{ Mpc}/h$ than for $r_* = 15 \text{ Mpc}/h$ and

¹⁷The WKB formula (6.104) has an enhanced sensitivity to the shape of the power spectrum at $k \sim (\ell + 1/2)/R_*$ due to the sharp increase of the function $q(\varkappa)$ in the vicinity of the point $\varkappa = 1/R_*$. This unphysical sensitivity disappears for higher multipoles.

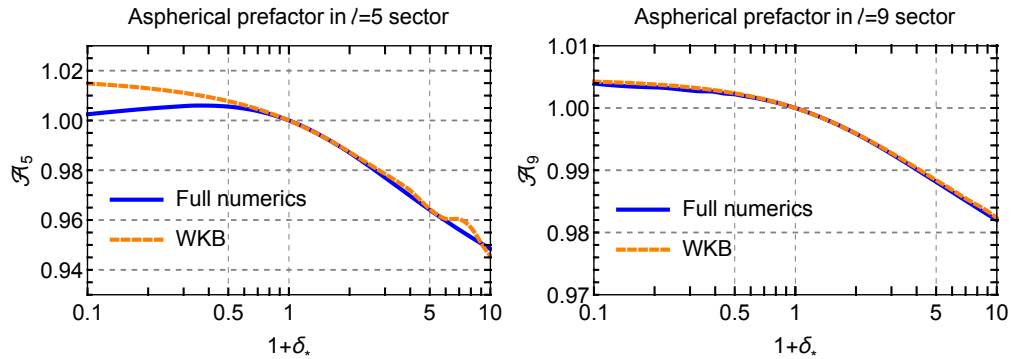


FIGURE 6.4: Comparison between the WKB approximation and the full numerical calculation for $\ell = 5$ (left panel) and $\ell = 9$ (right panel). The results are shown for $r_* = 10 \text{ Mpc}/h$.

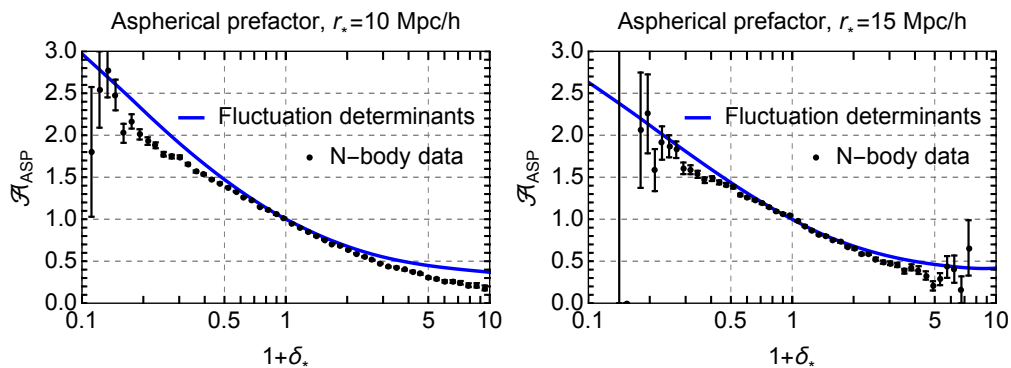


FIGURE 6.5: The aspherical prefactor computed from fluctuation determinants (solid blue curve) against that extracted from the N-body simulations (black dots). The cell radii are $r_* = 10 \text{ Mpc}/h$ (left panel) and $r_* = 15 \text{ Mpc}/h$ (right panel).

reaches 30% (100%) for underdense (overdense) tail. We interpret this discrepancy as the effect of short-scale physics that is not captured by the perfect-fluid hydrodynamics. In the next subsection we show how our results can be improved by renormalizing the contributions of short-scale modes.

Let us make a comment. The fact that the fluctuation determinants found in our calculation are always positive provides a consistency check of the saddle-point approximation developed in Sec. 5.1. In particular, it shows that there are no other saddle points of the path integral (5.5) that would branch off the spherical collapse dynamics at any value of δ_* within the considered range. Indeed, if it were the case the spectrum of fluctuations around the spherical collapse at this value of δ_* would contain a zero mode, and hence at least one of the determinants \mathcal{D}_ℓ would vanish, which is not observed.

6.5.2 Renormalization of short-scale contributions

Up to this point we have worked within pressureless perfect fluid hydrodynamics, which is known to break down at short scales. This introduces an error in our calculation that must be corrected. A similar issue arises in the perturbative calculation of the density correlation functions in the homogeneous background where a systematic way to take into account the corrections due to UV modes is provided by introduction of counterterms in the hydrodynamics equations. These counterterms are constructed as a double expansion in the number of spatial derivatives acting on the fields and in the powers of the density contrast [34]. We have encountered this procedure in Sec. 6.1 where we made contact between the calculation of the prefactor at small density contrast and the calculation of 1-loop corrections to the power spectrum. At that level the sensitivity to the short-scale physics reduced to a single counterterm $\gamma(z)$, see Eq. (6.17).

The situation is more complicated at large density contrasts δ_* which we are interested in now. In this case, the evaluation of the aspherical prefactor can be viewed as a 1-loop calculation in the non-trivial background of the spherical collapse solution. Then the counterterm is, in general, a functional of the background, restricted by the symmetries of the problem, but otherwise arbitrary. It is impossible to rigorously fix its form without going beyond the EFT framework. In what follows we consider two schemes for renormalization of the aspherical prefactor that are based on reasonable physical assumptions. The difference between the two models should be treated as an intrinsic theoretical uncertainty of our current determination of \mathcal{A}_{ASP} due to the lack of control over the UV physics.

We start by analyzing the UV sensitivity of the aspherical prefactor. The contribution of modes with $k > k_{\text{UV}} \gg 1/r_*$, $\ell \gg 1$ is described by the WKB expression (6.104). The sum over ℓ in the exponent can be rewritten as an integral,

$$\begin{aligned} \int_{k_{\text{UV}}}^{\infty} \frac{dkP(k)}{(2\pi)^3} \sum_{\ell} \frac{1}{\ell + 1/2} q\left(\frac{k}{\ell + 1/2}\right) &\simeq \int_{k_{\text{UV}}}^{\infty} \frac{dkP(k)}{(2\pi)^3} \int \frac{d\ell}{\ell + 1/2} q\left(\frac{k}{\ell + 1/2}\right) \\ &= \int_{k_{\text{UV}}}^{\infty} \frac{dkP(k)}{(2\pi)^3} \int \frac{d\mathcal{K}}{\mathcal{K}} q(\mathcal{K}). \end{aligned} \quad (6.111)$$

We observe that the integral over momenta and the background dependence contained in the function q factorize. In other words, all high- k modes contribute into \mathcal{A}_{ASP} in a universal way. Of course, this is true only within the domain of validity of the formula (6.104) which neglects the interaction among the short

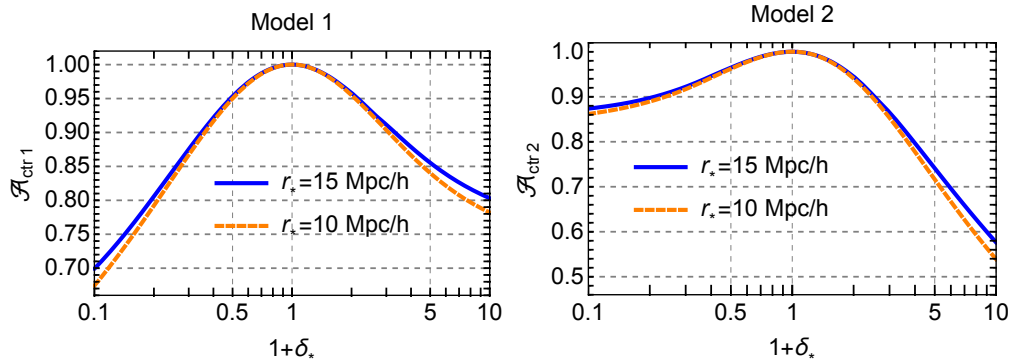


FIGURE 6.6: The counterterm prefactor for model 1 (left panel) and model 2 (right panel) evaluated for $\gamma_0 = 1.5 \text{ (Mpc/h)}^2$, $z = 0$ and cell radii $r_* = 10 \text{ Mpc/h}$ and $r_* = 15 \text{ Mpc/h}$.

modes and the departures from the hydrodynamic description. Precisely because of this inaccuracy, the integral over k in (6.111) should be renormalized.

The integral in (6.111) is proportional to the high- k contribution into the velocity dispersion

$$\sigma_v^2 \equiv \frac{1}{6\pi^2} \int dk P(k). \quad (6.112)$$

The same integral arises in the 1-loop correction to the power spectrum (see (6.22)) where it is renormalized by the substitution

$$\int \frac{dk P(k)}{(2\pi)^3} \mapsto \int \frac{dk P(k)}{(2\pi)^3} + \frac{315}{122\pi} \frac{\gamma(z)}{g^2(z)}. \quad (6.113)$$

We saw in Sec. 6.1.2 that this substitution also works for the aspherical prefactor at small δ_* . Our first model for the renormalization of \mathcal{A}_{ASP} is obtained by extending the prescription (6.113) to finite values of δ_* . It corresponds to an assumption that the main effect of renormalization in all quantities is the replacement of the tree-level velocity dispersion of high- k modes with its renormalized value¹⁸. For the redshift dependence of the counterterm we will use the scaling-universe approximation, as we did in Sec. 6.1.2. In this way we arrive at the following expression for the counterterm prefactor,

$$\mathcal{A}_{\text{ctr1}} = \exp \left(-\frac{315\gamma_0}{122\pi} (g(z))^{-\frac{2(n+1)}{n+3}} \times 2\hat{\lambda} \int \frac{d\mathcal{X}}{\mathcal{X}} q(\mathcal{X}) \right), \quad (6.114)$$

where γ_0 is the 1-loop counterterm from the power spectrum and n is the slope of the power spectrum at the mildly non-linear scales. For numerical estimates

¹⁸This assumption is supported by the observation [150] that the N-body data for bispectrum are well fitted by the EFT formula without any additional counterterms beyond γ (“0-parameter fit” in [150]). Inclusion of further independent counterterms allowed by the EFT framework does not significantly improve the quality of the fit.

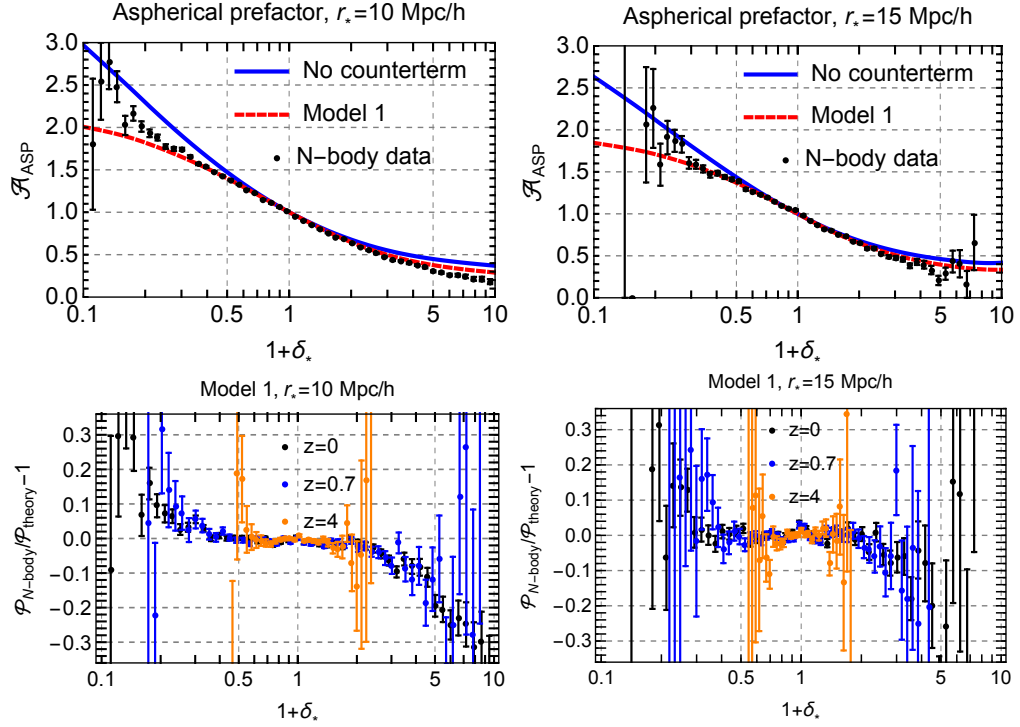


FIGURE 6.7: Upper panels: The aspherical prefactor in model 1 (dashed red curve) against the N-body data (black dots) for cell radii $r_* = 10$ Mpc/h (left panel) and $r_* = 15$ Mpc/h (right panel) at $z = 0$. The aspherical prefactor without the counterterm is reproduced for comparison (solid blue curve). Lower panels: Residuals for the PDF extracted from the N-body data compared to our theoretical prediction at several redshifts for $r_* = 10$ Mpc/h (left panel) and $r_* = 15$ Mpc/h (right panel).

we will use $\gamma_0 = 1.5 (\text{Mpc}/h)^2$, $n = -1.5$. The final answer for the aspherical prefactor is given by the product of (6.114) with the contribution obtained from the fluctuation determinants and described in the previous subsection. We will refer to the aspherical prefactor calculated using the counterterm (6.114) as “model 1”.

The counterterm prefactor (6.114) is plotted in the left panel of Fig. 6.6. We see that it captures the main qualitative features: it has a zero derivative at the origin where we expect the impact of shell-crossing to be negligible, and suppresses the probability for big under- and overdensities. In the upper panels of Fig. 6.7 we plot the aspherical prefactor in model 1 against the data. The aspherical prefactor without the counterterm is also shown for comparison. In the lower panels of Fig. 6.7 we show the residuals between the PDF measured from the N-body data and our theoretical template for several values of redshift. One observes a good agreement between the theory and the data. For $r_* = 10$ Mpc/h the residuals are at sub-percent level in the range $-0.6 < \delta_* < 1$. They degrade to 10% at $-0.8 < \delta_* < -0.6$ and $1 < \delta_* < 3$. Eventually they increase to $\sim 30\%$

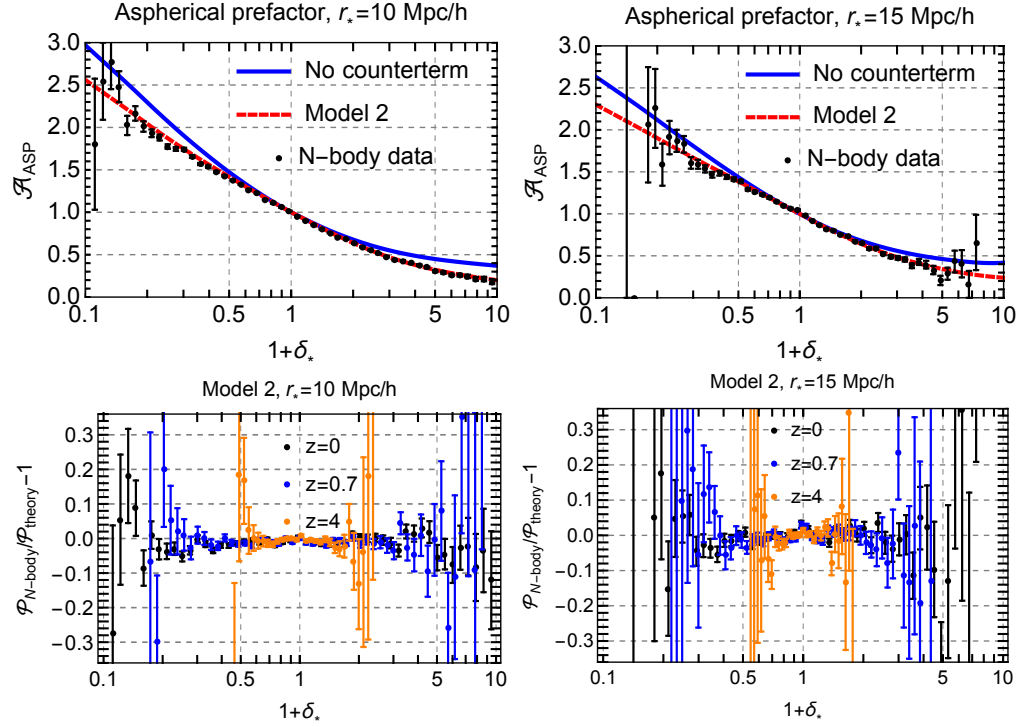


FIGURE 6.8: Upper panels: The aspherical prefactor in model 2 (dashed red curve) against the N-body data (black dots) for cell radii $r_* = 10 \text{ Mpc}/h$ (left panel) and $r_* = 15 \text{ Mpc}/h$ (right panel) at $z = 0$. The aspherical prefactor without the counterterm is reproduced for comparison (solid blue curve). Lower panels: Residuals for the PDF extracted from the N-body data compared to our theoretical prediction at several redshifts for $r_* = 10 \text{ Mpc}/h$ (left panel) and $r_* = 15 \text{ Mpc}/h$ (right panel).

at the tails. Overall, the agreement is slightly better for the underdensities than for the overdensities. Similar trends are observed for $r_* = 15 \text{ Mpc}/h$, though the precision of the N-body data is too low to see them unambiguously. It is worth noting that on general grounds one expects the effects of the UV physics to be weaker for larger cells.

As clear from Fig. 6.7, the model 1 systematically underestimates the aspherical prefactor for underdensities and overestimates for overdensities. This can be attributed to the following deficiency. We have taken the counterterm γ to be independent of δ_* . On the other hand, one expects the overdense regions to be more non-linear than the underdense ones, so that the effects of UV renormalization encapsulated by γ should be larger (smaller) at $\delta_* > 0$ ($\delta_* < 0$) than at $\delta_* = 0$. Comparing this with the formula (6.114) one sees that qualitatively such a dependence would act in the right direction to improve the agreement between the theory and the data.

To estimate a possible effect of the δ_* -dependence of γ , we use the following

crude model. We approximate the spherical collapse solution by top-hat density profile with the final under-/over-density δ_* . Treating such a profile as an open/closed separate universe, we replace the counterterm and the growth factor in Eq. (6.113) by $\gamma(\delta_*, z)$ and $D(\delta_*, z)$ — the counterterm and the growth factor in the separate universe. The latter is derived in Appendix G.4. To estimate $\gamma(\delta_*, z)$ we again use the power-law approximation for the power spectrum and obtain $\gamma(\delta_*, z) \propto (D(\delta_*, z))^{\frac{4}{n+3}}$. All in all, this leads to the replacement of $g(z)$ in the counterterm prefactor (6.114) by the density-dependent growth factor $D(\delta_*, z)$. Using the explicit expression for the latter, Eq. (G.39), we obtain model 2 for the counterterm,

$$\mathcal{A}_{\text{ctr2}} = \exp \left(-\frac{315\gamma_0}{122\pi} \left(\frac{g(z)}{F'(\delta_*)(1+\delta_*)} \right)^{-\frac{2(n+1)}{n+3}} \times 2\hat{\lambda} \int \frac{d\mathcal{Z}}{\mathcal{Z}} q(\mathcal{Z}) \right), \quad (6.115)$$

This counterterm prefactor is shown in the right panel of Fig. 6.6. Compared to the model 1, it gives less suppression at underdensities and stronger suppresses overdensities. In the upper panels of Fig. 6.8 we compare the aspherical prefactor in model 2 with the N-body data and the prefactor without the counterterm. In the lower panels of Fig. 6.8 we show the residuals between the PDF measured from the N-body data and our theoretical template for $z = 0, 0.7, 4$. One observes an excellent agreement between the theory and the data within the precision of the latter. This is striking given the crudeness of the model.

We leave a detailed investigation of the counterterms in the spherical collapse background for future and propose to treat the difference between the models 1 and 2 as a proxy for the theoretical uncertainty. Notice that this uncertainty estimate is internal to the theoretical approach and does not require any comparison with N-body simulations. We also emphasize that none of the two counterterm models proposed in this section introduces any additional fitting parameter, as the coefficient γ_0 entering in Eqs. (6.114), (6.115) must be the same as the one measured from the dark matter power spectrum.

Chapter 7

Summary of Part II

In the second part of this thesis we computed the 1-point probability distribution function (PDF) of the cosmic matter density field in spherical cells. Our approach makes use of the path integral description of large-scale structure. We identified the saddle point of the path integral that corresponds to the spherical collapse dynamics and yields the leading exponent of the PDF. Then we computed the prefactor given by the determinant of the quadratic fluctuations around the saddle-point solution. This can be viewed as a 1-loop calculation in perturbation theory around a fully non-linear background.

We showed that the prefactor factorizes into the contributions of fluctuations in different multipole sectors and evaluated the monopole contribution exactly. Next we considered the contribution of fluctuations with $\ell > 0$ which we called ‘the aspherical prefactor’ \mathcal{A}_{ASP} . We demonstrated that it is crucial for the consistency of the PDF, in particular, for ensuring that the mean density contrast evaluated using the PDF vanishes. Our final formula for the 1-point PDF has the form,

$$\bar{P}(\delta_*) = \mathcal{A}_{\text{ASP}}(\delta_*) \frac{\hat{C}(\delta_*)}{\sqrt{2\pi g^2 \sigma_{R_*}^2}} e^{-\frac{F^2(\delta_*)}{2g^2 \sigma_{R_*}^2}}, \quad (7.1)$$

where $g(z)$ is the linear growth factor, σ_{R_*} is the *linear* density variance at $z = 0$ filtered at the Lagrangian radius $R_* = r_*(1 + \delta_*)^{1/3}$, $F(\delta_*)$ is the linear overdensity corresponding to δ_* through the spherical collapse mapping, and the function $\hat{C}(\delta_*)$ is defined by the formula (5.29).

We computed the aspherical prefactor using several techniques. First, we treated the background perturbatively, which allowed us to capture the correct shape of the prefactor for small averaged densities. Second, we computed the partial contributions to the prefactor from sectors with high orbital numbers treating the

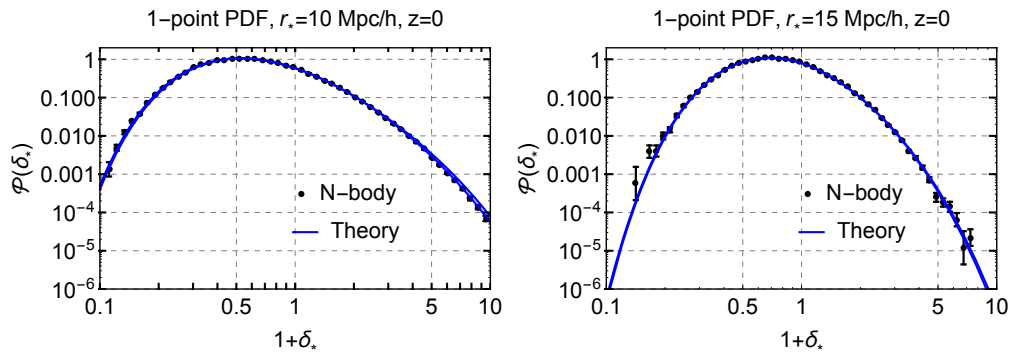


FIGURE 7.1: 1-point probability distribution function computed in this work (blue band) against that extracted from our N-body data (black dots). The results are presented for redshift zero, $z = 0$, and two cell radii, $r_* = 10 \text{ Mpc}/h$ (left panel) and $r_* = 15 \text{ Mpc}/h$ (right panel). The width of the theoretical band is set by the uncertainty in modelling the short-distance physics; it exceeds the line width only at the tails of the distribution.

background non-perturbatively. We showed that this limit allows one to use the WKB technique, which made possible a semi-analytic treatment of the problem. Finally, we developed a numerical procedure for a fully non-linear computation of the aspherical determinant on the grid. This procedure includes analytic factorization and cancellation of the so-called ‘IR-divergences’ — spurious enhanced contributions that appear in the dipole sector and are associated with large bulk flows. We implemented this procedure in an open-source Python code `AsPy` available at the following [link](#).

We compared the results of our computation to the N-body data. Despite a qualitative agreement, we observed a sizable quantitative discrepancy, which we attributed to the failure of the pressureless fluid approximation at short scales. We proposed two models for renormalization of the short-scale contributions in the spirit of the EFT of LSS. The two models agree at the percent level at moderate density contrasts and deviate by at most 30% at the tails of the distribution. We have suggested to use the difference between the two models as an estimate of the theoretical uncertainty of our approach stemming from the lack of control over the short-distance physics.

The resulting theoretical PDFs for cells with radii $r_* = 10 \text{ Mpc}/h$ and $15 \text{ Mpc}/h$ at $z = 0$ are shown against N-body data in Fig. 7.1. The lines corresponding to the two counterterm models are almost indistinguishable. We see that the theory and the data are in excellent agreement. The theoretical uncertainty is smaller for the larger radius, which is consistent with the expectation that the UV effects should be suppressed at large distances.

The 1-point PDF has a very distinctive sensitivity to the dynamics and initial statistics of the matter density perturbations. One observes from Eq. (7.1) that the dependence of the PDF on the filtered linear density variance $g\sigma_{R_*}$ factorizes. By varying δ_* one effectively changes the filtering radius, and thus probes the variance of the density field at different scales. Going to the underdense tail allows one to test the linear power spectrum at very small Lagrangian radii, i.e. at the scales which are beyond the regime of validity of the standard cosmological perturbation theory.

We have shown that the prefactor in (7.1) has only a weak dependence on cosmology. Thus, any variation of the cosmological parameters or extension of Λ CDM is expected to affect the PDF primarily through the leading exponent. Even a small change in the growth factor or the linear variance can have a strong effect on the PDF. On the other hand, the sensitivity to the non-linear dynamics at leading order is encoded in the spherical collapse mapping $F(\delta_*)$. It will be interesting to understand to which extent this property of the 1-point PDF can be used to constrain non-standard dark matter scenarios or modifications of gravity.

The expansion parameter in our approach is the linear density variance smoothed at the scale of the window function. Thus, corrections to our result for the aspherical prefactor are expected to scale as $O((g\sigma_{r_*})^2)$, c.f. Eq. (5.8). On the other hand, our comparison with the N-body data has not revealed any presence of such corrections for $(g\sigma_{r_*})^2$ as large as ~ 0.5 (for $z = 0$, $r_* = 10\text{Mpc}/h$, see Table 5.1). This indicates that the coefficient in front of the correction is suppressed. Nevertheless, as one decreases the cell radius, the corrections will grow and eventually the ‘semiclassical’ approximation is expected to break down. Another limitation of our method in its present form is its reliance on the existence of an analytic spherical collapse saddle-point solution. As discussed in Sec. 5.1.2, this assumption is actually violated for large overdensities $\delta_* \gtrsim 7$ where the saddle-point solution exhibits shell crossing. Remarkably, the N-body data still obey the ‘semiclassical’ scaling up to the maximal value $\delta_* = 9$ that we were able to explore. We have interpreted it as a consequence of the slow signal propagation in dark matter which implies that the information about the shell crossing in the inner part of the density profile does not have enough time to reach the boundary of the cell. However, an extension to yet higher overdensities will likely require a modification of the semiclassical method to properly take the shell crossing into account, cf. [96]. It would be highly instructive to map the domain of validity of the ‘semiclassical’ formula (7.1) in the space of cell radii r_* and densities δ_* using high-precision counts-in-cells statistics obtained from state of the art cosmological simulations.

Let us briefly comment on the relation between the PDF derived in this work and the log-normal distribution that has been widely used in the literature to model the counts-in-cells statistics. As discussed in Appendix I, the success of the log-normal model does not appear to have any physical meaning, but is a consequence of an accidental conspiracy between the spherical collapse dynamics and the shape of the power spectrum in our universe, that makes the combination $F(\delta_*)/\sigma_{R_*}$ entering in the exponent of (7.1) look similar to $\ln(1 + \delta_*)/\sigma_{\ln}$, where σ_{\ln} is the log-density variance. A change of the slope of the power spectrum would destroy this conspiracy. Even for the standard Λ CDM the approximation of F/σ_{R_*} by the logarithm does not work for large under- and over-densities. Moreover, the log-normal model does not incorporate the correct prefactor. As a result, it significantly deviates from the N-body data in the tails of the distribution (cf. Refs. [81, 91]).

Before concluding, we summarize several key features of our approach:

1. It clearly separates the leading exponent from the prefactor. This allows us to keep the saddle-point expansion under control and disentangle the cosmology-dependent effects from those of non-linear clustering.
2. We use the exact Λ CDM mapping for spherical collapse. This is crucial for the accuracy of our calculation, as the PDF is exponentially sensitive to the mapping.
3. It explicitly takes into account aspherical fluctuations along with the contributions beyond the single-stream pressureless perfect fluid approximation.
4. It is based on the first principles and does not introduce any fitting parameters.
5. It provides an intrinsic estimate of the theoretical uncertainty that does not require an input from the N-body data.
6. It increases the range of agreement between the analytic theory and N-body simulations compared to previous approaches.

In this thesis we have studied the simplest case of non-perturbative cosmological statistics: 1-point PDF of dark matter in real space for Gaussian adiabatic initial conditions. Applications to realistic observations, such as galaxy surveys, Lyman- α forest or 21 cm intensity mapping will require extension of the method to the biased tracers in redshift space. Another line of research is the statistics of the 2-dimensional projected density field and weak lensing convergence. Last

but not least, a generalization to the 2-point PDF will be very interesting as a way to probe the primordial non-Gaussianity.

Chapter 8

Concluding remarks

In this thesis we developed several analytic tools to describe the formation of cosmological large-scale structure. We mainly focused on two questions: non-linear evolution of baryon acoustic oscillations (BAO) and counts in cells statistics of the matter density field. Both questions were addressed using the path integral formalism, which has proven to be an extremely efficient tool in many areas of science ranging from economics to mathematical physics. We have shown that the path integral formulation of large-scale structure allows one to build a consistent and systematic framework that encompasses both perturbative and non-perturbative aspects of structure formation. The analytic tools developed in this thesis helped us explore the resummation of IR contributions relevant for the accurate description of the BAO and the probability distribution function of the spherically averaged matter density field. We hope that these tools will also find broad applications in other areas related to large-scale structure. Below we summarize main results as they appear in the thesis.

We have developed a systematic procedure to resum enhanced infrared (IR) contributions that are present in cosmological perturbation theory. A resummation of these contributions is required to capture the non-linear deformation of the BAO pattern due to bulk motions. The corresponding procedure is called ‘IR resummation’. We have shown that time-sliced perturbation theory (TSPT) provides an optimal framework for this task: the building blocks of this formalism are explicitly IR finite and therefore reveal a transparent IR structure of cosmological perturbation theory. We built a new method that allowed one to identify and resum the contributions affecting the BAO to any desired level of accuracy. Most importantly, this method has a simple and intuitive diagrammatic representation. We introduced power counting rules that allowed us to easily estimate

the contribution of each diagram in the perturbative expansion. This way one can clearly spot all the diagrams relevant at a given order of precision and resum them to all orders in perturbation theory. Moreover, our power-counting rules give an estimate of the theoretical error at each step of IR resummation. This allowed us to perform IR resummation for arbitrary n -point correlation function of matter and biased tracers at leading order in the IR corrections and to all orders in hard loops. We computed, for the first time, the next-to-leading IR corrections to the matter power spectrum and argued that they can be relevant given the accuracy level required by future surveys. The next-to-leading order soft corrections are also important for the robust estimation of the non-linear shift of the baryon acoustic peak in position space. Our results agree very well with the output of N-body simulations. The theoretical template obtained in this study has been used in the eBOSS data analysis of the BAO in the distribution of quasars [6].

We have also incorporated the effects of redshift space distortions. This has been done via a new method that allows one to map cosmological correlation functions from real to redshift space. This mapping preserves a transparent IR structure of the theory and retains advantageous properties of TSPT, such as IR finiteness and a simple diagrammatic representation. This allowed for an accurate description of the BAO by means of a systematic resummation of Feynman diagrams akin to the one used in the case of real space.

We expect that the path integral formulation of cosmological perturbation theory pursued in this thesis will also help to ameliorate our understanding of the UV counterterms required to properly account for the effects of short-scale physics. We leave this question for future study.

The second part of the thesis was devoted to counts in cells statistics. There we performed a non-perturbative calculation of the 1-point probability distribution function (PDF) for the spherically-averaged matter density field. To accomplish this task we represented the PDF as a path integral and evaluated it using the steepest-descent method. We have explicitly found the saddle point of this integral that corresponds to the spherical collapse dynamics and determines the leading exponent of the PDF. At a next step we used a combination of analytic and numerical methods to evaluate the prefactor, which contains the contribution of aspherical fluctuations on top of the fully non-linear spherical collapse background. We have also identified the sensitivity to the short-scale physics and argued that it must be properly renormalized. We have argued that UV renormalization of the aspherical prefactor requires the same UV counterterm

as the one-loop matter power spectrum, hence our theoretical templates do not have any free parameters whatsoever. Our approach is self-contained in the sense that it also provides a way to assess the theoretical uncertainty of the model. We checked our theoretical predictions against the results of N -body simulations and found an excellent agreement.

The final theoretical PDF splits into the prefactor and the leading exponent. The leading exponent is sensitive to the initial distribution of the density field and gives an extraordinary opportunity to probe the linear matter power spectrum at the scales where perturbation theory is not applicable. On the other hand, the prefactor contains some information on the n -point correlation functions, and therefore provides us with a relatively simple way to test the density field beyond the two-point statistics. We believe that our study will pave a way toward a systematic investigation of non-perturbative statistics as potentially powerful cosmological probes.

Appendix A

Conventions

In this Appendix we summarize our main notations and conventions. The Fourier transform is defined as,

$$\delta(\mathbf{x}) = \int_{\mathbf{k}} \delta(\mathbf{k}) e^{i\mathbf{k}\cdot\mathbf{x}}, \quad (\text{A.1})$$

where the integration measure in momentum space is

$$\int_{\mathbf{k}} = \int \frac{d^3k}{(2\pi)^3}, \quad (\text{A.2})$$

and its generalization to multiple wavenumbers,

$$\int_{\mathbf{k}_1 \dots \mathbf{k}_n} = \int \prod_{i=1}^n \frac{d^3k_i}{(2\pi)^3}. \quad (\text{A.3})$$

We also use the shorthand notation for the radial integral in momentum space,

$$\int [dk] = \int_0^\infty \frac{k^2 dk}{(2\pi)^3}, \quad (\text{A.4})$$

and its generalization to several wavenumbers,

$$\int [dk]^n = \int \prod_{i=1}^n \frac{k_i^2 dk_i}{(2\pi)^3}, \quad (\text{A.5})$$

The power spectrum is defined as,

$$\langle \delta(\mathbf{k}) \delta(\mathbf{k}') \rangle = (2\pi)^3 \delta_{\text{D}}^{(3)}(\mathbf{k} + \mathbf{k}') P(k), \quad (\text{A.6})$$

where $\delta_{\text{D}}^{(d)}(\mathbf{k})$ is the Dirac delta-function in a d -dimensional space.

We use the following notation for the sum of 3-dimensional wavenumbers:

$$\mathbf{k}_{1\dots n} = \mathbf{k}_1 + \dots + \mathbf{k}_n . \quad (\text{A.7})$$

We use the following definition for the spherical harmonics:

$$Y_0(\theta, \phi) = 1 , \quad (\text{A.8a})$$

$$Y_{\ell m}(\theta, \phi) = \frac{(-1)^{\ell+m}}{2^\ell \ell!} \left[\frac{2\ell+1}{4\pi} \frac{(\ell-|m|)!}{(\ell+|m|)!} \right]^{1/2} e^{im\phi} (\sin \theta)^{|m|} \left(\frac{d}{d \cos \theta} \right)^{\ell+|m|} (\sin \theta)^{2\ell} ,$$

$$\ell > 0 , \quad -\ell < m < \ell . \quad (\text{A.8b})$$

They obey the relations,

$$\Delta_\Omega Y_{\ell m} = -\ell(\ell+1)Y_{\ell m} , \quad Y_{\ell m}(-\mathbf{n}) = (-1)^\ell Y_{\ell m}(\mathbf{n}) , \quad Y_{\ell m}^*(\mathbf{n}) = Y_{\ell, -m}(\mathbf{n}) , \quad (\text{A.9})$$

where Δ_Ω is the Laplacian on a unit 2-dimensional sphere. All harmonics are orthogonal and normalized to 1 when integrated over a 2d sphere, except the monopole that has the norm 4π ,

$$\int d\Omega Y_{\ell m} Y_{\ell' m'}^* = (4\pi)^{\delta_{0\ell}} \delta_{\ell\ell'} \delta_{mm'} , \quad (\text{A.10})$$

where δ_{ij} is the Kronecker delta symbol. Note that our definition (A.8b) differs by a factor $(-1)^{\frac{m-|m|}{2}}$ from the standard conventions¹.

We expand the fields over spherical harmonics in position and Fourier space as,

$$\delta(\mathbf{x}) = \delta_0(r) + \sum_{\ell>0} \sum_{m=-\ell}^{\ell} \delta_{\ell m}(r) Y_{\ell m}(\mathbf{x}/r) , \quad (\text{A.11a})$$

$$\delta(\mathbf{k}) = \delta_0(k) + \sum_{\ell>0} \sum_{m=-\ell}^{\ell} (-i)^\ell \delta_{\ell m}(k) Y_{\ell m}(\mathbf{k}/k) . \quad (\text{A.11b})$$

Due to the relations (A.9) we have,

$$(\delta_{\ell m}(r))^* = (\delta_{\ell, -m}(r)) , \quad (\delta_{\ell m}(k))^* = (\delta_{\ell, -m}(k)) . \quad (\text{A.12})$$

The coefficient functions in the above expansions are related by,

$$\delta_{\ell m}(r) = 4\pi \int [dk] j_\ell(kr) \delta_{\ell m}(k) , \quad (\text{A.13})$$

¹“Digital Library of Mathematical Functions,” <http://dlmf.nist.gov>.

where $j_\ell(x)$ is the spherical Bessel function of order ℓ . It is related to the Bessel function of the first kind via

$$j_\ell(x) = \sqrt{\frac{\pi}{2x}} J_{\ell+1/2}(x). \quad (\text{A.14})$$

The first few functions are,

$$j_0(x) = \frac{\sin x}{x}, \quad j_1(x) = \frac{\sin x}{x^2} - \frac{\cos x}{x}, \quad j_2(x) = \left(-\frac{1}{x} + \frac{3}{x^3}\right) \sin x - \frac{3}{x^2} \cos x. \quad (\text{A.15})$$

Spherical Bessel functions $j_\ell(kr)$ with different arguments k form an orthogonal basis on the half-line with the normalization

$$\int_0^\infty dr r^2 j_\ell(k'r) j_\ell(kr) = \frac{\pi}{2k^2} \delta_D^{(1)}(k - k'). \quad (\text{A.16})$$

They are eigenmodes of the radial part of the Laplace operator,

$$\partial_r^2 j_\ell(kr) + \frac{2}{r} \partial_r j_\ell(kr) - \frac{\ell(\ell+1)}{r^2} j_\ell(kr) = -k^2 j_\ell(kr). \quad (\text{A.17})$$

Appendix B

Asymptotic behavior of the Γ_n vertices in the soft limit

In this Appendix we study in detail the form of the TSPT vertices with soft legs in real and redshift spaces. We will omit the superscript (r) in sections [B.1](#), [B.2](#), [B.3](#) where we will discuss only real space quantities. [Sec. B.4](#) is devoted to the redshift space vertices. First, we derive the leading order expression ([3.22](#)). Next, we extend the analysis to include the subleading corrections and obtain [Eq. \(3.62\)](#), as well as the expression for the four-point vertex evaluated on the modified linear power spectrum used in the derivation of [Eq. \(3.67\)](#).

B.1 Recursion relations for TSPT vertices

For convenience, we start by reviewing the main building of TSPT in the exact dynamics (ED) and Zel'dovich approximation (ZA). Note that by ‘exact dynamics’, as common in the LSS literature, we actually mean pressureless perfect fluid hydrodynamics [\[1\]](#) without the EFT corrections. To define the building blocks of TSPT one starts with the non-linear SPT kernels,

$$\alpha(\mathbf{k}_1, \mathbf{k}_2) \equiv \frac{(\mathbf{k}_1 + \mathbf{k}_2) \cdot \mathbf{k}_1}{k_1^2}, \quad \beta(\mathbf{k}_1, \mathbf{k}_2) \equiv \frac{(\mathbf{k}_1 + \mathbf{k}_2)^2 (\mathbf{k}_1 \cdot \mathbf{k}_2)}{2k_1^2 k_2^2}. \quad (\text{B.1})$$

These are used to write down the recursion relations for the vertices K_n and $\bar{\Gamma}_n$ [\[1\]](#). The seeds for these relation are $K_1 = 1$ and $\bar{\Gamma}_2$ given by [Eq. \(2.17a\)](#). Higher

vertices are different for ZA and ED. We have

$$\text{ZA: } K_2(\mathbf{k}_1, \mathbf{k}_2) = \sin^2(\mathbf{k}_1, \mathbf{k}_2) \equiv 1 - \frac{(\mathbf{k}_1 \cdot \mathbf{k}_2)^2}{k_1^2 k_2^2}, \quad (\text{B.2})$$

$$\text{ED: } K_2(\mathbf{k}_1, \mathbf{k}_2) = \frac{4}{7} \sin^2(\mathbf{k}_1, \mathbf{k}_2). \quad (\text{B.3})$$

For $n \geq 3$ the recursion relations read,

ZA:

$$\begin{aligned} K_n(\mathbf{k}_1, \dots, \mathbf{k}_n) = & \frac{1}{n} \left[\sum_{i=1}^n \alpha(\mathbf{k}_i, \sum_{1 \leq j \leq n, j \neq i} \mathbf{k}_j) K_{n-1}(\mathbf{k}_1, \dots, \check{\mathbf{k}}_i, \dots, \mathbf{k}_n) \right. \\ & \left. - \sum_{1 \leq i < j \leq n} I_2(\mathbf{k}_i, \mathbf{k}_j) K_{n-1}(\mathbf{k}_i + \mathbf{k}_j, \mathbf{k}_1, \dots, \check{\mathbf{k}}_i, \dots, \check{\mathbf{k}}_j, \dots, \mathbf{k}_n) \right], \end{aligned} \quad (\text{B.4a})$$

$$\bar{\Gamma}_n(\mathbf{k}_1, \dots, \mathbf{k}_n) = -\frac{1}{n-2} \sum_{1 \leq i < j \leq n} I_2(\mathbf{k}_i, \mathbf{k}_j) \bar{\Gamma}_{n-1}(\mathbf{k}_i + \mathbf{k}_j, \mathbf{k}_1, \dots, \check{\mathbf{k}}_i, \dots, \check{\mathbf{k}}_j, \dots, \mathbf{k}_n), \quad (\text{B.4b})$$

and

ED:

$$\begin{aligned} K_n(\mathbf{k}_1, \dots, \mathbf{k}_n) = & \frac{2}{2n+3} \left[\sum_{i=1}^n \alpha(\mathbf{k}_i, \sum_{1 \leq j \leq n, j \neq i} \mathbf{k}_j) K_{n-1}(\mathbf{k}_1, \dots, \check{\mathbf{k}}_i, \dots, \mathbf{k}_n) \right. \\ & - \sum_{1 \leq i < j \leq n} I_2(\mathbf{k}_i, \mathbf{k}_j) K_{n-1}(\mathbf{k}_i + \mathbf{k}_j, \mathbf{k}_1, \dots, \check{\mathbf{k}}_i, \dots, \check{\mathbf{k}}_j, \dots, \mathbf{k}_n) \\ & \left. - \frac{3}{2} \sum_{p=3}^{n-1} \frac{1}{p!(n-p)!} \sum_{\sigma} K_p(\mathbf{k}_{\sigma(1)}, \dots, \mathbf{k}_{\sigma(p)}) K_{n-p+1} \left(\sum_{l=1}^p \mathbf{k}_{\sigma(l)}, \mathbf{k}_{\sigma(p+1)}, \dots, \mathbf{k}_{\sigma(n)} \right) \right], \end{aligned} \quad (\text{B.5a})$$

$$\begin{aligned} \bar{\Gamma}_n(\mathbf{k}_1, \dots, \mathbf{k}_n) = & -\frac{1}{n-2} \sum_{1 \leq i < j \leq n} I_2(\mathbf{k}_i, \mathbf{k}_j) \bar{\Gamma}_{n-1}(\mathbf{k}_i + \mathbf{k}_j, \mathbf{k}_1, \dots, \check{\mathbf{k}}_i, \dots, \check{\mathbf{k}}_j, \dots, \mathbf{k}_n) \\ & - \frac{3}{2(n-2)} \sum_{p=3}^{n-1} \frac{1}{p!(n-p)!} \sum_{\sigma} K_p(\mathbf{k}_{\sigma(1)}, \dots, \mathbf{k}_{\sigma(p)}) \bar{\Gamma}_{n-p+1} \left(\sum_{l=1}^p \mathbf{k}_{\sigma(l)}, \mathbf{k}_{\sigma(p+1)}, \dots, \mathbf{k}_{\sigma(n)} \right). \end{aligned} \quad (\text{B.5b})$$

where

$$I_2(\mathbf{k}_1, \mathbf{k}_2) = \begin{cases} 2\beta(\mathbf{k}_1, \mathbf{k}_2) & \text{for ZA} \\ 2\beta(\mathbf{k}_1, \mathbf{k}_2) + \frac{3}{2} K_2(\mathbf{k}_1, \mathbf{k}_2) & \text{for ED} \end{cases} \quad (\text{B.6})$$

The notation $\check{\mathbf{k}}_i$ above means that the momentum \mathbf{k}_i is absent from the arguments of the corresponding function, and in the last lines of (B.5a), (B.5b) the

summation is performed over all permutations σ of n indices.

B.2 Γ_n vertices in the soft limit: leading order

We split the arguments of the vertices into ‘hard’ momenta \mathbf{k}_i , $1 \leq i \leq m$, $\mathbf{k}_m = -\sum_{i=1}^{m-1} \mathbf{k}_i$, that are fixed and ‘soft’ momenta \mathbf{q}_j , which are sent uniformly to zero,

$$\mathbf{q}_j = \varepsilon \tilde{\mathbf{q}}_j, \quad \varepsilon \rightarrow 0. \quad (\text{B.7})$$

To prove (3.22) we proceed by induction. Let us fix $m \geq 2$ and assume that Eq. (3.22) has been already proved for all $m' < m$. Equation (3.22) holds trivially for $n = m$. Now, suppose that it is valid for all n' such that $m \leq n' < n$. Our task is to show that it also holds for n .

We focus on the case of exact dynamics (perfect fluid hydrodynamics); the derivation for the Zel’dovich approximation can be recovered by simply ignoring all contributions due to the K_n kernels. We will use the shorthand $\mathbf{q} \equiv \sum_{j=1}^{n-m} \mathbf{q}_j$. It is convenient to decompose the $\bar{\Gamma}_n^w$ into two pieces,

$$\bar{\Gamma}_n^w = \bar{\Gamma}_{n,A}^w + \bar{\Gamma}_{n,B}^w, \quad (\text{B.8})$$

which correspond respectively to the first and second lines in the recursion relation (B.5b). Consider first $\bar{\Gamma}_{n,A}^w$. We have,

$$\begin{aligned} \bar{\Gamma}_{n,A}^w(\mathbf{k}_1, \dots, \mathbf{k}_m - \mathbf{q}, \mathbf{q}_1, \dots, \mathbf{q}_{n-m}) &= \frac{-1}{n-2} \left[\sum_{1 \leq i < j < m} I_2(\mathbf{k}_i, \mathbf{k}_j) \bar{\Gamma}_{n-1}^w(\mathbf{k}_i + \mathbf{k}_j, \dots, \check{\mathbf{k}}_i, \dots, \check{\mathbf{k}}_i, \dots) \right. \\ &+ \sum_{1 \leq i < m} I_2(\mathbf{k}_i, \mathbf{k}_m - \mathbf{q}) \bar{\Gamma}_{n-1}^w(\mathbf{k}_i + \mathbf{k}_m - \mathbf{q}, \dots, \check{\mathbf{k}}_i, \dots, \check{\mathbf{k}}_m - \check{\mathbf{q}}, \dots) \\ &+ \sum_{i=1}^{m-1} \sum_{j=1}^{n-m} I_2(\mathbf{k}_i, \mathbf{q}_j) \bar{\Gamma}_{n-1}^w(\dots, \mathbf{k}_i + \mathbf{q}_j, \dots, \check{\mathbf{q}}_j, \dots) \\ &+ \sum_{j=1}^{n-m} I_2(\mathbf{k}_m - \mathbf{q}, \mathbf{q}_j) \bar{\Gamma}_{n-1}^w(\dots, \mathbf{k}_m - \mathbf{q} + \mathbf{q}_j, \dots, \check{\mathbf{q}}_j, \dots) \\ &\left. + \sum_{1 \leq i < j \leq n-m} I_2(\mathbf{q}_i, \mathbf{q}_j) \bar{\Gamma}_{n-1}^w(\dots, \mathbf{q}_i + \mathbf{q}_j, \dots, \check{\mathbf{q}}_i, \dots, \check{\mathbf{q}}_j, \dots) \right]. \quad (\text{B.9}) \end{aligned}$$

Let us analyze the soft enhancement of various terms in this expression. The vertex functions in the first two lines have $n - m$ soft arguments, and hence, by the induction assumption, are of order $O(\varepsilon^{-n+m})$. On the other hand, the vertices $\bar{\Gamma}_{n-1}^w$ in the last three lines have one soft argument less and thus are

only $O(\varepsilon^{-n+m+1})$. In the third and fourth lines this is compensated by the enhancement of the kernels I_2 . Indeed,

$$I_2(\mathbf{k}_i, \mathbf{q}_j) \approx \frac{\mathbf{k}_i \cdot \mathbf{q}_j}{q_j^2} = O(1/\varepsilon). \quad (\text{B.10})$$

Finally, the kernel I_2 in the last line of (B.9) is of order $O(\varepsilon^0)$ and thus this term can be neglected in the leading approximation.

Keeping only contributions of order $O(\varepsilon^{-n+m})$ we obtain,

$$\begin{aligned} \bar{\Gamma}_{n,A}^{\prime w, LO} &= \frac{-1}{n-2} \left[\sum_{1 \leq i < j \leq m} I_2(\mathbf{k}_i, \mathbf{k}_j) \bar{\Gamma}_{n-1}^{\prime w}(\mathbf{k}_i + \mathbf{k}_j, \dots, \check{\mathbf{k}}_i, \dots, \check{\mathbf{k}}_j, \dots) \right. \\ &\quad + \sum_{j=1}^{n-m} \left(\sum_{i=1}^{m-1} \frac{(\mathbf{k}_i \cdot \mathbf{q}_j)}{q_j^2} \bar{\Gamma}_{n-1}^{\prime w}(\dots, \mathbf{k}_i + \mathbf{q}_j, \dots, \check{\mathbf{q}}_j, \dots) \right. \\ &\quad \left. \left. + \frac{(\mathbf{k}_m \cdot \mathbf{q}_j)}{q_j^2} \bar{\Gamma}_{n-1}^{\prime w}(\dots, \mathbf{k}_m - \sum_{l \neq j} \mathbf{q}_l, \dots, \check{\mathbf{q}}_j, \dots) \right) \right] \\ &= \frac{-1}{n-2} \left[\sum_{1 \leq i < j \leq m} I_2(\mathbf{k}_i, \mathbf{k}_j) \bar{\Gamma}_{n-1}^{\prime w}(\mathbf{k}_i + \mathbf{k}_j, \dots, \check{\mathbf{k}}_i, \dots, \check{\mathbf{k}}_j, \dots) \right. \\ &\quad \left. + \sum_{j=1}^{n-m} \mathcal{D}_{\mathbf{q}_j} \bar{\Gamma}_{n-1}^{\prime w}(\mathbf{k}_1, \dots, \mathbf{k}_m - \sum_{l \neq j} \mathbf{q}_l, \dots, \check{\mathbf{q}}_j, \dots) \right], \end{aligned} \quad (\text{B.11})$$

where in passing to the second equality we substituted $\mathbf{k}_m = -\sum_{i=1}^{m-1} \mathbf{k}_i$ and used

$$\begin{aligned} &\sum_{i=1}^{m-1} \frac{(\mathbf{k}_i \cdot \mathbf{q}_j)}{q_j^2} \left[\bar{\Gamma}_{n-1}^{\prime w}(\mathbf{k}_1, \dots, \mathbf{k}_i + \mathbf{q}_j, \dots, \mathbf{k}_m - \mathbf{q}_j, \dots, \check{\mathbf{q}}_j, \dots) \right. \\ &\quad \left. - \bar{\Gamma}_{n-1}^{\prime w}(\mathbf{k}_1, \dots, \mathbf{k}_i, \dots, \mathbf{k}_m - \sum_{l \neq j} \mathbf{q}_l, \dots, \check{\mathbf{q}}_j, \dots) \right] \\ &= \mathcal{D}_{\mathbf{q}_j} \bar{\Gamma}_{n-1}^{\prime w}(\mathbf{k}_1, \dots, \mathbf{k}_i, \dots, \mathbf{k}_m - \sum_{l \neq j} \mathbf{q}_l, \dots, \check{\mathbf{q}}_j, \dots). \end{aligned} \quad (\text{B.12})$$

Finally, inserting the expansion (3.22) for the vertices in (B.11) and using that the operators $\mathcal{D}_{\mathbf{q}_j}$ commute with each other, we arrive at

$$\begin{aligned} \bar{\Gamma}_{n,A}^{\prime w, LO} &= \frac{(-1)^{n-m}}{n-2} \prod_{l=1}^{n-m} \mathcal{D}_{\mathbf{q}_l} \left[- \sum_{1 \leq i < j \leq m} I_2(\mathbf{k}_i, \mathbf{k}_j) \bar{\Gamma}_{m-1}^{\prime w}(\mathbf{k}_i + \mathbf{k}_j, \dots, \check{\mathbf{k}}_i, \dots, \check{\mathbf{k}}_j, \dots, \mathbf{k}_m) \right. \\ &\quad \left. + (n-m) \bar{\Gamma}_m^{\prime w}(\mathbf{k}_1, \dots, \mathbf{k}_m) \right]. \end{aligned} \quad (\text{B.13})$$

We now turn to the second piece in (B.8). By inspection of the second line of (B.5b) one concludes that the terms of order $O(\varepsilon^{-n+m})$ can arise only if all $(n-m)$ soft wavenumbers \mathbf{q}_j appear as the arguments of the vertex function $\bar{\Gamma}_{n-p+1}^w$ (recall that the kernels K_p do not depend on the wiggly power spectrum and hence are not enhanced). The vertex must also depend on at least two hard momenta, which implies that p cannot exceed $m-1$. This yields for the LO contributions,

$$\begin{aligned} \bar{\Gamma}_{n,B}^{\prime w,LO}(\mathbf{k}_1, \dots, \mathbf{k}_m - \mathbf{q}, \mathbf{q}_1, \dots, \mathbf{q}_{n-m}) &= -\frac{3}{2(n-2)} \sum_{p=3}^{m-1} \frac{1}{p!(n-p)!} \times (n-m)! C_{n-p}^{n-m} \\ &\times \sum_{\sigma} K_p(\mathbf{k}_{\sigma(1)}, \dots, \mathbf{k}_{\sigma(p)}) \bar{\Gamma}_{n-p+1}^{\prime w} \left(\sum_{l=1}^p \mathbf{k}_{\sigma(l)}, \mathbf{k}_{\sigma(p+1)}, \dots, \mathbf{k}_{\sigma(m)} - \mathbf{q}, \mathbf{q}_1, \dots, \mathbf{q}_{n-m} \right), \end{aligned} \quad (\text{B.14})$$

where, in contrast to (B.5b), we have replaced the summation over all permutations of the arguments by the sum only over permutations of the hard wavenumbers and accounted for the multiplicity of the retained terms with the appropriate symmetry factor. Using Eq. (3.22) we obtain,

$$\begin{aligned} \bar{\Gamma}_{n,B}^{\prime w,LO} &= \frac{3(-1)^{n-m}}{2(n-2)} \prod_{l=1}^{n-m} \mathcal{D}_{\mathbf{q}_l} \left[-\sum_{p=3}^{m-1} \frac{1}{p!(m-p)!} \sum_{\sigma} K_p(\mathbf{k}_{\sigma(1)}, \dots, \mathbf{k}_{\sigma(p)}) \right. \\ &\quad \left. \times \bar{\Gamma}_{m-p+1}^{\prime w} \left(\sum_{l=1}^p \mathbf{k}_{\sigma(l)}, \mathbf{k}_{\sigma(p+1)}, \dots, \mathbf{k}_{\sigma(m)} \right) \right]. \end{aligned} \quad (\text{B.15})$$

One notices that this expression, when combined with the first line of (B.13), gives precisely the recursive formula for

$$\frac{(-1)^{n-m}}{n-2} \prod_{l=1}^{n-m} \mathcal{D}_{\mathbf{q}_l} [(m-2)\bar{\Gamma}_m^{\prime w}(\mathbf{k}_1, \dots, \mathbf{k}_m)]. \quad (\text{B.16})$$

Adding to this the second line of (B.13) yields (3.22). This is our final result. It has the same form in ED and ZA.

B.3 Γ_n vertices in the soft limit: NLO

In this section we study the subleading corrections of order $O(\varepsilon^{-n+3})$ to the expression (3.23). We carry out the derivation for ZA and ED in parallel. Whenever there are differences between these two cases we will use indices (ZA) or (ED).

Let us start with $\bar{\Gamma}_3'^w$. Expanding Eq. (3.13) in the soft wavenumber \mathbf{q} and keeping term up to $O((q/k)^0)$ we obtain,

$$\bar{\Gamma}_3'^w, LO+NLO(\mathbf{k}, -\mathbf{k} - \mathbf{q}, \mathbf{q}) = [\mathcal{D}_{\mathbf{q}} + \mathcal{E}_{\mathbf{q}}] \frac{\bar{P}_w(k)}{\bar{P}_s^2(k)}, \quad (\text{B.17})$$

where we introduced the new operator $\mathcal{E}_{\mathbf{q}}$ defined as,

$$\begin{aligned} \mathcal{E}_{\mathbf{q}}^{(ZA)} \bar{P}_w &= \left(2 \cos^2(\mathbf{q}, \mathbf{k}) - 1 + 2 \cos^2(\mathbf{q}, \mathbf{k}) (1 - n_s(k)) e^{\mathbf{q} \cdot \nabla} \right) \bar{P}_w, \\ \mathcal{E}_{\mathbf{q}}^{(ED)} \bar{P}_w &= \left(\mathcal{E}_{\mathbf{q}}^{(ZA)} + \frac{6}{7} \sin^2(\mathbf{q}, \mathbf{k}) (e^{\mathbf{q} \cdot \nabla} + 1) \right) \bar{P}_w, \quad n_s \equiv \frac{d \ln \bar{P}_s(k)}{d \ln k}. \end{aligned} \quad (\text{B.18})$$

As in the case of $\mathcal{D}_{\mathbf{q}}$, the operator $\mathcal{E}_{\mathbf{q}}$ acts only on the wiggly power spectrum, leaving all smoothly varying functions intact. Its action is of order $O(1)$,

$$\mathcal{E}_{\mathbf{q}} \bar{P}_w \sim O(1) \bar{P}_w. \quad (\text{B.19})$$

A new structure appears when we consider the subleading expansion of $\bar{\Gamma}_4'^w$. After a somewhat lengthy, but straightforward calculation using the recursion relations (B.4b), (B.5b) one obtains,

$$\bar{\Gamma}_4'^w, LO+NLO(\mathbf{k}, -\mathbf{k} - \mathbf{q}_1 - \mathbf{q}_2, \mathbf{q}_1, \mathbf{q}_2) = -[\mathcal{D}_{\mathbf{q}_1} \mathcal{D}_{\mathbf{q}_2} + \mathcal{D}_{\mathbf{q}_1} \mathcal{E}_{\mathbf{q}_2} + \mathcal{D}_{\mathbf{q}_2} \mathcal{E}_{\mathbf{q}_1} + \mathcal{F}_{\mathbf{q}_1 \mathbf{q}_2}] \frac{\bar{P}_w(k)}{\bar{P}_s^2(k)}, \quad (\text{B.20})$$

where

$$\begin{aligned} \mathcal{F}_{\mathbf{q}_1 \mathbf{q}_2}^{(ZA)} \bar{P}_w &= \frac{(\mathbf{q}_1 \cdot \mathbf{q}_2)}{q_1^2 q_2^2} \left[(\mathbf{k} \cdot \mathbf{q}_1) e^{\mathbf{q}_1 \cdot \nabla} (e^{\mathbf{q}_2 \cdot \nabla} - 1) + (\mathbf{k} \cdot \mathbf{q}_2) e^{\mathbf{q}_2 \cdot \nabla} (e^{\mathbf{q}_1 \cdot \nabla} - 1) \right] \bar{P}_w, \\ \mathcal{F}_{\mathbf{q}_1 \mathbf{q}_2}^{(ED)} \bar{P}_w &= \left[\mathcal{F}_{\mathbf{q}_1 \mathbf{q}_2}^{(ZA)} + \frac{3}{7} \sin^2(\mathbf{q}_1, \mathbf{q}_2) \mathcal{D}_{\mathbf{q}_1 + \mathbf{q}_2} \right] \bar{P}_w. \end{aligned} \quad (\text{B.21})$$

This operator is of order $O(\varepsilon^{-1})$. The expressions (B.17), (B.20) are special cases of Eq. (3.62) from the main text for $n = 3$ and 4. We now prove Eq. (3.62) for general n by induction.

Suppose that (3.62) holds for $\bar{\Gamma}_{n'}'^w, NLO$ for any $n' < n$. Assuming that all \mathbf{q}_i go uniformly to zero as in (B.7), we will expand the vertex $\bar{\Gamma}_n'^w(\mathbf{k}, -\mathbf{k} - \sum_{i=1}^{n-2} \mathbf{q}_i, \mathbf{q}_1, \dots, \mathbf{q}_{n-2})$ in powers of soft momenta and focus on the terms scaling like ε^{-n+2} (leading order) and ε^{-n+3} (next-to-leading order). The terms of the form $\Gamma_{n-p+1} K_p$ in the recursion relation (B.5b) scale at most as ε^{-n+4} because the K_p kernels are infrared safe and cannot produce new poles. Hence, we

concentrate on the part of the recursion relation (B.5b) with the $\bar{\Gamma}_{n-1}$ vertex,

$$\begin{aligned} \bar{\Gamma}_n'^w(\mathbf{k}, -\mathbf{k} - \mathbf{q}, \mathbf{q}_1, \dots, \mathbf{q}_{n-2}) &= \frac{-1}{n-2} \left[\sum_{j=1}^{n-2} I_2(\mathbf{k}, \mathbf{q}_j) \bar{\Gamma}_{n-1}'^w(\mathbf{k} + \mathbf{q}_j, -\mathbf{k} - \mathbf{q}, \dots, \check{\mathbf{q}}_j, \dots) \right. \\ &\quad + \sum_{j=1}^{n-2} I_2(-\mathbf{k} - \mathbf{q}, \mathbf{q}_j) \bar{\Gamma}_{n-1}'^w(\mathbf{k}, -\mathbf{k} - \mathbf{q} + \mathbf{q}_j, \dots, \check{\mathbf{q}}_j, \dots) \\ &\quad \left. + \sum_{\substack{i,j=1 \\ i < j}}^{n-2} I_2(\mathbf{q}_i, \mathbf{q}_j) \bar{\Gamma}_{n-1}'^w(\mathbf{k}, -\mathbf{k} - \mathbf{q}, \mathbf{q}_i + \mathbf{q}_j, \dots, \check{\mathbf{q}}_i, \dots, \check{\mathbf{q}}_j, \dots) \right] + O(\varepsilon^{-n+4}), \end{aligned} \quad (\text{B.22})$$

where we used the shorthand notation $\mathbf{q} = \sum_{i=1}^{n-2} \mathbf{q}_i$. The hard argument of the vertex in the first term in (B.22) is shifted by \mathbf{q}_j with respect to \mathbf{k} . Thus, we have to shift the argument in the expansion (3.62) for $\bar{\Gamma}_{n-1}'^w$ and keep the subleading terms in \mathbf{q}_j . Multiplying by $I_2(\mathbf{k}, \mathbf{q}_j)$ Taylor-expanded up to zeroth order in q_j we obtain,

$$\begin{aligned} A_j \equiv I_2(\mathbf{k}, \mathbf{q}_j) \bar{\Gamma}_{n-1}'^w(\mathbf{k} + \mathbf{q}_j, -\mathbf{k} - \mathbf{q}, \dots, \check{\mathbf{q}}_j, \dots) &\approx (-1)^{n-2} \left[\frac{(\mathbf{k} \cdot \mathbf{q}_j)}{q_j^2} \prod_{l \neq j}^{n-2} \mathcal{D}_{\mathbf{q}_l} \right. \\ &\quad + \frac{(\mathbf{k} \cdot \mathbf{q}_j)}{q_j^2} \sum_{m \neq j}^{n-2} \left(\mathcal{E}_{\mathbf{q}_m} + \frac{(\mathbf{q}_j \cdot \mathbf{q}_m)}{q_m^2} (e^{\mathbf{q}_m \cdot \nabla} - 1) \right) \prod_{l \neq j, m}^{n-2} \mathcal{D}_{\mathbf{q}_l} + \frac{(\mathbf{k} \cdot \mathbf{q}_j)}{q_j^2} \sum_{\substack{m_1 < m_2 \\ m_1, m_2 \neq j}}^{n-2} \mathcal{F}_{\mathbf{q}_{m_1} \mathbf{q}_{m_2}} \prod_{l \neq j, m_1, m_2}^{n-2} \mathcal{D}_{\mathbf{q}_l} \\ &\quad \left. + \left(2(1 - n_s) \cos^2(\mathbf{k}, \mathbf{q}_j) + \frac{6}{7} \sin^2(\mathbf{k}, \mathbf{q}_j) \right) \prod_{l \neq j}^{n-2} \mathcal{D}_{\mathbf{q}_l} \right] \frac{e^{\mathbf{q}_j \cdot \nabla} \bar{P}_w(k)}{\bar{P}_s^2(k)}. \end{aligned} \quad (\text{B.23})$$

In the second term in (B.22) we can directly substitute Eq. (3.62) for $\bar{\Gamma}_{n-1}'^w$ which yields,

$$\begin{aligned} B_j \equiv I_2(-\mathbf{k} - \mathbf{q}, \mathbf{q}_j) \bar{\Gamma}_{n-1}'^w(\mathbf{k}, -\mathbf{k} - \mathbf{q} + \mathbf{q}_j, \dots, \check{\mathbf{q}}_j, \dots) &\approx (-1)^{n-2} \left[- \frac{(\mathbf{k} \cdot \mathbf{q}_j)}{q_j^2} \prod_{l \neq j}^{n-2} \mathcal{D}_{\mathbf{q}_l} \right. \\ &\quad - \frac{(\mathbf{k} \cdot \mathbf{q}_j)}{q_j^2} \sum_{m \neq j}^{n-2} \mathcal{E}_{\mathbf{q}_m} \prod_{l \neq j, m}^{n-2} \mathcal{D}_{\mathbf{q}_l} - \frac{(\mathbf{k} \cdot \mathbf{q}_j)}{q_j^2} \sum_{\substack{m_1 < m_2 \\ m_1, m_2 \neq j}}^{n-2} \mathcal{F}_{\mathbf{q}_{m_1} \mathbf{q}_{m_2}} \prod_{l \neq j, m_1, m_2}^{n-2} \mathcal{D}_{\mathbf{q}_l} \\ &\quad \left. + \left(2 \cos^2(\mathbf{k}, \mathbf{q}_j) - 1 + \frac{6}{7} \sin^2(\mathbf{k}, \mathbf{q}_j) \right) \prod_{l \neq j}^{n-2} \mathcal{D}_{\mathbf{q}_l} - \sum_{m \neq j}^{n-2} \frac{(\mathbf{q}_m \cdot \mathbf{q}_j)}{q_j^2} \prod_{l \neq j}^{n-2} \mathcal{D}_{\mathbf{q}_l} \right] \frac{\bar{P}_w(k)}{\bar{P}_s^2(k)}. \end{aligned} \quad (\text{B.24})$$

Together the above contributions sum up to

$$\begin{aligned}
\frac{-1}{n-2} \sum_{j=1}^{n-2} (A_j + B_j) &= \frac{(-1)^{n-1}}{n-2} \left[(n-2) \prod_{l=1}^{n-2} \mathcal{D}_{\mathbf{q}_l} + (n-2) \sum_{m=1}^{n-2} \mathcal{E}_{\mathbf{q}_m} \prod_{l \neq m}^{n-2} \mathcal{D}_{\mathbf{q}_l} \right. \\
&+ (n-4) \sum_{m_1 < m_2}^{n-2} \mathcal{F}_{\mathbf{q}_{m_1} \mathbf{q}_{m_2}} \prod_{l \neq m_1, m_2}^{n-2} \mathcal{D}_{\mathbf{q}_l} + \sum_{m < j}^{n-2} \frac{(\mathbf{q}_m \cdot \mathbf{q}_j)}{q_m^2 q_j^2} \left((\mathbf{k} \cdot (\mathbf{q}_m + \mathbf{q}_j)) (e^{(\mathbf{q}_m + \mathbf{q}_j) \cdot \nabla} - 1) \right. \\
&\left. \left. - 2(\mathbf{k} \cdot \mathbf{q}_m) e^{\mathbf{q}_m \cdot \nabla} - 2(\mathbf{k} \cdot \mathbf{q}_j) e^{\mathbf{q}_j \cdot \nabla} \right) \prod_{l \neq m, j}^{n-2} \mathcal{D}_{\mathbf{q}_l} \right] \frac{\bar{P}_w(k)}{\bar{P}_s^2(k)}. \tag{B.25}
\end{aligned}$$

It remains to include the third term in (B.22). It is sufficient to consider only the leading behaviour of the vertex, as $I_2(\mathbf{q}_i, \mathbf{q}_j)$ is an order-one function. We obtain,

$$\begin{aligned}
&\frac{-1}{n-2} \sum_{i < j}^{n-2} I_2(\mathbf{q}_i, \mathbf{q}_j) \bar{\Gamma}_{n-1}^{\prime w}(\mathbf{k}, -\mathbf{k} - \mathbf{q}, \mathbf{q}_i + \mathbf{q}_j, \dots, \check{\mathbf{q}}_i, \dots, \check{\mathbf{q}}_j, \dots) \\
&\approx \frac{(-1)^{n-1}}{n-2} \sum_{i < j}^{n-2} \left[\frac{(\mathbf{k} \cdot (\mathbf{q}_i + \mathbf{q}_j))}{q_i^2 q_j^2} (e^{(\mathbf{q}_i + \mathbf{q}_j) \cdot \nabla} - 1) + \frac{6}{7} \sin^2(\mathbf{q}_i, \mathbf{q}_j) \mathcal{D}_{\mathbf{q}_i + \mathbf{q}_j} \right] \prod_{l \neq i, j}^{n-2} \mathcal{D}_{\mathbf{q}_l} \frac{\bar{P}_w(k)}{\bar{P}_s^2(k)}. \tag{B.26}
\end{aligned}$$

Combining this with (B.25) we obtain the representation (3.62) for $\bar{\Gamma}_n^{\prime w}$. QED.

In Sec. 3.5 we used the NLO expression for the four-point vertex $\bar{\Gamma}_n^{\prime w}(\mathbf{k}, -\mathbf{k}, \mathbf{q}, -\mathbf{q})$ evaluated using the modified power spectrum $e^{-g^2 \mathcal{S}} \bar{P}_w$. Let us derive this expression. As emphasized in the main text, it would be incorrect to just substitute $\bar{P}_w \mapsto e^{-g^2 \mathcal{S}} \bar{P}_w$ in the formula (B.20) because the combination $\mathcal{D}_{-\mathbf{q}} \mathcal{D}_{\mathbf{q}} [e^{-g^2 \mathcal{S}} \bar{P}_w]$ involves terms containing the operator \mathcal{S} with shifted argument. This shift generates additional NLO contributions that must be properly taken into account. Indeed, we have,

$$\begin{aligned}
\mathcal{D}_{\mathbf{q}} [e^{-g^2 \mathcal{S}} \bar{P}_w](\mathbf{k}) &= \frac{(\mathbf{k} \cdot \mathbf{q})}{q^2} \left(e^{-g^2 \mathcal{S}} \Big|_{\mathbf{k} + \mathbf{q}} \bar{P}_w(|\mathbf{k} + \mathbf{q}|) - e^{-g^2 \mathcal{S}} \Big|_{\mathbf{k}} \bar{P}_w(k) \right) \\
&= \mathcal{D}_{\mathbf{q}} e^{-g^2 \mathcal{S}} \Big|_{\mathbf{k}} \bar{P}_w(k) - g^2 \frac{(\mathbf{k} \cdot \mathbf{q})}{q^2} \Delta \mathcal{S} \Big|_{\mathbf{q}} e^{-g^2 \mathcal{S}} \Big|_{\mathbf{k}} \bar{P}_w(k) + O(\varepsilon), \tag{B.27}
\end{aligned}$$

where

$$\Delta \mathcal{S} \Big|_{\mathbf{q}} = 2 \int_{q' \leq k_S} [dq'] \bar{P}_s(q') \frac{(\mathbf{k} \cdot \mathbf{q}')(\mathbf{q} \cdot \mathbf{q}')}{q'^4} (1 - \cosh(\mathbf{q}' \cdot \nabla)). \tag{B.28}$$

Acting on (B.27) with $\mathcal{D}_{-\mathbf{q}}$ and again taking into account the shift in the argument of \mathcal{S} in the first term we obtain the desired expression,

$$\begin{aligned} \bar{\Gamma}_4'^w(\mathbf{k}, -\mathbf{k}, \mathbf{q}, -\mathbf{q})[e^{-g^2\mathcal{S}}\bar{P}_w] &= -[\mathcal{D}_{\mathbf{q}}\mathcal{D}_{-\mathbf{q}} + \mathcal{E}_{\mathbf{q}}\mathcal{D}_{-\mathbf{q}} + \mathcal{D}_{\mathbf{q}}\mathcal{E}_{-\mathbf{q}} + \mathcal{F}_{\mathbf{q},-\mathbf{q}}] \frac{e^{-g^2\mathcal{S}}\bar{P}_w(k)}{\bar{P}_s^2(k)} \\ &+ 4 \frac{(\mathbf{k} \cdot \mathbf{q})^2}{q^4} \int_{q' \leq k_S} [dq'] \bar{P}_s(q') \frac{(\mathbf{k} \cdot \mathbf{q}')(\mathbf{q} \cdot \mathbf{q}')}{q'^4} \sinh(\mathbf{q} \cdot \nabla) (1 - \cosh(\mathbf{q}' \cdot \nabla)) \frac{e^{-g^2\mathcal{S}}\bar{P}_w(k)}{\bar{P}_s^2(k)}. \end{aligned} \quad (\text{B.29})$$

This formula was used in the derivation of Eq. (3.67).

B.4 Asymptotic behavior of RSD vertices in the soft limit

In this Appendix we prove the asymptotic formula (4.48) for the redshift space vertices. For clarity we will omit the superscript (s) in the notation for the wiggly vertices and keep in mind that these quantities are evaluated in redshift space. In what follows it is useful to define the operator

$$\mathcal{D}_{\mathbf{q}}^z[\bar{P}_w(k)] = \frac{k_z q_z}{q^2} (e^{\mathbf{q} \cdot \nabla_{\mathbf{k}'}} - 1) \bar{P}_w(k') \Big|_{\mathbf{k}'=\mathbf{k}}. \quad (\text{B.30})$$

To prove (4.48) we proceed by induction. In Eq. (4.42) we have verified this formula for $n = 3$. Now, suppose it is valid for $n - 1$ and any m . Our aim is to prove it for n . Using the recursion relation (4.24) we write

$$\begin{aligned} \Gamma_n'^w(f; \mathbf{k}_1, \dots, \mathbf{k}_m - \mathbf{Q}, \mathbf{q}_1, \dots, \mathbf{q}_{n-m}) &= \Gamma_n'^w(r)(f; \mathbf{k}_1, \dots, \mathbf{k}_m - \mathbf{Q}, \mathbf{q}_1, \dots, \mathbf{q}_{n-m}) \\ &- \int_0^f d\mathcal{F} \left[\sum_{1 \leq i < j < m} I_2^{(s)}(\mathbf{k}_i, \mathbf{k}_j) \Gamma_{n-1}'^w(\mathcal{F}; \mathbf{k}_i + \mathbf{k}_j, \dots, \check{\mathbf{k}}_i, \dots, \check{\mathbf{k}}_j, \dots) \right. \\ &\quad + \sum_{i=1}^{m-1} I_2^{(s)}(\mathbf{k}_i, \mathbf{k}_m - \mathbf{Q}) \Gamma_{n-1}'^w(\mathcal{F}; \dots, \check{\mathbf{k}}_i, \dots, \mathbf{k}_m + \mathbf{k}_i - \mathbf{Q}, \dots) \\ &\quad + \sum_{i=1}^{m-1} \sum_{j=1}^{n-m} I_2^{(s)}(\mathbf{k}_i, \mathbf{q}_j) \Gamma_{n-1}'^w(\mathcal{F}; \dots, \mathbf{k}_i + \mathbf{q}_j, \dots, \check{\mathbf{q}}_j, \dots) \\ &\quad + \sum_{j=1}^{n-m} I_2^{(s)}(\mathbf{k}_m - \mathbf{Q}, \mathbf{q}_j) \Gamma_{n-1}'^w(\mathcal{F}; \dots, \mathbf{k}_m - \sum_{l \neq j} \mathbf{q}_l, \dots, \check{\mathbf{q}}_j, \dots) \\ &\quad \left. + \sum_{1 \leq i < j \neq n-m} I_2^{(s)}(\mathbf{q}_i, \mathbf{q}_j) \Gamma_{n-1}'^w(\mathcal{F}; \dots, \mathbf{q}_i + \mathbf{q}_j, \dots, \check{\mathbf{q}}_i, \dots, \check{\mathbf{q}}_j, \dots) \right], \end{aligned} \quad (\text{B.31})$$

where we have introduced a shorthand notation $\mathbf{Q} \equiv \sum_{i=1}^{n-m} \mathbf{q}_i$. Let us estimate the enhancement of various terms in this expression. The real-space vertex $\Gamma_n^{\prime w(r)}$ is of order $O(\varepsilon^{-n+m})$, as seen from Eq. (3.22). The vertices in the second and third lines have $n - m$ soft arguments and thus are also enhanced as $O(\varepsilon^{-n+m})$ according to our induction hypothesis. The vertices in the last three lines have one soft argument less and thus are only $O(\varepsilon^{-n+m+1})$. In the fourth and fifth lines, however, this is compensated by the poles in the $I_2^{(s)}$ kernels,

$$I_2^{(s)}(\mathbf{k}_i, \mathbf{q}_j) \approx \frac{k_{i,z} q_{j,z}}{q_j^2} = O(1/\varepsilon). \quad (\text{B.32})$$

Keeping only the terms $O(\varepsilon^{-n+m})$ we arrive at

$$\begin{aligned} \Gamma_n^{\prime w} = \Gamma_n^{\prime w(r)} - \int_0^f d\mathcal{F} & \left[\sum_{1 \leq i < j \leq m} I_2^{(s)}(\mathbf{k}_i, \mathbf{k}_j) \Gamma_{n-1}^{\prime w}(\mathcal{F}; \mathbf{k}_i + \mathbf{k}_j, \dots, \check{\mathbf{k}}_i, \dots, \check{\mathbf{k}}_j, \dots) \right. \\ & + \sum_{j=1}^{n-m} \sum_{i=1}^{m-1} \frac{k_{i,z} q_{j,z}}{q_j^2} \Gamma_{n-1}^{\prime w}(\mathcal{F}; \dots, \mathbf{k}_i + \mathbf{q}_j, \dots, \check{\mathbf{q}}_j, \dots) \\ & \left. + \sum_{j=1}^{n-m} \frac{k_{m,z} q_{j,z}}{q_j^2} \Gamma_{n-1}^{\prime w}(\mathcal{F}; \dots, \mathbf{k}_m - \sum_{l \neq j} \mathbf{q}_l, \dots, \check{\mathbf{q}}_j, \dots) \right]. \end{aligned} \quad (\text{B.33})$$

Next, we use that $\mathbf{k}_m = -\sum_{i=1}^{m-1} \mathbf{k}_i$ due to momentum conservation and rewrite the last two terms as

$$\begin{aligned} & \sum_{j=1}^{n-m} \sum_{i=1}^{m-1} \frac{k_{i,z} q_{j,z}}{q_j^2} \left[\Gamma_{n-1}^{\prime w}(\mathcal{F}; \dots, \mathbf{k}_i + \mathbf{q}_j, \dots, \check{\mathbf{q}}_j, \dots) - \Gamma_{n-1}^{\prime w}(\mathcal{F}; \dots, \mathbf{k}_m - \sum_{l \neq j} \mathbf{q}_l, \dots, \check{\mathbf{q}}_j, \dots) \right] \\ & = \sum_{j=1}^{n-m} \mathcal{D}_{\mathbf{q}_j}^z \Gamma_{n-1}^{\prime w}(\dots, \mathbf{k}_m - \sum_{l \neq j} \mathbf{q}_l, \dots, \check{\mathbf{q}}_j, \dots) \\ & \approx (-1)^{n-m-1} \sum_{j=1}^{n-m} \mathcal{D}_{\mathbf{q}_j}^z \prod_{l \neq j} (\mathcal{D}_{\mathbf{q}_l}^{(r)} + \mathcal{F} \mathcal{D}_{\mathbf{q}_l}^z) \Gamma_m^{\prime w}(\mathcal{F}; \mathbf{k}_1, \dots, \mathbf{k}_m) \\ & = (-1)^{n-m-1} \frac{\partial}{\partial \mathcal{F}} \left(\prod_{l=1}^{n-m} (\mathcal{D}_{\mathbf{q}_l}^{(r)} + \mathcal{F} \mathcal{D}_{\mathbf{q}_l}^z) \right) \Gamma_m^{\prime w}(\mathcal{F}; \mathbf{k}_1, \dots, \mathbf{k}_m). \end{aligned} \quad (\text{B.34})$$

On the other hand, the first term in square brackets in (B.33) reads,

$$\begin{aligned}
& \sum_{1 \leq i < j \leq m} I_2^{(s)}(\mathbf{k}_i, \mathbf{k}_j) \Gamma_{n-1}'^{lw}(\mathcal{F}; \mathbf{k}_i + \mathbf{k}_j, \dots, \check{\mathbf{k}}_i, \dots, \check{\mathbf{k}}_j, \dots) \\
& \approx (-1)^{n-m} \prod_{l=1}^{n-m} (\mathcal{D}_{\mathbf{q}_l}^{(r)} + \mathcal{F} \mathcal{D}_{\mathbf{q}_l}^z) \sum_{1 \leq i < j \leq m} I_2^{(s)}(\mathbf{k}_i, \mathbf{k}_j) \Gamma_{m-1}'^{lw}(\mathcal{F}; \mathbf{k}_i + \mathbf{k}_j, \dots, \check{\mathbf{k}}_i, \dots, \check{\mathbf{k}}_j, \dots) \\
& = (-1)^{n-m-1} \prod_{l=1}^{n-m} (\mathcal{D}_{\mathbf{q}_l}^{(r)} + \mathcal{F} \mathcal{D}_{\mathbf{q}_l}^z) \frac{\partial}{\partial \mathcal{F}} \Gamma_m'^{lw}(\mathcal{F}; \mathbf{k}_1, \dots, \mathbf{k}_m),
\end{aligned} \tag{B.35}$$

where in the last equality we again used the relation (4.24). Combining Eqs. (B.34) and (B.35) we obtain,

$$\Gamma_n'^{lw} = \Gamma_n'^{lw(r)} + (-1)^{n-m} \int_0^f d\mathcal{F} \frac{\partial}{\partial \mathcal{F}} \left(\prod_{l=1}^{n-m} (\mathcal{D}_{\mathbf{q}_l}^{(r)} + \mathcal{F} \mathcal{D}_{\mathbf{q}_l}^z) \Gamma_m'^{lw}(\mathcal{F}; \mathbf{k}_1, \dots, \mathbf{k}_m) \right). \tag{B.36}$$

Integration and use of Eq. (3.22) for the real space vertex $\Gamma_n'^{lw(r)}$ yields the formula (4.48). QED

Appendix C

NLO polynomials

The functions appearing Eq. (3.75) are given by

$$\begin{aligned}
h_1(x, y) &= \frac{1}{k_{osc}} \int \frac{d\Omega_q d\Omega_{q'}}{(4\pi)^2} \frac{c_{kq} c_{kq'} (q c_{kq} + q' c_{kq'}) s_{qq'}^2 q q'}{(q^2 + 2qq' c_{qq'} + q'^2)} \sin((q c_{kq} + q' c_{kq'})/k_{osc}) \Big|_{\substack{q=xk_{osc} \\ q'=yk_{osc}}} \\
&= -\frac{1}{60x^2 y^2} (720 + x^4 - 12y^2 + y^4 - 2x^2(6 + y^2)) \cos[x] \cos[y] \\
&\quad - \frac{1}{240x^3 y^3} (x^2 - y^2)^4 (\text{Ci}[|x - y|] - \text{Ci}[x + y]) \\
&\quad - \frac{1}{240x^3 (x^2 - y^2) y^3} \left\{ -2y \left(x^8 - 2x^6(3 + 2y^2) + 2x^4(-300 + 5y^2 + 3y^4) \right. \right. \\
&\quad \left. \left. + y^2(-1440 + 24y^2 - 2y^4 + y^6) - 2x^2(-720 - 240y^2 + y^4 + 2y^6) \right) \cos[y] \sin[x] \right. \\
&\quad \left. + 2 \left(x \left(x^8 - 2x^6(1 + 2y^2) + x^4(24 - 2y^2 + 6y^4) + 2x^2(-720 + 240y^2 + 5y^4 - 2y^6) \right. \right. \right. \\
&\quad \left. \left. + y^2(1440 - 600y^2 - 6y^4 + y^6) \right) \cos[x] + (x^2 - y^2) \left(1440 + x^6 - 600y^2 - 6y^4 \right. \right. \\
&\quad \left. \left. + y^6 - x^4(6 + y^2) - x^2(600 - 204y^2 + y^4) \right) \sin[x] \right) \sin[y] \Big\}, \quad (\text{C.1})
\end{aligned}$$

and

$$\begin{aligned}
h_2(x, y) &= -\frac{1}{k_{osc}} \int \frac{d\Omega_q d\Omega_{q'}}{(4\pi)^2} \frac{c_{kq} c_{kq'} (q c_{kq} + q' c_{kq'}) s_{qq'}^2 q q'}{(q^2 + 2qq' c_{qq'} + q'^2)} \sin(q c_{kq} / k_{osc}) \Big|_{q=xk_{osc}, q'=yk_{osc}} \\
&= -\frac{1}{192x^8 y^3} \left\{ x \cos[x] \left(4xy (3x^8 + 27y^6 - 3x^2 y^4 (21 + y^2) + x^4 y^2 (-3 + 5y^2) \right. \right. \\
&\quad \left. \left. - x^6 (9 + 5y^2) \right) + 3(x-y)^3 (x+y)^3 (x^4 - 9y^2 + x^2 (-3 + y^2)) \log \left[\frac{(x-y)^2}{(x+y)^2} \right] \right) \\
&\quad + \left(4xy (9x^6 - 6x^8 + x^4 (3 + 4x^2) y^2 + x^2 (63 - 26x^2) y^4 + 3(-9 + 4x^2) y^6) \right. \\
&\quad \left. - 3(x-y)^3 (x+y)^3 (2x^4 - 9y^2 + x^2 (-3 + 4y^2)) \log \left[\frac{(x-y)^2}{(x+y)^2} \right] \right) \sin[x] \Big\}, \quad (\text{C.2})
\end{aligned}$$

where $c_{kq} = \mathbf{k} \cdot \mathbf{q} / (kq)$, $c_{kq'} = \mathbf{k} \cdot \mathbf{q}' / (kq')$, $c_{qq'} = \mathbf{q} \cdot \mathbf{q}' / (qq')$, $s_{qq'}^2 = 1 - c_{qq'}^2$. Note that instead of averaging over the directions of \mathbf{q} and \mathbf{q}' one can equivalently average over the direction of the external wavenumber \mathbf{k} and either \mathbf{q} or \mathbf{q}' . In particular, h_2 can be evaluated setting $\mathbf{q}' = q'(0, 0, 1)$, $\mathbf{k} = k(0, s_k, c_k)$, $\mathbf{q} = q(s_q s_\phi, s_q c_\phi, c_q)$ and integrating first over ϕ , then c_k and then c_q . The integral h_1 can be evaluated by first averaging over the direction of \mathbf{k} in a frame where the z -axis is chosen along $\mathbf{q} + \mathbf{q}'$, and $\mathbf{q} = q(0, s_q, c_q)$. Then one uses that

$$c_q = \frac{(\mathbf{q} + \mathbf{q}')^2 + q^2 - q'^2}{2q|\mathbf{q} + \mathbf{q}'|}, \quad c_{qq'} = \frac{(\mathbf{q} + \mathbf{q}')^2 - q^2 - q'^2}{2qq'} \quad (\text{C.3})$$

and performs the average over $c_{qq'}$. For the last integral it is helpful to do the substitution $dc_{qq'} = |\mathbf{q} + \mathbf{q}'| / (qq') d|\mathbf{q} + \mathbf{q}'|$, with integration boundaries from $|q - q'|$ to $q + q'$.

Appendix D

Shift of the BAO in momentum space

As discussed in the main text, at LO the IR resummation leads to a simple damping of the wiggly component in the power spectrum. In this appendix we evaluate the NLO contribution and show that it contains a term describing the shift of the phase of BAO. Namely, we derive Eq. (3.94). Our calculation is similar to the one performed in [107] with the main difference that the IR resummation procedure allows us to consistently take into account the BAO damping. Besides, we retain certain NLO terms that were omitted in [107].

According to Eq. (3.73) we need to compute the 1-loop correction to the power spectrum using the damped wiggly spectrum as an input. It is convenient to use the standard SPT expression (see [1] for the derivation using TSPT),

$$P^{1-loop}(z, k) = D(z)^4 \left[6P(k) \int [dq] E_3(\mathbf{k}, \mathbf{q}, -\mathbf{q}) P(q) + 2 \int [dq] (E_2(\mathbf{k}-\mathbf{q}, \mathbf{q}))^2 P(q) P(|\mathbf{k}-\mathbf{q}|) \right], \quad (\text{D.1})$$

where E_n are the SPT kernels F_n (G_n) for the density (velocity divergence) power spectrum. The first and second terms in brackets are identified as P_{13} and P_{22} respectively. Performing the smooth + wiggly decomposition we see that the term P_{13} contributes only to the part proportional to $P_w(k)$ and thus does not affect the BAO phase. In the P_{22} term we split the integration into soft and hard parts,

$$P_{w,22} [e^{-k^2 D(z)^2 \Sigma^2} P_w] = 4D(z)^4 \left[\int_{q \leq k_S} [dq] + \int_{q \geq k_S} [dq] \right] (E_2(\mathbf{k} - \mathbf{q}, \mathbf{q}))^2 \times P_s(q) P_w(|\mathbf{k} - \mathbf{q}|) e^{-(\mathbf{k}-\mathbf{q})^2 D(z)^2 \Sigma^2}. \quad (\text{D.2})$$

	ED $P_{\delta\delta}$	ED $P_{\Theta\Theta}$	ZA $P_{\delta\delta}$	ZA $P_{\Theta\Theta}$
Υ	$\frac{3}{7}$	$-\frac{1}{7}$	0	-1
\varkappa	1	1	0	0

TABLE D.1: The values of Υ, \varkappa for different power spectra in ED and ZA.

The integral over the hard modes vanishes as it involves a rapidly oscillating function. In the soft part we use the expression,

$$E_2(\mathbf{k} - \mathbf{q}, \mathbf{q}) = \frac{(\mathbf{k} \cdot \mathbf{q})}{2q^2} \left(1 + \frac{\mathbf{k} \cdot \mathbf{q}}{k^2} + \Upsilon \frac{q^2}{(\mathbf{k} \cdot \mathbf{q})} \sin^2(\mathbf{k}, \mathbf{q}) + O(q^2/k^2) \right), \quad (\text{D.3})$$

where the coefficient Υ is different in ED and ZA and depends on the type of the power spectrum under consideration; its values are given in Table D.1. Next, using the representation (3.89) we write,

$$\begin{aligned} P_w(|\mathbf{k} - \mathbf{q}|) = P_w(k) & \left[\cos \frac{(\hat{\mathbf{k}} \cdot \mathbf{q})}{k_{osc}} + \frac{d \log f_{env}}{d \log k} \left(\frac{k_{osc}}{k} \sin \frac{(\hat{\mathbf{k}} \cdot \mathbf{q})}{k_{osc}} - \frac{(\hat{\mathbf{k}} \cdot \mathbf{q})}{k} \cos \frac{(\hat{\mathbf{k}} \cdot \mathbf{q})}{k_{osc}} \right) \right. \\ & + \frac{q^2}{2kk_{osc}} \sin^2(\mathbf{k}, \mathbf{q}) \sin \frac{(\hat{\mathbf{k}} \cdot \mathbf{q})}{k_{osc}} \left. \right] + k_{osc} \frac{dP_w(k)}{dk} \left[- \sin \frac{(\hat{\mathbf{k}} \cdot \mathbf{q})}{k_{osc}} \right. \\ & \left. + \frac{d \log f_{env}}{d \log k} \frac{(\hat{\mathbf{k}} \cdot \mathbf{q})}{k} \sin \frac{(\hat{\mathbf{k}} \cdot \mathbf{q})}{k_{osc}} + \frac{q^2}{2kk_{osc}} \sin^2(\mathbf{k}, \mathbf{q}) \cos \frac{(\hat{\mathbf{k}} \cdot \mathbf{q})}{k_{osc}} \right]. \end{aligned} \quad (\text{D.4})$$

Expanding also the exponent in (D.2) and integrating over angles one obtains,

$$P_{w,22}[e^{-k^2 D(z)^2 \Sigma^2} P_w] = D(z)^4 e^{-k^2 D(z)^2 \Sigma^2} \left[\tilde{H}(z, k) P_w(k) + \tilde{S}(z, k) \frac{dP_w(k)}{dk} \right], \quad (\text{D.5})$$

where the form of $\tilde{H}(z, k)$ is unimportant for our purposes. For the second term we have

$$\tilde{S}(z, k) = k \left(1 - \frac{1}{2} \frac{d \log f_{env}}{d \log k} \right) s_1 + k(s_2 + s_3) - k^3 D(z)^2 \Sigma_a^2 \quad (\text{D.6})$$

where

$$s_1 = -8\pi k_{osc} \int_0^{k_S} dq q P_s(q) \int_0^1 d\mu \mu^3 \sin(q\mu/k_{osc}) \quad (\text{D.7a})$$

$$s_2 = -8\pi \Upsilon k_{osc} \int_0^{k_S} dq q P_s(q) \int_0^1 d\mu \mu(1 - \mu^2) \sin(\mu q/k_{osc}), \quad (\text{D.7b})$$

$$s_3 = 2\pi \int_0^{k_S} dq q^2 P_s(q) \int_0^1 d\mu \mu^2(1 - \mu^2) \cos(q\mu k_{osc}), \quad (\text{D.7c})$$

and Σ_a^2 has been defined in (3.74a). In the region of BAO oscillations the enveloping function is well approximated by the form (cf. Eq. (3.6))

$$f_{env}(k) \propto k^{-m} e^{-(k/k_{Silk})^2} \quad (\text{D.8})$$

with $m \approx 3/2$. Finally, combining (D.5) with the contribution of $P_{w,13}$ and the last term in (3.73) we obtain Eqs. (3.94), (3.95) with

$$s = (1 + m/2)s_1 + s_2 + s_3 , \quad \Sigma_{Silk}^2 = s_1/k_{Silk}^2 . \quad (\text{D.9})$$

Appendix E

Bias expansion at one loop

In order to obtain the bias kernels M_n at one loop we have to go to the second order in Π , i.e. we need only

$$\begin{aligned}\Pi_{ij}^{[1]} &= \frac{\partial_i \partial_j \delta}{\Delta}, \\ \Pi_{ij}^{[2]} &= \frac{\partial_i \partial_j}{\Delta} (\Theta(1 + \delta) - \delta) + \frac{\partial_i \partial_j}{\Delta} \left(\partial_l \delta \frac{\partial_l \Theta}{\Delta} \right) - \frac{\partial_i \partial_j \partial_l \delta}{\Delta} \frac{\partial_l \Theta}{\Delta}.\end{aligned}\tag{E.1}$$

At first order there is a single operator in the bias expansion, $\text{tr}\Pi^{[1]} = \delta$. At second order there are two operators,

$$\begin{aligned}\mathcal{O}_1^{[2]} &\equiv \frac{1}{2} (\text{tr}[\Pi^{[1]}])^2 = \frac{\delta^2}{2}, \\ \mathcal{O}_2^{[2]} &\equiv \frac{1}{2} \text{tr}[(\Pi^{[1]})^2] = \frac{1}{2} \frac{\partial_i \partial_j \delta}{\Delta} \frac{\partial_i \partial_j \delta}{\Delta}.\end{aligned}\tag{E.2}$$

At third order we have:

$$\begin{aligned}\mathcal{O}_1^{[3]} &\equiv \frac{1}{6} (\text{tr}[\Pi^{[1]}])^3 = \frac{\delta^3}{6}, \\ \mathcal{O}_2^{[3]} &\equiv \frac{1}{2} \text{tr}[(\Pi^{[1]})^2] \text{tr}[\Pi^{[1]}] = \frac{1}{2} \frac{\partial_i \partial_j \delta}{\Delta} \frac{\partial_i \partial_j \delta}{\Delta} \delta, \\ \mathcal{O}_3^{[3]} &\equiv \frac{1}{6} \text{tr}[(\Pi^{[1]})^3] = \frac{1}{6} \frac{\partial_i \partial_j \delta}{\Delta} \frac{\partial_i \partial_l \delta}{\Delta} \frac{\partial_l \partial_i \delta}{\Delta}, \\ \mathcal{O}_4^{[3]} &\equiv \frac{1}{2} \text{tr}[\Pi^{[2]} \Pi^{[1]}] = \frac{1}{2} \left\{ \frac{\partial_i \partial_j}{\Delta} (\Theta \delta + \Theta - \delta) \frac{\partial_i \partial_j \delta}{\Delta} \right. \\ &\quad \left. + \left[\frac{\partial_i \partial_j}{\Delta} \left(\partial_l \delta \frac{\partial_l \Theta}{\Delta} \right) - \frac{\partial_i \partial_j \partial_l \delta}{\Delta} \frac{\partial_l \Theta}{\Delta} \right] \frac{\partial_i \partial_j \delta}{\Delta} \right\}.\end{aligned}\tag{E.3}$$

Going into Fourier space and using the decomposition (2.8) we obtain (4.72) with the following kernels:

$$\begin{aligned}
M_1^{(r)}(\mathbf{k}) &= b_1, \\
M_2^{(r)}(\mathbf{k}_1, \mathbf{k}_2) &= b_1 K_2(\mathbf{k}_1, \mathbf{k}_2) + b_2 + b_{\mathcal{O}_2^{[2]}} \frac{(\mathbf{k}_1 \cdot \mathbf{k}_2)^2}{k_1^2 k_2^2}, \\
M_3^{(r)}(\mathbf{k}_1, \mathbf{k}_2, \mathbf{k}_3) &= b_1 K_3(\mathbf{k}_1, \mathbf{k}_2, \mathbf{k}_3) + b_2 [K_2(\mathbf{k}_1, \mathbf{k}_2) + \text{perm.}] \\
&+ b_{\mathcal{O}_2^{[2]}} \left[\frac{(\mathbf{k}_1 \cdot \mathbf{k}_{23})^2}{k_1^2 k_{23}^2} K_2(\mathbf{k}_2, \mathbf{k}_3) + \text{perm.} \right] + b_3 + b_{\mathcal{O}_2^{[3]}} \left[\frac{(\mathbf{k}_1 \cdot \mathbf{k}_2)^2}{k_1^2 k_2^2} + \text{perm.} \right] \\
&+ b_{\mathcal{O}_3^{[3]}} \frac{(\mathbf{k}_1 \cdot \mathbf{k}_2)(\mathbf{k}_2 \cdot \mathbf{k}_3)(\mathbf{k}_3 \cdot \mathbf{k}_1)}{k_1^2 k_2^2 k_3^2} + b_{\mathcal{O}_4^{[3]}} \left[\frac{(\mathbf{k}_1 \cdot \mathbf{k}_{23})^2}{k_1^2 k_{23}^2} \left(1 - \frac{1}{2} K_2(\mathbf{k}_2, \mathbf{k}_3) \right) \right. \\
&\left. + \frac{(\mathbf{k}_3 \cdot \mathbf{k}_2)}{k_{23}^2 k_1^2 k_2^2 k_3^2} \left[(\mathbf{k}_1 \cdot \mathbf{k}_2)(\mathbf{k}_1 \cdot \mathbf{k}_3)(k_2^2 + k_3^2) - (\mathbf{k}_2 \cdot \mathbf{k}_3)((\mathbf{k}_1 \cdot \mathbf{k}_3)^2 + (\mathbf{k}_1 \cdot \mathbf{k}_2)^2) \right] + \text{perm.} \right],
\end{aligned} \tag{E.4}$$

where ‘perm.’ means terms obtained by cyclic permutations of the momenta $\mathbf{k}_1, \mathbf{k}_2, \mathbf{k}_3$. Note that the $M_n^{(r)}$ kernels written above are manifestly IR safe. The kernels in redshift space are obtained using the recursion relations similar to (4.32). In particular, we have

$$\begin{aligned}
M_1^{(s)}(\mathbf{k}) &= b_1 + f\mu^2, \\
M_2^{(s)}(\mathbf{k}_1, \mathbf{k}_2) &= M_2^{(r)}(\mathbf{k}_1, \mathbf{k}_2) + \left\{ \mu_1^2 + \mu_2^2 - 2 \frac{(\mathbf{k}_1 \cdot \mathbf{k}_2)}{k_1 k_2} \mu_1 \mu_2 \right\} b_1 f,
\end{aligned} \tag{E.5}$$

where $\mu_i \equiv (\hat{\mathbf{k}}_i \cdot \hat{\mathbf{z}})$. The expression for $M_3^{(s)}$ is rather cumbersome and we do not present it here.

For reference we also write down the SPT kernels for biased tracers in redshift space. Compared to [15] we add the tidal bias. It appears convenient to change the bias basis and consider

$$\delta_h = b_1 \delta + \frac{b_2}{2} \delta^2 + b_{\mathcal{G}_2} \mathcal{G}_2 + \frac{b_3}{6} \delta^3 + b_{\mathcal{G}_3} \mathcal{G}_3 + b_{(\mathcal{G}_2 \delta)} \mathcal{G}_2 \delta + b_{\Gamma_3} \Gamma_3, \tag{E.6}$$

where

$$\begin{aligned}
\mathcal{G}_2(\Phi) &= (\partial_i \partial_j \Phi)^2 - (\partial^2 \Phi)^2, \\
\mathcal{G}_3(\Phi) &= -\partial_i \partial_j \Phi \partial_j \partial_k \Phi \partial_k \partial_i \Phi - \frac{1}{2} (\partial^2 \Phi)^3 + \frac{3}{2} (\partial_i \partial_j \Phi)^2 \partial^2 \Phi, \\
\Gamma_3 &= \mathcal{G}_2(\Phi) - \mathcal{G}_2(\Phi_v),
\end{aligned} \tag{E.7}$$

and we introduced the velocity potential defined via $\Delta\Phi_v = \Theta$. Acting along the lines of Sec. 7.4.1 of [15] we obtain

$$Z_1(\mathbf{k}) = b_1 + f\mu^2, \quad (\text{E.8a})$$

$$\begin{aligned} Z_2(\mathbf{k}_1, \mathbf{k}_2) &= \frac{b_2}{2} + b_{\mathcal{G}_2} \left(\frac{(\mathbf{k}_1 \cdot \mathbf{k}_2)^2}{k_1^2 k_2^2} - 1 \right) + b_1 F_2(\mathbf{k}_1, \mathbf{k}_2) + f\mu^2 G_2(\mathbf{k}_1, \mathbf{k}_2) \\ &\quad + \frac{f\mu k}{2} \left(\frac{\mu_1}{k_1} (b_1 + f\mu_2^2) + \frac{\mu_2}{k_2} (b_1 + f\mu_1^2) \right), \end{aligned} \quad (\text{E.8b})$$

$$\begin{aligned} Z_3(\mathbf{k}_1, \mathbf{k}_2, \mathbf{k}_3) &= \frac{b_3}{6} + b_{\mathcal{G}_3} \left[-\frac{(\mathbf{k}_1 \cdot \mathbf{k}_2)(\mathbf{k}_2 \cdot \mathbf{k}_3)(\mathbf{k}_3 \cdot \mathbf{k}_1)}{k_1^2 k_2^2 k_3^2} - \frac{1}{2} + \frac{3}{2} \frac{(\mathbf{k}_1 \cdot \mathbf{k}_2)^2}{k_1^2 k_2^2} \right] \\ &\quad + b_{(\mathcal{G}_2\delta)} \left[\frac{(\mathbf{k}_1 \cdot \mathbf{k}_2)^2}{k_1^2 k_2^2} - 1 \right] + 2b_{\Gamma_3} \left[\frac{(\mathbf{k}_1 \cdot (\mathbf{k}_2 + \mathbf{k}_3))^2}{k_1^2 (\mathbf{k}_2 + \mathbf{k}_3)^2} - 1 \right] [F_2(\mathbf{k}_2, \mathbf{k}_3) - G_2(\mathbf{k}_2, \mathbf{k}_3)] \\ &\quad + b_1 F_3(\mathbf{k}_1, \mathbf{k}_2, \mathbf{k}_3) + f\mu^2 G_3(\mathbf{k}_1, \mathbf{k}_2, \mathbf{k}_3) + \frac{(f\mu k)^2}{2} (b_1 + f\mu_1^2) \frac{\mu_2 \mu_3}{k_2 k_3} \\ &\quad + f\mu k \frac{\mu_3}{k_3} [b_1 F_2(\mathbf{k}_1, \mathbf{k}_2) + f\mu_1^2 G_2(\mathbf{k}_1, \mathbf{k}_2)] + f\mu k (b_1 + f\mu_1^2) \frac{\mu_{23}}{k_{23}} G_2(\mathbf{k}_2, \mathbf{k}_3) \\ &\quad + b_2 F_2(\mathbf{k}_1, \mathbf{k}_2) + 2b_{\mathcal{G}_2} \left[\frac{(\mathbf{k}_1 \cdot (\mathbf{k}_2 + \mathbf{k}_3))^2}{k_1^2 (\mathbf{k}_2 + \mathbf{k}_3)^2} - 1 \right] F_2(\mathbf{k}_2, \mathbf{k}_3) + \frac{b_2 f\mu k}{2} \frac{\mu_1}{k_1} \\ &\quad + b_{\mathcal{G}_2} f\mu k \frac{\mu_1}{k_1} \left[\frac{(\mathbf{k}_2 \cdot \mathbf{k}_3)^2}{k_2^2 k_3^2} - 1 \right], \end{aligned} \quad (\text{E.8c})$$

where $\mathbf{k} = \mathbf{k}_1 + \mathbf{k}_2 + \mathbf{k}_3$ and the kernel Z_3 must be symmetrized in its arguments.

Appendix F

Simplification of NLO IR resummed integrands: example of bispectrum in redshift space

At face value, IR resummation requires using the dressed anisotropic power spectrum

$$P_{nw}(p) + e^{-p^2 \Sigma_{tot}^2(\mu_{\mathbf{p}})} P_w(p) \quad (\text{F.1})$$

as an input in loop calculations. This prescription causes technical complications that one would like to minimize. We have seen in Sec. 4.6.2 that in the case of one-loop power spectrum one can pull the anisotropic damping factor outside the momentum integral without changing the order of approximation of the final result. Here we discuss the general situation for an 1-loop n -point correlator and illustrate it on the example of bispectrum. We will work in terms of SPT diagrams.

Consider an SPT one-loop diagram for some n -point function and substitute the linear power spectrum in it by its IR-resummed counterpart (F.1). Depending on the topology of the diagram the wiggly power spectrum can be:

- (a) outside the loop and depend only on an external momentum. In this case the loop integral contains only the isotropic smooth power spectrum P_{nw} and its evaluation is straightforward.

- (b) inside the loop and be multiplied by a combination of kernels without IR singularities at finite values of the loop momentum \mathbf{p} (we choose \mathbf{p} to coincide with the argument of P_w). An example of such contribution is given by the second term in (4.88) which is part of P_{13} diagram in SPT language. As we discussed in Sec. 4.6.2, such contributions are exponentially suppressed and can be safely neglected.
- (c) inside the loop and be multiplied by a combination of kernels with a single IR singularity at $p = p_0$, where p_0 is a linear combinations of external momenta. This is the case of the third term in (4.88) which comes from the P_{22} diagram. In such diagram the argument of the damping factor can be substituted by \mathbf{p}_0 ,

$$e^{-p^2 \Sigma_{tot}^2(\mu_{\mathbf{p}})} P_w(p) \rightarrow e^{-p_0^2 \Sigma_{tot}^2(\mu_{\mathbf{p}_0})} P_w(p). \quad (\text{F.2})$$

Then the damping factor can be taken out of the loop integral.

- (d) inside the loop and be multiplied by a combination of kernels with more than one IR singularity. We are not aware of any convenient method to simplify these contributions, so in this case the anisotropic damping factor must be kept inside the integral.

Applying the above algorithm to the one-loop correction to the bispectrum we obtain the following expression,

$$B^{(s) \text{ IR res, NLO}}(\mathbf{k}_1, \mathbf{k}_2, \mathbf{k}_3) = B^{(s) 1-loop}[P_{nw}] + \tilde{B}_w^{(s) 1-loop}(\mathbf{k}_1, \mathbf{k}_2, \mathbf{k}_3), \quad (\text{F.3})$$

where $B^{(s) 1-loop}[P_{nw}]$ is evaluated using only the smooth power spectrum and

$$\tilde{B}_w^{(s) 1-loop} = \tilde{B}_{411,w}^{(s)} + \tilde{B}_{321-II,w}^{(s)} + \tilde{B}_{321-I,w}^{(s)} + \tilde{B}_{222,w}^{(s)}. \quad (\text{F.4})$$

Here the individual terms read,

$$\begin{aligned} \tilde{B}_{411,w}^{(s)} &= 12 Z_1(\mathbf{k}_2) Z_1(\mathbf{k}_3) \left[e^{-k_2^2 \Sigma_{tot}^2(\mu_2)} P_w(k_2) P_{nw}(k_3) + e^{-k_3^2 \Sigma_{tot}^2(\mu_3)} P_{nw}(k_2) P_w(k_3) \right] \\ &\quad \times \int [dp] Z_4(-\mathbf{p}, \mathbf{p}, -\mathbf{k}_2, -\mathbf{k}_3) P_{nw}(p) \quad + 2 \text{ cyclic perm.}, \end{aligned} \quad (\text{F.5a})$$

$$\begin{aligned} \tilde{B}_{321-II,w}^{(s)} &= 6 Z_1(\mathbf{k}_2) Z_2(\mathbf{k}_2, \mathbf{k}_3) \left[e^{-k_2^2 \Sigma_{tot}^2(\mu_2)} P_w(k_2) P_{nw}(k_3) + e^{-k_3^2 \Sigma_{tot}^2(\mu_3)} P_{nw}(k_2) P_w(k_3) \right] \\ &\quad \times \int [dp] Z_3(-\mathbf{p}, \mathbf{p}, \mathbf{k}_3) P_{nw}(p) \quad + 5 \text{ permutations}, \end{aligned} \quad (\text{F.5b})$$

$$\begin{aligned}
 \tilde{B}_{321-I,w}^{(s)} &= 6Z_1(\mathbf{k}_3)e^{-k_3^2\Sigma_{\text{tot}}^2(\mu_3)}P_w(k_3) \\
 &\quad \times \int [dp]Z_3(-\mathbf{p}, \mathbf{p} - \mathbf{k}_2, -\mathbf{k}_3)Z_2(\mathbf{p}, \mathbf{k}_2 - \mathbf{p})P_{nw}(p)P_{nw}(|\mathbf{k}_2 - \mathbf{p}|) \\
 &\quad + 12Z_1(\mathbf{k}_3)P_{nw}(k_3)e^{-k_2^2\Sigma_{\text{tot}}^2(\mu_2)} \\
 &\quad \times \int [dp]Z_3(-\mathbf{p}, \mathbf{p} - \mathbf{k}_2, -\mathbf{k}_3)Z_2(\mathbf{p}, \mathbf{k}_2 - \mathbf{p})P_w(p)P_{nw}(|\mathbf{k}_2 - \mathbf{p}|) \\
 &\quad + 5 \text{ permutations,}
 \end{aligned} \tag{F.5c}$$

$$\begin{aligned}
 \tilde{B}_{222,w}^{(s)} &= 8 \int [dp]Z_2(-\mathbf{p}, \mathbf{p} + \mathbf{k}_1)Z_2(-\mathbf{p} - \mathbf{k}_1, \mathbf{p} - \mathbf{k}_2)Z_2(\mathbf{p} + \mathbf{k}_2, \mathbf{p}) \\
 &\quad \times e^{-p^2\Sigma_{\text{tot}}^2(\mu_p)}P_w(p)P_{nw}(|\mathbf{p} + \mathbf{k}_1|)P_{nw}(|\mathbf{p} - \mathbf{k}_2|) + 2 \text{ cyclic perm.}
 \end{aligned} \tag{F.5d}$$

We observe that the terms (F.5a), (F.5b) are of type (a), the term (F.5c) is of type (c), whereas (F.5d) is of type (d).

Appendix G

Dynamics of spherical collapse

G.1 Spherical collapse in Einstein–de Sitter universe

Consider a spherically symmetric density perturbation in a spatially flat universe filled with non-relativistic matter. For concreteness, we focus on the case of an overdensity. We study the motion of a spherical shell of matter enclosing the total mass M . Before the onset of shell-crossing the mass within the shell is conserved. Due to Newton's theorem (or Birkhoff's theorem in general relativity) the mechanical energy of the shell is conserved, so we write,

$$\frac{1}{2} \left(\frac{dy}{d\tau} \right)^2 - \frac{GM}{y} = \mathcal{E}, \quad (\text{G.1})$$

where y is the physical radius of the shell and τ is the physical time. The conserved energy \mathcal{E} is negative for the case of an overdensity. It is straightforward to obtain the solution to (G.1) in a parametric form,

$$y = -\frac{GM}{2\mathcal{E}}(1 - \cos \theta), \quad (\text{G.2a})$$

$$\tau = \frac{GM}{(-2\mathcal{E})^{3/2}}(\theta - \sin \theta). \quad (\text{G.2b})$$

Next, we switch from the variables y , τ to the comoving radius of the shell $r = y/a$ and the scale factor a . We use,

$$a = \left(\frac{8\pi G}{3} \rho_i a_i^3 \right)^{1/3} \left(\frac{3}{2} \tau \right)^{2/3}, \quad (\text{G.3})$$

$$M = \frac{4\pi}{3} \rho_i a_i^3 R^3, \quad (\text{G.4})$$

where ρ_i , a_i and R are the matter density, the scale factor and the comoving radius of the shell at some early time when the universe was almost homogeneous. Note that R has a finite limit at $a_i \rightarrow 0$ which coincides with the Lagrangian radius of the shell. Substitution of (G.3), (G.4) into Eqs. (G.2), gives,

$$r = R \left(\frac{2}{9} \right)^{1/3} \frac{1 - \cos \theta}{(\theta - \sin \theta)^{2/3}}, \quad (\text{G.5a})$$

$$a = \left(\frac{9}{2} \right)^{1/3} \frac{4\pi G}{3(-2\mathcal{E})} \rho_i a_i^3 R^2 (\theta - \sin \theta)^{2/3}, \quad (\text{G.5b})$$

We now recall the definition of the spherically averaged density contrast (5.11). Expressing it through the enclosed mass M , the radius of the shell and the mean density of the universe ρ_{univ} we obtain,

$$1 + \bar{\delta}(r) = \frac{3M}{4\pi y^3 \rho_{\text{univ}}} = \left(\frac{R}{r} \right)^3, \quad (\text{G.6})$$

where in the second equality we used that $\rho_{\text{univ}} = \rho_i a_i^3 / a^3$. This gives the relation (5.13) between the Lagrangian and Eulerian radii of the shell. Besides, we have from (G.5a),

$$\bar{\delta} = \mathcal{F}(\theta), \quad \text{where } \mathcal{F}(\theta) \equiv \frac{9}{2} \frac{(\theta - \sin \theta)^2}{(1 - \cos \theta)^3} - 1. \quad (\text{G.7})$$

It remains to relate the constant \mathcal{E} to the initial overdensity. To this end, we consider Eqs. (G.5b), (G.7) at the initial time. The parameter θ is initially small, so we can expand,

$$a_i = \frac{\theta_i^2}{2} \frac{4\pi G}{3(-2\mathcal{E})} \rho_i a_i^3 R^2, \quad \bar{\delta}_i(R) = \frac{3}{20} \theta_i^2, \quad (\text{G.8})$$

which gives

$$\mathcal{E} = -\frac{5}{3} \frac{\bar{\delta}_i(R)}{a_i} \frac{4\pi G}{3} \rho_i a_i^3 R^2. \quad (\text{G.9})$$

Substituting \mathcal{E} back into (G.5b) and introducing the rescaled linear density contrast $\bar{\delta}_L(R) \equiv a \bar{\delta}_i(R) / a_i$ we arrive at

$$\bar{\delta}_L(R) = \mathcal{G}(\theta) \equiv \frac{3}{20} [6(\theta - \sin \theta)]^{2/3}. \quad (\text{G.10})$$

Equations (G.7), (G.10) together provide a mapping between the linear and non-linear averaged density contrasts at a given moment of time expressed parametrically through the so-called development angle θ . The functions f and F

used in the main text (see Eq. (5.14)) are the superpositions

$$f = \mathcal{F} \circ \mathcal{G}^{-1}, \quad F = \mathcal{G} \circ \mathcal{F}^{-1}. \quad (\text{G.11})$$

We now derive several useful expressions for the fields characterizing the spherical collapse that are required for the calculation of linear fluctuations around the spherical collapse saddle point in Sec. 6.2. It is convenient to choose the logarithm of the growth factor as a new time variable,

$$\eta = \ln a. \quad (\text{G.12})$$

The key object is the linear density profile which we rescale to zero redshift. This will be denoted by $\delta_{L|0}(R)$. All other quantities are sourced by it and should be understood as functions of η and R . We first rewrite (G.10)

$$\theta - \sin \theta = \frac{e^{3\eta/2}}{6} \left(\frac{20}{3} \bar{\delta}_{L|0}(R) \right)^{3/2}, \quad (\text{G.13a})$$

which implicitly defines the function $\theta(\eta, R)$. Then we obtain the relations,

$$\frac{\partial \theta}{\partial R} = \frac{3(\theta - \sin \theta)}{2(1 - \cos \theta)} \cdot \frac{\bar{\delta}'_{L|0}(R)}{\bar{\delta}_{L|0}(R)}, \quad \frac{\partial \theta}{\partial \eta} = \frac{3(\theta - \sin \theta)}{2(1 - \cos \theta)}, \quad (\text{G.13b})$$

$$\frac{\partial r}{\partial R} = \left(\frac{2}{9} \right)^{1/3} \frac{1 - \cos \theta}{(\theta - \sin \theta)^{2/3}} \left[1 + R \frac{\bar{\delta}'_{L|0}}{\bar{\delta}_{L|0}} \left(\frac{3(\theta - \sin \theta) \sin \theta}{2(1 - \cos \theta)^2} - 1 \right) \right], \quad (\text{G.13c})$$

which yield the overdensity field,

$$\delta = \left[\frac{r^2}{R^2} \frac{\partial r}{\partial R} \right]^{-1} - 1 = \frac{9(\theta - \sin \theta)^2}{2(1 - \cos \theta)^3} \left[1 + R \frac{\bar{\delta}'_{L|0}}{\bar{\delta}_{L|0}} \left(\frac{3(\theta - \sin \theta) \sin \theta}{2(1 - \cos \theta)^2} - 1 \right) \right]^{-1} - 1. \quad (\text{G.13d})$$

We also need the velocity potential Ψ defined as

$$\partial_r \Psi = -u_r / \mathcal{H},$$

where u_r is the radial velocity of collapsing matter, $u_r = \frac{\partial r}{\partial t}$, and $\mathcal{H} = \frac{1}{a} \frac{da}{dt}$. Here t is the conformal time. We obtain,

$$\partial_r \Psi = -\frac{\partial r}{\partial \eta} = -R \left(\frac{2}{9} \right)^{1/3} \frac{1 - \cos \theta}{(\theta - \sin \theta)^{2/3}} \left[\frac{3(\theta - \sin \theta) \sin \theta}{2(1 - \cos \theta)^2} - 1 \right]. \quad (\text{G.13e})$$

Finally, the rescaled velocity divergence is

$$\Theta \equiv -\frac{\partial_i u_i}{\mathcal{H}} = \left(\frac{\partial r}{\partial R} \right)^{-1} \frac{\partial}{\partial R} \partial_r \Psi + \frac{2}{r} \partial_r \Psi. \quad (\text{G.13f})$$

In the case of an underdensity, the spherically symmetric dynamics is similar with only minor modifications. Without repeating the analysis, we summarize the relevant expressions,

$$\mathcal{G}(\theta) = \frac{3}{20}[6(\text{sh } \theta - \theta)]^{2/3}, \quad \mathcal{F}(\theta) = \frac{9(\text{sh } \theta - \theta)^2}{2(\text{ch } \theta - 1)^3} - 1, \quad (\text{G.14a})$$

$$\text{sh } \theta - \theta = \frac{e^{3\eta/2}}{6} \left(-\frac{20}{3} \bar{\delta}_{L|0}(R) \right)^{3/2}, \quad (\text{G.14b})$$

$$\frac{\partial \theta}{\partial R} = \frac{3(\text{sh } \theta - \theta) \bar{\delta}'_{L|0}}{2(\text{ch } \theta - 1) \bar{\delta}_{L|0}}, \quad \frac{\partial \theta}{\partial \eta} = \frac{3(\text{sh } \theta - \theta)}{2(\text{ch } \theta - 1)}, \quad (\text{G.14c})$$

$$r = R \left(\frac{2}{9} \right)^{1/3} \frac{\text{ch } \theta - 1}{(\text{sh } \theta - \theta)^{2/3}}, \quad (\text{G.14d})$$

$$\frac{\partial r}{\partial R} = \left(\frac{2}{9} \right)^{1/3} \frac{\text{ch } \theta - 1}{(\text{sh } \theta - \theta)^{2/3}} \left[1 + R \frac{\bar{\delta}'_{L|0}}{\bar{\delta}_{L|0}} \left(\frac{3(\text{sh } \theta - \theta) \text{sh } \theta}{2(\text{ch } \theta - 1)^2} - 1 \right) \right], \quad (\text{G.14e})$$

$$\delta = \frac{9(\text{sh } \theta - \theta)^2}{2(\text{ch } \theta - 1)^3} \left[1 + R \frac{\bar{\delta}'_{L|0}}{\bar{\delta}_{L|0}} \left(\frac{3(\text{sh } \theta - \theta) \text{sh } \theta}{2(\text{ch } \theta - 1)^2} - 1 \right) \right]^{-1} - 1, \quad (\text{G.14f})$$

$$\partial_r \hat{\Psi} = -R \left(\frac{2}{9} \right)^{1/3} \frac{\text{ch } \theta - 1}{(\text{sh } \theta - \theta)^{2/3}} \left[\frac{3(\text{sh } \theta - \theta) \text{sh } \theta}{2(\text{ch } \theta - 1)^2} - 1 \right]. \quad (\text{G.14g})$$

G.2 Spherical collapse in Λ CDM

Here we discuss how the previous results are modified in Λ CDM. In the presence of a cosmological constant Λ the equation (G.1) for the trajectory of a spherical shell is replaced by [157, 158],

$$\frac{1}{2} \left(\frac{dy}{d\tau} \right)^2 - \frac{GM}{y} - \frac{\Lambda y^2}{6} = \mathcal{E}. \quad (\text{G.15})$$

Unlike Eq. (G.1), this cannot be solved analytically, so one has to resort to numerical integration. It is convenient to use the scale factor¹ a as the time variable and switch from y to the variable

$$\zeta \equiv R/r, \quad (\text{G.16})$$

where $r = y/a$ and $R = \lim_{a \rightarrow 0} r$. One uses the Hubble equation,

$$\frac{1}{a^2} \left(\frac{da}{d\tau} \right)^2 = \frac{8\pi G}{3} \rho_{\text{univ}} + \frac{\Lambda}{3}, \quad (\text{G.17})$$

and the relations $\rho_{\text{univ}} = \rho_0/a^3$, $\Lambda = 8\pi G \rho_0 \Omega_\Lambda / \Omega_m$, with ρ_0 the present-day average *matter* density and $\Omega_\Lambda = 1 - \Omega_m$. Then Eq. (G.15) takes the following

¹We choose the scale factor to be normalized to 1 at the present epoch.

form,

$$\left(1 - \frac{d \ln \zeta}{d \ln a}\right)^2 = \left(1 + \frac{\Omega_\Lambda}{\Omega_m} a^3\right)^{-1} \left(\zeta^3 + \frac{\Omega_\Lambda}{\Omega_m} a^3 + \frac{3\mathcal{E}}{4\pi G \rho_0 R^2} a \zeta^2\right). \quad (\text{G.18})$$

To fix the value of the energy \mathcal{E} , we observe that Eq. (G.6) still applies in Λ CDM, so we have,

$$1 + \bar{\delta}(r) = \zeta^3, \quad (\text{G.19})$$

which at early times gives $\zeta = 1 + (a\bar{\delta}_i(R))/(3a_i)$. Substituting this into (G.18) and matching terms linear in a at $a \rightarrow 0$, we recover the same expression for \mathcal{E} , as in the EdS case,

$$\frac{3\mathcal{E}}{4\pi G \rho_0 R^2} = -\frac{5}{3} \frac{\bar{\delta}_i(R)}{a_i}. \quad (\text{G.20})$$

The next step is to express the initial overdensity in terms of the linear density contrast $\bar{\delta}_L(R)$ at the redshift z , at which we want to establish the spherical collapse mapping. To this end we write,

$$\frac{\bar{\delta}_i(R)}{a_i} = \frac{g(z)}{g(z_i)} \bar{\delta}_i(R) \frac{g(z_i)}{a_i} \frac{1}{g(z)} = \frac{g_\Lambda}{g(z)} \bar{\delta}_L(R). \quad (\text{G.21})$$

In the last equality we have used that at early times the growth factor is proportional to a ,

$$g(z_i) = g_\Lambda \cdot a_i \quad (\text{G.22})$$

where g_Λ is a constant². Collecting the relations (G.20), (G.21) and inserting them into Eq. (G.18) we cast the latter in the form,

$$\left(1 - \frac{d \ln \zeta}{d \ln a}\right)^2 = \left(1 + \frac{\Omega_\Lambda}{\Omega_m} a^3\right)^{-1} \left(\zeta^3 - \frac{5g_\Lambda}{3g(z)} \bar{\delta}_L(R) a \zeta^2 + \frac{\Omega_\Lambda}{\Omega_m} a^3\right). \quad (\text{G.23})$$

With this in hand, the algorithm to construct the spherical collapse mapping goes as follows:

- (i) Fix a value $\bar{\delta}_L(R)$ of the spherically averaged linear overdensity at redshift z ;
- (ii) Solve Eq. (G.23) from $a = 0$ to $a = (1+z)^{-1}$ with the initial condition $\zeta|_{a=0} = 1$;
- (iii) Compute f as $f(\bar{\delta}_L(R); z) = \zeta^3((1+z)^{-1}) - 1$.

The function F is then found as the inverse of f .

²Recall that we normalize $g(z)$ to be 1 at $z = 0$, which leads to a constant offset between g and a in the matter-dominated era. For our reference cosmology $g_\Lambda = 1.328$.

As discussed in Sec. 5.1.2, the functions f and F computed in this way are very weakly depending on the redshift and, somewhat surprisingly, coincide with the corresponding functions in EdS cosmology at the level of a few per mil in the relevant range of density contrasts.

Before concluding this section, we note that the formulas derived above can be used to obtain a first order differential equation for the growth factor g as a function of a in the Λ CDM universe. To this end, we assume that the overdensity is small at all times, so that we can linearize Eq. (G.19),

$$\zeta = 1 + \frac{g(a)}{3g(a_i)} \bar{\delta}_i(R) .$$

Substituting this into (G.23) and also linearizing it in $\bar{\delta}_i(R)$ we arrive at,

$$\frac{dg}{da} = \left(1 + \frac{\Omega_\Lambda}{\Omega_m} a^3\right)^{-1} \left(-\frac{3g(a)}{2a} + \frac{5g_\Lambda}{2}\right), \quad (\text{G.24})$$

which is to be integrated with the boundary condition $g|_{a=1} = 1$.

G.3 Monopole response matrix

In this section we derive analytic expressions for the monopole response matrix $Q_0(k_1, k_2)$ introduced in Eq. (5.34) and the monopole fluctuation determinant (6.1). These results are used in Sec. 6.1 for the perturbative calculation of the aspherical prefactor and for validating our numerical code (see Appendix H). The starting point of the derivation is the relation provided by the spherical collapse mapping,

$$F(\bar{\delta}_W) = \bar{\delta}_L(r_*(1 + \bar{\delta}_W)^{1/3}) . \quad (\text{G.25})$$

We consider a monopole fluctuation on top of the saddle-point configuration (5.26), (5.27), so we write

$$\delta_L(R) = \hat{\delta}_L(R) + \delta_{L,0}^{(1)}(R) , \quad \bar{\delta}_W = \delta_* + \bar{\delta}_W^{(1)} + \bar{\delta}_W^{(2)} , \quad (\text{G.26})$$

where the terms $\bar{\delta}_W^{(1)}$ and $\bar{\delta}_W^{(2)}$ are linear and quadratic in $\delta_{L,0}^{(1)}$ respectively. Substituting these expressions into (G.25), Taylor expanding the two sides and grouping

the terms of linear and quadratic order, we obtain two equations,

$$F'(\delta_*) \bar{\delta}_W^{(1)} = \frac{R_* \bar{\delta}'_L(R_*)}{3(1 + \delta_*)} \bar{\delta}_W^{(1)} + \bar{\delta}_{L,0}^{(1)}(R_*), \quad (\text{G.27a})$$

$$F'(\delta_*) \bar{\delta}_W^{(2)} + \frac{F''(\delta_*)}{2} (\bar{\delta}_W^{(1)})^2 = \frac{R_* \bar{\delta}'_L(R_*)}{3(1 + \delta_*)} \bar{\delta}_W^{(2)} + \frac{R_*^2}{18(1 + \delta_*)^2} \left(\bar{\delta}''_L(R_*) - 2\bar{\delta}'_L(R_*) \right) (\bar{\delta}_W^{(1)})^2 \\ + \frac{R_*}{2(1 + \delta_*)} \bar{\delta}_W^{(1)} (\bar{\delta}_{L,0}^{(1)})'(R_*), \quad (\text{G.27b})$$

where R_* is defined in (5.20). Next we use the expressions

$$\bar{\delta}'_L(R_*) = -\frac{3F(\delta_*)}{R_*} \left(1 - \frac{\xi_{R_*}}{\sigma_{R_*}^2} \right), \quad (\text{G.28a})$$

$$\bar{\delta}''_L(R_*) = \frac{12F(\delta_*)}{R_*^2} \left(1 - \frac{\xi_{R_*}}{\sigma_{R_*}^2} \right) - F(\delta_*) \frac{\Sigma_{R_*}^2}{\sigma_{R_*}^2}, \quad (\text{G.28b})$$

where $\sigma_{R_*}^2$, ξ_{R_*} are defined in Sec. 5.1.2 and

$$\Sigma_{R_*}^2 = 4\pi \int [dk] k^2 |W_{\text{th}}(kR_*)|^2 P(k). \quad (\text{G.29})$$

Substituting (G.28a) into (G.27a) we get,

$$\bar{\delta}_W^{(1)} = \frac{\bar{\delta}_{L,0}^{(1)}(R_*)}{\hat{C}(\delta_*)}, \quad (\text{G.30})$$

where $\hat{C}(\delta_*)$ is introduced in Eq. (5.29). We note in passing that this relation implies an expression for the linear monopole response kernel $S(k)$ (see Eq. (5.34)),

$$S(k) = \frac{W_{\text{th}}(kR_*)}{\hat{C}(\delta_*)}$$

From (G.27b) we further obtain,

$$\bar{\delta}_W^{(2)} = -\frac{\hat{E}(\delta_*)}{\hat{C}^3(\delta_*)} \left(\bar{\delta}_{L,0}^{(1)}(R_*) \right)^2 + \frac{1}{(1 + \delta_*) \hat{C}^2(\delta_*)} \bar{\delta}_{L,0}^{(1)}(R_*) \bar{\delta}_{L,0}^{(1)}(R_*), \quad (\text{G.31})$$

where

$$\hat{E}(\delta_*) = \frac{F''(\delta_*)}{2} + \frac{F'(\delta_*)}{1 + \delta_*} + \frac{F(\delta_*)}{(1 + \delta_*)^2} \frac{R_*^2 \Sigma_{R_*}^2}{18\sigma_{R_*}^2}, \quad (\text{G.32})$$

and we have used the identity,

$$(\bar{\delta}_{L,0}^{(1)})'(R_*) = \frac{3}{R_*} \left(\bar{\delta}_{L,0}^{(1)}(R_*) - \bar{\delta}_{L,0}^{(1)}(R_*) \right).$$

Finally, switching from position to momentum space,

$$\bar{\delta}_{L,0}^{(1)}(R_*) = 4\pi \int [dk] W_{\text{th}}(kR_*) \delta_{L,0}^{(1)}(k), \quad \delta_{L,0}^{(1)}(R_*) = 4\pi \int [dk] \frac{\sin(kR_*)}{kR_*} \delta_{L,0}^{(1)}(k),$$

and comparing (G.31) to Eq. (5.34) we arrive at the following expression for the monopole response matrix,

$$Q_0(k_1, k_2) = -\frac{4\pi\hat{E}}{\hat{C}^3} W_{\text{th}}(k_1R_*) W_{\text{th}}(k_2R_*) + \frac{2\pi}{(1+\delta_*)\hat{C}^2} \left[W_{\text{th}}(k_1\hat{R}_*) \frac{\sin(k_2R_*)}{k_2R_*} + \frac{\sin(k_1R_*)}{k_1R_*} W_{\text{th}}(k_2R_*) \right], \quad (\text{G.33})$$

To evaluate the monopole fluctuation determinant \mathcal{D}_0 defined in (6.1), we observe that the matrix $\mathbb{1} + 2\hat{\lambda}\sqrt{P}Q_0\sqrt{P}$ can be written as

$$\mathbb{1}(k_1, k_2) + a(k_1)b(k_2) + b(k_1)a(k_2)$$

with

$$a(k) = 2\hat{\lambda}\sqrt{P(k)} W_{\text{th}}(kR_*), \quad b(k) = \left[-\frac{2\pi\hat{E}}{\hat{C}^3} W_{\text{th}}(kR_*) + \frac{2\pi}{(1+\delta_*)\hat{C}^2} \frac{\sin kR_*}{kR_*} \right] \sqrt{P(k)}.$$

The general formula for the determinant of a matrix of this form is derived in Appendix D of Ref. [9]. Applying it to the case at hand and using the expression (5.29) for $\hat{\lambda}$ gives,

$$\mathcal{D}_0 = 1 + \frac{2F}{\hat{C}^2} \left[\hat{E} - \frac{\hat{C}}{(1+\delta_*)} \frac{\xi_{R_*}}{\sigma_{R_*}^2} \right] + \frac{F^2}{(1+\delta_*)^2 \hat{C}^2} \left[\left(\frac{\xi_{R_*}}{\sigma_{R_*}^2} \right)^2 - \frac{\sigma_{1R_*}^2}{\sigma_{R_*}^2} \right], \quad (\text{G.34})$$

where we have defined

$$\sigma_{1R_*}^2 = 4\pi \int [dk] \left(\frac{\sin(kR_*)}{kR_*} \right)^2 P(k). \quad (\text{G.35})$$

It is instructive to compare the full result (G.34) to a trace approximation which treats the matrix $2\hat{\lambda}\sqrt{P}Q_0\sqrt{P}$ as small, (G.34),

$$\begin{aligned} \mathcal{D}_0 &= \exp \left\{ \text{Tr} \ln(\mathbb{1} + 2\hat{\lambda}\sqrt{P}Q_0\sqrt{P}) \right\} \\ &\approx 1 + 2\hat{\lambda} \text{Tr}(\sqrt{P}Q_0\sqrt{P}) = 1 + \frac{2F}{\hat{C}^2} \left[\hat{E} - \frac{\hat{C}}{1+\delta_*} \frac{\xi_{R_*}}{\sigma_{R_*}^2} \right]. \end{aligned} \quad (\text{G.36})$$

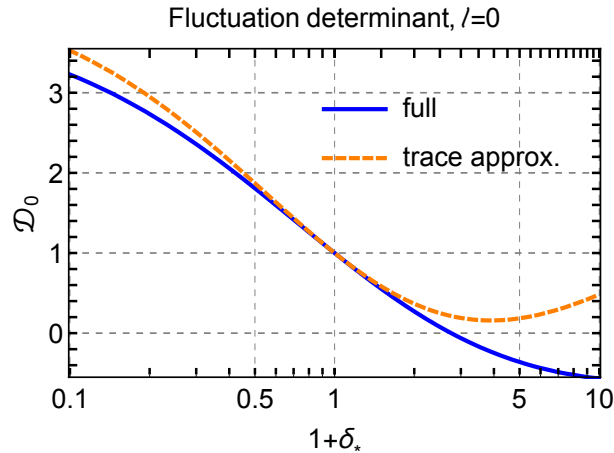


FIGURE G.1: Monopole fluctuation determinant \mathcal{D}_0 (blue, solid) and its trace approximation (orange, dashed). Note that the determinant crosses zero at $\delta_* \approx 1.75$.

We see that it reproduces the first two terms in (G.34), but misses the third one. In Fig. G.1 we display the trace approximation versus the full result (G.34) for our reference cosmology. We observe that, though the trace approximation is, strictly speaking, applicable only for $\delta_* \ll 1$, it works quite well in the range $\delta_* \in [-0.9, 1]$. Still, at larger overdensities it deviates significantly from the true result.

G.4 Growth factor in a spherically-symmetric separate universe

To estimate the dependence of the UV counterterm on the density in Sec. 6.5.2, we need the linear growth factor for perturbations in the background of a spherical top-hat overdensity³. Due to the Birkhoff theorem, such an overdensity can be treated as a separate closed universe. Then the linear growth factor does not depend on the wavenumber of the mode and can be derived by considering spherically symmetric top-hat perturbations.

Consider a spherically symmetric lump of matter with a top-hat profile, whose final density contrast w.r.t. the unperturbed cosmology is equal to δ . Let us additionally perturb this lump by a linear fluctuation $\delta_L^{(1)}$. According to the spherical collapse mapping, this fluctuation produces the following perturbation

³We are talking about overdensity for concreteness. For an underdensity the reasoning is exactly the same.

of the non-linear density $\delta^{(1)}$,

$$\delta^{(1)} = \frac{\delta_L^{(1)}}{F'(\delta_*)}. \quad (\text{G.37})$$

The density contrast in the separate universe should be normalized to the background density of that universe,

$$\delta_{\text{su}}^{(1)} = \frac{\delta^{(1)}}{1 + \delta_*}. \quad (\text{G.38})$$

This gives for the growth factor in the separate universe:

$$D(\delta_*, z) = \frac{g(z)}{F'(\delta_*)(1 + \delta_*)}. \quad (\text{G.39})$$

Note that the dependence of the growth factor on redshift and density factorize.

Appendix H

Numerical procedure for aspherical determinants

In this Appendix we discuss the details of our numerical method, which is implemented in the open-source code `AsPy`¹ written in `Python` using `scipy` and `numpy` libraries.

We first cast the partial differential equations (6.36) in the form suitable for numerical solution using finite differences. In this section we will omit the subscript ℓ denoting linear aspherical perturbations. We switch to the Lagrangian coordinate R comoving with the background flow, which allows us to absorb the shift terms into the time derivative,

$$\frac{\partial}{\partial \eta} - \partial_r \hat{\Psi} \frac{\partial}{\partial r} \equiv \frac{d}{d\eta} \Big|_{\text{flow}} . \quad (\text{H.1})$$

Equations (6.36a), (6.36b) take the form,

$$\frac{d\delta}{d\eta} = A_1(\eta, R)\delta + A_2(\eta, R)\Theta + A_3(\eta, R)\partial_R\Psi , \quad (\text{H.2a})$$

$$\frac{d\Theta}{d\eta} = \frac{3}{2}\delta + A_4(\eta, R)\Theta + A_5(\eta, R)\partial_R\Psi + \ell(\ell + 1)A_6(\eta, R)\Psi , \quad (\text{H.2b})$$

¹<https://github.com/Michalychforever/AsPy>

where we defined the following background functions:

$$A_1 = \hat{\Theta}, \quad A_4 = -\frac{1}{2} + 2 \left(\hat{\Theta} - \frac{2}{r} \partial_r \hat{\Psi} \right), \quad (\text{H.3a})$$

$$A_2 = 1 + \hat{\delta}, \quad A_5 = \frac{1}{\frac{\partial r}{\partial R}} \left(\frac{1}{\frac{\partial r}{\partial R}} \partial_R \hat{\Theta} - \frac{4}{r} \left(\hat{\Theta} - 3 \frac{\partial_r \hat{\Psi}}{r} \right) \right), \quad (\text{H.3b})$$

$$A_3 = \frac{1}{\left(\frac{\partial r}{\partial R}\right)^2} \partial_R \hat{\delta}, \quad A_6 = 2 \left(\hat{\Theta} - 3 \frac{\partial_r \hat{\Psi}}{r} \right) \frac{1}{r^2}. \quad (\text{H.3c})$$

The initial conditions for the density and velocity fields are given by Eqs. (6.38a). Note that Eqs. (H.2) do not contain spatial derivatives of δ or Θ , so we do not need to impose any boundary conditions on them.

The Euler and continuity equations are supplemented by the Poisson equation

$$\left(\partial_r^2 + \frac{2\partial_r}{r} - \frac{\ell(\ell+1)}{r^2} \right) \Psi(\eta, R) = \Theta(\eta, R). \quad (\text{H.4})$$

The boundary conditions for the velocity potential are given by,

$$\begin{aligned} \Psi(\eta, R) &\propto r^\ell(R), \quad \text{at } R \rightarrow 0 \\ \Psi(\eta, R_{max}) &= e^{(\eta-\eta_{min})} \Psi(\eta_{min}, R_{max}). \end{aligned} \quad (\text{H.5})$$

The boundary condition at the origin is dictated by the structure of the Poisson equation (6.36c). The second condition comes from the assumption that at spatial infinity the velocity potential follows the linear evolution, which is justified since the background profile falls off quickly outside the window function.

We work on an equally-spaced rectangular lattice with $N_R \times N_\eta$ nodes and physical size $[R_{min}, R_{max}] \times [\eta_{min}, 0]$. We implement an implicit second-order Runge-Kutta scheme (RK2) for the Euler and continuity equations. For the Poisson equation we use an implicit second-order finite difference scheme.

We use the discrete version of the fluctuation operator obtained by rewriting the integrals in the exponent of (5.38) in a discrete form and taking the corresponding Gaussian integral. This yields,

$$\mathcal{O}_\ell = \delta_{ij} + 2\hat{\lambda} \frac{\Delta k}{(2\pi)^3} k_i k_j Q_\ell(k_i, k_j) \sqrt{P(k_i)P(k_j)}, \quad (\text{H.6})$$

with $i, j = 0, \dots, N$; $\Delta k = (k_N - k_0)/N$. One can check that this definition gives the correct continuous limit for the trace²:

$$\sum_{i=0}^N \frac{\Delta k k_i^2}{(2\pi)^3} Q_\ell(k_i, k_i) P(k_i) \xrightarrow{N \rightarrow \infty} \int_0^\infty [dk] Q_\ell(k, k) P(k) = \text{Tr } Q_\ell P. \quad (\text{H.7})$$

We implement the algorithm for computing the aspherical determinant from Sec. 6.2.3. At the first step the code computes the background functions (H.3) required for solving the fluid equations on the grid. To this end we make a sample of ~ 20 values of δ_* in the range $[-0.9, 9]$ and use the spherical collapse linear profile (5.27) to compute the non-linear background configuration defined by the equations from Sec. G.1.

At the second step we sample the momentum space and compute the evolution of linear fluctuations given by the finite difference approximation to the equations (H.2), (H.4) with appropriate initial and boundary conditions for each momentum k_i from the sample. We use the sample of $N = 200$ wavenumbers which we found sufficient for our purposes.

We found that the following grid parameters lead to a good convergence for most of the multipoles in the δ_* -range of interest:

$$\begin{aligned} R_{min} &= 10^{-2} \text{Mpc}/h, & R_{max} &= 10 \cdot R_*, & N_R &= 1000, \\ \eta_{min} &= -7, & N_\eta &= 500. \end{aligned} \quad (\text{H.8})$$

For the dipole we increased the spatial extent of the grid to $R_{max} = 15 \cdot R_*$, $N_R = 1500$. We have run several tests and found that increasing the grid resolution further or moving the box boundaries can only change the final results at the 0.1% level.

At the third step we use the linear wavefunctions computed in step 2 to construct the sources $\Upsilon_{\Theta, \delta}$ for all different pairs of momenta (k_i, k_j) , $i, j = 0, \dots, N$. For the dipole sector, we also construct the sources $B_{\Theta, \delta}$

At the fourth step we solve the finite difference equations for the time evolution of $\mu^{(2)}$ and $r_\eta^{(2)}$ obtained by discretizing Eqs. (6.55). This yields the matrix $Q_\ell(k_i, k_j)$, which is used to obtain the desired determinant. In the dipole sector we separately compute $\check{Q}_\ell(k_i, k_j)$, $B(k_i)$, and A using (6.55) with the corresponding sources (6.70). The final determinant is obtained upon multiplying the IR-sensitive determinant \mathcal{D}_{IR} and the IR-safe determinant $\det(\mathbb{1} + 2\hat{\lambda}\sqrt{P}\check{Q}_\ell\sqrt{P})$.

²We do not assign the weight 1/2 to the boundary values, but choose IR and UV cutoffs to make sure that the results are independent of them.

As a cross-check, we computed A both by solving Eqs. (6.55) and from the relation (6.82), which yielded results that agree at the per mil level.

We have validated our code by computing the determinant of the monopole fluctuations and comparing it to the analytic expression (G.34). The results of this test are displayed in Fig. H.1. Numerical procedure agrees with the analytic formula at per mil level.

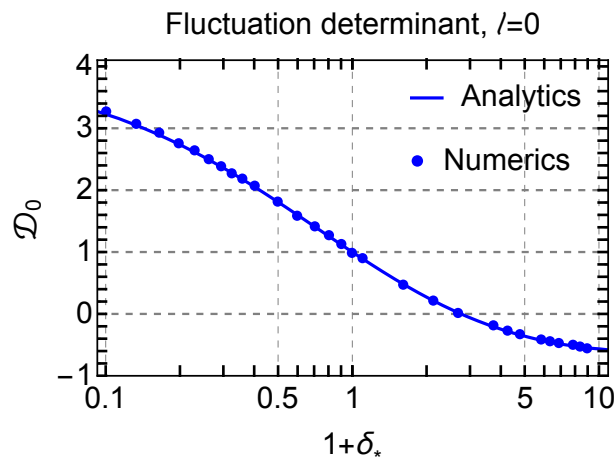


FIGURE H.1: The fluctuation determinant in the monopole sector: the result of our numerical procedure (dots) vs. Eq. (G.34) (line).

Appendix I

A comment on log-normal model

It has long been known that the observed counts-in-cells distribution can be well approximated by log-normal [74–77],

$$\bar{P}_{\text{log-normal}}(\delta_*) = \frac{1}{\sqrt{2\pi\sigma_{\text{ln}}^2(1+\delta_*)}} \exp\left\{-\frac{(\ln(1+\delta_*) + \sigma_{\text{ln}}^2/2)^2}{2\sigma_{\text{ln}}^2}\right\}, \quad (\text{I.1})$$

where $\sigma_{\text{ln}}^2 = \langle [\ln(1+\delta_*)]^2 \rangle$ is the log-density variance, to be fitted from the data. The mean of the distribution (I.1) is adjusted to ensure $\langle \delta_* \rangle = 0$. The success of this model is partially due to the fact that the spherical collapse mapping $F(\delta_*)$ is close to $\ln(1+\delta_*)$ for moderate density contrasts, see the left panel of Fig. I.1. The difference grows for bigger $|\delta_*|$, but, curiously enough, gets largely compensated by the scale dependence of σ_{R_*} . This compensation is a mere coincidence due to the shape of the power spectrum at mildly non-linear scales [79, 80]. Indeed, consider, for example, a universe with a power-law power spectrum $P(k) \propto k^n$. In such a universe the variance scales as $\sigma_{R_*}^2 \propto (1+\delta_*)^{-1-n/3}$, which clearly depends on the slope n . On the other hand, spherical collapse mapping is determined exclusively by dynamics and is insensitive to the statistics of the initial conditions. One concludes that changing the slope of the power spectrum would destroy the conspiracy and the log-normal model would fail.

Although the log-normal PDF gives a good leading order approximation, it does not incorporate the correct prefactor. As a consequence, it is unable to describe the data with the accuracy better than $\sim 10\%$ even at moderate densities and quickly deviates from the data in the tails [81, 91]. This is illustrated in the right

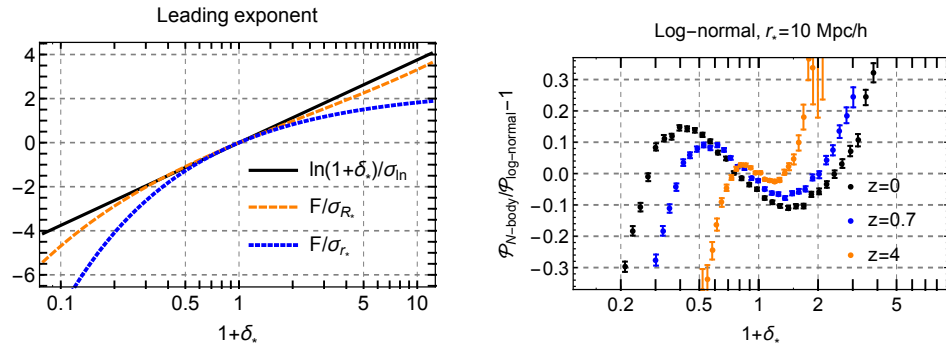


FIGURE I.1: Left panel: The functions defining the leading exponential behavior of the log-normal PDF (I.1) and our theoretical PDF (5.30). The log-variance σ_{\ln} is found from the fit to N-body data. Right panel: Residuals of the N-body data with respect to the best fit log-normal models at different redshifts. σ_{\ln} is refitted for each z independently. The cell radius is $r_* = 10 \text{ Mpc}/h$.

panel of Fig. I.1 where we show the residuals of the N-body data with respect to the best fit log-normal model.

Bibliography

- [1] D. Blas et al., JCAP 1607 (2016) 052, 1512.05807.
- [2] D. Blas et al., JETP Lett. 103 (2016) 624, 1602.04188, [Pisma Zh. Eksp. Teor. Fiz.103,no.10,708(2016)].
- [3] D. Blas et al., JCAP 1607 (2016) 028, 1605.02149.
- [4] M.M. Ivanov, M.S. Pshirkov and G.I. Rubtsov, Phys. Rev. D94 (2016) 063004, 1606.01480.
- [5] M.M. Ivanov and A.A. Tokareva, JCAP 1612 (2016) 018, 1610.05330.
- [6] M. Ata et al., Mon. Not. Roy. Astron. Soc. 473 (2018) 4773, 1705.06373.
- [7] E. Bellini et al., Phys. Rev. D97 (2018) 023520, 1709.09135.
- [8] M.M. Ivanov and S. Sibiryakov, JCAP 1807 (2018) 053, 1804.05080.
- [9] M.M. Ivanov, A.A. Kaurov and S. Sibiryakov, (2018), 1811.07913.
- [10] M.M. Ivanov et al., (2018), 1811.10997.
- [11] J.F. Donoghue, M.M. Ivanov and A. Shkerin, (2017), 1702.00319.
- [12] S. Weinberg, Rev. Mod. Phys. 61 (1989) 1.
- [13] C.P. et al. (Particle Data Group), Chin. Phys. C 40 ((2016)) 100001.
- [14] A. Schneider et al., JCAP 1604 (2016) 047, 1503.05920.
- [15] F. Bernardeau et al., Phys. Rept. 367 (2002) 1, astro-ph/0112551.
- [16] E.T. Vishniac, MNRAS 203 (1983) 345.
- [17] B. Jain and E. Bertschinger, Astrophys. J. 456 (1996) 43, astro-ph/9503025.
- [18] R. Scoccimarro and J. Frieman, Astrophys. J. Suppl. 105 (1996) 37, astro-ph/9509047.

-
- [19] P. Creminelli et al., JCAP 1312 (2013) 025, 1309.3557.
- [20] D. Blas, M. Garny and T. Konstandin, JCAP 1309 (2013) 024, 1304.1546.
- [21] J.J.M. Carrasco et al., JCAP 1407 (2014) 056, 1304.4946.
- [22] N.S. Sugiyama and D.N. Spergel, JCAP 1402 (2014) 042, 1306.6660.
- [23] A. Kehagias and A. Riotto, Nucl. Phys. B873 (2013) 514, 1302.0130.
- [24] M. Peloso and M. Pietroni, JCAP 1305 (2013) 031, 1302.0223.
- [25] D. Blas, M. Garny and T. Konstandin, JCAP 1401 (2014) 010, 1309.3308.
- [26] D.J. Eisenstein, H.j. Seo and M.J. White, Astrophys. J. 664 (2007) 660, astro-ph/0604361.
- [27] M. Crocce and R. Scoccimarro, Phys. Rev. D77 (2008) 023533, 0704.2783.
- [28] L. Senatore and M. Zaldarriaga, JCAP 1502 (2015) 013, 1404.5954.
- [29] T. Baldauf et al., Phys. Rev. D92 (2015) 043514, 1504.04366.
- [30] D. Baumann et al., JCAP 1207 (2012) 051, 1004.2488.
- [31] J.J.M. Carrasco, M.P. Hertzberg and L. Senatore, JHEP 09 (2012) 082, 1206.2926.
- [32] T. Baldauf, L. Mercolli and M. Zaldarriaga, Phys. Rev. D92 (2015) 123007, 1507.02256.
- [33] S. Foreman, H. Perrier and L. Senatore, JCAP 1605 (2016) 027, 1507.05326.
- [34] A.A. Abolhasani, M. Mirbabayi and E. Pajer, JCAP 1605 (2016) 063, 1509.07886.
- [35] SDSS, D.J. Eisenstein et al., Astrophys. J. 633 (2005) 560, astro-ph/0501171.
- [36] 2dFGRS, S. Cole et al., Mon. Not. Roy. Astron. Soc. 362 (2005) 505, astro-ph/0501174.
- [37] BOSS, S. Alam et al., Mon. Not. Roy. Astron. Soc. 470 (2017) 2617, 1607.03155.
- [38] DES, T.M.C. Abbott et al., Submitted to: Mon. Not. Roy. Astron. Soc. (2017), 1712.06209.

-
- [39] BOSS, T. Delubac et al., *Astron. Astrophys.* 574 (2015) A59, 1404.1801.
- [40] J.E. Bautista et al., *Astron. Astrophys.* 603 (2017) A12, 1702.00176.
- [41] J. Hou et al., (2018), 1801.02656.
- [42] Y. Liang et al., *Mon. Not. Roy. Astron. Soc.* 459 (2016) 4020, 1511.04391.
- [43] C. Zhao et al., (2018), 1802.03990.
- [44] Z. Slepian et al., (2015), 1512.02231.
- [45] Z. Slepian et al., *Mon. Not. Roy. Astron. Soc.* 469 (2017) 1738, 1607.06097.
- [46] D.W. Pearson and L. Samushia, *Mon. Not. Roy. Astron. Soc.* 478 (2018) 4500, 1712.04970.
- [47] D.J. Eisenstein et al., *Astrophys. J.* 664 (2007) 675, astro-ph/0604362.
- [48] H.J. Seo et al., *Astrophys. J.* 720 (2010) 1650, 0910.5005.
- [49] M. Schmittfull et al., *Phys. Rev. D* 92 (2015) 123522, 1508.06972.
- [50] A. Obuljen et al., *JCAP* 1709 (2017) 012, 1610.05768.
- [51] H.M. Zhu et al., *Phys. Rev. D* 96 (2017) 123502, 1611.09638.
- [52] H.M. Zhu, U.L. Pen and X. Chen, (2016), 1609.07041.
- [53] M. Schmittfull, T. Baldauf and M. Zaldarriaga, *Phys. Rev. D* 96 (2017) 023505, 1704.06634.
- [54] BOSS, F. Beutler et al., *Mon. Not. Roy. Astron. Soc.* 464 (2017) 3409, 1607.03149.
- [55] BOSS, A.J. Ross et al., *Mon. Not. Roy. Astron. Soc.* 464 (2017) 1168, 1607.03145.
- [56] M. Peloso et al., *JCAP* 1507 (2015) 001, 1505.07477.
- [57] Z. Ding et al., *Mon. Not. Roy. Astron. Soc.* 479 (2018) 1021, 1708.01297.
- [58] D. Baumann, D. Green and M. Zaldarriaga, *JCAP* 1711 (2017) 007, 1703.00894.
- [59] D. Baumann et al., (2018), 1803.10741.
- [60] BOSS, F. Beutler et al., *Mon. Not. Roy. Astron. Soc.* 466 (2017) 2242, 1607.03150.

-
- [61] BOSS, S. Satpathy et al., *Mon. Not. Roy. Astron. Soc.* 469 (2017) 1369, 1607.03148.
- [62] M. Crocce and R. Scoccimarro, *Phys. Rev. D* 73 (2006) 063519, astro-ph/0509418.
- [63] T. Matsubara, *Phys. Rev. D* 77 (2008) 063530, 0711.2521.
- [64] Z. Vlah et al., *JCAP* 1603 (2016) 057, 1509.02120.
- [65] L.F. de la Bella et al., *JCAP* 1711 (2017) 039, 1704.05309.
- [66] L. Senatore and G. Trevisan, *JCAP* 1805 (2018) 019, 1710.02178.
- [67] M. Mirbabayi, M. Simonović and M. Zaldarriaga, (2014), 1412.3796.
- [68] T. Matsubara, *Phys. Rev. D* 78 (2008) 083519, 0807.1733, [Erratum: *Phys. Rev. D* 78, 109901 (2008)].
- [69] L. Senatore and M. Zaldarriaga, (2014), 1409.1225.
- [70] Z. Vlah, E. Castorina and M. White, *JCAP* 1612 (2016) 007, 1609.02908.
- [71] E. Hubble, *The Astrophysical Journal* 79 (1934) 8.
- [72] DES, L. Clerkin et al., *Mon. Not. Roy. Astron. Soc.* 466 (2017) 1444, 1605.02036.
- [73] DES, D. Gruen et al., *Phys. Rev. D* 98 (2018) 023507, 1710.05045.
- [74] P. Coles and B. Jones, *Mon. Not. Roy. Astron. Soc.* 248 (1991) 1.
- [75] L. Kofman et al., *Astrophys. J.* 420 (1994) 44, astro-ph/9311028.
- [76] I. Kayo, A. Taruya and Y. Suto, *Astrophys. J.* 561 (2001) 22, astro-ph/0105218.
- [77] 2dFGRS, V. Wild et al., *Mon. Not. Roy. Astron. Soc.* 356 (2005) 247, astro-ph/0404275.
- [78] L. Hurtado-Gil et al., *Astron. Astrophys.* 601 (2017) A40, 1703.01087.
- [79] F. Bernardeau, *Astron. Astrophys.* 291 (1994) 697, astro-ph/9403020.
- [80] F. Bernardeau and L. Kofman, *Astrophys. J.* 443 (1995) 479, astro-ph/9403028.
- [81] A. Klypin et al., (2017), 1706.01909.
- [82] F. Bernardeau, *Astrophys. J.* 392 (1992) 1.

-
- [83] P. Valageas and R. Schaeffer, *Astron. Astrophys.* 328 (1997) 435, astro-ph/9710128.
- [84] P. Valageas, *Astron. Astrophys.* 337 (1998) 655, astro-ph/9807033.
- [85] P. Valageas, *Astron. Astrophys.* 382 (2002) 412, astro-ph/0107126.
- [86] F. Bernardeau and P. Reimberg, *Phys. Rev. D* 94 (2016) 063520, 1511.08641.
- [87] C. Uhlemann et al., *Mon. Not. Roy. Astron. Soc.* 460 (2016) 1529, 1512.05793.
- [88] F. Bernardeau, C. Pichon and S. Codis, *Phys. Rev. D* 90 (2014) 103519, 1310.8134.
- [89] F. Bernardeau, *Astron. Astrophys.* 312 (1996) 11, astro-ph/9602072.
- [90] F. Bernardeau, S. Codis and C. Pichon, *Mon. Not. Roy. Astron. Soc.* 449 (2015) L105, 1501.03670.
- [91] C. Uhlemann et al., *Mon. Not. Roy. Astron. Soc.* 466 (2017) 2067, 1607.01026.
- [92] C. Uhlemann et al., *Mon. Not. Roy. Astron. Soc.* 473 (2018) 5098, 1705.08901.
- [93] R.K. Sheth, *Mon. Not. Roy. Astron. Soc.* 300 (1998) 1057, astro-ph/9805319.
- [94] J. Betancort-Rijo and M. Lopez-Corredoira, *Astrophys. J.* 566 (2002) 623, astro-ph/0110624.
- [95] T.Y. Lam and R.K. Sheth, *Mon. Not. Roy. Astron. Soc.* 386 (2008) 407, 0711.5029.
- [96] E. Pajer and D. van der Woude, *JCAP* 1805 (2018) 039, 1710.01736.
- [97] S. Matarrese, L. Verde and R. Jimenez, *Astrophys. J.* 541 (2000) 10, astro-ph/0001366.
- [98] C. Uhlemann et al., *Mon. Not. Roy. Astron. Soc.* 474 (2018) 2853, 1708.02206.
- [99] O. Leicht et al., (2018), 1808.09968.
- [100] Y. Feng et al., *Mon. Not. Roy. Astron. Soc.* 463 (2016) 2273, 1603.00476.

-
- [101] J. Kim et al., *J. Korean Astron. Soc.* 44 (2011) 217, 1112.1754.
- [102] D.S. Gorbunov and V.A. Rubakov, *Introduction to the theory of the early universe: Cosmological perturbations and inflationary theory* (, 2011).
- [103] H.J. Seo and D.J. Eisenstein, *Astrophys. J.* 665 (2007) 14, astro-ph/0701079.
- [104] P.J.E. Peebles, Princeton University Press (1980).
- [105] M.H. Goroff et al., *Astrophys. J.* 311 (1986) 6.
- [106] D. Blas et al., *JCAP* 1411 (2014) 039, 1408.2995.
- [107] B.D. Sherwin and M. Zaldarriaga, *Phys. Rev. D* 85 (2012) 103523, 1202.3998.
- [108] Y. Noh, M. White and N. Padmanabhan, *Phys. Rev. D* 80 (2009) 123501, 0909.1802.
- [109] S. Anselmi and M. Pietroni, *JCAP* 1212 (2012) 013, 1205.2235.
- [110] N. Padmanabhan and M. White, *Phys. Rev. D* 80 (2009) 063508, 0906.1198.
- [111] D. Blas, J. Lesgourgues and T. Tram, *JCAP* 1107 (2011) 034, 1104.2933.
- [112] S. Tassev, *JCAP* 1406 (2014) 012, 1311.6316.
- [113] E. Bellini and M. Zumalacarregui, *Phys. Rev. D* 92 (2015) 063522, 1505.03839.
- [114] D.H. Weinberg et al., *Phys. Rept.* 530 (2013) 87, 1201.2434.
- [115] R.E. Smith, R. Scoccimarro and R.K. Sheth, *Phys. Rev. D* 77 (2008) 043525, astro-ph/0703620.
- [116] F. Prada et al., *Mon. Not. Roy. Astron. Soc.* 458 (2016) 613, 1410.4684.
- [117] X. Xu et al., *Astrophys. J.* 718 (2010) 1224, 1001.2324.
- [118] T. Matsubara and V. Desjacques, *Phys. Rev. D* 93 (2016) 123522, 1604.06579.
- [119] J.C. Jackson, *Mon. Not. Roy. Astron. Soc.* 156 (1972) 1P, 0810.3908.
- [120] E. Jennings, C.M. Baugh and S. Pascoli, *Mon. Not. Roy. Astron. Soc.* 410 (2011) 2081, 1003.4282.
- [121] N. Kaiser, *Mon. Not. Roy. Astron. Soc.* 227 (1987) 1.

-
- [122] A.J.S. Hamilton, *Astrophys. J.* 385 (1992) L5.
- [123] J.A. Peacock and S.J. Dodds, *Mon. Not. Roy. Astron. Soc.* 267 (1994) 1020, astro-ph/9311057.
- [124] M. Pietroni, *JCAP* 0810 (2008) 036, 0806.0971.
- [125] N. Kaiser, *Astrophys. J.* 284 (1984) L9.
- [126] P. McDonald and A. Roy, *JCAP* 0908 (2009) 020, 0902.0991.
- [127] T. Baldauf et al., *JCAP* 1110 (2011) 031, 1106.5507.
- [128] L. Senatore, *JCAP* 1511 (2015) 007, 1406.7843.
- [129] M. Mirbabayi, F. Schmidt and M. Zaldarriaga, *JCAP* 1507 (2015) 030, 1412.5169.
- [130] R. Angulo et al., *JCAP* 1509 (2015) 029, 1503.08826.
- [131] V. Desjacques, D. Jeong and F. Schmidt, *Phys. Rept.* 733 (2018) 1, 1611.09787.
- [132] V. Assassi et al., *JCAP* 1408 (2014) 056, 1402.5916.
- [133] U. Seljak, *JCAP* 1203 (2012) 004, 1201.0594.
- [134] V. Desjacques, D. Jeong and F. Schmidt, (2018), 1806.04015.
- [135] J.E. McEwen et al., *JCAP* 1609 (2016) 015, 1603.04826.
- [136] X. Fang et al., *JCAP* 1702 (2017) 030, 1609.05978.
- [137] D. Bertolini et al., *Phys. Rev. D* 93 (2016) 123505, 1512.07630.
- [138] H. Gil-Marín et al., *JCAP* 1211 (2012) 029, 1209.3771.
- [139] T. Nishimichi et al., *JCAP* 1801 (2018) 035, 1708.00375.
- [140] M. Peloso and M. Pietroni, *JCAP* 1701 (2017) 056, 1609.06624.
- [141] E. Noda, M. Peloso and M. Pietroni, *JCAP* 1708 (2017) 007, 1705.01475.
- [142] M. Lewandowski et al., *Phys. Rev. D* 97 (2018) 063526, 1512.06831.
- [143] A. Perko et al., (2016), 1610.09321.
- [144] A.J.S. Hamilton, *Mon. Not. Roy. Astron. Soc.* 312 (2000) 257, astro-ph/9905191.
- [145] M. Simonović et al., *JCAP* 1804 (2018) 030, 1708.08130.

-
- [146] A. Andreassen et al., Phys. Rev. D95 (2017) 085011, 1604.06090.
- [147] H. Kleinert, Path Integrals in Quantum Mechanics, Statistics, Polymer Physics, and Financial Markets (World Scientific, Singapore 2002).
- [148] P. Valageas, Astron. Astrophys. 382 (2002) 477, astro-ph/0109408.
- [149] G. 't Hooft, Phys. Rev. D14 (1976) 3432, [,70(1976)].
- [150] T. Baldauf et al., JCAP 1505 (2015) 007, 1406.4135.
- [151] T. Baldauf et al., (2016), 1602.00674.
- [152] E. Pajer and M. Zaldarriaga, JCAP 1308 (2013) 037, 1301.7182.
- [153] R.E. Angulo et al., JCAP 1510 (2015) 039, 1406.4143.
- [154] V. Assassi et al., JCAP 1511 (2015) 024, 1505.06668.
- [155] S. Foreman and L. Senatore, JCAP 1604 (2016) 033, 1503.01775.
- [156] B. Horn, L. Hui and X. Xiao, JCAP 1409 (2014) 044, 1406.0842.
- [157] P.J.E. Peebles, Astrophys. J. 284 (1984) 439.
- [158] O. Lahav et al., Mon. Not. Roy. Astron. Soc. 251 (1991) 128.

